MODELING AND EXPERIMENTAL STUDIES TO OPTIMIZE THE PERFORMANCE
OF A HYDROGEN – BROMINE FUEL CELL

By

Venkata Raviteja Yarlagadda

Submitted to the graduate degree program in Chemical and Petroleum engineering and the
Graduate Faculty of the University of Kansas in partial fulfillment of the requirements for the
degree of Doctor of Philosophy.

_____

Chairperson Dr. Trung Van Nguyen

_____

Dr. Susan Williams

_____

Dr. Prajna Dhar

_____

Dr. Kevin Leonard

_____

Dr. Xianglin Li

Date Defended: June 26, 2015

The Dissertation Committee for Venkata Raviteja Yarlagadda

certifies that this is the approved version of the following dissertation:

MODELING AND EXPERIMENTAL STUDIES TO OPTIMIZE THE PERFORMANCE
OF A HYDROGEN – BROMINE FUEL CELL

_____

Chairperson Dr. Trung Van Nguyen

_____

Dr. Susan Williams

_____

Dr. Prajna Dhar

_____

Dr. Kevin Leonard

_____

Dr. Xianglin Li

Date approved: June 26, 2015

Abstract

The regenerative Hydrogen-Bromine (H_2-Br_2) fuel cells are considered to be one of the viable systems for large scale energy storage because of their high energy conversion efficiency, flexible operation, highly reversible reactions and low capital cost. The preliminary performance of a H_2-Br_2 fuel cell using both conventional as well as novel materials (Nafion and electrospun composite membranes along with platinum and rhodium sulfide electrocatalysts) was discussed. A maximum power density of 0.65 W/cm^2 was obtained with a thicker Br_2 electrode (780 μm) and cell temperature of 45°C. The active area and wetting characteristics of Br_2 electrodes were improved upon by either pre-treating with HBr or boiling them in de-ionized water. On the other hand, similar or better performances were obtained using dual fiber electrospun composite membranes (maximum power densities of 0.61 W/cm^2 and 0.45 W/cm^2 obtained with 25 μm and 65 μm electrospun membranes at 45°C) versus using Nafion membranes (maximum power densities of 0.52 W/cm^2 and 0.41 W/cm^2 obtained with Nafion 212 and Nafion 115 membranes at 45°C). The rhodium sulfide (Rh_xS_y) electrocatalyst proved to be more stable in the presence of HBr/Br_2 than pure Pt. However, the H_2 oxidation activity on Rh_xS_y was quite low compared to that of Pt. In conclusion, a stable H_2 electrocatalyst that can match the hydrogen oxidation activity obtained with Pt and a membrane with low Br_2/Br^- permeability are essential to prolong the lifetime of a H_2-Br_2 fuel cell.

A 1D mathematical model was developed to serve as a theoretical guiding tool for the experimental studies. The impact of convective and diffusive transport and kinetic rate on the performance of a H_2-Br_2 fuel cell is shown in this study. Of the two flow designs (flow-by and flow-through) incorporated in this study, the flow-through design demonstrated better performance, which can be attributed to the dominant convective transport inside the porous

electrode. Both experimental and simulated results validated that for the electrode properties and operating conditions selected, increasing the thickness of the Br_2 electrode beyond a certain value does not have any effect on the discharge performance of the fuel cell. The reactant concentration available inside the Br_2 electrode was greatly increased by operating the fuel cell at higher feed flow rates. Finally, the fuel cell configuration involving a thinner Br_2 electrode with higher specific active surface area was found to be the optimal choice for generating high performance.

The commercially available carbon gas diffusion electrodes (GDEs) were commonly used as Br_2 electrodes in the H_2-Br_2 fuel cell. However, the specific surface area of commercial carbon GDEs is quite low and needs to be enhanced. In order to improve the active surface area of carbon GDEs, a study was conducted where multi-walled carbon nanotubes (MWCNTs) were grown directly on the carbon electrode fiber surface. The results from multi-step chronoamperometry study have shown that the synthesized carbon GDEs with MWCNTs have 7 to 75 times higher active surface area than that of a plain GDE. The carbon GDE with a dense distribution of short MWCNTs evaluated in a H_2-Br_2 fuel cell has 29 times higher active surface area than that of a plain carbon electrode and was found to be highly durable at an electrolyte flow rate of 10 cc/min/cm^2. The performance of the best MWCNT GDE (1 layer) measured at 80% discharge voltage efficiency in a H_2-Br_2 fuel cell was found to be 16 times higher compared to that obtained using three layers of plain carbon electrodes. Finally, the preliminary material cost analysis has shown that the MWCNT-based carbon electrodes offer significant cost advantages over the plain carbon electrodes.

Acknowledgements

TABLE OF CONTENTS

LIST OF FIGURES

LIST OF TABLES

NOMECLATURE

a	Active surface area per unit electrode volume, cm^2/cm^3
A	Electrode surface area parallel to the fluid flow, cm^2
C_j	Concentration of species j, mol/cm^3
D_j	Diffusion coefficient of species j, cm^2/s
f	Stoichiometric ratio
F	Faraday's constant, C/mole e^-
H	Height of the electrode surface parallel to CSTM, cm
i_x	Charge transfer current density, A/cm^2
$i_{o,ref}$	Exchange current density, A/cm^2
k	Permeability of the electrode, N/atm
$k_H{}^+$	Proton conductivity, S/cm
n	Number of electrons involved in the electrochemical reaction
N_j	Molar flux of species j, mol/cm^2 s
p_j	Anodic reaction order of species j
P	Total pressure, atm
q_j	Cathodic reaction order of species j
Q	Volumetric flow rate of the electrolyte at the flow field inlet, cm^3/s
R	Gas constant, J/mol K
R_j	Reaction rate of species j, mol/cm^3 s
s_j	Stoichiometric coefficient of species j
S	Length of the CSTM inlet, cm
T	Temperature, K
U_{ref}	Open circuit potential at reference conditions, V

U^o	Standard electrode potential, V
v_{avg}	Average velocity of the electrolyte at the CSTM inlet, cm/s
W	Width of CSTM inlet, cm
x	Axial coordinate, cm
Z_j	Electrical charge of species j
EES	Electrical energy storage
PHS	Pumped hydro storage
FES	Flywheel energy storage
CAES	Compressed air energy storage
DLC	Double-layer capacitor
SMES	Superconducting magnetic energy storage
SNG	Synthetic natural gas
TES	Thermal energy storage
PCM	Phase change materials
RFB	Redox flow battery
CVD	Chemical vapor deposition
CNT	Carbon nanotube
GDE	Gas Diffusion Electrode
Greek	
ε	Porosity
μ	Viscosity, g/cm s
ϕ	Potential, V
δ	Thickness, cm

α	Transfer coefficient
γ	Exponent in the composition dependence of the ex. current density

Subscripts and superscripts

Br_2	Bromine electrode
eff	Effective
ref	Reference
a	Anodic
c	Cathodic
H_2	Hydrogen electrode
+	ionic
SHE	Standard hydrogen electrode
RE	Reference electrode
s	electronic
avg	average
CSTM	Continuous Stirred Tank Mixer
Br^-	bromide
H^+	proton
m	membrane
MWCNT	Multi-Wall Carbon Nanotube

CHAPTER 1

Introduction

1.1. Significance of Electrical Energy Storage

Electrical Energy Storage (EES) is an essential requirement because conventional power generating facilities (coal-fired or nuclear) have to be equipped to meet the varying power demands, which is quite challenging.[1] On a given day, the power demand varies from time to time and so does the price associated with it. The power suppliers often use supplemental units such as oil and gas-fired generators to meet the peak power demand that usually lasts only for a few hours. The supplemental units are flexible, but their usage is less efficient due to two major reasons. First, the supplemental units operate on more expensive fuel than the base load (coal-fired or nuclear) power plants. Second, the capital cost associated with installation and operation of supplemental units is quite high. These limitations can be overcome by incorporating EES systems into the power generating industry.

The EES system operates by storing electrical energy in a different form of energy that can be converted back to electrical energy when needed. The combination of EES and electrical power grid offers many advantages. With EES in place, the base load power plants can be designed to operate to meet average power demands rather than peak demands, which is known as either peak shaving or load leveling.[2] Moreover, the quick response time capability of the non-mechanical EES systems prevents service interruptions and assists with continuous and flexible supply of electricity. From the consumer's perspective, EES can minimize the electricity costs since it enables them to store electricity when the power prices are low and use it during the hours of peak power demand. Also, EES helps consumers when power failures occur during natural disasters.

The other emerging need for EES is to utilize intermittent renewable energy sources such as wind and solar. The use of renewable energy sources in the electricity generation was projected to increase from 18% in 2007 to 23% in 2035. Hydroelectric and wind energy were predicted to comprise 54% and 26% of the renewable electricity generation respectively.[3,4] Due to their unpredictable nature, a reliable EES technology is needed to exploit the full potential of renewable energy sources.

1.2. Different Types of EES Systems

Based on the energy form used, the EES technologies are categorized into mechanical, electrical, chemical, electrochemical, and thermal energy storage systems.

1.2.1. Mechanical Storage Systems

Pumped hydro storage (PHS), compressed air energy storage (CAES), and flywheel energy storage (FES) are the widely known mechanical energy storage systems. Both PHS and CAES use potential energy whereas FES uses kinetic energy.

PHS is the most widely installed large scale EES system. In the PHS technology, the water is pumped between two reservoirs situated at different elevations. During the off-peak hours, the water is pumped from a lower reservoir to an upper reservoir (charge process).[2,5] When needed, electricity is generated by pumping the water back from the upper reservoir to the lower reservoir through a reversible turbine-generator. On the other hand, CAES technology stores energy in the form of compressed air (typically between 4 and 8 MPa) and when required, the stored energy is extracted using a combustion turbine-generator.[2] There are several limitations despite PHS and CAES technologies being commercially available with large scale electrical energy storage capability and long lifetime. These technologies require large amounts of land and high installation costs. Also, a lot of trees and vegetation needs to

be cleared for construction, which creates environmental issues.[2] Moreover, the CAES technology is limited by its low round-trip efficiency.

In the case of FES technology, the electricity is stored in the form of kinetic energy by rotating the flywheel. The mass and speed of the flywheel rotation dictate the amount of energy stored. By reducing the speed of the flywheel, electricity can be extracted using an electrical generator. The advantages of implementing FES technology include excellent cycle stability, low maintenance, and high power densities. However, the FES technology is limited by slow response times, large maintenance costs, and high self-discharge rates due to air resistance.[2]

1.2.2. Electrical Storage Systems

Double-layer capacitor (DLC) and superconducting magnetic energy storage (SMES) are the widely known electrical energy systems.

The conventional electrical capacitors consist of two metal plates separated by a non-conducting layer of dielectric and stores the energy electrostatically. When there is a potential difference across the metal plates, an electric field develops across the dielectric resulting in the accumulation of positive charge at one plate and negative charge at the other plate. The energy density of conventional electrical capacitors is low and limited by the area of the dielectric material.[2] However, the recently developed electrochemical double-layer capacitors have much higher energy storage capacity. Electrochemical double-layer capacitors, also known as supercapacitors electrostatically store the electrical energy by separating the charge formed in a Helmholtz double-layer at the interface between a conductive electrode (usually a solid carbon electrode with high surface area) surface and a liquid electrolyte.[2,6] The charge distance separation in the electrical double layer is in the order of a few angstroms (3 to 8 Angstroms).[7] DLCs are capable of fast charge and discharge cycles due to their extremely low

internal resistance. The advantages of DLCs include high power density capability, short response times, and long life time.[7] However, they are limited by low energy density values making them unsuitable for storing energy over longer periods of time. Also, the capital costs for installing DLCs are very high.

SMES systems store electrical energy in an inductor made from superconducting material. They can also store electrical energy in the magnetic field created by passage of electric current. The inductors are usually soaked in liquid helium to keep them in a superconducting state. The energy stored in a SMES system is calculated using the equation, $E = 0.5LI^2$, where L is the inductance of the coil and I is the electric current passing through the inductor coil. SMES systems have very high energy conversion efficiency (typically greater than 97%) and fast response times.[2] However, the installation cost is very high and the strong magnetic field has a negative impact on the environment.

1.2.3. Chemical Storage Systems

Hydrogen (H_2) and synthetic natural gas (SNG) are generated as energy carriers in widely installed chemical storage systems. In the presence of excess electricity, water is split into H_2 and oxygen (O_2) using an electrolyzer. In order to produce SNG (or methane), there is an additional step where H_2 is reacted with carbon dioxide. When required, the energy carriers are used to generate electricity. The advantage of the chemical storage systems is that they can store large amounts of energy (usually in Twh). However, the chemical energy storage technologies are still in the research and development phase and haven't been commercialized yet.[8] While SNG can take advantage of the already existing gas grid infrastructure, the efficiency of power generation using SNG is less than 35%, which is quite low. Currently, research efforts are underway to commercialize the chemical storage technologies.[8]

1.2.4. Thermal Storage Systems

Thermal energy storage (TES) systems store materials in insulated containments to preserve their temperatures (high or low). Based on the temperature of the materials, heat or cold can be extracted and used to generate electricity using heat engine cycles. Depending on the operating temperature of the energy storage materials, the TES systems are classified into either low-temperature or high-temperature TES systems.[2] The storage of sensible heat is the widely used method of all the thermal energy storage technologies. It is accomplished by simply changing the temperature of storage mediums such as water. One of the other important TES technologies involves latent heat storage, which can be accomplished using phase change materials (PCM).[2] Materials such as molten salt and paraffin wax that undergo solid to liquid phase change are widely used as PCMs. The advantage of using latent heat storage is that a large amount of energy can be stored within a small volume and with minimal change in temperature. The disadvantages include slow response times, low round trip efficiency and large investments required to build the infrastructure.[2]

1.3. Benefits of Electrochemical Energy Storage Systems

Electrochemical energy storage systems provide direct conversion between electrical and chemical energy. The fast response time (typically in milliseconds) coupled with high performance and low cost makes electrochemical energy storage superior to other forms of energy storage described in the previous sections.[9,10] While the widely installed mechanical energy storage systems require special terrain, the electrochemical energy storage systems don't, making them suitable for both stationary and mobile applications.[9] Also, most of the electrochemical energy storage systems have low impact on the environment and hence can be stationed near residential locations. Some of the widely used electrochemical energy systems

include electrochemical capacitors, secondary or rechargeable batteries, and flow batteries.[9,10] Figure 1.1 shows the energy and power densities of capacitors, electrochemical capacitors, batteries, and fuel cells/flow batteries.[10] As shown in Figure 1.1, the high power densities of electrochemical capacitors contribute towards the power quality management but they are not suitable for large scale energy storage because of their low energy densities. On the other hand, batteries and flow batteries have the potential for large scale energy storage and will be discussed in the following sections.
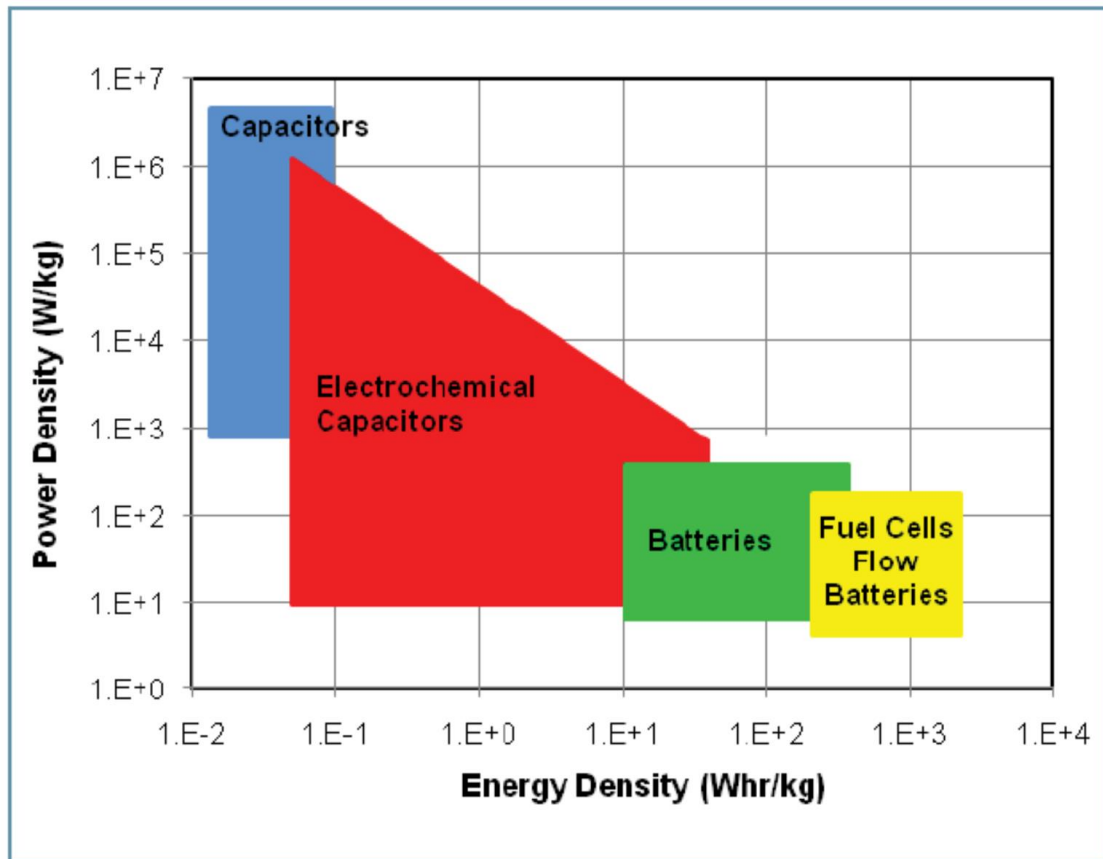
Figure 1.1. Power and energy densities of energy storage technologies[10]

[Nguyen *et al.* (2010)]

1.3.1. Secondary Batteries (Rechargeable Batteries)

Secondary or rechargeable batteries are the oldest and most widely used electrochemical energy storage devices. Some of the mature and commercially available battery technologies are discussed in this section.

1.3.1.1. Lead-Acid Batteries

Lead-acid batteries are the most widely used electrochemical energy storage devices due to their reliability, high efficiency (70%-76%), and low cost.[2] The lead acid battery consists of lead (Pb) and lead oxide (PbO_2) electrodes in a sulfuric acid electrolyte (concentrations close to 6M). During discharge, Pb and PbO_2 electrodes are converted to lead sulfate, the electrolyte loses the dissolved sulfuric acid, and water is generated. The process is reversed during charge. The cell reactions are shown below.

$$\textbf{Pb electrode: } Pb + SO_4^{2-} \underset{\text{charge}}{\overset{\text{discharge}}{\rightleftharpoons}} PbSO_4 + 2e^-$$

$$\textbf{PbO}_2 \textbf{ electrode: } PbO_2 + SO_4^{2-} + 4H^+ + 2e^- \underset{\text{charge}}{\overset{\text{discharge}}{\rightleftharpoons}} PbSO_4 + 2H_2O$$

$$\textbf{Overall: } Pb + PbO_2 + 2H_2SO_4 \underset{\text{charge}}{\overset{\text{discharge}}{\rightleftharpoons}} 2PbSO_4 + 2H_2O$$
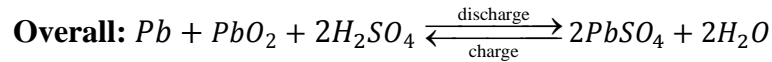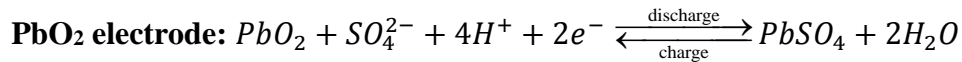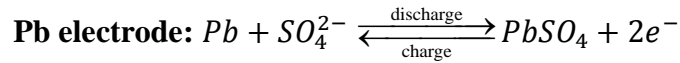
The disadvantages of lead-acid batteries include overcharging and freezing point depression of the electrolyte. While charging the lead-acid battery, the water in the electrolyte can decompose to hydrogen and oxygen gases, resulting in the loss of electrolyte and leading to poor discharge performance. The electrolyte in the lead-acid battery is diluted during discharge and more likely to freeze during winter.[11]

1.3.1.2. Sodium-Sulfur Batteries

Sodium sulfur batteries consist of molten sulfur and sodium electrodes separated by a beta alumina ceramic electrolyte.[2,6] During discharge, the sodium in the negative electrode is

oxidized and generates electrons that travel through the external circuit and the sodium ions flow through the electrolyte to combine with sulfur anions generated by the reduction reaction of sulfur and form polysulfides. The beta alumina ceramic electrolyte allows only the Na^+ to pass through as it is a poor electronic conductor. During charge, sulfide in sodium polysulfides is oxidized to sulfur and the sodium ions are released to be transported through the electrolyte to the sodium electrode where they are reduced to sodium metal. The electrochemical reactions associated with the sodium-sulfur battery are shown below.

$$\text{Na electrode: } 2Na \underset{\text{charge}}{\overset{\text{discharge}}{\rightleftharpoons}} 2Na^+ + 2e^-$$

$$\text{S electrode: } xS + 2e^- \underset{\text{charge}}{\overset{\text{discharge}}{\rightleftharpoons}} S_x^{2-}$$

$$\text{Overall: } 2Na + xS \underset{\text{charge}}{\overset{\text{discharge}}{\rightleftharpoons}} Na_2S_x$$
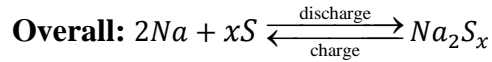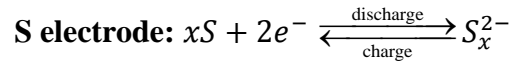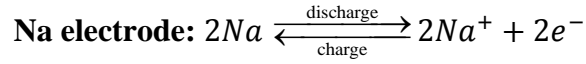
The major drawbacks associated with this system are high temperature operation (between 300 and 350°C), which consumes a part of the battery's own stored energy. Also, potential fires could result when elemental sodium comes into contact with air or moisture.[2,9]

1.3.1.3. Lithium-Ion Batteries

One of the other battery systems that are widely used for small scale applications are lithium-ion batteries.[2,6] A lithium-ion battery consists of a lithiated metal oxide ($LiCoO_2$, $LiMO_2$, $LiNiO_2$ etc.) electrode and a graphitic carbon electrode separated by a lithium salt electrolyte ($LiPF_6$). During charge, the metal ions in the lithiated metal oxide electrode are oxidized and the Li ions are released to move through the electrolyte to the carbon electrode where they are reduced to lithium metal and get intercalated in the graphitic carbon electrode. When the cell needs to discharge, the reverse process occurs. The cell reactions are shown below.

Lithiated metal oxide electrode: $CoO_2 + Li^+ + e^- \underset{\text{charge}}{\overset{\text{discharge}}{\rightleftarrows}} LiCoO_2$

Graphitic carbon electrode: $LiC_6 \underset{\text{charge}}{\overset{\text{discharge}}{\rightleftarrows}} Li^+ + e^- + C_6$
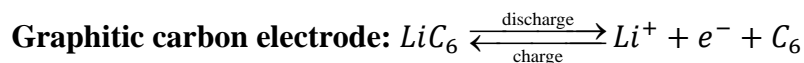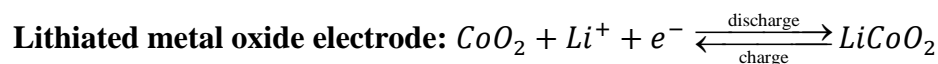
Over 50% of the small scale appliances such as laptops, batteries, and hybrid electrical vehicles use lithium-ion batteries.[2] Lithium-ion batteries are currently replacing the lead-acid batteries due to their significantly higher energy densities. However, the major limitation is the flammable nature of the electrolytes used in the lithium-ion batteries.[9]

1.3.2. Limitations of Secondary Battery Technologies

Secondary battery technologies suffer from two major limitations. First, the electro-active species are stored internally in the secondary batteries. As a result, the power density and energy density of the battery are coupled. The power density of the battery depends upon the catalytic, electrical, and transport properties of the electrode whereas the energy density is correlated to the mass of the electro-active species. When more energy is required, multiple battery units have to be added which leads not only to unnecessary costs (e.g. cost of electrodes, electrolytes, and separators) but also to lower cell efficiencies due to increase in internal resistances.[9] Second, electrodes in the secondary battery are also part of the electrochemical fuel and, hence, undergo significant physical and chemical changes during the charge and discharge cycles.[10]

1.3.3. Flow Batteries/Reversible Fuel Cells

The limitations of secondary batteries can be overcome by using flow batteries or reversible fuel cells. The electro-active species in the flow batteries are stored externally and hence the energy density and power density can be decoupled. The electro-active species are only introduced into the power conversion device when required.[9,10,12,13] While flow batteries can be considered as reversible fuel cells, a lot of fuel cell technologies such as hydrogen–oxygen

system cannot be considered as flow batteries because of their poor reversibility. Note that, while a reversible fuel cell is essentially a flow battery, what differentiates a fuel cell from a flow battery is that the reactions at one or both of the fuel cell electrodes require a catalyst. A conventional redox flow battery (RFB) has all the electroactive species stored outside the power conversion device in the form of liquid electrolytes (e.g. all vanadium, iron-chromium etc.). Some of the other conventional RFBs have a gaseous reactant flowing through one or both the electrodes (e.g. hydrogen-bromine, hydrogen-chlorine etc.). The systems where one of the electro-active species is stored internally are labelled as hybrid flow batteries (e.g. zinc-bromine, zinc-chlorine etc.). RFBs are suitable for energy storage applications with power ratings from 1 KW to 100's of MW.[9,12-13]

Figure 1.2 shows a schematic of a RFB.[10] In the presence of excess energy either from wind or solar, the power conversion device is used to store the electrical energy in the form of chemical energy (charge process) and the process is reversed when electrical energy is required (discharge process). The concentration of the electroactive species in the storage tanks can be controlled and monitored. A membrane or a porous separator is usually present between the anode and the cathode to prevent the crossover of unwanted electro-active species and to allow the common counter ion carrier to maintain electroneutrality. The crossover of unwanted electro-active species results in a chemical short circuit. The fact that the electrodes of these RFBs act as the conversion sites for the reactants and are not part of the reactant/product system implies these systems have much longer cycle life than conventional rechargeable batteries.[9,12-13] The energy level in these fuel cells is determined by the concentration and volume of the reactants whereas the power level is determined by the electrode size and number of cells in

the stack. Since the electrodes are separated from the electro-active reactants, they are immune to physical and chemical degradation.
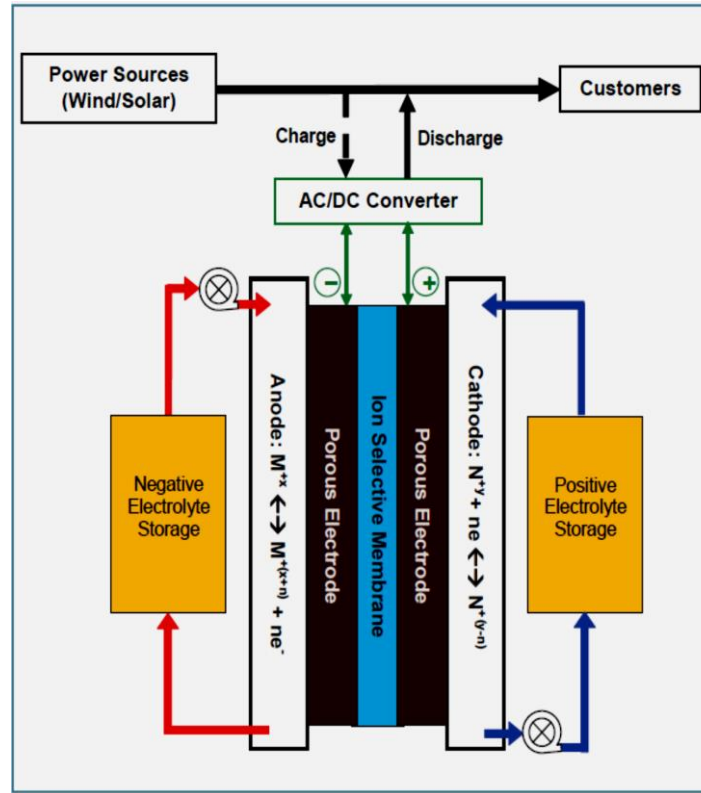
Figure 1.2. Schematic of a redox flow battery during discharge[10] [Nguyen *et al.* (2010)]

There are few limitations with using RFBs for electrical energy storage. First, the RFB systems require a lot of infrastructure such as pumps, storage tanks, and sensors.[9,10] Second, most of the RFBs are still in the research phase and only a few RFBs such as the all vanadium and zinc-bromine systems are commercially deployed.[9]

1.3.4. Redox Flow Battery Chemistries

Table 1.1 shows some of the mature redox flow battery chemistries that were commercially deployed for large scale EES.

Table 1.1. Different redox flow battery chemistries with reactions and cell potentials[9,10,11,13]

System	Reactions	E_{cell}^0
Iron/Chromium	Iron: $Fe^{2+} \underset{charge}{\overset{discharge}{\rightleftarrows}} Fe^{3+} + e^-$ Chromium: $Cr^{3+} + e^- \underset{charge}{\overset{discharge}{\rightleftarrows}} Cr^{2+}$	1.2 V
Bromine/Polysulfide	Bromine: $Br_2 + 2e^- \underset{charge}{\overset{discharge}{\rightleftarrows}} 2Br^-$ Polysulfide: $2S_2^{2-} \underset{charge}{\overset{discharge}{\rightleftarrows}} S_4^{2-} + 2e^-$	1.5 V
All Vanadium	Negative: $V^{2+} \underset{charge}{\overset{discharge}{\rightleftarrows}} V^{3+} + e^-$ Positive: $VO_2^+ + e^- \underset{charge}{\overset{discharge}{\rightleftarrows}} VO^{2+}$	1.3 V
Zinc/Bromine (Hybrid)	Zinc: $Zn \underset{charge}{\overset{discharge}{\rightleftarrows}} Zn^{2+} + 2e^-$ Bromine: $Br_2 + 2e^- \underset{charge}{\overset{discharge}{\rightleftarrows}} 2Br^-$	1.8 V

Of all the redox flow technologies listed in Table 1.1, all vanadium system is the most mature and widely commercialized system. Maria Skyllas-Kazacos and co-workers proposed the all-vanadium flow battery system in 1984 at the University of New South Wales.[9,14] The advantage of using an all vanadium system is that the crossover issues are minimal. The electrolyte used in both the electrodes are essentially composed of a single element (vanadium in this case) with different oxidation states. The crossover of common vanadium cations might result in an efficiency loss but the electrolytes can still be electrochemically restored to their original forms.[9,14] Often, some of the all vanadium systems use a microporous separator instead of a proton conducting membrane. The limitations of the all vanadium system are high prices of vanadium and the low solubility of vanadium in the electrolyte solution. Some of the

practical demonstrations include a 250 kW/520 kWh system established in South Africa (2001) and a 250 kW/1 MWh system installed by Hydro Tasmania in Australia for wind energy storage (2003). Also, a 1 MW/8 MWh vanadium redox flow battery demonstration was funded by United States Department of Energy (DOE) in 2010.[9]

The first 1 kW iron-chromium redox flow battery prototype was developed in 1980 by National Aeronautics and Space Administration (NASA) and other similar demonstrations were developed by Japan and Spain in the mid 1990s.[9] The reason behind exploring iron-chromium system was the availability and low cost of iron and chromium materials. However, the iron-chromium system was not widely commercialized because the energy densities were low and chromium reactions were very slow, thus requiring expensive catalysts. Bromine-polysulfide redox flow battery was one of the other mature technologies that was considered because of the abundance and low cost of active species used in them. The bromine-polysulfide RFB was tested by Regenesys technology from 1993 to 2006 and was later acquired by VRB power systems.[9] A 12 MW/120 MWh bromine-polysulfide RFB at utility scale was demonstrated by Regenesys technology.[9] Even though the bromine-polysulfide battery came close to commercialization, technical issues such as cross contamination, and expensive sodium polysulfide synthesis process restricted their advancement.[9,12-14]

The hybrid zinc-bromine battery is one of the other flow battery systems that was successfully demonstrated for energy storage.[2,9] One of the projects was a 250 kW/500 kWh utility system installed in New South Wales, Australia to complement an existing 20 kW photovoltaic system.[9] The scale up and commercialization of zinc-bromine flow battery is still limited by formation of zinc dendrites that result in short-circuiting across the microporous separator.[9,12] Also, bromine complexing agents used in this system are quite expensive.

In addition to the above discussed RFBs, vanadium-polyhalide, hydrogen-bromine, and zinc-cerium are among the several other promising flow battery technologies.[10] Several research efforts conducted in this area have identified the reversible hydrogen-bromine (H_2-Br_2) fuel cell as one of the suitable systems for large scale electrical energy storage because of its numerous advantages such as rapid Br_2 and H_2 reaction kinetics, low cost ($1-$3 per kg of hydrobromic acid), and relative abundance of the active materials used in this system.[15-19] However, the toxicity and corrosivity of the HBr/Br_2 electrolyte used in this system poses major safety and durability challenges that need to be addressed.

1.4. History of Reversible Hydrogen-Bromine (H_2-Br_2) Fuel Cell

Hydrogen-Bromine (H_2-Br_2) fuel cell was first investigated by Werner and Glass in 1965.[15] In this study, the properties (electrical conductivity and density) of hydrobromic acid-bromine-water solutions were determined. Also, the preliminary H_2-Br_2 fuel cell performance was measured in this study. The H_2-Br_2 fuel cell received a lot of attention between mid-1970s and early 1980s due to the energy crisis and was considered for storing solar and wind energy.[16,17] Between mid-1980s and late 1980s, NASA and Texas Instruments examined the feasibility of reversible H_2-Br_2 fuel cells for aerospace and solar energy storage applications.[20,21] A more stable Nafion membrane, which was newly introduced into the fuel cell market in early 1980s was incorporated to improve the performance of these H_2-Br_2 fuel cells. A start-up company by the name of Solar Reactor Technologies, Inc. in collaboration with University of Florida examined H_2-Br_2 and H_2-Cl_2 fuel cell systems for grid storage.[21] This start-up company was eventually shut down due to lack of government's interest in solar energy during 1990s.[21] However, the recent interest in renewable energy storage has generated interest in H_2-Br_2 and other flow battery technologies.

1.5. Regenerative Hydrogen-Bromine (H_2-Br_2) Fuel Cell

The regenerative H_2-Br_2 fuel cell has been a subject of notable interest and is considered as one of the suitable candidates for large scale electrical energy storage. A conventional H_2-Br_2 fuel cell consists of a H_2 electrode and a Br_2 electrode separated by a proton exchange membrane as shown in Figure 1.3.[22] The starting material in the H_2-Br_2 fuel cell system is hydrobromic acid (HBr). With excess energy from either wind or solar, the HBr solution is electrolyzed to form H_2 and Br_2 at their respective electrodes (charge process) and the process is reversed during discharge. Also, the bromide (Br⁻) ion in the solution may react with neutral bromine (Br_2) species to form a tri-bromide (Br_3^-) complex. The electrochemical and complexation reactions involved in this fuel cell system are shown below.

Electrochemical reactions

$$\textbf{H}_2 \textbf{ electrode: } H_2 \underset{\text{charge}}{\overset{\text{discharge}}{\rightleftharpoons}} 2H^+ + 2e^- \quad E^o_{H_2} = 0\ V$$

$$\textbf{Br}_2 \textbf{ electrode: } Br_2 + 2e^- \underset{\text{charge}}{\overset{\text{discharge}}{\rightleftharpoons}} 2Br^- \quad E^o_{Br_2} = 1.09\ V$$

$$\textbf{Overall: } Br_2 + H_2 \underset{\text{charge}}{\overset{\text{discharge}}{\rightleftharpoons}} 2HBr \quad E^o_{cell} = 1.09\ V$$
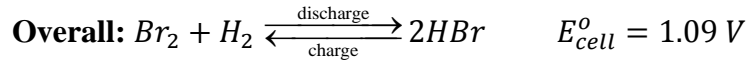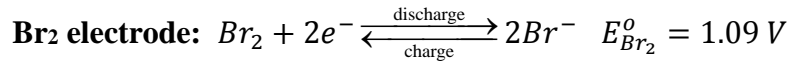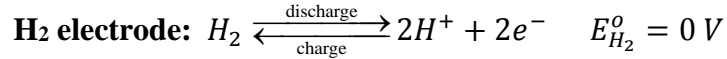
where $E^o_{H_2}$, $E^o_{Br_2}$, and E^o_{cell} represent the hydrogen, bromine, and overall cell potentials at standard conditions (concentration of 1M and activity of 1 for aqueous and pure species, and pressure of 1atm for gaseous species at 25°C).

Complexation reactions

$Br_2 + Br^- \longleftrightarrow Br_3^-$ $\textbf{K}_{eq} = \textbf{16}$

$2Br_2 + Br^- \longleftrightarrow Br_5^-$ $\textbf{K}_{eq} = \textbf{40}$ [19]

where K_{eq} is the equilibrium constant. The HBr electrolyte complexes the Br_2 present in the

H_2-Br_2 system thereby enhancing its solubility. The overall cell potential can be calculated for

the deviation in standard concentration conditions by using the Nernst equation.

$$E = E^o - \frac{RT}{nF} \ln \frac{(a_{H^+})^2 (a_{Br^-})^2}{(p_{H_2})(a_{Br_2})}$$ [1.1]

where a_i represents the activity of aqueous species; p_i represents the partial pressure of gas; R

represents the universal gas constant; T represents the temperature in K; n represents the

number of electrons in the reaction and F represents the Faraday constant.

The temperature dependence on the cell potential is determined by the following equation.

$$\left(\frac{\partial E}{\partial T}\right)_p = \frac{\Delta S}{nF}$$ [1.2]

where E and S represents the cell potential and entropy
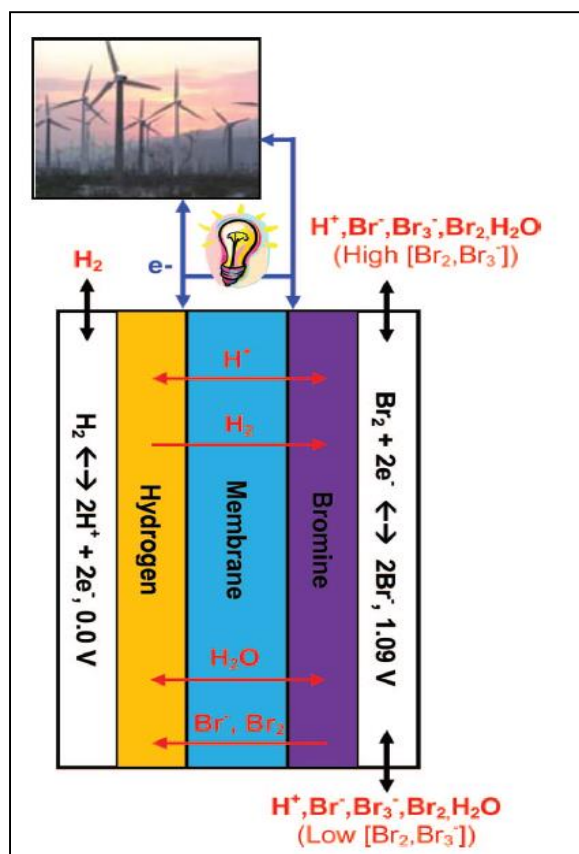
Figure 1.3. Schematic of a reversible H_2-Br_2 fuel cell system[22] [Kreutzer *et al.* (2012)]

1.6. Components of a Reversible H_2-Br_2 Fuel Cell

A reversible H_2-Br_2 fuel cell consists of the H_2 and Br_2 electrodes, an ion exchange membrane, two flow field plates, and two current collectors enclosed between the end plates.

1.6.1. H_2 Electrode

The H_2 electrode configuration used in a polymer electrolyte membrane fuel cell is used in a H_2-Br_2 fuel cell as well.[23] High surface area carbon supported platinum (Pt) catalyst is used to catalyze the hydrogen oxidation and evolution (HOR/HER) reactions. The catalyst ink is prepared by mixing the Pt catalyst with a Nafion ionomer and polytetrafluoroethylene (PTFE) suspension, which is then coated onto the microporous layer (MPL) of a bi-layer carbon gas

diffusion materia to form a gas diffusion electrode (GDE). The purpose of the Nafion ionomer is to provide ionic pathways for the hydronium ions (H_3O^+) whereas the Pt/C catalyst provides electronic conduction pathways. Finally, the PTFE dispersion assists in handling two phase (gas and liquid) transport and prevents the H_2 electrode from flooding.[23] The H_2 electrode is hot pressed onto an ion exchange membrane (usually Nafion) to provide continuous ionic conduction pathways between the Nafion ionomer present in the catalyst layer (CL) and the membrane.

One of the other approaches used to synthesize H_2 electrodes was by coating the Pt catalyst ink directly onto the membrane. These types of electrodes are known as catalyst coated membranes (CCMs). The CCMs are later physically coupled with the gas diffusion layers to form the H_2 electrodes.

1.6.2. Br_2 Electrode

While the H_2 reactions currently require the use of precious metal catalysts like platinum, the bromine reactions don't since reasonable exchange current densities can be obtained with carbon materials.[24] Even though the exchange current density of the Br_2 reactions on platinum is two orders of magnitude higher than that on plain carbon materials, the corrosivity and toxicity of hydrobromic acid (HBr) and Br_2 species makes it impractical to use any noble metal catalysts in the Br_2 electrode.[24] Carbon electrodes with high porosity are widely used to maximize the utilization of aqueous reactants (HBr/Br_2).

1.6.3. Membrane

The Br_2 electrode and the H_2 electrode are separated by a proton exchange membrane (Nafion). The structure of Nafion is shown in Figure 1.4. As shown in Figure 1.4, the Nafion structure consists of a Teflon backbone (-CF_2-CF_2-) with sulfonate (-SO_3H) groups. The protons are

migrated along the SO$_3$H groups. The SO$_3$H groups are hydrophilic and hence attract liquid water. Nafion membranes are commercially available in different thicknesses.[23] Nafion 112 (51 μm), Nafion 115 (127 μm), and Nafion 212 (51 μm) are the widely used proton exchange membranes. The difference between Nafion 112 and Nafion 212 membranes is their synthesis process. Nafion 112 membrane is synthesized by an extrusion process whereas Nafion 212 is synthesized by a solution casting process. The advantage of the solution casting process is that it avoids membrane dehydration, which is usually a limitation associated with extrusion at high temperatures.
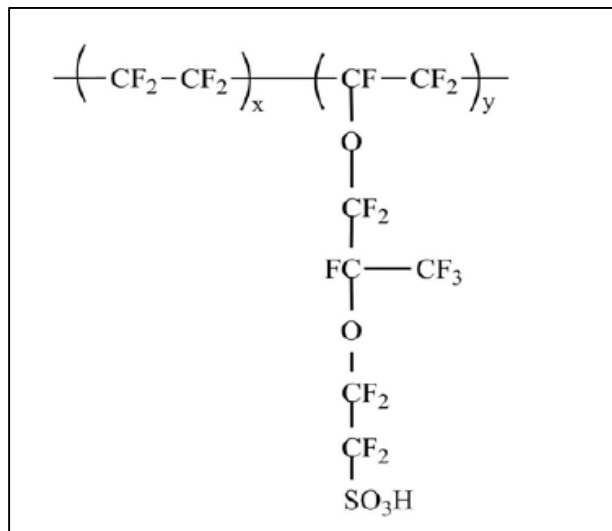
Figure 1.4. Structure of a Nafion membrane

1.6.4. Flow Field Plates and Current Collectors

Graphite or carbon blocks are widely used as flow plates because they are immune to corrosion unlike most of the metals. A polymeric binder of some kind is required to fabricate these graphite blocks. The graphite layers in the graphite block might be de-laminated since bromine can attack the polymeric binder (shown in Figure 1.5). In conclusion, graphite flow fields can

be used in the H$_2$ electrode but not in the Br$_2$ electrode. Tantalum and Niobium are the only two metals that can withstand the corrosive Br$_2$ environment.[25]

On the other hand, current collectors can be fabricated from either stainless steel or copper. However, they might need to be replaced occasionally if they come into contact with HBr/Br$_2$ solution due to leakage in the fuel cell stack.
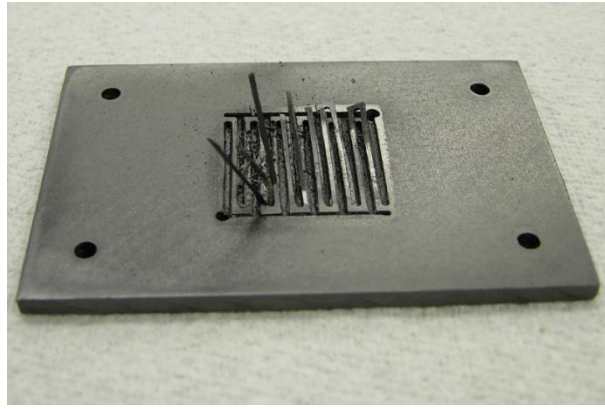
Figure 1.5. Graphite flow field after being exposed to HBr/Br$_2$ solution

1.7. Performance of a H$_2$-Br$_2$ Fuel Cell

For every electrode or half-cell in an electrochemical system, there is a voltage source (electrochemical potential) and three resistance sources (activation, ohmic and mass transport resistances). These are represented by the schematic and circuit-analog drawings shown in Figure 1.6. Since these resistances are in series, the voltage losses are additive and can be represented by the following equation.

$$\Delta V(voltage\ loss) = IR_{total} = I(R_{act} + R_{ohm} + R_{mass}) \qquad [1.3]$$
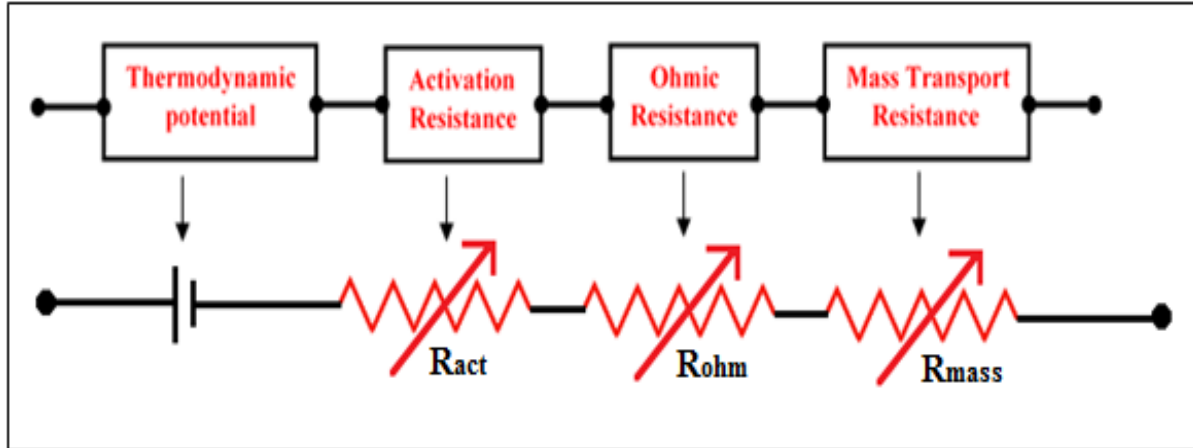
Figure 1.6. Voltage (electrochemical potential) and resistance sources (activation, ohmic, and mass transport resistances) represented by a schematic and a circuit analog

The open circuit voltage (OCV) represents the voltage between the two electrode terminals of a electrochemical cell at zero current. The polarization curve is obtained by plotting voltage versus current density. A potential below the OCV is applied to discharge the electrochemical cell. The activation resistance (R_{act}), often represented by the Butler-Volmer or similar equations, can be linear or non-linear (exponential) depending on the magnitude of the exchange current density or the rate constant (shown in Figure 1.7). As shown in Figure 1.7, the performance (polarization curve) trend is linear when the exchange current density is high and non-linear when it is low. The performance regions associated with ohmic (R_{ohm}) and mass transport (R_{mass}) resistances are usually linear.
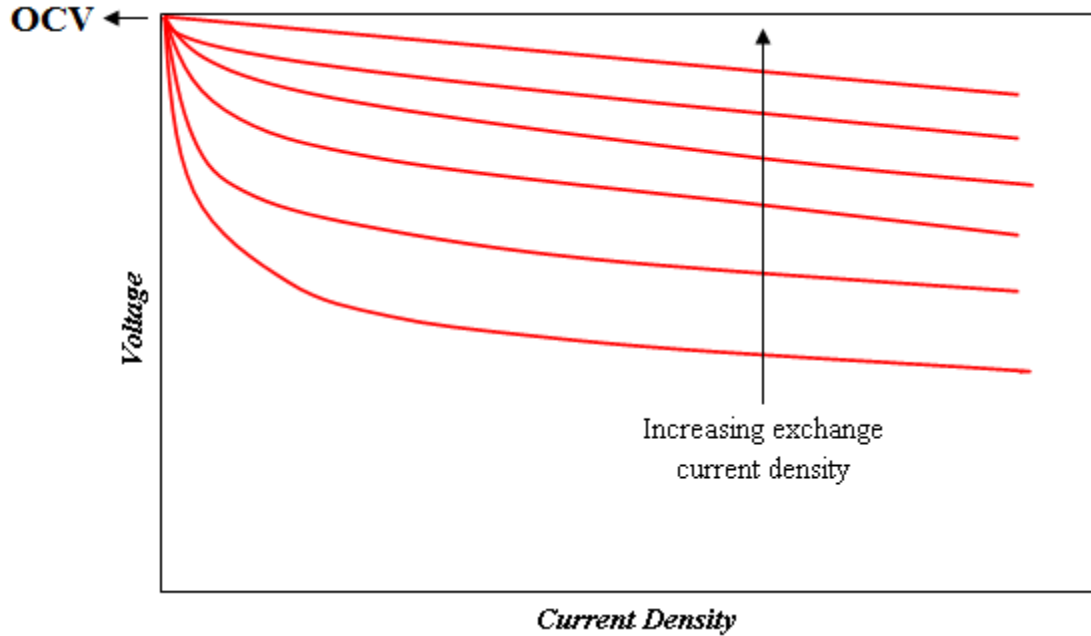
Figure 1.7. Effect of exchange current density on the activation resistance

Figure 1.8 shows two sets of typical fuel cell polarization curves highlighting the activation, ohmic, and transport controlled regimes. The first set of polarization curves represents a reaction with a low exchange current density like the oxygen reaction and the second set of polarization curves represents a reaction with high exchange current density like the hydrogen or bromine reactions. At low currents, the activation loss arises from slow electrochemical reactions at the electrode surface. The large activation loss in a Hydrogen-Oxygen (H_2-O_2) fuel cell is caused by the slow kinetics of the oxygen reduction reaction. The ohmic loss is caused by ionic resistance in the electrolytes and electrodes, electronic resistance in the electrodes, current collectors and finally the contact resistances. The voltage drop is directly proportional to the resistance (R_{ohm}) and current (I) as shown in the following equation.

$$V = IR_{ohm} \qquad\qquad [1.4]$$

At higher current densities, the concentration loss occurs due to reactant depletion. The transport rate of reactants to the electrode surface cannot support the required reaction rate. This results in mass transport limited performance. For a full electrochemical cell with two electrodes, there is another set of voltage and resistances. One can combine the voltage sources and the resistances at both electrodes for the whole cell to calculate the total voltage losses of an electrochemical cell.
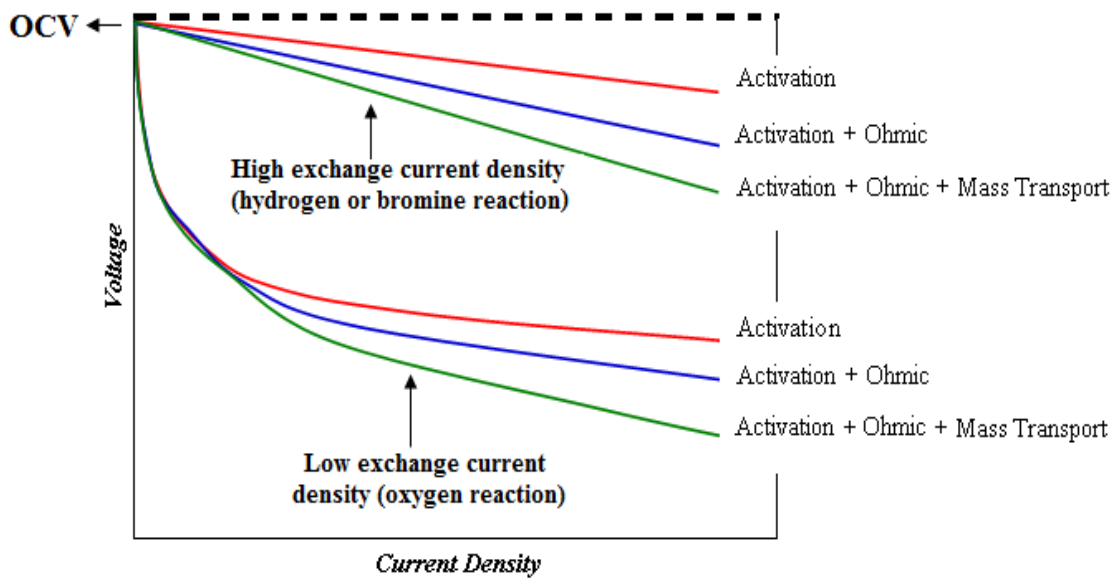
Figure 1.8. Electrochemical cell performances showing different voltage losses associated with high and low exchange current density reactions

The performance of H_2-Br_2 and H_2-O_2 fuel cells is shown in Figure 1.9. Even though the H_2-O_2 fuel cells are known for their higher gravimetric energy density and long cell life, their performance is affected by the sluggish oxygen reduction kinetics as shown in Figure 1.9.[22] In the case of the Hydrogen-Bromine (H_2-Br_2) fuel cells, faster reaction kinetics reduces the

23

activation losses and enhances the electric-to-electric energy conversion efficiency. Due to the rapid kinetics of bromine and hydrogen reactions, the performance of a H_2-Br_2 fuel cell is often limited by mass transport. The bromine electrode has been identified as the most likely transport limiting component because of the slower liquid phase transport rates of its aqueous species. A recent study by Kreutzer et al. comparing the performance of the H_2-O_2 and H_2-Br_2 systems shows that the latter is a suitable option for energy storage because of its high energy conversion efficiency and power density capability.[22]
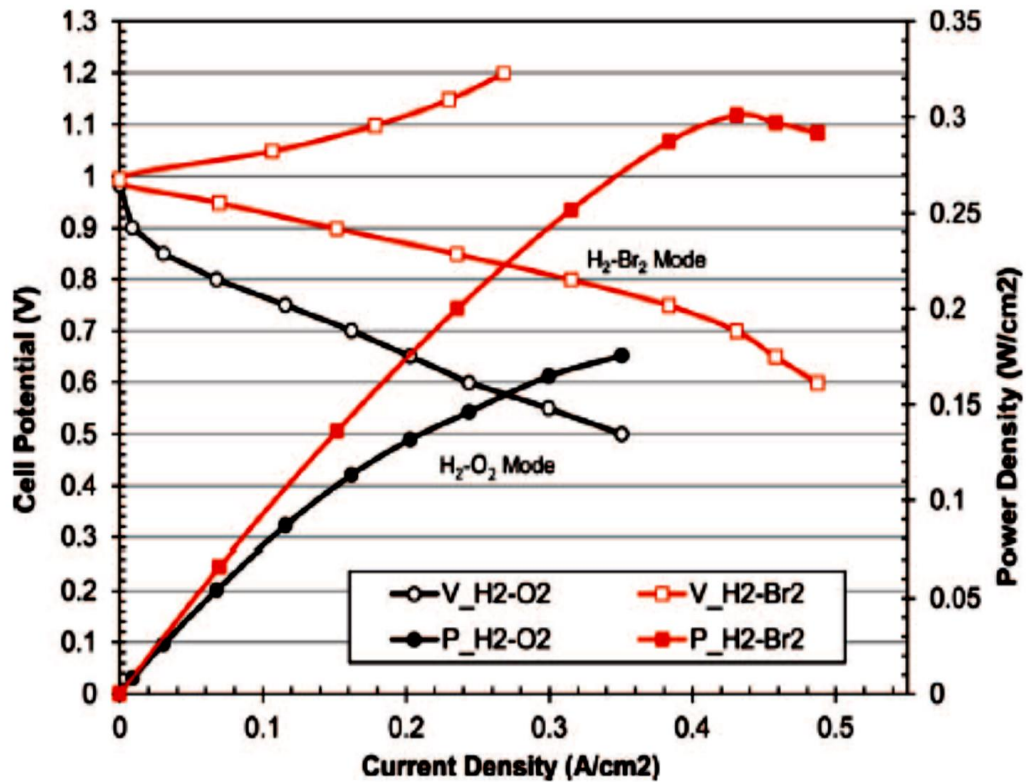
Figure 1.9. Performance of H_2-Br_2 and H_2-O_2 fuel cells at room temperature (25°C) [22]

[Kreutzer *et al.* (2012)]

1.8. Motivation and Objectives

The H_2-Br_2 fuel cell has been extensively studied in the past highlighting numerous advantages and some limitations of the system.[15-19,22,24] Despite the numerous attractive features offered by the H_2-Br_2 fuel cell, there are some major material-related challenges that need to be solved to bring this system to commercialization. During fuel cell operation, especially in the charge direction, there is a possibility of species such as bromine (Br_2), bromide (Br^-), and tri-bromide (Br_3^-) crossing over to the H_2 electrode through the polymer electrolyte membrane due to electroosmotic drag. Subsequently, this will poison and corrode the platinum (Pt) catalyst. The crossover may severely affect the fuel cell performance. Fuel cell lifetime is reduced as the rate of crossover increases.

There are two possible approaches to limit the effect of crossover. The first approach is to use a membrane that is impermeable to bromine, bromide, and tri-bromide cross over. The second approach is to use an alternative H_2 catalyst with similar activity as Pt that is stable in the HBr/Br_2 environment. Hence, alternative catalyst and membrane materials are required to prolong the lifetime of the H_2-Br_2 fuel cell. In chapter 2, the preliminary performance of a H_2-Br_2 fuel cell using both conventional as well as novel materials (Nafion and electrospun composite membranes along with Pt and Rh_xS_y electrocatalysts) will be discussed. The electrospun composite membranes were provided by Dr. Pintauro's research group at Vanderbilt University.

Several experimental investigations have been conducted to evaluate the H_2-Br_2 fuel cell system but only a few mathematical models exist in literature.[27,28] In chapter 3, a one-dimensional, steady state mathematical model of a H_2-Br_2 fuel cell based on dilute solution theory is developed to identify the transport processes and components that limit the

performance of this system and component and cell designs that will enhance the performance of the system. Also, the purpose of this model is to serve as a theoretical guiding tool for the future experimental studies of this system. Several case studies impacting the kinetic rate and mass transport in the fuel cell are discussed in this study by varying the magnitude of the key parameters.

Typically, a plain porous gas diffusion electrode (GDE) with high porosity was used as the Br_2 electrode However, the specific surface area of commercially available porous carbon GDEs is quite low and needs to be improved. The high porosity facilitates the liquid electrolyte to access most of the active surface area associated with the carbon electrode. Hence, it is important that morphological properties (porosity and tortuosity) of the carbon electrode remain undisturbed while improving the active surface area. Hence, an alternate approach that can increase the active surface area without affecting the transport related morphological properties like porosity and tortuosity of the electrode is needed.

A novel approach to enhance the existing carbon electrode surface area without significantly affecting the porosity and the electrode thickness is discussed in chapters 4 and 5. The aim of this approach is to grow nanotubes directly onto the electrode fiber surface to create high active surface area. The synthesis of these carbon nanotube (CNT) electrodes and their preliminary performance are presented in chapter 4. In chapter 5, the optimization process employed to increase the active surface area and durability of the CNT based electrodes is discussed. Also, the durability and performance of the CNT based electrodes are analyzed in chapter 5. Finally, a preliminary cost analysis from the materials perspective that highlights the cost benefits of using novel CNT based electrodes over commercially available porous carbon electrodes is shown in chapter 5.

1.9. References

1. Paul Denholm, Erik Ela, Brendan Kirby, and Michael Milligan, "The Role of Energy Storage with Renewable Electricity Generation," *Technical Report*, NREL/TP-6A2-47187, January 2010.

2. Haisheng Chen, Thang Ngoc Cong, Wei Yang, Chunqing Tan, Yongliang Li, and Yulong Ding, "Progress in electrical energy storage system: A critical review," *Progress in Natural Science*, **19**, 291–312 (2009).

3. Marco Tortora, "Sustainable systems and energy management at the regional level: comparative approaches," Chapter 3, pg. 45 (2011).

4. Nicholas Apergis and James E. Payne, "Renewable and non-renewable energy consumption-growth nexus: Evidence from a panel error correction model," *Energy Economics*, **34**, 733–738 (2012).

5. Paul Denholm and Gerald L. Kulcinski, "Life cycle energy requirements and greenhouse gas emissions from large scale energy storage system," *Energy Conversion and Management*, **45**, 2153-2172 (2004).

6. Zhenguo Yang, Jianlu Zhang, Michael C. W. Kintner-Meyer, Xiaochuan Lu, Daiwon Choi, John P. Lemmon, and Jun Liu, "Electrochemical Energy Storage for Green Grid," *Chem. Rev.*, **111** (5), 3577–3613 (2011).

7. V. M. Dileepan, "A Study of Super Capacitor Based Mobile Charging Units in Isolated Power Systems and Automobile Applications," Internal Journal on Applications in Electrical and Electronics Engineering, **1** (3), 9-11 (2015).

8. L.Wagner, "Overview of Energy Storage Methods," Research Report by MORA Associates, December 2007.

9. M. Skyllas-Kazacos, M.H. Chakrabarti, S.A. Hajimolana, F.S. Mjalli, and M. Saleem, "Progress in Flow Battery Research and Development," J. *Electrochem. Soc.*, **158** (8), R55-R79 (2011).

10. Trung Nguyen and Robert F. Savinell, "Flow Batteries," *Electrochemical Society Interface*, **19** (3), 54-56 (2010).

11. Naveen Singamsetti and Sabri Tosunoglu, "A Review of Rechargeable Battery Technologies," *The 8th International Symposium on Management, Engineering and Informatics, MEI 2012, and The 16th World Multi-Conference on Systemics, Cybernetics and Informatics*, WMSCI 2012, Orlando, Florida, July 17-20 (2012).

12. Adam Z. Weber, Matthew M. Mench, Jeremy P. Meyers, Philip N. Ross, Jeffrey T. Gostick, and Qinghua Liu, "Redox flow batteries: a review," *J. Appl. Electrochem.*, **41**, 1137-1164 (2011).

13. C. Ponce de Leon, A. Frias-Ferrer, J. Gonzalez-Garcia, D. A. Szanto, and F. C. Walsh, "Redox flow cells for energy conversion," *J. Power Sources*, **160**, 716-732 (2006).

14. M. Skyllas-Kazacos, G. Kazacos, G. Poon, and H. Verseema, "Recent advances with UNSW vanadium-based redox flow batteries," *International Journal of Energy Research*, **34**, 182-189 (2010).

15. Werner Glass and G. H. Boyle, "Performance of Hydrogen-Bromine Fuel Cells," *Advances in chemistry series*, **47**, 203-220 (1965).

16. R. S. Yeo and D. T. Chin, "A Hydrogen-Bromine Cell for Energy Storage Applications," *J. Electrochem. Soc.*, **127** (3), 549-555 (1980).

17. G. G. Barna, S. N. Frank, T. H. Teherani and L. D. Weedon, "Lifetime Studies in H_2/Br_2 Fuel Cells," J. *Electrochem. Soc.*, **131** (9), 1973-1980 (1984).

18. J.A. Kosek and A.B. LaConti, "Investigation of Bromine Complexed Hydrogen/Bromine Regenerative Fuel Cells for Portable Electric Power," *Final Report for U.S. Army Mobility Equipment Research and Development Command*. General Electric, Electrochemical Energy Conversion Programs (1984).

19. V. Livshits, A. Ulus and E. Peled, "High-power H_2/Br_2 fuel cell," *Electrochemistry communications*, **8**, 1358-1362 (2006).

20. L.H. Thaller, "Redox Flow Cell Energy Storage Systems," *NASA Technical Memorandum 79143*. National Aeronautics and Space Administration, Lewis Research Center (1979).

21. Yu. V. Tolmachev, "Hydrogen-Halogen Electrochemical Cells: A Review of Applications and Technologies," *Russian Journal of Electrochemistry*, **50** (4), 301-316 (2014).

22. Haley Kreutzer, Venkata Yarlagadda, and Trung Van Nguyen, "Performance Evaluation of a Regenerative Hydrogen-Bromine Fuel Cell," *J. Electrochem Soc.*, **159** (7), F331-F337 (2012).

23. Yun Wang, Ken S. Chen, Jeffrey Mishler, Sung Chan Cho, and Xavier Cordobes Adroher, "A review of polymer electrolyte membrane fuel cells: Technology, applications, and needs on fundamental research," *Applied Energy*, **88**, 981–1007 (2011).

24. Kyu Taek Cho, Paul Ridgeway, Adam Z. Weber, Sophia Haussener, Vincent Battagalia, and Venkat Srinivasan, "High Performance Hydrogen/Bromine Flow Battery Redox Flow Battery for Grid-Scale Energy Storage," *J. Electrochem. Soc.*, **159** (11), A1806-A1815 (2012).

25. Bruce D. Craig and David S. Anderson, "Handbook of Corrosion Data," *2nd edition*, published by ASM International, December 1994.

26. Rungsima Yeetsorn, Michael W. Fowler and Costas Tzoganakis, "A Review of Thermoplastic Composites for Bipolar Plate Materials in PEM Fuel Cells," *Chapter 16*, Nanocomposites with Unique Properties and Applications in Medicine and Industry, book edited by John Cuppoletti, August 2011.

27. R.F. Savinell and S.D. Fritts, "Theoretical Performance of a Hydrogen-Bromine Rechargeable SPE Fuel Cell," *J. Power Sources*, **22**, 423-440 (1988).

28. S. D. Fritts and R. F. Savinell, "Simulation Studies on the Performance of the Hydrogen Electrode Bonded to Proton Exchange Membranes in the Hydrogen-Bromine Fuel Cell," J. *Power Sources*, **28**, 301-315 (1989).

CHAPTER 2

A Comprehensive Study of an Acid-Based Reversible Hydrogen-Bromine Fuel Cell System

2.1. Introduction

A conventional H_2-Br_2 fuel cell consists of a H_2 electrode and a Br_2 electrode separated by a proton exchange membrane. However, microporous membrane and membrane-less versions of several fuel cell systems have also been investigated.[1-3] Recently, Braff et al. developed a membrane-less version of the H_2-Br_2 flow battery to reduce the cost and ease the hydration requirements associated with the system.[1] As discussed in the first chapter, the H_2-Br_2 fuel cell needs a membrane that limits the crossover of unwanted species (Br_2, Br^-, and Br_3^-), and an active electrocatalyst for hydrogen reactions that is stable in the corrosive HBr/Br_2 environment. In this chapter, studies involving novel membrane and catalyst materials will be discussed.

An optimum membrane should have high conductivity and ionic selectivity as well as be resistant to negative hydration effects. The negative hydration effects can be explained as follows. When the proton exchange membrane (PEM) is not hydrated, the transport of protons across the membrane effectively goes to zero due to the incomplete dissociation of ionic groups ($-SO_3^-H^+$) within the membrane.[4] When a membrane is too hydrated, the polymer swells causing the ionic pathways through the membrane to open up and allow larger chemical species to diffuse across the membrane. The ionic selectivity has been shown to change drastically with the relative hydration of the PEM.[5] Several previous studies have explored using electrospun nanofiber composite membranes (usually a blend of inert polymer and Nafion) for

PEM and direct methanol fuel cells in order to address issues such as the excessive swelling and high permeability of commercially available Nafion membranes.[6-8]

The purpose of making electrospun composite membranes is to create a sufficient number of ionic pathways available for protons to move through the membrane, while also physically preventing the membrane from swelling at high relative humidity. Even though the electrospun composite membranes reduce the crossover of unwanted species, it is challenging to fabricate a membrane that can completely prevent the crossover of unwanted species while also allowing for sufficient ionic conductivity of desired species. However, the electrospun composite membrane may reduce the rate of crossover enough to prolong the life of catalyst materials used in the fuel cell. In conclusion, an active H_2 electrocatalyst stable in HBr/Br_2 environment is still needed to avoid any negative impact of crossover species on the H_2-Br_2 fuel cell performance.

Prior works have shown that the instability of Pt catalyst material in HBr/Br_2 environment was due to blockage of active sites (poisoning) and dissolution of catalyst material (corrosion).[9,10] The poisoning effect is reversible and thus can be mitigated to a certain extent by holding the H_2 electrode at hydrogen evolution potentials. However, the corrosion effect is irreversible and hence the catalyst material that decomposes over time cannot be recovered. Several previous works have screened transition metal chalcogenides as oxygen reduction catalysts for hydrochloric acid (HCl) electrolysis and conventional direct methanol fuel cells (DMFC).[11,12] Of the transition metal chalcogenides investigated, rhodium sulfide (Rh_xS_y) was identified as one of the stable and active electrocatalysts for the oxygen reduction reaction in the presence of a corrosive acidic environment.[11-15] Similarly, the activity of H_2 reactions on transition metal sulfides was examined in some of the previous works as well.[16,17] The Rh_xS_y

catalyst was also found to be a stable (in HBr/Br$_2$ environment) and active electrocatalyst for hydrogen evolution reaction during HBr electrolysis.[10,17,18] Even though some of the other transition metal sulfides such as cobalt ruthenium sulfide (Co$_{1-x}$Ru$_x$S$_2$), ruthenium sulfide (RuS$_2$), and tungsten disulfide (WS$_2$) were stable in highly corrosive HBr/Br$_2$ solutions, their hydrogen evolution reaction and hydrogen oxidation reaction (HER/HOR) activity was too low to be considered as active electrocatalysts.[17]

The Rh$_x$S$_y$ electrocatalyst is composed of multiple phases such as Rh$_2$S$_3$, Rh, Rh$_3$S$_4$, and Rh$_{17}$S$_{15}$. Prior works have identified metallic Rh, Rh$_{17}$S$_{15}$ and Rh$_3$S$_4$ to be the likely active phases for HER/HOR.[11,13] Since the price of Rh is equally high as platinum, the only advantage it offers is its stability. An alternate approach to reduce the impact of crossover is to alter the fuel cell system design or operation to allow platinum to be used as a feasible electrocatalyst. For example, Cho et al. claims that maintaining the hydrogen electrode at a hydrogen evolution potential or a continuous flow of H$_2$ gas through the hydrogen electrode prevents Pt catalyst poisoning by bromine and bromide ions.[19] However, even the leverage provided by smart system design or operation may still fail in situations such as emergency system shut down or loss of hydrogen environment. The best possible solution to avoid the impact of crossover is to develop a stable electrocatalyst with decent activity for hydrogen reactions.

In this chapter, preliminary fuel cell test results with conventional Nafion membranes and Pt electrocatalysts are discussed in the first section. The preliminary results include the effect of Br$_2$ electrode pre-treatment, fuel cell operating temperature, and Br$_2$ electrode thickness on the H$_2$-Br$_2$ fuel cell performance. The second section focuses on studies of Pt involving the performance evaluation of electrospun composite membranes and the stability and Rh$_x$S$_y$ (purchased from BASF) electrocatalysts in an actual fuel cell fixture.

2.2. Experimental

2.2.1. H₂-Br₂ Fuel Cell Assembly

The components required to assemble a H_2-Br_2 fuel cell are end plates, current collectors, flow field plates, and a membrane electrode assembly (MEA). The fuel cell components are shown in Figure 2.1. The side of the MEA with H_2 electrode (Pt/C electrode) hot pressed onto the membrane along with the Teflon gasket is shown in Figure 2.1c. The Teflon gasket acts as a sealing agent in the fuel cell assembly. As shown in Figure 2.1d, a graphite flow field plate was used in the H_2 electrode whereas a tantalum flow field than can withstand the
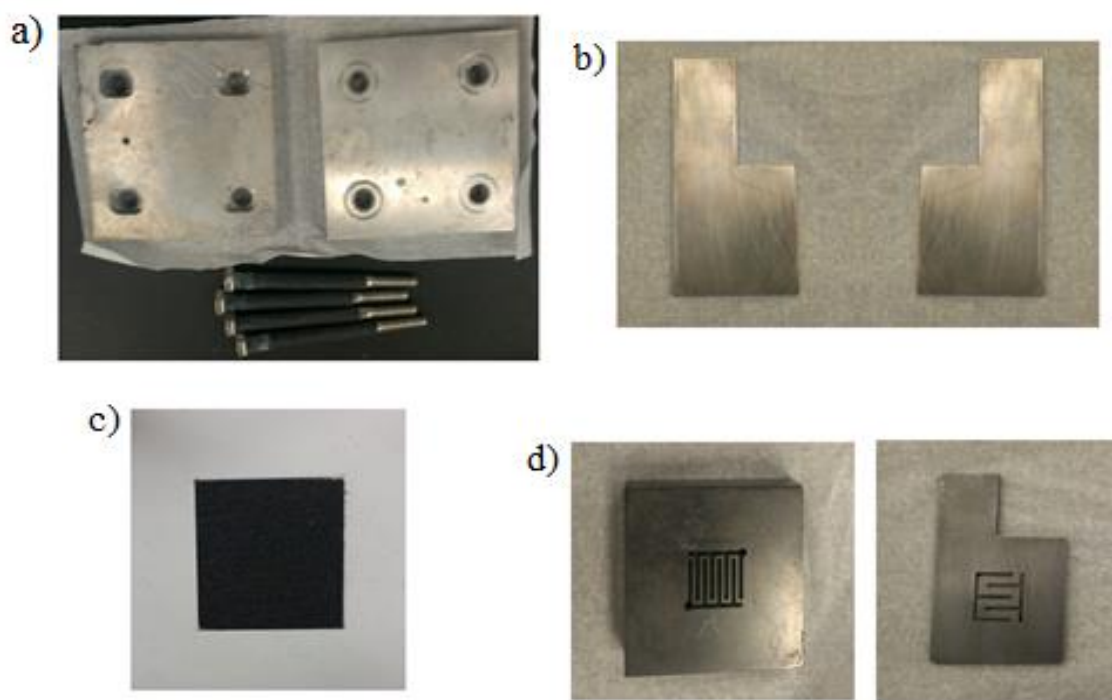
Figure 2.1. H_2-Br_2 fuel cell components (a. aluminum end plates with fittings, b. Stainless steel current collectors, c. membrane electrode assembly, and d. graphite and tantalum flow field plates)

corrosive nature of HBr/Br$_2$ was used in the bromine electrode compartment. Figures 2.1a and 2.1b show the aluminum endplates and stainless steel current collectors respectively. Prior to assembling the fuel cell, flow field plates and current collectors were polished to ensure good electrical contact. The H$_2$-Br$_2$ fuel cell after assembly is shown in Figure 2.2. On the Br$_2$ side, the tantalum plate serves as a flow field and a current collector. The HBr/Br$_2$ electrolyte was fed through the side inlet in the Teflon block located behind the tantalum flow field plate whereas the H$_2$ gas was fed through the side inlet in the graphite flow field block.
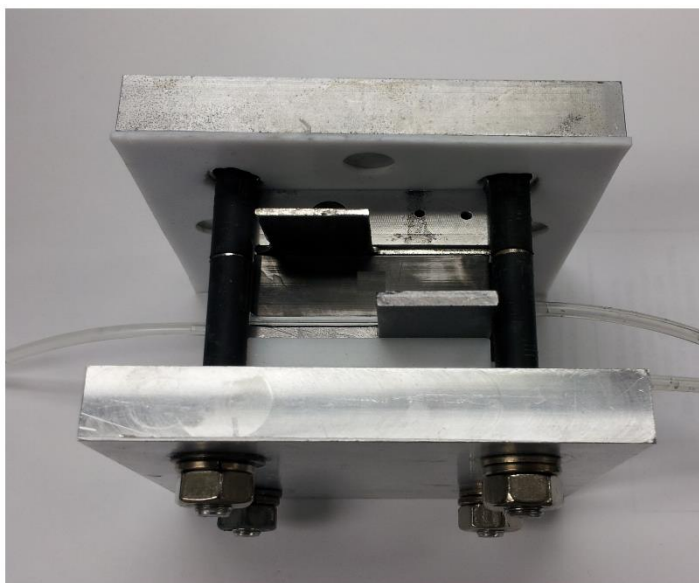
Figure 2.2. H$_2$-Br$_2$ fuel cell fixture after assembly

Flow field plates (4 cm x 4cm) with a flow area of 2.25 cm^2 (1.5 cm x 1.5 cm) were used in this study. The dimensions of the electrodes and the Teflon gasket openings were 1.7 cm x 1.7 cm and 1.8 cm x 1.8 cm respectively. The electrodes were centered to cover the whole flow

area. The currents measured during the experiment were normalized to the flow area (2.25 cm^2).

2.2.2. Flow Field Designs

Figure 2.3 shows the flow field designs (interdigitated and serpentine) used to transport the reactants and products to and from the electrodes of the fuel cell. The flow field plates were in constant contact with the electrodes. The dominant transport mechanism when using the serpentine flow field design is diffusion since it forces the reactants to flow parallel to the electrode surface. However, there is a small amount of convection as a result of a pressure gradient between the adjacent channels in the serpentine flow field (shown by the arrows). On the other hand, the intergitated flow field design consists of dead-end channels, which forces the reactants to flow through the gas diffusion layer. The dominant transport mechanism when using the interdigitated flow field design is convection and as a result the diffusion distance between the gas diffusion layer and catalyst layer for the reactants was reduced. The interdigitated flow fields, which have shown to provide the best utilization of the electrode area, were used in this study because of their flow-through versus flow-by characteristics of other flow fields such as the straight-parallel-channel and serpentine-channel flow fields.[20]
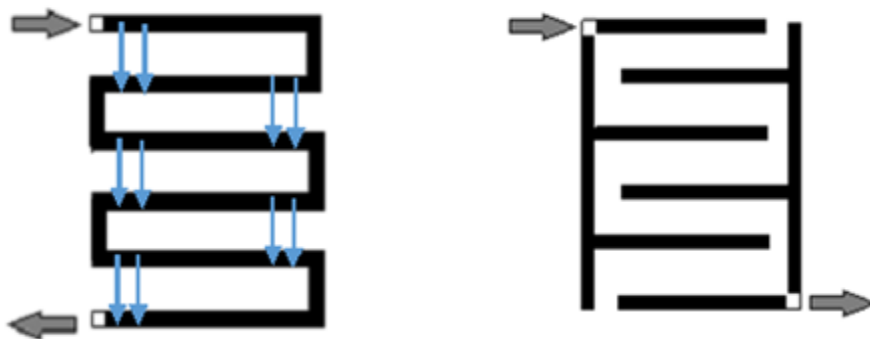
Figure 2.3. Serpentine (left) and Interdigitated (right) flow field designs

2.2.3. H_2-Br_2 Fuel Cell Operation

After assembling the H_2-Br_2 fuel cell, the following procedure is implemented to obtain the polarization curve. A potentiostat/galvanostat from Arbin Instruments was used to control the applied potential and measure the current.

1. Initially, humidified H_2 gas and HBr/Br_2 electrolyte were recirculated through the hydrogen and bromine electrodes respectively to establish an open circuit voltage (OCV).

2. The reactants were recirculated through their respective electrodes for 30 minutes to hydrate the membrane and the ionomer present in the H_2 electrode.

3. Next, the discharge performance was acquired by applying potentials in steps of 50 mV between OCV (1V for 2M HBr/1M Br_2 and 1.03V for 2M HBr/2M Br_2) and 0.6V.

4. The charge performance was acquired by applying potentials in steps of 50 mV between OCV (1V for 2M HBr/1M Br_2 and 1.03V for 2M HBr/2M Br_2) and 1.25V.

5. At each voltage step, current was measured for atleast 5 minutes or until it reaches steady state.

6. The polarization curve was measured until reproducible performance was obtained.

7. Finally, the internal resistance of the fuel cell was measured using EIS.

8. A continuous H_2 flow was maintained throughout the entire experiment to minimize the crossover of unwanted species (Br_2, Br^-, and Br_3^- to the H_2 side).

2.2.4. Experimental Setup (Concentrations, Flow rates, and Catalyst Loadings)

A plain SGL carbon (10AA) gas diffusion electrode (GDE) was used as the Br_2 electrode and a bi-layer carbon gas diffusion medium (SGL 35BC) coated with Pt/C or Rh_xS_y (BASF)/C was used as the hydrogen electrode. The Pt electrode was obtained from TVN systems, Inc., and

the Rh_xS_y electrode was prepared by painting a solution of Rh_xS_y/C and Nafion on the microporous layer (MPL) of the bi-layer carbon gas diffusion medium with a brush. The catalyst (Pt or Rh_xS_y) loading in the hydrogen electrode was approximately 0.5 mg/cm^2.

The membrane electrode assemblies (MEAs) were made with commercially available Nafion (212 and 115) and electrospun composite membranes. A 2M HBr/2M Br_2 electrolyte mixture was fed to the Br_2 electrode in the H_2-Br_2 fuel cell experiments that examine the effect of pre-treated Br_2 electrodes, fuel cell operating temperature, Br_2 electrode thickness, and electrospun composite membranes. A 2M HBr/1M Br_2 electrolyte mixture was fed to the Br_2 electrode for the catalyst stability studies. H_2 gas at 122 kPa was recirculated through the H_2 electrode. A peristaltic pump by Stenner (Model EW-74206) was used to pump the HBr and Br_2 solution. A diaphragm pump (Model BL 30 purchased from KNF Neuberger), Inc.) was used to pump the H_2 into the fuel cell. The H_2 and HBr/Br_2 pump flow rates were 1380 cm^3/min (97.2 A/cm^2 equivalent current density) and 1.5 cm^3/min (4.3 A/cm^2 equivalent current density for 2M Br_2 and 2.15 A/cm^2 limiting current density for 1M Br_2 during discharge) respectively. Interdigitated flow fields were used for all the experimental studies. Also, liquid water at a flow rate of 0.05 cm^3/min was injected using a mini-pump (Fischer Scientific Model 3385) into the H_2 electrode to humidify the H_2 gas which facilitated hydration of the ionomer phase in the hydrogen electrode.[21] All the experiments were conducted at room temperature (~22°C) unless otherwise specified. At the end of each experiment, the internal ohmic resistance of the fuel cell was acquired using Electrochemical Impedance Spectroscopy (Gamry EIS 300, Amplitude: 5mV and Frequency range: 0.1Hz to 100 kHz).

2.2.5. Preliminary H$_2$-Br$_2$ Fuel Cell Studies

The preliminary H$_2$-Br$_2$ fuel cell studies involve four different sections. For all the preliminary studies, a bi-layer porous carbon electrode (SGL 35BC) with Pt catalyst was used as the H$_2$ electrode.

1. First, the H$_2$-Br$_2$ fuel cell performance of plain carbon and Pt as bromine electrodes was measured.

2. Second, the effect of pre-treated Br$_2$ electrodes (SGL 10AA carbon electrodes soaked in 2M HBr and boiled in DI water) on the H$_2$-Br$_2$ fuel cell performance was examined.

3. Third, the effect of temperature (25°C and 45°C) on the fuel cell performance was investigated.

4. Finally, the effect of Br$_2$ electrode thickness (390 μm and 780 μm) on the fuel cell performance was studied.

2.2.6. Evaluation of Electrospun Composite Membrane and RhxSy Catalyst in a H$_2$-Br$_2$ Fuel Cell

The dual fiber electrospun composite membranes used in this study are composed of 55 vol. % Nafion perfluorosulfonic (PFSA) acid ionomer and 45 vol. % inert (uncharged) polyphenylsulfone (PPSU) polymer. The electrospun membrane used in this study was made by allowing the inert polymer (PPSU) to soften, flow, and fill the void space between PFSA nanofibers.[22,23] The inert polymer (PPSU) was used to control the swelling of the ionic Nafion phase, which in turn helped in reducing the crossover of unwanted species across the membrane. The steady state permeability of bromine species (Br$_2$ and Br$_3^-$) in the electrospun composite membranes used in this study is an order of magnitude lower than that of the

commercially available Nafion membranes.[22] Finally, the performance of dual fiber electrospun composite membranes was evaluated in an actual fuel cell fixture at 25°C and 45°C.

The stability of Pt and Rh_xS_y electrocatalysts was determined through accelerated testing. Initially, two fuel cell stacks with Pt and Rh_xS_y as H_2 electrode catalysts were assembled and the stability study was conducted over a week's period of time. On day 1, the fuel cell polarization (discharge and charge) curves were obtained for both the stacks and, subsequently, the H_2 flow was secured (no flow) to the hydrogen electrode with HBr/Br_2 electrolyte stored in the Br_2 electrode. The hydrogen side was not pressurized (ambient conditions) thus allowing the HBr/Br_2 electrolyte to slowly diffuse through the membrane to the H_2 electrode and interact with the catalyst layer. The fuel cell performance was acquired on odd numbered days (1, 3, 5, and 7) with the polarization curves obtained on day 1 being the initial performance. Between the consecutive runs, the stacks were stored with HBr/Br_2 electrolyte present in the Br_2 electrode and H_2 electrode at ambient conditions. This test is considered to be a highly severe accelerated test because the catalyst on the hydrogen side was neither protected by hydrogen or by cathodic protection. Note that while bromine is much more corrosive to a metal than bromide, in the presence of hydrogen it is quickly converted to bromide. Furthermore, it has been reported that bromide adsorption is voltage dependent. At voltages more negative than +60 mV of the hydrogen standard equilibrium potential, hydrogen is more preferentially adsorbed than bromide.[28] So, platinum can be protected by maintaining high hydrogen adsorption level, by using pressurized hydrogen on platinum at open circuit voltage condition or by applying a sufficiently negative overpotential to the platinum electrode (i.e., cathodic protection).

The next study was aimed at examining the feasibility of Pt as a H_2 electrocatalyst under the following fuel cell testing conditions. In the first case, the initial performance of the H_2-Br_2 fuel cell was measured and the system was allowed to sit at rest condition for 8 hours with the H_2 flow terminated (similar to the testing condition described above). After 8 hours, the performance of the fuel cell was measured again to check whether there is any impact of crossover on the performance. The second case study was performed under similar conditions as described above, but with a minor change. During this experiment, the H_2 pump was allowed to run with the H_2 gas recirculating at 122 kPa for the next 8 hours after measuring the initial performance. The HBr/Br_2 pump was stopped during the rest condition for both fuel cell stacks.

The final test looked at the effect of HBr/Br_2 crossover in real time, while the fuel cell is operating in the discharge regime. In this experiment, the fuel cell was operated at a constant discharge potential (in this case at 0.8V). After reaching a steady state current at the chosen discharge potential, a small volume of 2M HBr solution was injected into the hydrogen electrode. As soon as a small drop of 2M HBr entered the electrode, the H_2 pump was secured with the H_2 side still pressurized at 122 kPa. The fuel cell was maintained at OCV for approximately 8 minutes to allow the HBr to interact with the H_2 electrode. After 8 minutes, the discharge current of the fuel cell was measured at 0.8 V for another 10 to 12 minutes to observe whether there was any impact on performance due to Br^- in the H_2 electrode. Next, a mixture of 2M HBr/1M Br_2 was injected into the hydrogen electrode and the same procedure explained above for the HBr injection was implemented to examine the effect of Br^- and Br_2 crossover on the fuel cell performance. The HBr/Br_2 pump was operated continuously during the entire experiment.

2.3. Results and Discussion

2.3.1. Platinum and Carbon as Electrocatalysts for Bromine Reactions

The Br_2/Br^- reaction kinetics on plain carbon substrates is fast enough to eliminate the need for a catalyst in the Br_2 electrode.[24] Moreover, the Br_2 and Br^- species will eventually poison and corrode most of the precious metal catalysts used in the Br_2 electrode. Figure 2.4 compares the performance of a H_2-Br_2 fuel cell with plain carbon (a single layer of SGL 10AA) and Pt catalyst coated Toray 090 as Br_2 electrodes (a previous study conducted by Kreutzer et al.).[20] The MEAs were prepared with Nafion 212 as the membrane and a Pt catalyst coated SGL 35BC as the H_2 electrode.

As shown in Figure 2.4, the performance of the H_2-Br_2 fuel cell with a carbon electrode in both kinetic and mass transport controlled regions is comparable to that of a Pt electrode. During discharge, especially at higher current densities, the membrane becomes dehydrated due to the transport of liquid water from the H_2 electrode to the Br_2 electrode by electroosmosis resulting in mass transport limited performance (as seen in Figure 2.4 for the fuel cell with Pt on Toray 090 as the Br_2 electrode). However, the fuel cell with carbon as a Br_2 electrode did not exhibit mass transport limited performance due to the fact that liquid water injection approach studied by Wood et al. was employed to keep the membrane hydrated during the entire study.[21] This is the reason for the superior performance exhibited by the fuel cell with the carbon electrode over the Pt electrode in the mass transport controlled region. Plain SGL 10AA GDLs were used as the Br_2 electrodes for rest of the fuel cell experimental studies discussed in this study.
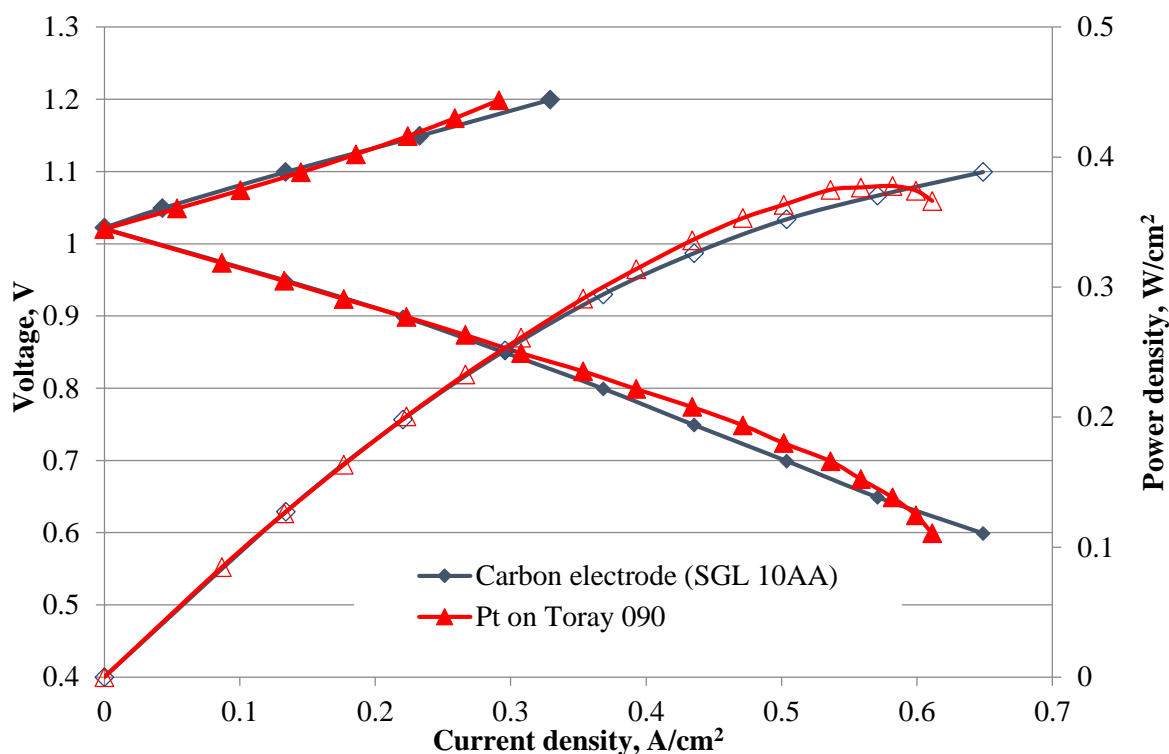
Figure 2.4. Performance of H_2-Br_2 fuel cell with plain SGL 10AA carbon and Pt catalyst coated Toray 090 as Br_2 electrodes at room temperature (~22°C)

2.3.2. Effect of Pre-treated Br₂ Electrodes on Fuel Cell Performance

The aim of the electrode pre-treatment is to increase the hydrophilicity and active surface area of the Br_2 carbon electrodes. To examine the effect of pre-treated Br_2 electrodes on fuel cell performance, three different experiments were conducted. Initially, fuel cell performance was obtained using 2 layers of dry SGL 10AA carbon electrodes. The SGL 10AA carbon electrodes were boiled in DI water and soaked in 2M HBr for subsequent experiments. Nafion 212 membranes were used in the MEAs developed for this study. The HBr/Br_2 electrolyte and humidified H_2 gas were recirculated through the Br_2 and H_2 electrodes respectively for 30 minutes to hydrate the dry MEA prior to measuring the fuel cell performance. The presence of

aqueous HBr electrolyte next to the membrane helps to quickly hydrate the cell and obtain stable performance.

Figure 2.5 compares the performance of a H_2-Br_2 fuel cell acquired with pre-treated and untreated carbon electrodes. As shown in Figure 2.5, the fuel cell discharge performance obtained with untreated (dry) carbon electrodes in the second run is higher compared to that in the first run (maximum discharge power density of 0.58 W/cm^2 obtained in second run compared to 0.49 W/cm^2 obtained in first run). The discharge performance in the first run is low over the whole discharge regime. During the first run, the electrodes were dry and hence hydrophobic to a certain extent. As a result, the reactants may not be able to access the entire active area of the carbon electrodes. As the first run progressed, the active area and wetting property of the carbon electrodes increased with their continuous exposure to HBr/Br$_2$ electrolyte solution. The first run acts like a pre-treatment step for the carbon electrodes.

Also note that when an interdigitated flow field is used, the electrolyte is forced to flow through the porous electrode. This configuration forces the electrolyte to penetrate into the carbon material and assist in wetting the carbon surface. For flow-by electrodes using parallel-straight channels where the electrolyte is not forced to flow through the electrodes, it may take much longer time for the carbon surface to become wetted. Furthermore, we believe that the passage of current may lead to surface chemical modifications and increased wetting in two ways. First, the electrolyte may be forced into the bromine electrode region that was not previously wetted during charge and discharge. Second, the bromine/bromide reaction may alter the carbon material surface to make it more wetted. Hence, the discharge performance of the H_2-Br_2 fuel cell with dry SGL 10AA carbon electrodes shows improvement in the second run. The fuel cell discharge performance curves obtained with the carbon electrodes boiled in

DI water and those soaked in 2M HBr in the first run are similar and match reasonably well with those of the untreated carbon electrodes obtained in the second run. A similar performance improvement was observed by Cho et al. when using porous carbon electrodes pre-treated with sulfuric acid instead of untreated ones.[24]
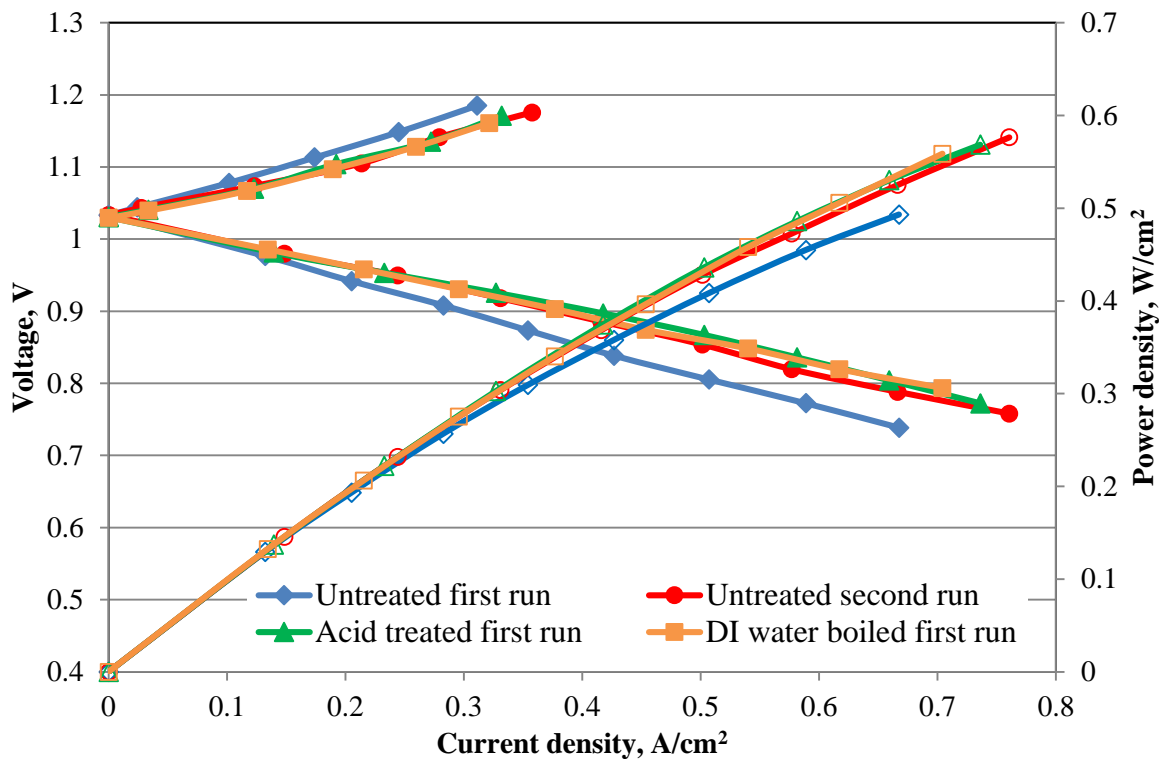
Figure 2.5. Effect of Br_2 electrode pre-treatment (untreated, acid treated, and DI water boiled) on the H_2-Br_2 fuel cell performance (voltage: solid markers and power density: open markers) at room temperature (~22°C)

The major conclusion based on these experimental results is that the untreated carbon electrodes generate the same discharge performance as pre-treated electrodes but after multiple discharge and charge cycles. The number of discharge and charge cycles required to condition the untreated carbon electrodes may go up as the electrode thickness increases. Thus, pre-

treating the carbon electrodes prior to use assists with the HBr/Br$_2$ electrolyte gaining access to most of the active area immediately. Also, similar discharge performances obtained with carbon electrodes boiled in DI water and acid soaked in 2M HBr suggests that the wetting characteristic of an electrode plays a significant role in enhancing the area accessible to the aqueous reactants, and either treatment method can be used to achieve this effect. We recommend that regardless of the type of carbon electrode used, one should always try to pre-treat it in order to promote wetting and allow for high fuel cell performance to be achieved right away.

2.3.3. Effect of Temperature on the Fuel Cell Performance

The performance of a H$_2$-Br$_2$ fuel cell can be enhanced in several ways. One such way is to boost the H$_2$ and Br$_2$ reaction kinetics as well as the transport processes inside the electrodes by increasing the fuel cell operating temperature. A similar study was conducted in our previous work but with uneven temperature control across the fuel cell fixture.[20] In this study, the H$_2$ gas entering the fuel cell, HBr/Br$_2$ electrolyte, and the fuel cell were heated to the same temperature in order to minimize the temperature gradient across the fuel cell stack.

Figure 2.6 shows the results of the H$_2$-Br$_2$ fuel cell temperature studies with Nafion 212 and Nafion 115 membranes. The fuel cell performance is significantly improved in both the kinetic and mass transport controlled regions as the temperature increases from 25°C to 45°C. The internal ohmic resistance for the fuel cell with Nafion 212 membrane decreased by 28% as the temperature was raised from 25°C to 45°C (0.18 Ω-cm^2 at 25°C versus 0.13 Ω-cm^2 at 45°C). A similar decrease in internal ohmic resistance at higher temperatures was observed for the fuel cell with Nafion 115 membrane (0.4 Ω-cm^2 at 25°C versus 0.3 Ω-cm^2 at 45°C) as well. The decrease in ohmic resistance can be attributed to improvement in the diffusivity of reactant

species and Nafion conductivity. In other words, molecular and ionic transport were significantly enhanced. The fuel cell performance at 45°C is enhanced compared to our prior study (maximum power density of 0.52 W/cm^2 in this study versus 0.46 W/cm^2 in our previous study for the case where Nafion 212 membrane was used). Also, the fuel cell performance was enhanced by using a thinner membrane. Even though the performance of the fuel cell decreases with a thicker membrane, the crossover rate of Br$_2$ and Br$^-$ species may be lowered. The performance trends shown in Figure 2.6 also match reasonably well with the previous studies.[19,24]
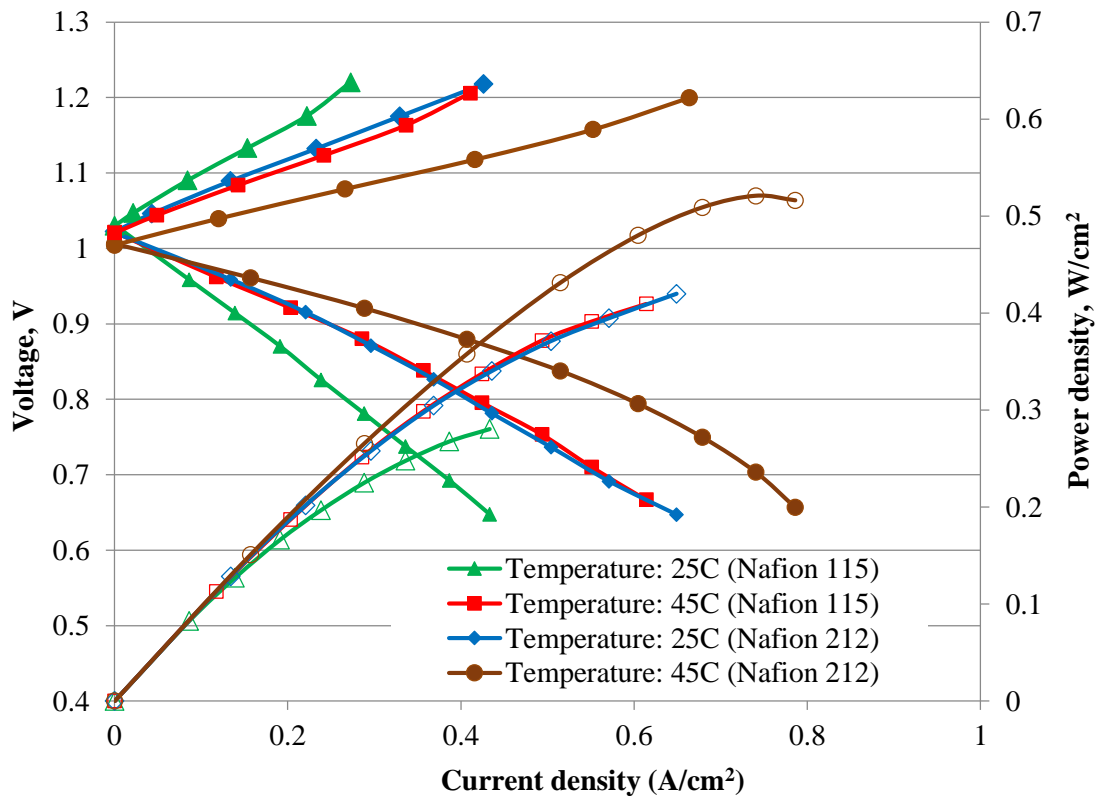
Figure 2.6. Effect of temperature (25°C and 45°C) and membrane (Nafion 212 and Nafion 115) thickness on H$_2$-Br$_2$ fuel cell performance (voltage: solid markers and power density: open markers)

2.3.4. Effect of Br₂ Electrode Thickness on the Fuel Cell Performance

The H_2-Br_2 fuel cell performance can also be enhanced by increasing the Br_2 electrode thickness in this case because the commercial gas diffusion media used in fuel cells have very low specific surface areas. Figure 2.7 compares the performance of a fuel cell with two different electrode thicknesses, 390 μm (one piece of SGL 10AA electrode) and 780 μm (two pieces of SGL 10AA carbon electrode) respectively. The bromine electrode thickness in this study was increased by adding an additional SGL 10AA carbon electrode. The two SGL 10AA carbon electrodes were stacked together to increase the electrode thickness. The rest of the fuel cell configuration remains unchanged. The active area of the Br_2 electrode improves upon increasing the electrode thickness. In other words, the number of reaction sites increases, which is evident from the improvement in the fuel cell performance upon employing a thicker Br_2 electrode. An 18% increase in maximum power density was observed upon adding an additional Br_2 electrode at 25 °C. The increase in the ohmic loss by an additional bromine electrode was insignificant relative to the power density gain (ohmic resistance increased by 6 mΩ upon adding an additional bromine electrode at 25°C). As shown in Figure 2.7, the performance of the fuel cell can be further enhanced by operating the fuel cell with a thicker electrode at a higher temperature (two layers of SGL 10AA carbon electrodes at 45°C). A peak power density of 0.65 W/cm² was obtained with the thicker Br_2 electrode at 45°C.

Based on a previous modeling study conducted on the H_2-Br_2 fuel cell system, increasing the electrode layers beyond a certain limit may result in diffusion limited performance due to the increase in the ionic and molecular diffusion pathways.[25] An alternate approach that can increase the active surface area without affecting the transport related morphological properties like porosity and tortuosity of the electrode is to grow nanotubes directly onto the electrode

fiber surface to create high active surface area.[26] This is a more suitable option compared to using a multi-layered carbon electrode approach because the electrode surface area can be improved without affecting the porosity/tortuosity or the electrode thickness.
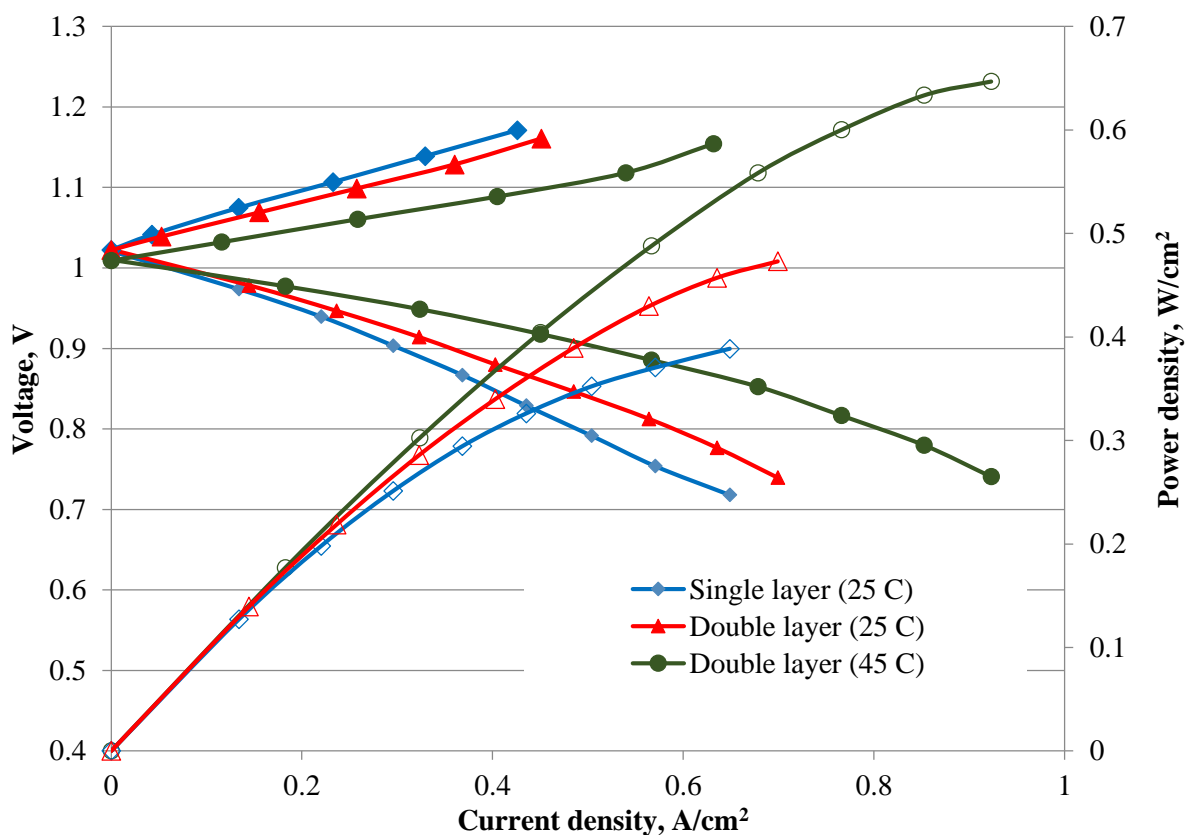
Figure 2.7. Effect of Br$_2$ electrode thickness (single layer: 390 μm at 25°C and double layer: 780 μm at 25°C and 45°C) on H$_2$-Br$_2$ fuel cell performance (voltage: solid markers and power density: open markers)

2.3.5. Composite Membrane Studies

In this study, the performance of dual fiber electrospun composite membranes consisting of 55 vol. % PFSA and 45 vol. % PPSU were evaluated in an actual fuel cell at 25°C and 45°C

respectively. The thicknesses of the membrane samples evaluated were 25 μm (area specific resistance equivalent to that of Nafion 212 membrane) and 65 μm (area specific resistance equivalent to that of Nafion 115 membrane) respectively. Nafion 212 has more ionic clusters than the electrospun membrane as reported in a recent study by Dowd et al.[27] The crossover rate of Br_2 and Br^- of these electrospun composite membranes was also lower than that of the conventional Nafion membranes because the PFSA phase does not swell as much since it is restricted by the inert PPSU phase.[22]

The thickness of the electrospun membranes was optimized to approximately match the area specific resistance of the Nafion membranes.[22] The preliminary performance of these electrospun membranes compared with that of the commercial Nafion membranes are shown in Figures 2.8 and 2.9. As shown in Figures 2.8 and 2.9, the performance of both 25 μm and 65 μm thick electrospun membranes are either comparable or slightly better compared to that of Nafion 212 and Nafion 115 membranes at 25°C and 45°C. At 45°C, the maximum power densities of 25 μm and 65 μm electrospun membranes were 0.61 W/cm^2 and 0.45 W/cm^2 compared to 0.52 W/cm^2 and 0.41 W/cm^2 obtained with Nafion 212 and Nafion 115 membranes.

The sharp drop in the discharge performance for the fuel cell stack with Nafion 212 membrane (shown in Figure 2.8) at 45°C may be attributed to the dehydration of the ionomer in the hydrogen catalyst layer and the hydrogen side of the MEA due to inadequate anode gas humidification. Note that, water is dragged from the H_2 side to the Br_2 side during discharge, and since Nafion 212 is thicker (~ 50 μm) than the composite membrane (~ 25 μm), it is more likely to become dehydrated at higher current densities than the composite membrane. The preliminary fuel cell performances obtained with electrospun membranes were on par with the

commercially available Nafion membranes and hence look very promising for future studies. Also, the lower permeability of unwanted species associated with the electrospun membranes is an additional benefit.[22,23]
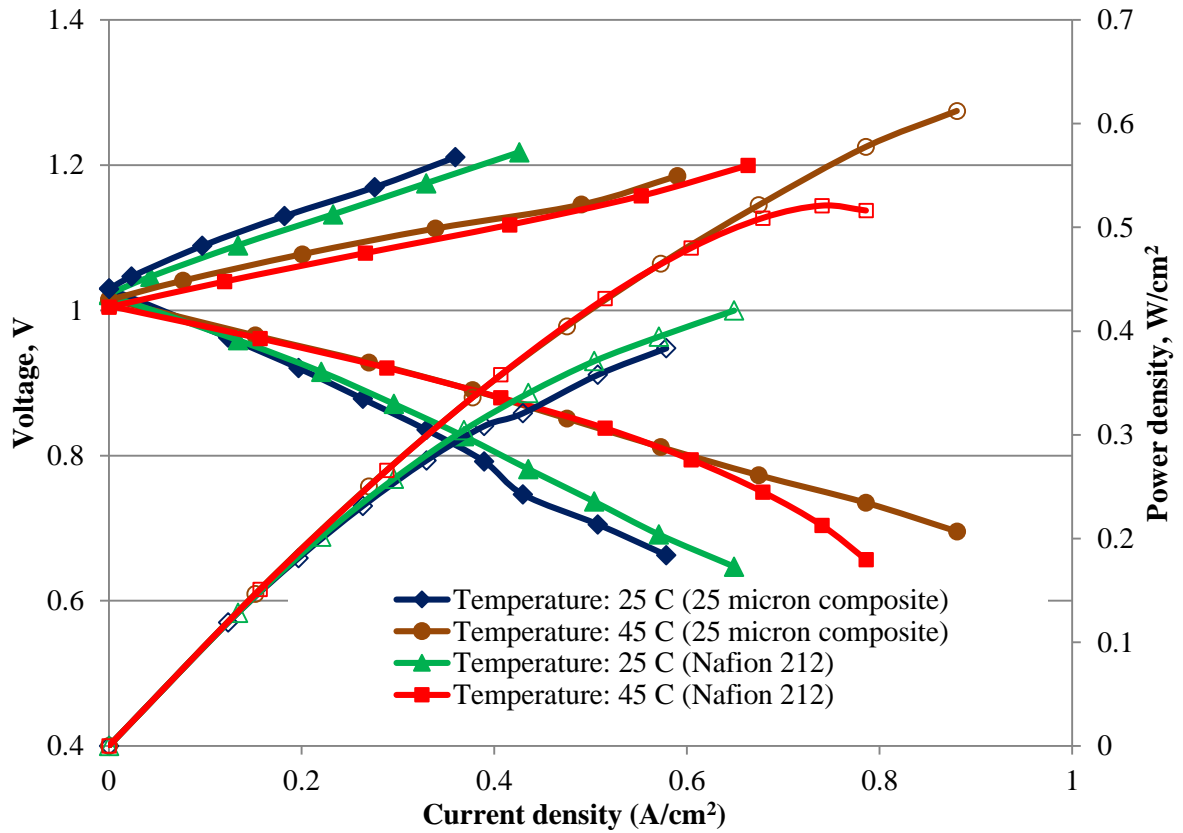
Figure 2.8. Performance (voltage: solid markers and power density: open markers) comparison between Nafion 212 and 25 micron thick dual fiber electrospun composite membranes at 25°C and 45°C
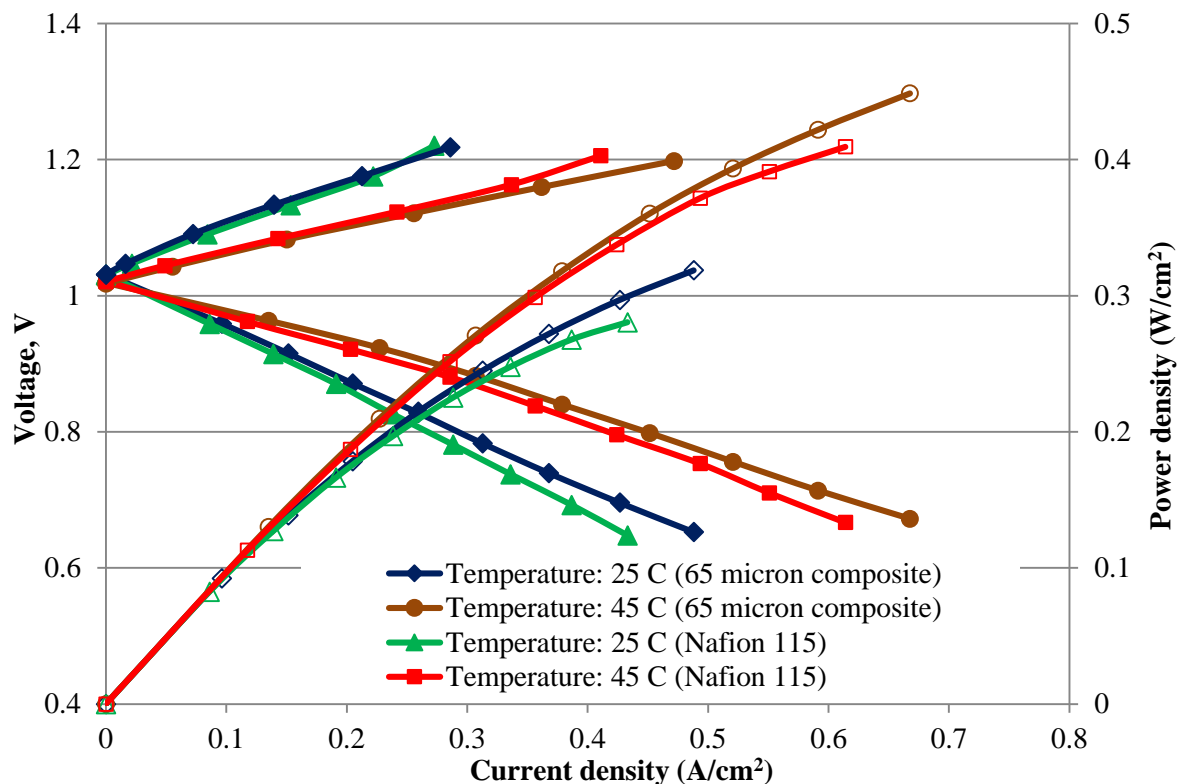
Figure 2.9. Performance (voltage: solid markers and power density: open markers) comparison between Nafion 115 and 65 micron thick dual fiber electrospun composite membranes at 25°C and 45°C

2.3.6. Electrocatalyst Stability Studies

In this section, the stability of Pt and Rh_xS_y electrocatalysts in a H_2-Br_2 fuel cell was examined. Figures 2.10 and 2.11 show the performance curves obtained with Pt/C and Rh_xS_y/C catalysts over a week. As explained in the experimental section, the H_2 flow was shut off and HBr/Br_2 electrolyte was stored in the Br_2 electrode between the subsequent fuel cell experiments. As shown in Figure 2.10, the discharge performance of the fuel cell was significantly reduced beyond day 1 due to the exposure of Pt catalyst layer in the H_2 electrode to Br_2, HBr⁻, and

HBr$_3^-$ species. The Pt catalyst layer was both poisoned and corroded by the bromine and bromide species that crossed over from the Br$_2$ electrode to the H$_2$ electrode.
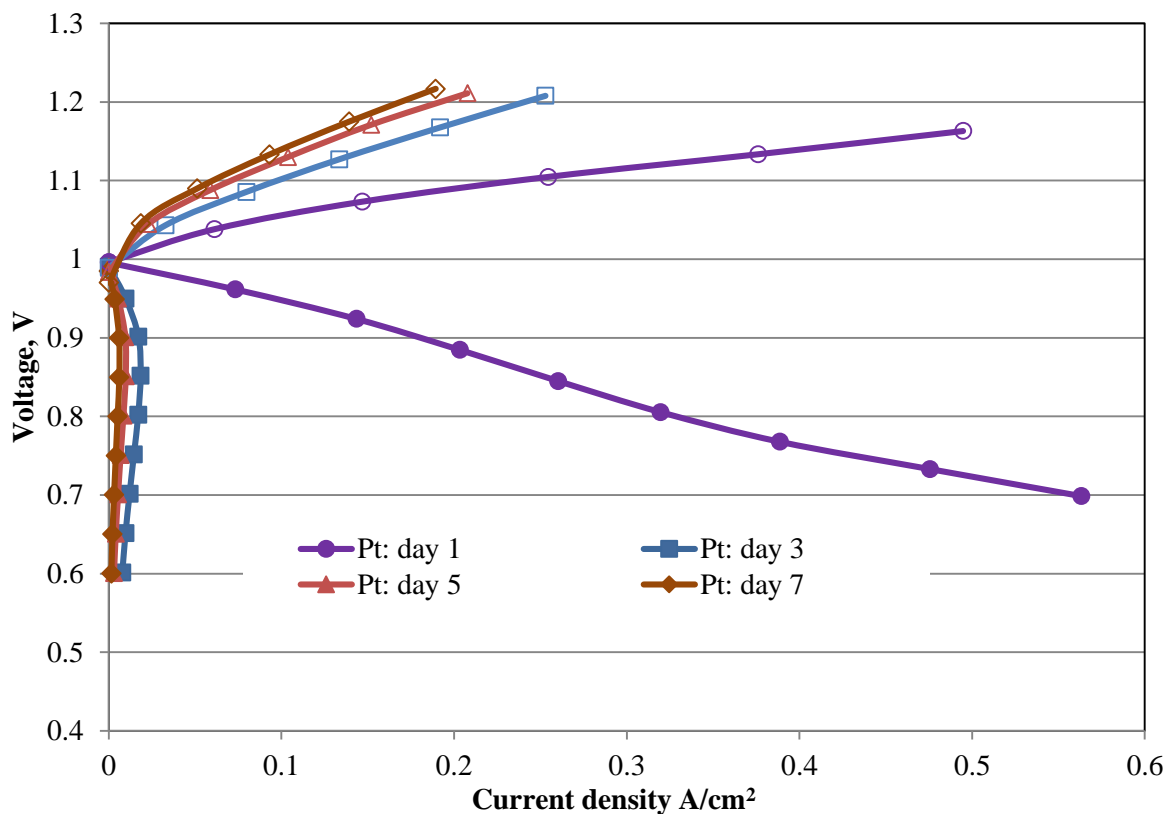
Figure 2.10. A week-long stability study with Pt as a H$_2$ electrocatalyst in a H$_2$-Br$_2$ fuel cell (cell performance measured on days 1, 3, 5, and 7)

The poisoning occurs due to the adsorption of Br$^-$ species onto the active Pt catalyst sites.[9,28] As a result, the hydrogen atoms were deprived of active catalyst sites for reaction. Also, the Pt catalyst was corroded in the presence of Br$_2$ and Br$_3^-$ species leading to the loss of active sites for the electrochemical reactions to occur. The discharge performance obtained on day 3 and beyond was severely affected due to the combined effect of poisoning and corrosion. However, the effect of HBr and Br$_2$ crossover was not too severe in the charge direction

compared to that in the discharge direction as seen in Figure 2.10. This is due to the fact that the poisoning effect is reversible since the adsorbed Br⁻ species can be removed at hydrogen evolution potentials and eventually flushed out by the H_2 gas flowing through the electrode.[28] The charge performances beyond day 1 show significantly higher overpotential which may be attributed to the permanent loss of platinum due to the dissolution of Pt catalyst. A continual decrease in charge performance on day 3 and beyond was observed as the platinum catalyst in the hydrogen electrode was further exposed to the HBr/Br_2 solution.
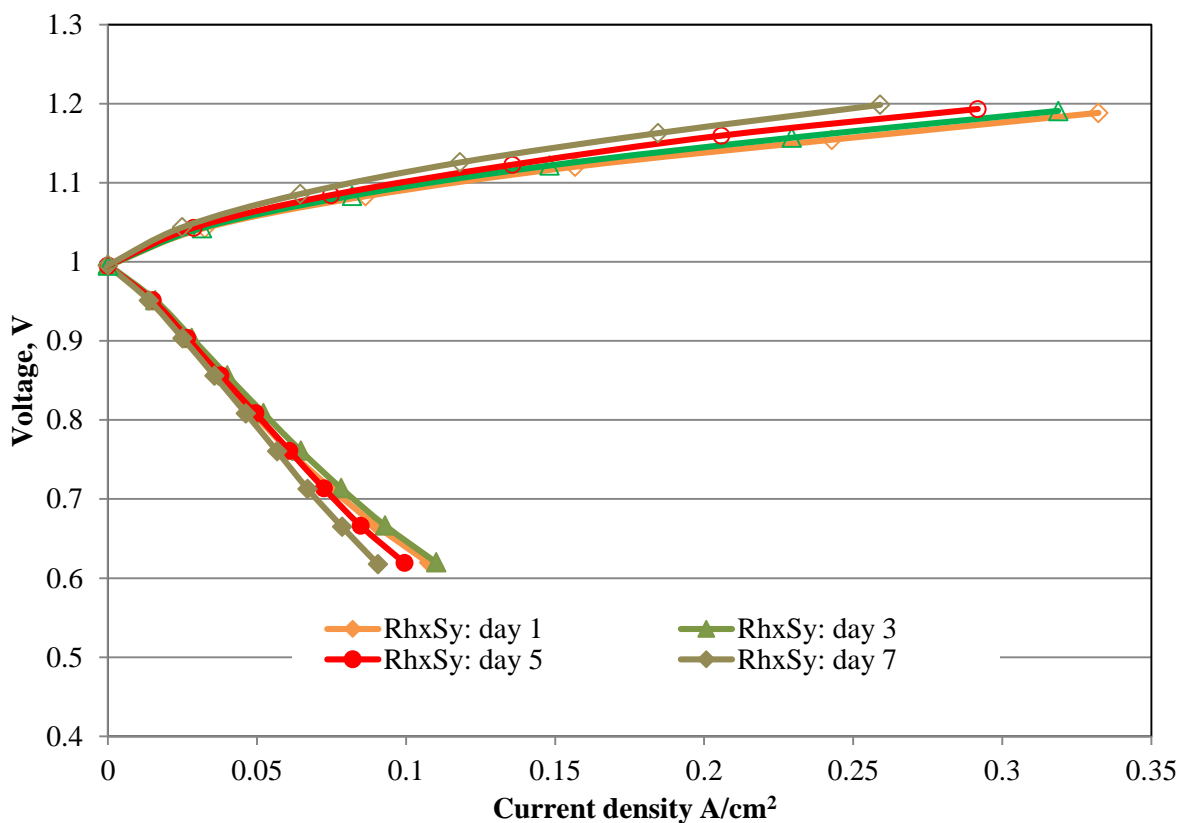
Figure 2.11. A week-long stability study with Rh_xS_y as a H_2 electrocatalyst in a H_2-Br_2 fuel cell (cell performance measured on days 1, 3, 5, and 7)

The performance of the fuel cell stack with Rh_xS_y shown in Figure 2.11 was almost unaffected by the crossover of Br_2, Br^-, and Br_3^- species. The slight decrease in both discharge and charge performance beyond day 1 could be attributed to dissolution of any free Rh metal present in the Rh_xS_y catalyst upon interacting with the crossover species.[10] Figure 2.12 compares the performance of Pt and Rh_xS_y catalysts on days 1 and 7. As shown in Figure 2.12, the charge performance of Rh_xS_y on day 1 was comparable to that of Pt whereas the discharge performance of Rh_xS_y was quite low. However, the discharge performance of the fuel cell with Rh_xS_y catalyst was unaffected over the week-long period of testing, which shows the superior stability of the Rh_xS_y catalyst over Pt.
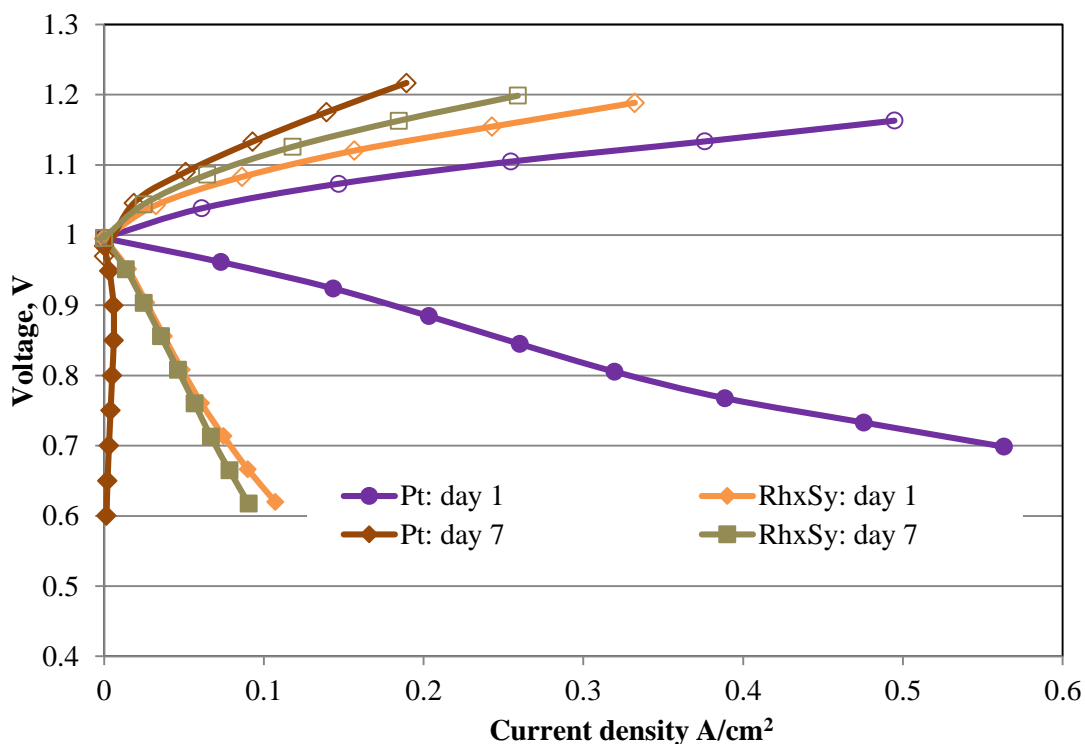
Figure 2.12. Comparing the stability of Pt and Rh_xS_y electrocatalysts on days 1 and 7 in a

H_2-Br_2 fuel cell

2.3.7. Feasibility of Pt Catalyst in a H$_2$-Br$_2$ Fuel Cell

The following sections discuss the feasibility of the Pt catalyst in a H$_2$-Br$_2$ fuel cell fixture. In the first case study, two fuel cell stacks were assembled and tested under different experimental conditions. Figure 2.13 shows the two performance curves acquired with the first fuel cell stack, where the H$_2$ was shut off (H$_2$ side was not pressurized) in between the runs. The time period between the two runs was 8 hours. The fuel cell was allowed to stay at rest condition for the entire 8 hours between the two runs. As expected, the fuel cell performance was affected due to Br$_2$ and Br$^-$ crossover. Since there was no recirculation of pressurized H$_2$ on the other side, the Br$_2$ and Br$^-$ species were able to crossover with little resistance. A huge drop in discharge performance was observed after 8 hours. Based on the work done by Xu et al., bromide adsorption is voltage dependent and is believed to increase as the voltage at the H$_2$ electrode becomes more positive leading to higher adsorption of bromide and higher equilibrium potential.[28] This positive shift in the hydrogen equilibrium potential causes the current density to decrease resulting in poor performance.[29] Note that Br$_2$ in the presence of H$_2$ is converted immediately to Br$^-$. So, most of the adsorbed species will be Br$^-$, not Br$_2$, when H$_2$ is present. Overall, the catalyst is both poisoned and corroded in the absence of H$_2$ recirculation.
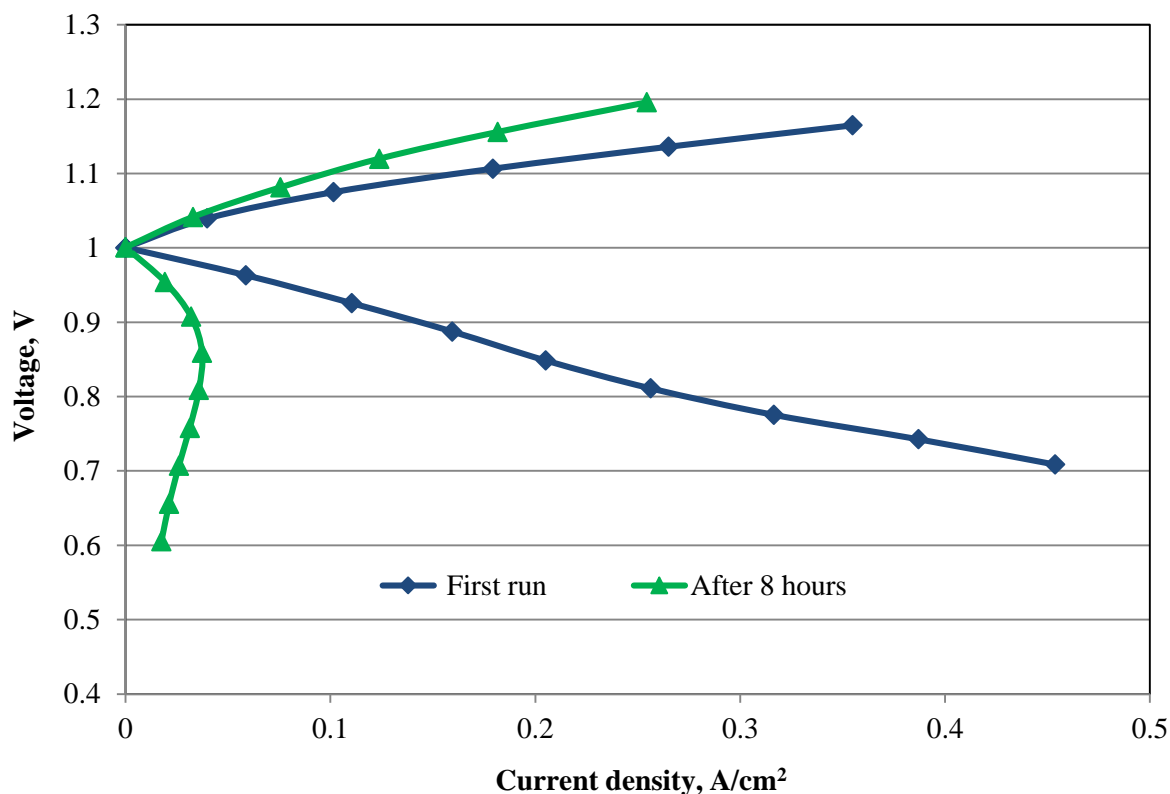
Figure 2.13. Stability study of Pt as a H_2 electrocatalyst in a H_2-Br_2 fuel cell with H_2 pump shut off (H_2 side was not pressurized between the two runs)

Figure 2.14 shows the results obtained with the second stack, where the H_2 gas was continuously circulated between the two performance runs. As shown in Figure 2.14, the performance was unaffected due to the resistance offered by the continuous H_2 recirculation against the crossover of Br_2 and Br^- species. It is suspected that when H_2 pressure is maintained while the HBr/Br_2 pump is stopped, the H_2 gas will push the HBr/Br_2 solution away from the membrane/bromine electrode interface thus reducing the chance for HBr/Br_2 electrolyte to crossover to the H_2 side. Furthermore, there is a concern that even with hydrogen pressure in the hydrogen compartment, the diffusion rate of hydrogen through the electrolyte, created in the hydrogen electrode by cross-over of bromine solution, to the platinum surface may not be

fast enough to keep the platinum surface protected from bromine and bromide ions, especially during open circuit. The study by Cho et al. shows reduced platinum dissolution rate when a hydrogen atmosphere or hydrogen evolution potential was applied to the hydrogen electrode during rest or standby, not zero corrosion rate.[30] In conclusion, the continuous H_2 recirculation offers resistance towards the species crossover, which in turn prolongs the life of the fuel cell. However, the continuous gas recirculation in not practical and hence not a suitable permanent solution to avoid crossover issues.
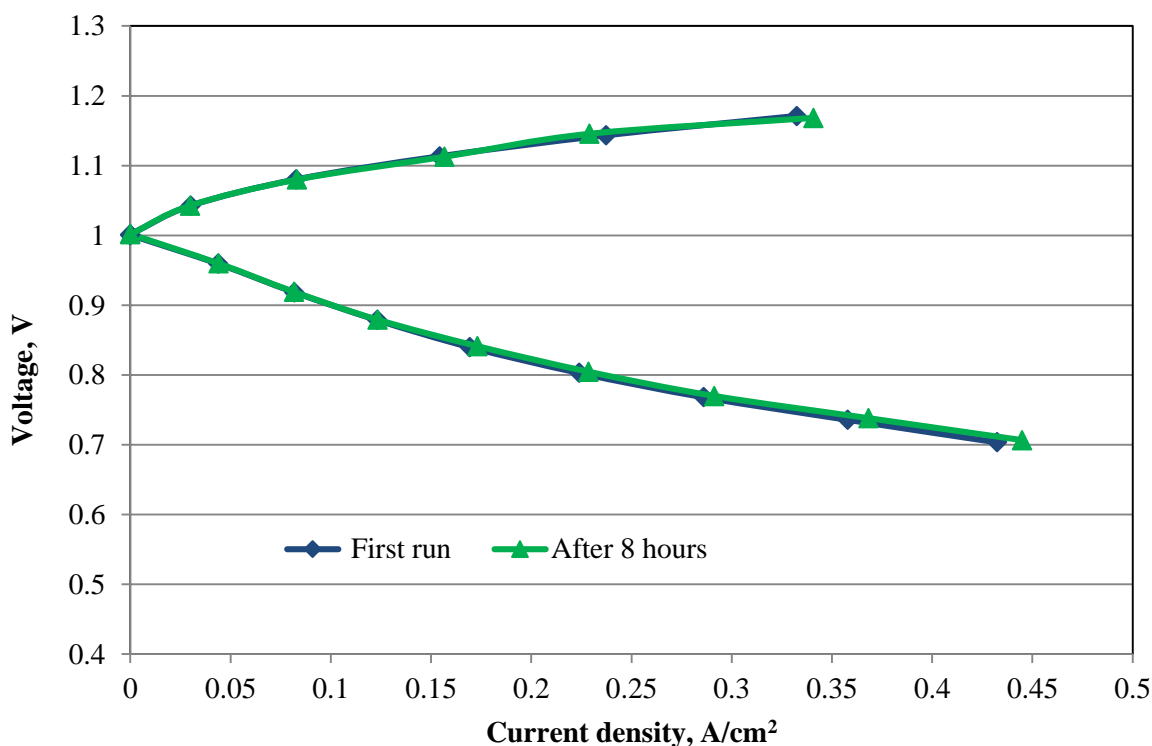
Figure 2.14. Stability study of Pt as a H_2 electrocatalyst in a H_2-Br_2 fuel cell with H_2 pump on (H_2 pressure maintained between the two runs)

The Br_2 and Br^- adsorption on platinum is reversible and potential dependent. Note that, Br_2 in the presence of H_2 is converted immediately to Br^-. So, most of the adsorbed species

will be Br⁻, not Br₂ when H₂ is present. Also, H₂ is more preferentially adsorbed than Br₂ and Br⁻ at potentials more negative than +100 mV of the H₂ electrode equilibrium potential. In this potential range, flushing the electrode with H₂ will help remove both Br₂ and Br⁻ from the electrode. At potentials more positive than +100 mV, Br⁻ is more strongly adsorbed than H₂ leading to a positive shift in the hydrogen equilibrium potential and therefore lower oxidation current density for a given applied voltage.

The next case study involves injecting HBr and HBr/Br₂ solutions directly into the H₂ electrode to simulate the Br⁻ and Br₂ species crossover. The objective of this study, which is designed to bypass the long wait time associated with the slow crossover rate of the aqueous species from the bromine side to the hydrogen side, was to observe the immediate effect of Br₂ and Br⁻ species crossover on the fuel cell discharge performance. The testing protocol was explained in detail in the experimental section. Figure 2.15 shows the results obtained in this study. Initially, HBr alone was injected to observe the impact of Br⁻ ion crossover. A 2M HBr solution was injected twice and for each injection, the fuel cell was allowed to stay at OCV (for approximately 8 minutes) for the Br⁻ ions to interact with the Pt catalyst layer. As shown in Figure 2.15, the performance was unaffected after the two injections (A & B). Since the microporous layer of the H₂ electrode is extremely hydrophobic, it is highly improbable for the Br⁻ ions to reach the Pt catalyst layer. Hence, the performance of the fuel cell was not affected. However, the performance of the fuel cell was affected once a mixture of HBr and Br₂ is injected (see Figure 2.15 points C & D). The performance deteriorated with each injection. Even though liquid could not penetrate into the highly hydrophobic microporous layer, the Br₂ species in vapor state could still diffuse through the microporous layer to contact the Pt catalyst layer and, subsequently, poison and corrode the platinum catalyst. This case

study suggests two major conclusions. First, there is an instantaneous effect once the Br_2 species interacts with the Pt catalyst. Second, the effect of Br_2 vapor on the Pt catalyst is as severe as liquid bromine or bromide ions. The occurrence of events such as emergency shutdowns or having to idle the system prior to complete degradation of the H_2-Br_2 fuel cell still needs to be studied.
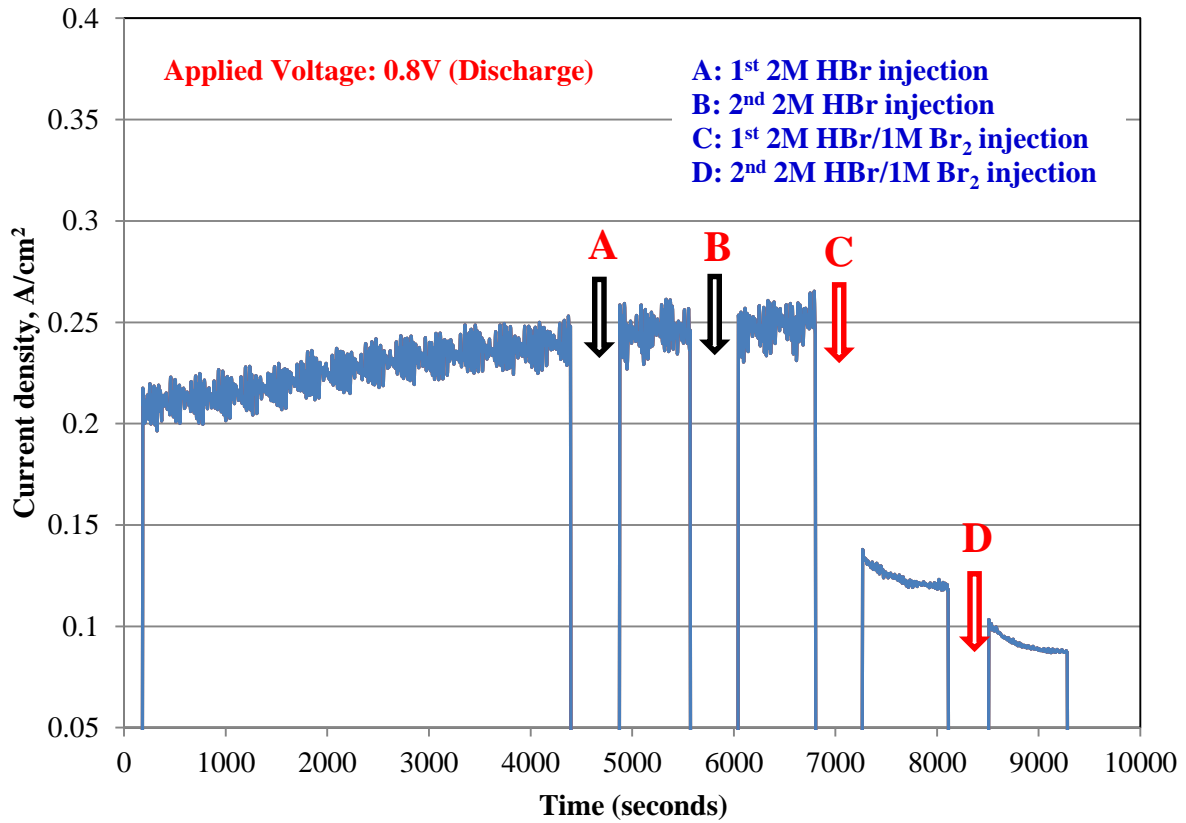
Figure 2.15. Effect of HBr (locations A and B) and HBr/Br_2 (locations C and D) injections on the discharge performance of a H_2-Br_2 fuel cell held at a constant voltage, 0.8V

2.4. Conclusions

The attractive features as well as some of the material related issues corresponding to the H_2-Br_2 fuel cell are discussed in this study. Preliminary fuel cell test results clearly highlighted the

immense energy storage potential of the H_2-Br_2 fuel cell, which is a result of the highly reversible electrochemical reactions associated with the reactants used in this system. The novel dual fiber electrospun composite membranes (PFSA/PPSU) have been tested in an actual H_2-Br_2 fuel cell. The preliminary performance of these electrospun membranes look quite promising indicating that they might be an alternative to Nafion membranes.

The Pt catalyst is prone to corrosion and poisoning due to the crossover of Br_2 and Br^- species from the Br_2 electrode to the H_2 electrode. Both Pt and Rh_xS_y catalysts were evaluated in an actual fuel cell to determine their activity and stability. The stability of Rh_xS_y in HBr/Br_2 environment was excellent compared to that of Pt. However, the H_2 oxidation activity of Rh_xS_y was quite low and needs to be improved for it to be used as an electrocatalyst in the H_2 electrode. The feasibility of using a Pt catalyst under different experimental conditions was evaluated. The lifetime of the fuel cell could be prolonged through continuous flow of H_2 gas and keeping the H_2 electrode pressurized. Using an alternative H_2 electrocatalyst that is stable and active is still the best option to solve the crossover issues since there is a possibility of a Pt catalyst system design failing under certain situations such as loss of hydrogen environment.

2.5. References

1. William A. Braff, Martin Z. Bazant, and Cullen R. Buie, "Membrane-less hydrogen bromine flow battery," *Nature Communications*, **4**, Article: 2346 (2013).

2. Marc-Antoni Goulet and Erik Kjeang, "Co-laminar flow cells for electrochemical energy conversion," *J. Power Sources*, **260**, 186-196 (2014).

3. E. R. Choban, J. S. Spendelow, L. Gancs, A. Wieckowski, and P. J. A. Kenis, "Membraneless laminar flow-based micro fuel cells operating in alkaline, acidic, and acidic/alkaline media," *Electrochimica Acta*, **50**, 5390-5398 (2005).

4. E. Aleksandrova, S. Hink, R. Hiesgen, and E. Roduner, "Spatial distribution and dynamics of proton conductivity in fuel cell membranes: potential and limitations of electrochemical atomic force microscopy measurements," *J. Physics: Condensed Matter*, **23**, Article: 234109 (2011).

5. P.J. James, J.A. Elliott, T.J. McMaster, J.M. Newton, A.M.S. Elliott, S. Hanna, and M.J. Miles, "Hydration of Nafion® studied by AFM and x-ray scattering," *J. of Materials Science*, **35**, 5111-5119 (2000).

6. S. W. Choi, Y. Z. Fu, Y. R. Ahn, S. M. Jo, A. Manthiram, "Nafion-impregnated electrospun polyvinylidene fluoride composite membranes for direct methanol fuel cells," *J. Power Sources*, **180**, 167-171 (2008).

7. Ryouhei Takemori and Hiroyoshi Kawakami, "Electrospun nanofibrous blend membranes for fuel cell electrolytes," *J. Power Sources*, **195**, 5957-5961 (2010).

8. Takuya Tamura and Hiroyoshi Kawakami, "Aligned Electrospun Nanofiber Composite Membranes for Fuel Cell Electrolytes," *Nano Lett.*, **10**, 1324-1328 (2010).

9. M. Goor-Dar, N. Travitsky, and E. Peled, "Study of hydrogen redox reactions on platinum nanoparticles in concentrated HBr solutions," *J. Power Sources*, **197**, 111-115 (2012).

10. N. Singh, S. Mubeen, J. Lee, H. Metiu, M. Moskovits, and E. W. McFarland, "Stable electrocatalysts for autonomous photoelectrolysis of hydrobromic acid using single-junction solar cells," *Energy Environ. Sci.*, **7**, 978-981 (2014).

11. Joseph M. Ziegelbauer, Andrea F. Gulla, Cormac O᾽Laoire, Christian Urgeghe, Robert J. Allen, and Sanjeev Mukerjee, "Chalcogenide electrocatalysts for oxygen-depolarized aqueous hydrochloric acid electrolysis," *Electrochimica Acta*, **52**, 6282-6294 (2007).

12. Dimitrios C. Papageorgopoulos, Fang Liu, and Olaf Conrad, "A study of RhxSy/C and RuSex/C as methanol-tolerant oxygen reduction catalysts for mixed-reactant fuel cell applications," *Electrochimica Acta*, **52**, 4982-4986 (2007).

13. Andrea F. Gulla, Lajos Gancs, Robert J. Allen, and Sanjeev Mukerjee, "Carbon-supported low-loading rhodium sulfide electrocatalysts for oxygen depolarized cathode applications," *Applied Catalysis A: General*, **326**, 227-235 (2007).

14. Chen Jin, Wei Xia, Tharamani Chikka Nagaiah, Junsong Guo, Xingxing Chen, Michael Bron, Wolfgang Schuhmann, and Martin Muhler, "On the role of the thermal treatment of sulfide Rh/CNT catalysts applied in the oxygen reduction reaction," *Electrochimica Acta*, **54**, 7186-7193 (2009).

15. Joseph M. Ziegelbauer, Daniel Gatewood, Andrea F. Gulla, Maxime J.-F. Guinel, Frank Ernst, David E. Ramaker, and Sanjeev Mukerjee, "Fundamental Investigation of Oxygen Reduction Reaction on Rhodium Sulfide-Based Chalcogenides," *J. Phys. Chem.*, **113**, 6955-6968 (2009).

16. Jacob Bonde, Poul G. Moses, Thomas F. Jaramillo, Jens K. Norskov, and Ib Chorkendorff, "Hydrogen evolution on nano-particulate transition metal sulfides," *Faraday Discussions*, **140**, 219-231 (2008).

17. Anna Ivanovskaya, Nirala Singh, Ru-Fen Liu, Haley Kreutzer, Jonas Baltrusaitis, Trung Van Nguyen, Horia Metiu, and Eric McFarland, "Transition Metal Sulfide Hydrogen Evolution Catalysts for Hydrobromic Acid Electrolysis," *Langmuir*, **29**, 480-492 (2013).

18. Trung Van Nguyen, Haley Kreutzer, Venkata Yarlagadda, Eric McFarland, and Nirala Singh, "HER/HOR catalysts for the H_2-Br_2 Fuel Cell System," *ECS Transactions*, **53** (7), 75-81 (2013).

19. Kyu Taek Cho, Paul Albertus, Vincent Battaglia, Aleksander Kojic, Venkat Srinivasan, and Adam Z. Weber, "Optimization and Analysis of High-Power Hydrogen/Bromine-Flow Batteries for Grid-Scale Energy Storage," *Energy Technol.*, **1**, 596-608 (2013).

20. Haley Kreutzer, Venkata Yarlagadda, and Trung Van Nguyen, "Performance Evaluation of a Regenerative Hydrogen-Bromine Fuel Cell," *J. Electrochem Soc.*, **159** (7), F331-F337 (2012).

21. David Wood III, Jung S. Yi, and Trung V. Nguyen, "Effect of direct liquid water injection and interdigitated flow field on the performance of proton exchange membrane fuel cells," *Electrochimica Acta*, **43**, 3795-3809 (1998).

22. J. W. Park, R. Wycisk, and P. N. Pintauro, "Membranes for a Regenerative H_2/Br_2 Fuel Cell," *ECS Transactions*, **50** (2), 1217-1231 (2012).

23. J. B. Ballengee and P. N. Pintauro, "Composite Fuel Cell Membranes from Dual-Nanofiber Electrospun Mats," *Macromolecules*, **44**, 7307-7314 (2011).

24. Kyu Taek Cho, Paul Ridgeway, Adam Z. Weber, Sophia Haussener, Vincent Battagalia, and Venkat Srinivasan, "High Performance Hydrogen/Bromine Flow Battery Redox Flow Battery for Grid-Scale Energy Storage," *J. Electrochem. Soc.*, **159** (11), A1806-A1815 (2012).

25. Venkata Yarlagadda and Trung Van Nguyen, "A 1D Mathematical Model of a H_2/Br_2 fuel cell," *J. Electrochem Soc.*, **160** (6), F535-F547 (2013).

26. Venkata Yarlagadda and Trung Van Nguyen, "High Surface Area Carbon Electrodes for the Bromine Reactions in H_2-Br_2 Fuel Cells," *ECS Transactions*, **58** (36), 25-32 (2014).

27. Regis Paul Dowd Jr., Trung Van Nguyen, David S Moore, Peter N Pintauro and Jun Woo Park, "Conductive AFM Study to Differentiate between the Surface Ionic Conductivity of Nafion and Electrospun Membranes," *ECS Transactions*, **58** (1), 607-613 (2013).

28. Jing Xu and Daniel Scherson, "Quantitative Correlations between the Normal Incidence Differential Reflectance and the Coverage of Adsorbed Bromide on a Polycrystalline Platinum Rotating Disk Electrode," *Anal. Chem.*, **85**, 2795-2801 (2013).

29. Haley M. Kreutzer, "Characterization of Hydrogen-Bromine Flow Battery for Electrical Energy Storage," MS Thesis, University of Kansas, Lawrence, KS, USA, May 2012.

30. Michael C. Tucker, Kyu Taek Cho, Adam Z. Weber, Guangyu Lin, and Trung Van Nguyen, "Optimization of electrode characteristics for the Br_2/H_2 redox flow cell," *J. Appl. Electrochem.*, **45**, 11-19 (2015).

CHAPTER 3

A 1D Mathematical Model of a Regenerative Hydrogen-Bromine Fuel Cell

3.1. Literature Review

Savinell and Fritts modeled both the H_2-Br_2 fuel cell and H_2 electrode bonded membrane electrode assembly (MEA) and investigated the effect of kinetic, transport and catalyst particle properties on the performance of the system.[1,2] It was reported that, transport properties of the membrane play a prominent role in controlling the fuel cell performance. However, the effect of bromine electrode properties on the fuel cell performance was not examined in detail. Zhang and Weidner examined the performance of a gas-phase H_2-Br_2 flow battery by comparing both modeling and experimental results.[3] Higher current densities compared to liquid electrolyte systems were reported on both charge and discharge, which was attributed to the high mass transfer rate associated with gas transport. Braff and Buie predicted the performance of a novel H_2-Br_2 laminar flow cell operating under dominant convective transport regime using a two-dimensional mathematical model.[4] This design was employed to reduce cross-over losses and to eliminate the need for a membrane.

Recently, Cho et al. developed a two-dimensional model to study the impact of flow-by (operated under dominant diffusive transport) and flow-through (operated under dominant convective transport) modes on the performance of their liquid phase H_2-Br_2 fuel cell.[5] Of the two flow modes, the flow-through case, where convection is the dominant transport mechanism was shown as a favorable option due to higher reactant utilization. However, the effect of electrode properties and kinetic rate on the performance of the H_2-Br_2 fuel cell was not examined in their modeling study. Huskinson et al. developed a model to determine the effect of several parameters such as exchange current density, membrane thickness, diffusion

layer thickness, and hydrogen pressure on the H_2-Br_2 fuel cell performance.[6] However, the empirical approach used in the model limits its predictability to the conditions of the data used. To address these issues specified above, a liquid phase H_2-Br_2 fuel cell is modeled in this study to investigate the effect of convective and diffusive transport and kinetic rate on the fuel cell performance. Also, the purpose of this model was to serve as a theoretical guiding tool for the future experimental studies of this system.

3.2. Model Development

As shown in Figures 3.1a and 3.1b, the model region consists of a porous bromine electrode filled with HBr-Br_2 solution, a proton conducting membrane electrolyte, and a porous hydrogen electrode. The fuel cell system was assumed to operate at steady state and under isothermal conditions. Also, transport is assumed to be limited to the x direction. The parameters δ_1, δ_2, and δ_3 represent the thickness of Br_2 electrode, membrane, and H_2 electrode, respectively. The anodic and cathodic reactions associated with the fuel cell are shown below.

$$\frac{1}{2} Br_2 + e^- \longleftrightarrow Br^- \qquad E^0 = 1.09 \text{ V}$$

$$\frac{1}{2} H_2 \longleftrightarrow H^+ + e^- \qquad E^0 = 0 \text{ V}$$

=====================================

$$\frac{1}{2} H_2 + \frac{1}{2} Br_2 \underset{charge}{\overset{discharge}{\rightleftharpoons}} H^+ + Br^- \quad E_{cell} = 1.09 \text{ V}$$
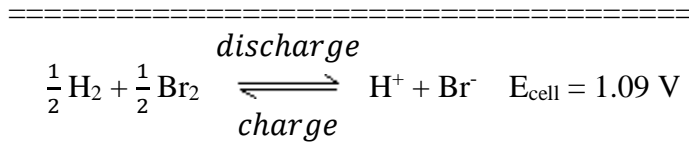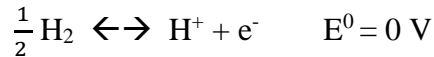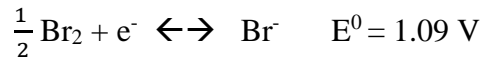
Since the bromine reactions do not need any precious metal catalysts, the Br_2 electrode was assumed to be a plain porous carbon electrode without any catalyst layer.[5] In an actual H_2-Br_2 fuel cell, the H_2 electrode is composed of a gas diffusion layer (GDL) on a carbon-

supported platinum catalyst layer (CL). However, attributing to the faster gas transport rate, the gas diffusion layer in the H_2 electrode was not included in the modeling domain. Since the electronic conductivity of the solid phase (carbon) is much higher than the ionic conductivity, by almost three orders of magnitude, the electronic potential in the electrode was assumed to be constant. Also, two different flow field modes, namely, flow-by (serpentine) and flow-through (interdigitated)[7] were included in the model. A Continuous Stirred Tank Mixer (CSTM) was used to specify the electrolyte concentrations at the electrode/flow channel interface in the flow-by mode as shown in Figure 3.1a.

In the flow-by mode (Figure 3.1a),the electrolyte is transported through the electrode mainly by diffusion and migration whereas the electrolyte is forced to convectively penetrate into the porous electrode in the case of the flow-through mode (Figure 3.1b). So, for the flow-by mode, diffusion and migration were assumed to be the dominant transport mechanisms and convective transport inside the porous electrode was assumed to be negligible. For the flow-through mode, diffusion, migration, and convection were assumed to be the major transport mechanisms inside the porous electrode with convection being the dominant transport mechanism. Porous electrode theory was applied to develop the flux expressions for each of the species (H^+, Br^-, and Br_2). In these studies, the crossover of bromide and bromine species across the membrane and the tri-bromide complexation reaction ($Br_2 + Br^- \leftrightarrow Br_3^-$) were not considered. The effect of electroosmotic drag in the membrane was also neglected.
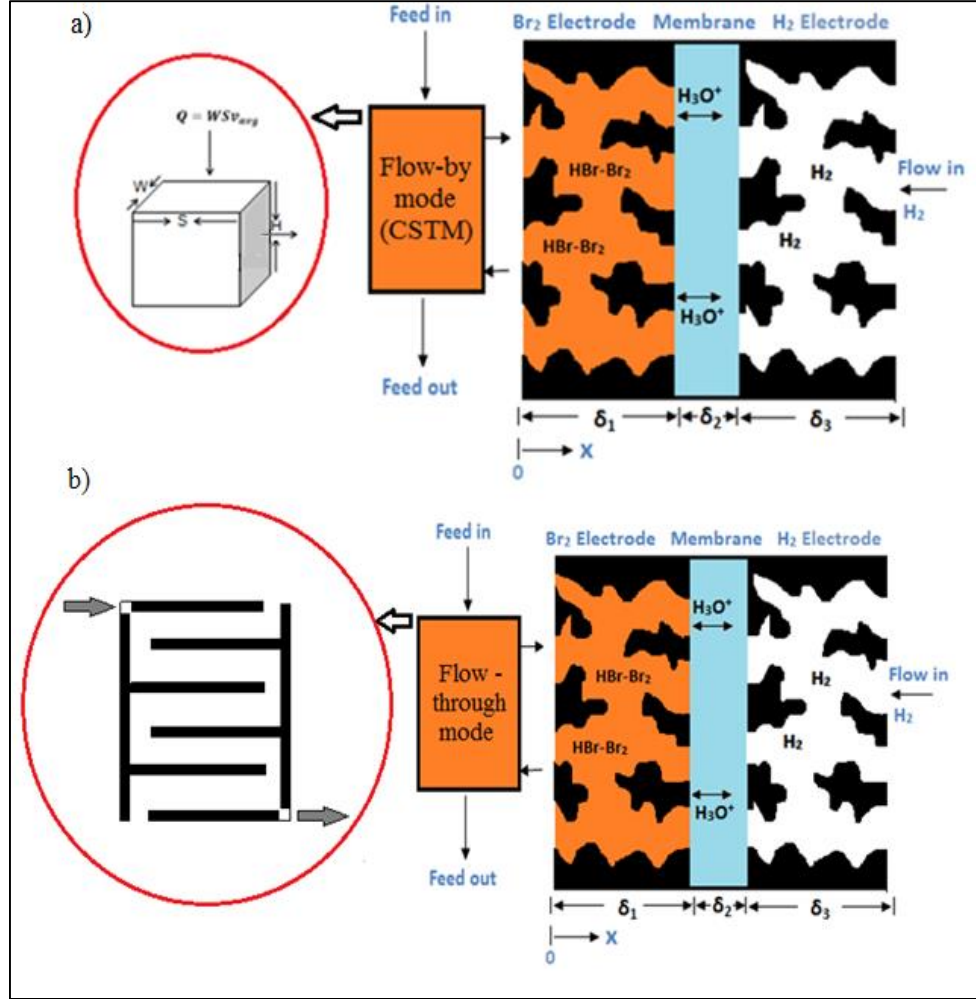
Figure 3.1. Modeling domain of a H_2-Br_2 fuel cell in (a) flow-by and (b) flow-through

modes

3.2.1. Governing Equations

The variables involved in the model are the concentrations of Br^-, Br_2 and H^+ (C_{Br^-}, C_{Br2}, and

C_{H^+}) in the Br_2 electrode and ionic phase potential (ϕ_+) in the Br_2 electrode, membrane, and

H_2 electrode.

Inside the bromine electrode ($0 < x < \delta_1$), the steady state material balance of species j

in the bulk electrolyte is expressed by the following equation:

$$-\nabla \cdot N_j + R_j = 0 \quad (j = Br^- \, and \, Br_2) \tag{3.1}$$

where N_j is the flux of the species j and R_j is the generation term involving species j in the electrochemical reaction. Since the protons do not participate in the electrochemical reaction in this electrode, the material balance for the proton in the Br_2 electrode is shown below:

$$-\nabla \cdot N_j = 0 \quad (j = H^+) \tag{3.2}$$

The flux (N_j) and reaction (R_j) terms in the material balance are represented by the following equations:

$$N_j = -D_j^{eff} \frac{dC_j}{dx} - \frac{Z_j D_j^{eff} F C_j}{RT} \frac{d\phi_+}{dx} \quad (flow - by) \tag{3.3}$$

$$N_j = v_x C_j - D_j^{eff} \frac{dC_j}{dx} - \frac{Z_j D_j^{eff} F C_j}{RT} \frac{d\phi_+}{dx} \quad (flow - through) \tag{3.4}$$

$$R_j = \frac{a_{Br_2} s_j i_x}{nF} \tag{3.5}$$

where ϕ_+ is the ionic phase potential; C_j is the concentration of species j; v_x is the velocity of the feed stream in the x direction; Z_j is the electrical charge of species j; a_{Br_2} is the specific active surface area per unit electrode volume; s_j is the stoichiometric coefficient of species j in the reaction; i_x is the charge transfer current density for the electrochemical reaction in the electrode; n is the number of electrons involved in the reaction; and F, R, and T are Faraday constant, gas constant, and temperature, respectively. The modeling efforts to develop a correlation between the feed stream velocity (v_x) and the electrode thickness (x) are explained in detail under the Appendix section. The relation between the ordinary diffusion coefficient (D_j) and the effective diffusion coefficient (D_j^{eff}) is shown below.

$$D_j^{eff} = D_j \varepsilon_{Br_2}^{1.5} \tag{3.6}$$

The Bruggeman factor 1.5 approximates the effect of porosity (ε) and tortuosity inside the porous electrode. For the flow-by mode, inserting equations [3.2], [3.3] and [3.5] into equation [3.1] yields

$$D_j \varepsilon_{Br_2}^{1.5} \frac{d^2 C_j}{dx^2} + \frac{z_j D_j \varepsilon_{Br_2}^{1.5} F}{RT}\left(C_j \frac{d^2 \phi_+}{dx^2} + \frac{dC_j}{dx}\frac{d\phi_+}{dx}\right) + \frac{a_{Br_2} s_j i_x}{nF} = 0 \quad (j = Br^- \text{ and } Br_2) \qquad [3.7]$$

For the flow-through mode, inserting equations [3.2], [3.4], and [3.5] yields

$$-v_x \frac{dC_j}{dx} + D_j \varepsilon_{Br_2}^{1.5}\frac{d^2 C_j}{dx^2} + \frac{z_j D_j \varepsilon_{Br_2}^{1.5} F}{RT}\left(C_j \frac{d^2 \phi_+}{dx^2} + \frac{dC_j}{dx}\frac{d\phi_+}{dx}\right) + \frac{a_{Br_2} s_j i_x}{nF} = 0 \ (j = Br^- \text{ and } Br_2) \qquad [3.8]$$

The expression derived by White et al. from the Butler-Volmer equation is used to calculate the charge transfer current density i_x.[8]

$$i_x = i_{o,ref,Br_2} X_{Br_2}$$

$$X_{Br_2} = \left[\prod_j \left(\frac{c_j}{c_{j,ref}}\right)^{p_j} e^{\left[\frac{\alpha_a F}{RT}(\phi_s - \phi_+ - U_{Br_2 ref})\right]} - \prod_j \left(\frac{c_j}{c_{j,ref}}\right)^{q_j} e^{\left[-\frac{\alpha_c F}{RT}(\phi_s - \phi_+ - U_{Br_2 ref})\right]}\right]$$

where

$$U_{Br_2 ref} = U_{Br_2}^o - \frac{RT}{nF}\sum_j s_j \ln C_{j,ref} - U_{RE}^0$$

$$p_j = \gamma_j + \frac{\alpha_a s_j}{n} \quad \text{and} \quad q_j = \gamma_j - \frac{\alpha_c s_j}{n} \quad (j = Br_2 \text{ and } Br^-) \qquad [3.9]$$

where i_{o,ref,Br_2} is the exchange current density of the bromine reaction at the reference concentrations, $C_{j,ref}$ is the reference concentration of species j, ϕ_s is the potential of the solid electronic phase, $U_{Br_2 ref}$ is the equilibrium potential of the bromine reaction relative to the reference electrode (U_{RE}^0) at the reference concentrations, $U_{Br_2}^o$ is the standard electrode potential of the bromine reaction, U_{RE}^0 is the standard hydrogen electrode (SHE) potential, γ_j is the exponent in the composition dependence of the exchange current density, and α_a and α_c are the anodic and cathodic transfer coefficients of the bromine reaction respectively. Also, the electroneutrality condition applies to the electrolyte in the bromine electrode.

$$\sum_j Z_j C_j = 0 \ (j = H^+ and \ Br^-) \tag{3.10}$$

The bromine and bromide species were assumed to be absent in the membrane ($\delta_1 < x < \delta_2$) and the H_2 electrode ($\delta_2 < x < \delta_3$) based on the no-crossover assumption. For modeling conveniences, the concentrations of Br_2 and Br^- were set to zero in these components. The proton conductivities ($k_{H^+}^m$, $k_{H^+}^{H_2}$) and concentration (C_{H^+}) were assumed to be constant and uniform across the membrane and the H_2 electrode. However, $k_{H^+}^{H_2}$ is calculated based on the effective ionomer volume fraction in the H_2 electrode. The material balance in the hydrogen electrode is expressed as:

$$k_{H^+}^{H_2} \frac{d^2\phi_+}{dx^2} + \frac{a_{H_2} s_j i_{o.ref,H_2} X_{H_2}}{nF} = 0 \tag{3.11}$$

where X_{H_2} in the hydrogen electrode is expressed using equation [3.9] where j = H^+ and H_2. i_{o,ref,H_2} corresponds to the exchange current density of the hydrogen reaction; a_{H_2} represents the specific active surface area per unit electrode volume of the hydrogen electrode; and $U_{Br_2.ref}$ is replaced by $U_{H_2,ref}$, which is the equilibrium potential of the hydrogen reaction at the reference concentrations.

$$U_{H_2 ref} = U_{H_2}^o - \frac{RT}{nF} \sum_j s_j \ln C_{j,ref} - U_{RE}^0 \quad (j = H_2 \ and \ H^+) \tag{3.12}$$

where $U_{H_2}^o$ is the standard hydrogen electrode potential.

The governing equations described above apply for both flow-by and flow-through modes with the sole exception being the absence of the velocity term ($v_x = 0$) while solving the flow-by case. The governing equations for the flow-by and flow-through modes are summarized in Tables 3.1 and 3.2.

Table 3.1. Governing equations for flow-by mode

Variable	Br$_2$ electrode
C_{Br^-}	$D_{Br^-}\varepsilon^{1.5}\dfrac{d^2C_{Br^-}}{dx^2} + \dfrac{z_{Br^-}D_{Br^-}\varepsilon^{1.5}F}{RT}\left(C_{Br^-}\dfrac{d^2\phi_+}{dx^2} + \dfrac{dC_{Br^-}}{dx}\dfrac{d\phi_+}{dx}\right) + \dfrac{a_{Br_2}s_{Br^-}i_x}{nF} = 0$
C_{Br_2}	$D_{Br_2}\varepsilon^{1.5}\dfrac{d^2C_{Br_2}}{dx^2} + \dfrac{a_{Br_2}s_{Br_2}i_x}{nF} = 0$
C_{H^+}	$D_{H^+}\varepsilon^{1.5}\dfrac{d^2C_{H^+}}{dx^2} + \dfrac{z_{H^+}D_{H^+}\varepsilon^{1.5}F}{RT}\left(C_{H^+}\dfrac{d^2\phi_+}{dx^2} + \dfrac{dC_{H^+}}{dx}\dfrac{d\phi_+}{dx}\right) = 0$
ϕ_+	$C_{H^+}Z_{H^+} + Z_{Br^-}C_{Br^-} = 0$

where

$$i_x = i_{o,ref,Br_2}\left[\prod_j\left(\frac{c_j}{c_{j,ref}}\right)^{p_{j1}} e^{\left[\frac{\alpha_{a1}F}{RT}(\phi_s-\phi_+-U_{Br_2ref})\right]} - \prod_j\left(\frac{c_j}{c_{j,ref}}\right)^{q_{j1}} e^{\left[-\frac{\alpha_{c1}F}{RT}(\phi_s-\phi_+-U_{Br_2ref})\right]}\right]$$

The subscript 1 in the above equation represents the Br$_2$ electrode where j = Br$_2$ and Br$^-$.

Variable	Membrane
C_{Br^-}	N/A
C_{Br_2}	N/A
C_{H^+}	$C_{H^+} - C_{H^+}^m = 0$
ϕ_+	$k_{H^+}^m\dfrac{d^2\phi_+}{dx^2} = 0$

Variable	H$_2$ electrode
C_{Br^-}	N/A
C_{Br_2}	N/A
C_{H^+}	$C_{H^+} - C_{H^+}^{H_2} = 0$
ϕ_+	$k_{H^+}^{H_2}\dfrac{d^2\phi_+}{dx^2} + \dfrac{a_{H_2}s_{H^+}i_x}{nF} = 0$

where

$$i_x = i_{o,ref,H_2}\left[\prod_j\left(\frac{c_j}{c_{j,ref}}\right)^{p_{j2}} e^{\left[\frac{\alpha_{a2}F}{RT}(\phi_s-\phi_+-U_{H_2ref})\right]} - \prod_j\left(\frac{c_j}{c_{j,ref}}\right)^{q_{j2}} e^{\left[-\frac{\alpha_{c2}F}{RT}(\phi_s-\phi_+-U_{H_2ref})\right]}\right]$$

The subscript 2 in the above equation represents the H$_2$ electrode where j=H$_2$ and H$^+$.

Table 3.2. Governing equations for flow-through mode

Variable	Br$_2$ electrode
C_{Br^-}	$-v_x \frac{dC_{Br^-}}{dx} + D_{Br^-}\varepsilon^{1.5}\frac{d^2 C_{Br^-}}{dx^2} + \frac{z_{Br^-}D_{Br^-}\varepsilon^{1.5}F}{RT}\left(C_{Br^-}\frac{d^2\phi_+}{dx^2} + \frac{dC_{Br^-}}{dx}\frac{d\phi_+}{dx}\right) + \frac{a_{Br_2}s_{Br^-}i_x}{nF} = 0$
C_{Br_2}	$-v_x\frac{dC_{Br_2}}{dx} + D_{Br_2}\varepsilon^{1.5}\frac{d^2 C_{Br_2}}{dx^2} + \frac{a_{Br_2}s_{Br_2}i_x}{nF} = 0$
C_{H^+}	$-v_x\frac{dC_{H^+}}{dx} + D_{H^+}\varepsilon^{1.5}\frac{d^2 C_{H^+}}{dx^2} + \frac{z_{H^+}D_{H^+}\varepsilon^{1.5}F}{RT}\left(C_{H^+}\frac{d^2\phi_+}{dx^2} + \frac{dC_{H^+}}{dx}\frac{d\phi_+}{dx}\right) = 0$
ϕ_+	$C_{H^+}Z_{H^+} + Z_{Br^-}C_{Br^-} = 0$

where

$$i_x = i_{o,ref,Br_2}\left[\Pi_j\left(\frac{c_j}{c_{j,ref}}\right)^{p_{j1}}e^{\left[\frac{\alpha_{a1}F}{RT}(\phi_s-\phi_+-U_{Br_2ref})\right]} - \Pi_j\left(\frac{c_j}{c_{j,ref}}\right)^{q_{j1}}e^{\left[-\frac{\alpha_{c1}F}{RT}(\phi_s-\phi_+-U_{Br_2ref})\right]}\right]$$

The subscript 1 in the above equation represents the Br$_2$ electrode where j = Br$_2$ and Br$^-$.

Variable	Membrane
C_{Br^-}	N/A
C_{Br_2}	N/A
C_{H^+}	$C_{H^+} - C_{H^+}^m = 0$
ϕ_+	$k_{H^+}^m\frac{d^2\phi_+}{dx^2} = 0$

Variable	H$_2$ electrode
C_{Br^-}	N/A
C_{Br_2}	N/A
C_{H^+}	$C_{H^+} - C_{H^+}^{H_2} = 0$
ϕ_+	$k_{H^+}^{H_2}\frac{d^2\phi_+}{dx^2} + \frac{a_{H_2}s_{H^+}i_x}{nF} = 0$

where

$$i_x = i_{o,ref,H_2}\left[\Pi_j\left(\frac{c_j}{c_{j,ref}}\right)^{p_{j2}}e^{\left[\frac{\alpha_{a2}F}{RT}(\phi_s-\phi_+-U_{H_2ref})\right]} - \Pi_j\left(\frac{c_j}{c_{j,ref}}\right)^{q_{j2}}e^{\left[-\frac{\alpha_{c2}F}{RT}(\phi_s-\phi_+-U_{H_2ref})\right]}\right]$$

The subscript 2 in the above equation represents the H$_2$ electrode where j=H$_2$ and H$^+$

3.2.2. Boundary Conditions

There are four distinct boundaries associated with the modeling domain shown in Figures 3.1a and 3.1b. At the Br_2 electrode entrance, the boundary conditions vary depending on the type of flow mode employed.

3.2.2.1. Flow-By Mode

The CSTM in the model domain represents the flow-by channels in the flow field plate. The model relevant to the flow-by case was an absolute1D diffusion model. The consumption of reactants and generation of products along the axial direction is accounted by introducing the CSTM-like boundary condition at the entrance of the Br_2 electrode. This boundary condition establishes a more realistic condition since it is not possible to have an infinite reactant flow rate in order to maintain a constant feed concentration at the electrode entrance. Depending on the consumption rate of Br_2 and generation rate of Br^- in the CSTM, the concentrations of Br^- and Br_2 were fixed at the Br_2 electrode entrance ($x = 0$) by the following equation.

$$C_j = C_{j,in} - \left(-D_j^{eff} \frac{dC_j}{dx} - \frac{Z_j D_j^{eff} F C_j}{RT} \frac{d\phi_+}{dx} \right) \frac{A}{Q} \quad (j = Br_2 \text{ and } Br^-) \qquad [3.13]$$

where $C_{j,in}$ is the feed concentration of the species j in the feed stream. In Figure 3.1a, the electrode cross-sectional surface area (A) parallel to the fluid flow and volumetric flow rate (Q) of the feed entering the CSTM are represented by the following expressions:

$$A = WH \qquad [3.14]$$

$$Q = WSv_{avg} \qquad [3.15]$$

where W is the width of the flow field plate inlet which is also the width of the electrode, S is the length of the flow field plate inlet, H is the height of the electrode surface parallel to the flow field plate inlet through which the reactant enters and the product leaves the Br_2 electrode,

and v_{avg} is the average velocity of the liquid electrolyte entering the flow field plate. The concentration of H^+ was fixed by electroneutrality, and the flux of Br^- generated at the electrode entrance was equal to the flux of protons transported across the membrane to the Br_2 electrode.

3.2.2.2. Flow-Through Mode

In the flow-through mode, the concentrations of Br_2 and Br^- at the Br_2 electrode entrance were fixed and equal to the feed concentrations.

$$C_j = C_{j,in} \quad (j = Br_2 \ and \ Br^-) \tag{3.16}$$

Also, half the channels in the flow field are inlets and the other half are outlets. The CSTM boundary condition was irrelevant in this case as the variations along the axial direction inside the electrode were captured directly using the momentum balance equations. The concentration of H^+ was fixed by electroneutrality, and the ionic potential gradient was fixed to zero at the electrode entrance.

The boundary conditions at the remaining interfaces apply for both flow-by and flow-through modes. At the interface between the Br_2 electrode and the membrane ($x = \delta_1$), the fluxes of Br_2 and Br^- were equal to zero (no crossover assumption), and the flux of protons coming across the interface is equal to the ionic phase current density in the membrane (flux continuity). The flux of protons across the interface between the membrane and the hydrogen electrode ($x = \delta_2$) is continuous as well. In other words, the ionic phase current densities in the membrane and the H_2 electrode are equal at the interface. Moreover, Br_2 and Br^- species do not exist at both the membrane/H_2 electrode interface and the H_2 electrode end interface ($x = \delta_3$). The concentration of protons was fixed in the membrane phase and at both the membrane/H_2 electrode interface and the H_2 electrode end interface. Finally, the ionic potential

at the H_2 electrode end interface was set to a reference potential ($\phi_+ = 0$). The boundary conditions for the flow-by and flow-through modes are listed in Tables 3.3 and 3.4.

Table 3.3. Boundary conditions for flow-by mode

		Interface		
Variable	$x = 0$	$x = \delta_1$	$x = \delta_2$	$x = \delta_3$
C_{Br^-}	$C_{Br^-} = C_{Br^-,in} - \dfrac{N_{Br^-}H}{Sv_{avg}}$	$N_{Br^-} = 0$	N/A	N/A
C_{Br_2}	$C_{Br_2} = C_{Br_2,in} - \dfrac{N_{Br_2}H}{Sv_{avg}}$	$N_{Br_2} = 0$	N/A	N/A
C_{H^+}	$C_{H^+} = -\dfrac{Z_{Br}-C_{Br^-}}{Z_{H^+}}$	$C_{H^+} = -\dfrac{Z_{Br}-C_{Br^-}}{Z_{H^+}}$	$C_{H^+} = C_{H^+}^m$	$C_{H^+} = C_{H^+}^{H_2}$
ϕ_+	$N_{Br^-} = N_{H^+}$	$N_{H^+} = \dfrac{k_{H^+}^m}{F}\dfrac{d\phi_+^m}{dx}$	$\dfrac{d\phi_+^m}{dx} = \dfrac{k_{H^+}^{H_2}}{k_{H^+}^m}\dfrac{d\phi_+^{H_2}}{dx}$	$\phi_+ = 0$

where

$$N_{Br^-} = -D_{Br^-}^{eff}\frac{dC_{Br^-}}{dx} - \frac{Z_{Br}-D_{Br^-}^{eff}FC_{Br^-}}{RT}\frac{d\phi_+}{dx}$$

$$N_{Br_2} = -D_{Br_2}^{eff}\frac{dC_{Br_2}}{dx}$$

$$N_{H^+} = -D_{H^+}^{eff}\frac{dC_{H^+}}{dx} - \frac{Z_{H^+}D_{H^+}^{eff}FC_{H^+}}{RT}\frac{d\phi_+}{dx}$$

The governing equations and boundary conditions for the whole model domain was solved in potentiostatic mode using the BANDJ technique developed by Newman at the University of California at Berkeley.[9] The first step to solve the model was to assign initial guess values to the concentrations (C_{Br_2}, C_{Br^-}, and C_{H^+}) and the ionic potential (ϕ_+). The model was then solved to obtain the concentration and ionic potential profiles at each applied potential

(ϕ_s). It took approximately 4 to 5 iterations and 4 seconds for the model to meet the convergence criterion specified in Table 3.5 at each potential step.

The whole model was developed and solved in Fortran 4.0 (1994 - 1995 version) using a Dell Inspiron 5520 laptop (Intel (R) Core (TM) i5-3210M CPU @ 2.5Hz). Based on the concentration and ionic potential profiles in the Br_2 electrode, the average charge transfer current density across the whole electrode region was calculated using Simpson's method. Different case studies impacting the kinetics and mass transport, especially in the Br_2 electrode, were investigated in this work by varying the magnitude of the key operating parameters.

Table 3.4. Boundary conditions for flow-through mode

	Interface			
Variable	$x = 0$	$x = \delta_1$	$x = \delta_2$	$x = \delta_3$
C_{Br^-}	$C_{Br^-} = C_{Br^-,in}$	$N_{Br^-} = 0$	N/A	N/A
C_{Br_2}	$C_{Br_2} = C_{Br_2,in}$	$N_{Br_2} = 0$	N/A	N/A
C_{H^+}	$C_{H^+} = -\dfrac{Z_{Br^-}C_{Br^-}}{Z_{H^+}}$	$C_{H^+} = -\dfrac{Z_{Br^-}C_{Br^-}}{Z_{H^+}}$	$C_{H^+} = C_{H^+}^m$	$C_{H^+} = C_{H^+}^{H_2}$
ϕ_+	$\dfrac{d\phi_+}{dx} = 0$	$N_{H^+} = \dfrac{k_{H^+}^m}{F}\dfrac{d\phi_+^m}{dx}$	$\dfrac{d\phi_+^m}{dx} = \dfrac{k_{H^+}^{H_2}}{k_{H^+}^m}\dfrac{d\phi_+^{H_2}}{dx}$	$\phi_+ = 0$

where

$$N_{Br^-} = -D_{Br^-}^{eff}\frac{dC_{Br^-}}{dx} - \frac{Z_{Br^-}D_{Br^-}^{eff}FC_{Br^-}}{RT}\frac{d\phi_+}{dx} + v_xC_{Br^-}$$

$$N_{Br_2} = -D_{Br_2}^{eff}\frac{dC_{Br_2}}{dx} + v_xC_{Br_2}$$

$$N_{H^+} = -D_{H^+}^{eff}\frac{dC_{H^+}}{dx} - \frac{Z_{H^+}D_{H^+}^{eff}FC_{H^+}}{RT}\frac{d\phi_+}{dx} + v_xC_{H^+}$$

3.3. Results and Discussion

The parameters of focus in this study are a_{Br_2} (specific active surface area of the Br$_2$ electrode), v_{avg} (average feed velocity), and $k_{H^+}^m$ (membrane conductivity). First, the fuel cell discharge and charge performance obtained from experimental results and model data were compared to validate the model. Second, the concentration of Br$_2$ was varied, and its impact on the fuel cell discharge and charge performance was examined. Third, the impact of flow-by and flow-through modes on the fuel cell performance was studied. Fourth, a case study was conducted to study the effect of the Br$_2$ electrode thickness on the H$_2$-Br$_2$ fuel cell discharge performance. Fifth, the feed average velocity (v_{avg}) was varied to analyze the effect of the CSTM-like boundary condition (flow-by mode) at the Br$_2$ electrode entrance. Sixth, the effect of convection inside the porous electrode (flow-through mode) on the fuel cell performance was studied. Seventh, the magnitude of the specific active surface area of the Br$_2$ electrode (a_{Br_2}) was varied, and its impact on the performance of the fuel cell in the activation-controlled region was studied. Finally, the magnitude of the membrane conductivity ($k_{H^+}^m$) was varied and its effect on the fuel cell performance was examined.

3.3.1. Experimental Validation

A H$_2$/Br$_2$ fuel cell stack was assembled by placing the membrane electrode assembly (MEA) and graphite and tantalum flow field plates between aluminum compression end plates. Interdigitated flow field plates with a flow area of 2.25 cm^2 (1.5 cm X 1.5 cm) were used in this study. The MEA comprises of a plain SGL carbon (10AA) cathode (Br$_2$ electrode) and a SGL carbon (35BC) anode (H$_2$ electrode) with a catalyst loading of 0.5 mg Pt/cm^2 hot pressed onto a Nafion® 212 membrane. Catalyst-coated SGL carbon (35BC) materials were obtained from TVN Systems, Inc.

An electrolyte mixture of 2M HBr and 2M Br_2 was fed to the cathode, and H_2 gas at 3 psig was recirculated through the anode. A sparging bottle was used to humidify the H_2 gas before it enters the fuel cell. Also, the liquid water injection approach proposed by Wood et al. was employed to keep the ionomer phase in the H_2 electrode well hydrated.[10] The aim of this liquid water injection approach was to eliminate the effect of membrane dehydration observed at higher current densities. A mini-pump (Fischer Scientific Model 3385) was used to inject the liquid water into the cell at a flow rate of 0.05 cm^3/min. Any excess liquid water condensed in the H_2 electrode is swept away by the interdigitated flow field. The electrolyte mixture (HBr/Br_2) was pumped to the Br_2 electrode at a flow rate of 1.5 cm^3/min (4.3 A/cm^2 equivalent) using a peristaltic pump by Stenner (Model EW-74206). Hydrogen gas, on the other side, was recirculated at a flow rate of 1380 cm^3/min (97.2 A/cm^2 equivalent). The performance of the fuel cell was evaluated under potentiostatic mode using a potentiostat/galvanostat from Arbin Instruments. After the fuel cell was assembled, it was tested with H_2 pumped to the anode side and HBr/Br_2 pumped to the cathode side. Discharge performance of the fuel cell was obtained between OCV (1.014 V) and 0.8 V at room temperature. Electronic potential in steps of 50 mV was applied from 0.95 to 0.8 V. At each potential step, the cell was allowed to discharge for 5 minutes to obtain a steady state current before moving on to the next step.
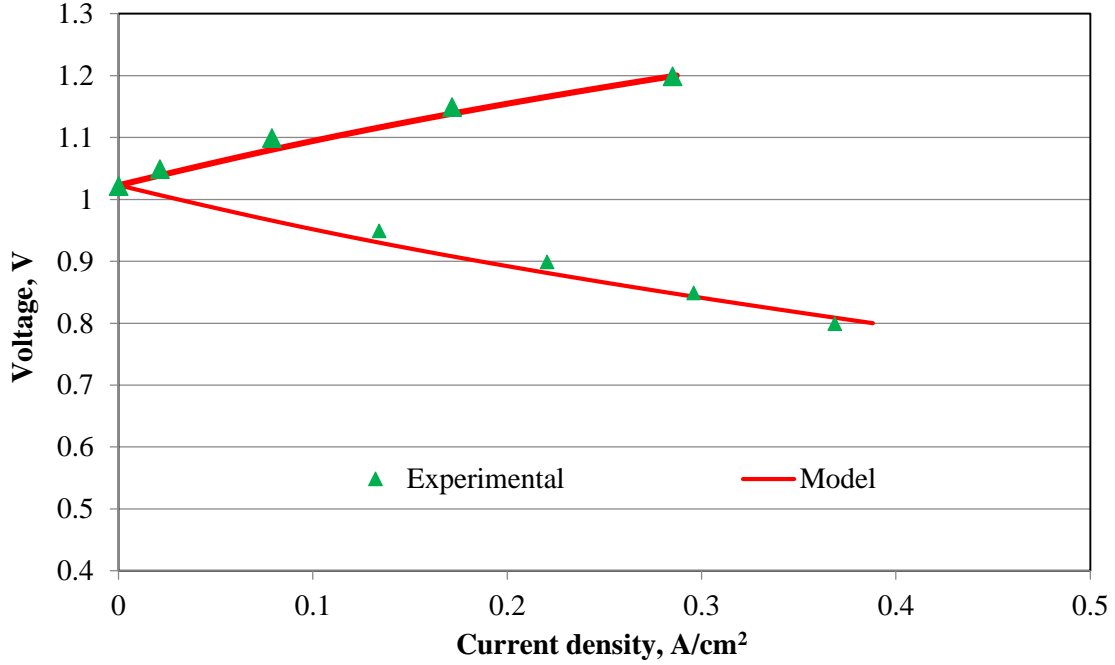
Figure 3.2. Comparison of experimental and model results (model validation for the flow-through mode)

Figure 3.2 compares the experimental discharge and charge performance of the SGL10AA (thickness=390 μm) cathode to the model results. Tables 3.5 and 3.6 show the base case parameters used in this model. The active surface area ($a_{Br_2} = 3600$ cm^2/cm^3) and membrane conductivity ($k_{H^+}^m = 0.023$ S/cm) of the Br$_2$ electrode were adjusted in order to fit the model results to the experimental data for the base case. These values are listed in Table 3.5 as well. As shown in Figure 3.2, both the experimental discharge and charge performance data of the H$_2$-Br$_2$ fuel cell are in good agreement with the base case model results. The model results shown in Figure 3.2 correspond to the flow-through mode (interdigitated flow field). For the subsequent case studies, while comparing the flow-by and flow-through model results at constant active surface area, the value was adjusted to 8800 cm^2/cm^3. The membrane conductivity remains unchanged.

Furthermore, the model results (discharge and charge performance) obtained for two different Br_2 concentrations in a H_2-Br_2 fuel cell operating under flow-through mode are shown in Figure 3.3 in order to validate the predictive capability of this mathematical model. The concentration of HBr was fixed to 2M. As shown in Figure 3.3, discharge performance improves upon increasing the concentration of Br_2 from 1M to 2M whereas the charge performance is decreased, mainly as a result of the vertical voltage shift in the Open Circuit Voltage (OCV) when the concentration of Br_2 increases from 1M to 2M. The OCV increase upon increasing the Br_2 concentration is as expected based on the Nernst equation. This model prediction agreed reasonably well with the experimental data published in previous studies.[11,12]

3.3.2. Comparison of Flow-By and Flow-Through Modes

In this section, the effect of flow field design on the H_2-Br_2 fuel cell performance was examined. Figure 3.4 compares the discharge and charge performances obtained with flow-by (serpentine) and flow-through (interdigitated) modes. The discharge and charge performance of a H_2-Br_2 fuel cell operating under flow-through mode was higher than that under flow-by mode. In the flow-through mode, the electrolyte was transported into the porous Br_2 electrode by forced convection, which enhances the mass transport and thus the performance. The flow-through model developed in the supporting material section corresponds to the interdigitated flow field employed in the experimental studies. Instead of using an empirical mass transfer coefficient, which was generally used to model the flow-through electrodes, the momentum balance equations were solved directly to obtain the flow dynamics in the electrode. In the flow-by mode, the electrolyte has to diffuse into the electrode, which limits the mass transport and consequently, the fuel cell performance. Even though a serpentine flow field was used in the experimental studies, we make an assumption that the flow condition can be represented

by that of a flow-by electrode. That is, we assume that there is minimal electrolyte flow through the electrode due to cross-flow as a result of a pressure gradient between the adjacent channels in the flow field.

Table 3.5. Parameters used in the base case

Thickness of the Br_2 electrode (δ_1)	310 μm
Porosity of the Br_2 electrode (ε_{Br2})	0.85
Hydrobromic acid bulk concentration	0.002 mol/cm^3
Hydrobromic acid reference concentration	0.002 mol/cm^3
Bromine bulk concentration	0.002 mol/cm^3
Bromine reference concentration	0.002 mol/cm^3
Width of the CSTM inlet and the Br_2 electrode (W)	1 cm
Height of electrode surface parallel to the CSTM (H)	1 cm
Length of the CSTM inlet (S)	1 cm
Cross sectional area of the flow field (flow-through mode)	0.3 cm^2
Volumetric flow rate of HBr/Br_2 entering the flow field (Q)	0.025 cm^3/sec
Average velocity of HBr/Br_2 entering the flow field (v_{avg})	0.083 cm/sec
Exchange current density of Br_2/Br^- reaction (i_{o,ref,Br_2})[a]	0.55 mA/cm^2
Active surface area per unit Br_2 electrode volume (a_{Br_2})[b]	3.60×10^3 cm2/cm^3
Diffusion coefficient of Bromine (D_{Br_2})	1.2 × 10^{-5} cm^2/sec
Diffusion coefficient of Bromine (D_{Br^-})	2.08 × 10^{-5} cm^2/sec
Diffusion coefficient of Proton (D_{H^+})	9.31 × 10^{-5} cm^2/sec
Anodic and cathodic transfer coefficients of Br_2/Br^- and H^+/H_2 reactions (α_a, α_c)	0.5
Thickness of the membrane (δ_2)	50 μm

Conductivity of the membrane $(k_{H^+}^m)^b$	0.023 S/cm
Thickness of H_2 electrode (δ_3)	10 μm
Concentration of protons inside the membrane and H_2 electrode $(C_{H^+}^m, C_{H^+}^{H_2})$	0.001 mol/cm^3
Conductivity of ionomer fraction present in the H_2 electrode $(k_{H^+}^{H_2})$ [c]	0.005 S/cm
Exchange current density of H^+/H_2reaction $(i_{o,ref,H_2})^d$	1.0 mA/cm^2
Active surface area per unit H_2 electrode volume $(a_{H_2})^d$	5.77×10^5 cm^2/cm^3
Porosity of the H_2 electrode (ε_{H_2})	0.2
Open circuit potential of the fuel cell[b]	1.023 V
Convergence criterion	1×10^{-9}

[a] Obtained from Ref. 5

[b] Adjusted to fit the experimental trend

[c] Calculated using the approach described in Ref. 13

[d] Obtained from Ref. 11

_____

Table 3.6. Kinetic parameters

Species	p_j	q_j	s_j	γ_j	Z_j
Br_2	-0.25	0.75	-0.5	0.5	0
Br^-	1.5	-0.5	1.0	1.0	-1.0
H^+	-0.5	1.5	1.0	1.0	1.0
H_2	0.75	-0.25	-0.5	0.5	0
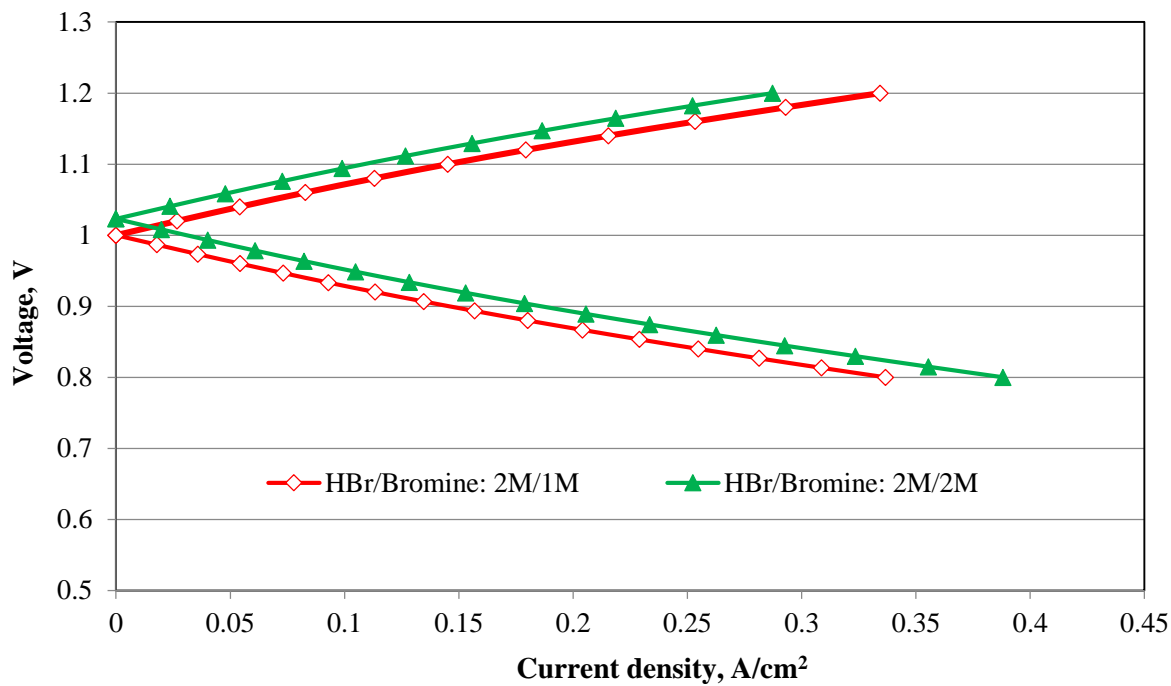
Figure 3.3. Effect of Br_2 concentration on the H_2-Br_2 fuel cell performance (flow-through mode)
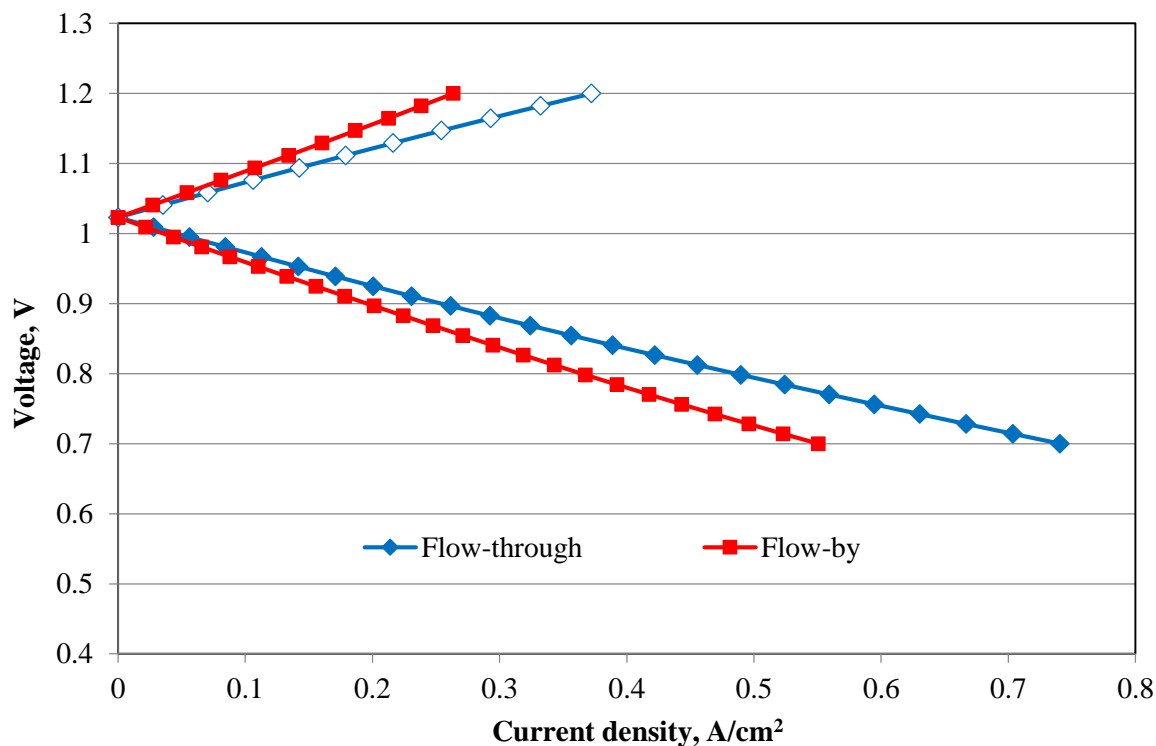
Figure 3.4. Effect of flow-field design on the H_2-Br_2 fuel cell performance

In order to better comprehend the transport phenomenon in these flow modes, the concentration, reaction rate, and the overpotential profiles inside the Br_2 electrode are plotted at a single applied voltage (0.8 V) as shown in Figures 3.5a, 3.5b and 3.5c. As shown in Figure 3.5a, the x-axis represents the electrode thickness (x), and the solid lines and dashed lines in the plot correspond to the concentration profiles of Br_2 and Br^-, respectively. During discharge, Br_2 (represented by solid lines) was consumed and Br^- (represented by dashed lines) was generated inside the bromine electrode. The concentration profiles of Br_2 (solid lines) and Br^- (dashed lines) inside the Br_2 electrode for both the flow-through and flow-by modes are shown in Figure 3.5a. The concentration of Br_2 across the bromine electrode was almost depleted in the flow-by mode whereas the concentration of Br_2 in the flow-through mode remains fairly constant and equal to feed concentration for the most part of the electrode. Figures 3.5b and 3.5c show the reaction rate (in mol/cm^3-s) and the overpotential ($\eta = \phi_s - \phi_+ - U_{Br_2 ref}$) profiles of flow-by and flow-through modes inside the Br_2 electrode.

The higher performance obtained with the flow-through mode can be explained as follows. The reaction rate in the electrode is a function of the reactant and product concentrations and the ionic potential. In the flow-through case, the peak reaction rate occurred around 0.025 cm can be attributed to the high reactant (Br_2) concentration and minimal ionic resistance. The high reactant concentration was a result of dominant convective transport inside the Br_2 electrode. The forced convection of the electrolyte into the Br_2 electrode drives the ionic species much faster and closer to the membrane, which results in lower ionic resistance. Beyond 0.025 cm, the concentration of Br_2 begins to decrease as the influence of diffusion and migration begin to come into effect as the fluid velocity decreases to zero at the membrane interface. This explains the decrease in reaction rates beyond 0.025 cm. On the other hand, the

dominant transport mechanism in the flow-by mode is diffusion, which is a slow process. Even though the ionic resistance is minimal close to the membrane, the high reactant (Br_2) depletion results in low reaction rates. Hence, the reaction rate trend inside the Br_2 electrode for the flow-by mode is mainly controlled by the reactant and product concentrations. As concentration of the reactant depletes, the reaction rate decreases inside the Br_2 electrode as shown in Figure 3.5b. This case study demonstrates the significance of the flow-through mode by which the mass transport inside the Br_2 electrode can be greatly enhanced. Once again, the model predictions depicted above match reasonably well with the published experimental results.[11,12]
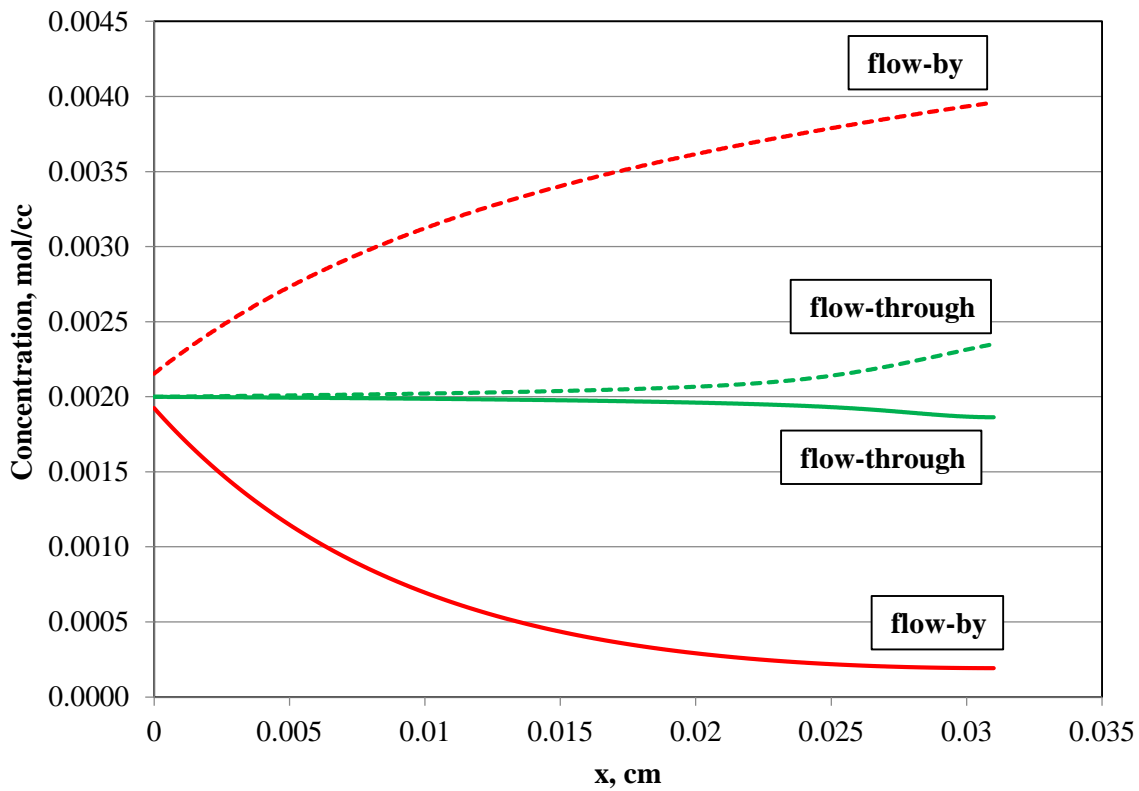
(a)
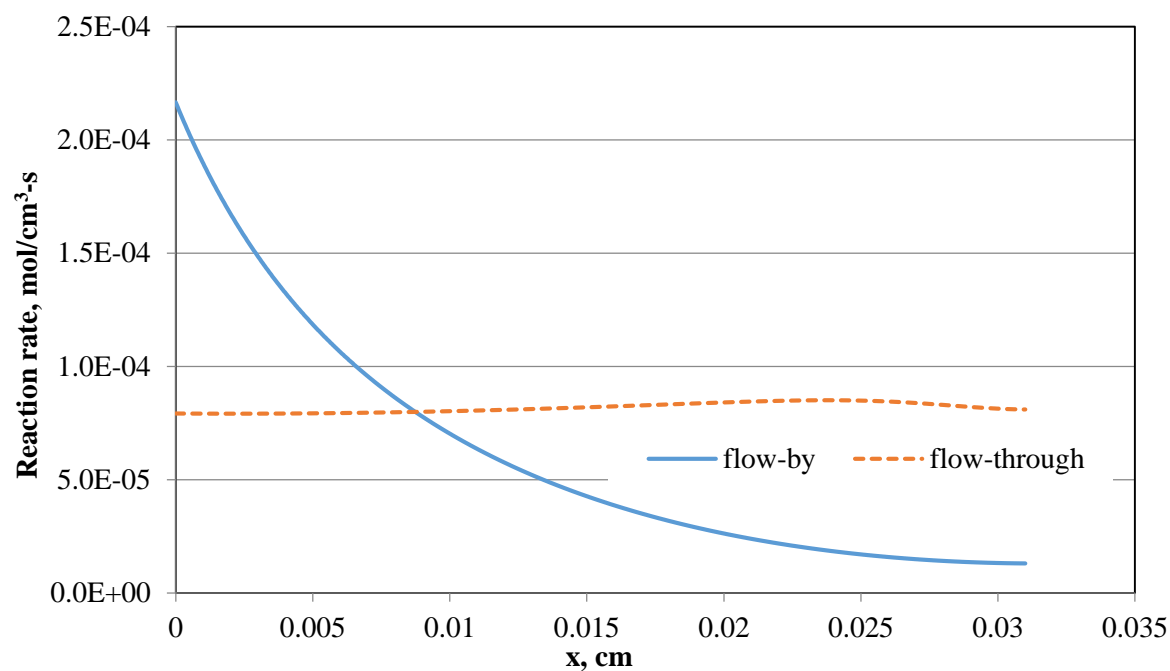
(b)
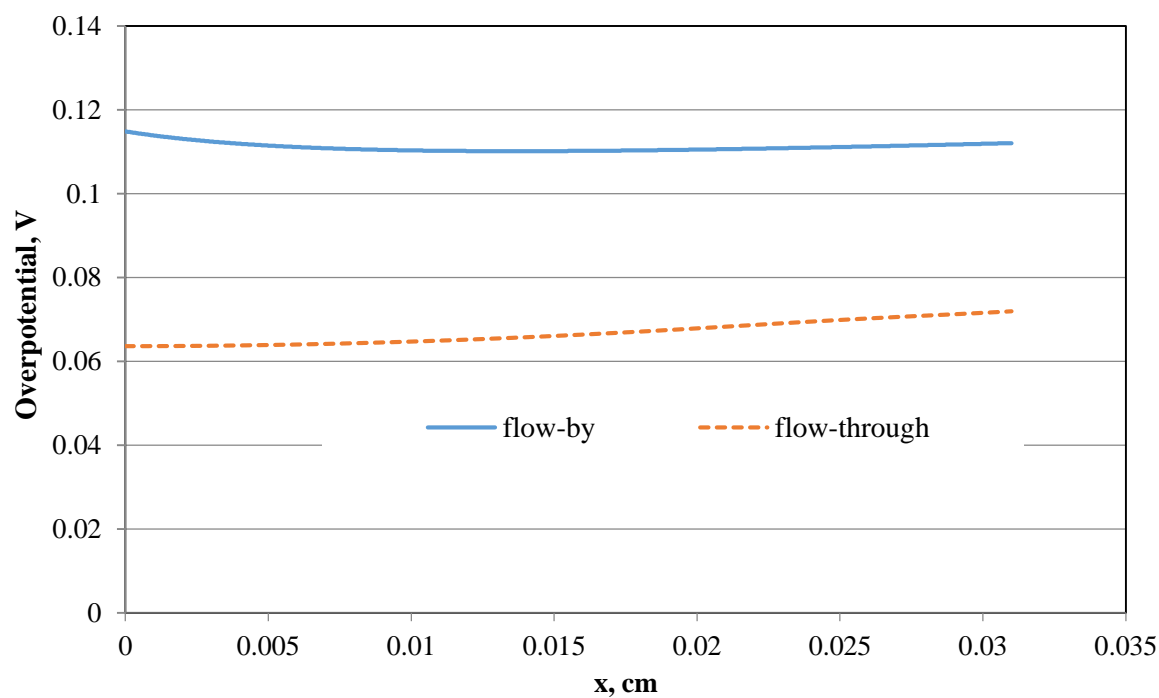
(c)

Figure 3.5. Effect flow-field design on (a) concentration profiles (b) reaction rate profiles (c) overpotential profiles at 0.8 V

3.3.3. Effect of Br$_2$ Electrode Thickness

3.3.3.1. Flow-By Mode (Serpentine)

In this case study, the discharge performance of a H$_2$-Br$_2$ fuel cell operating under flow-by mode was examined by varying the Br$_2$ electrode thickness. Figure 3.6 shows the simulation results obtained for different thicknesses. As shown in Figure 3.6, the discharge performance was not affected by increasing the cathode thickness beyond 200 μm. On the other hand, the performance of thinner cathodes (50 μm and 100 μm) clearly indicate that an optimal cathode thickness or surface area is required to overcome the kinetic limitations. In order to understand this phenomenon further, concentration profiles of Br$^-$ (dashed lines) and Br$_2$ (solid lines) inside the bromine electrode are plotted at a single applied potential within the activation-controlled region, 0.8 V, as shown in Figure 3.7a. Also, the reaction rate profiles (in mol/cm^3-s) inside the Br$_2$ electrode are plotted at the same applied voltage (0.8 V) in Figure 3.7b. The Br$_2$ concentration and the reaction rate profiles of thinner cathodes (50 and 100 μm) show a clear indication that the electrode was being under-utilized. Even though the local reaction rates are high at low electrode thicknesses (i.e., electrode volumes), the low discharge performance observed in Figure 3.7b can be attributed to lack of enough active surface area (a_{Br_2}). This explains the kinetically-limited performance at the lower Br$_2$ electrode thicknesses of 50 and 100 μm. Once the cathode thickness is increased to 200 microns, the electrode was almost completely utilized and hence further increase in the electrode thickness does not have any significant impact on the discharge performance.
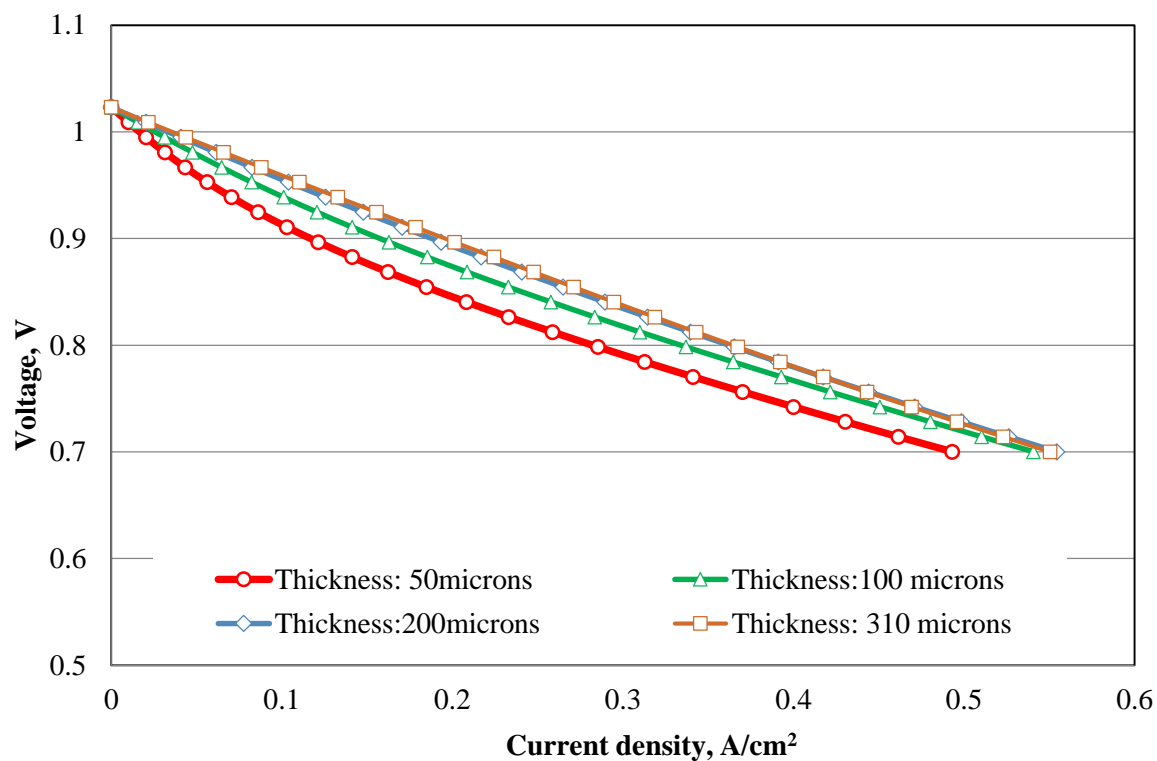
Figure 3.6. Effect of Br$_2$ electrode thickness on the performance of a H$_2$-Br$_2$ fuel cell (flow-

by mode
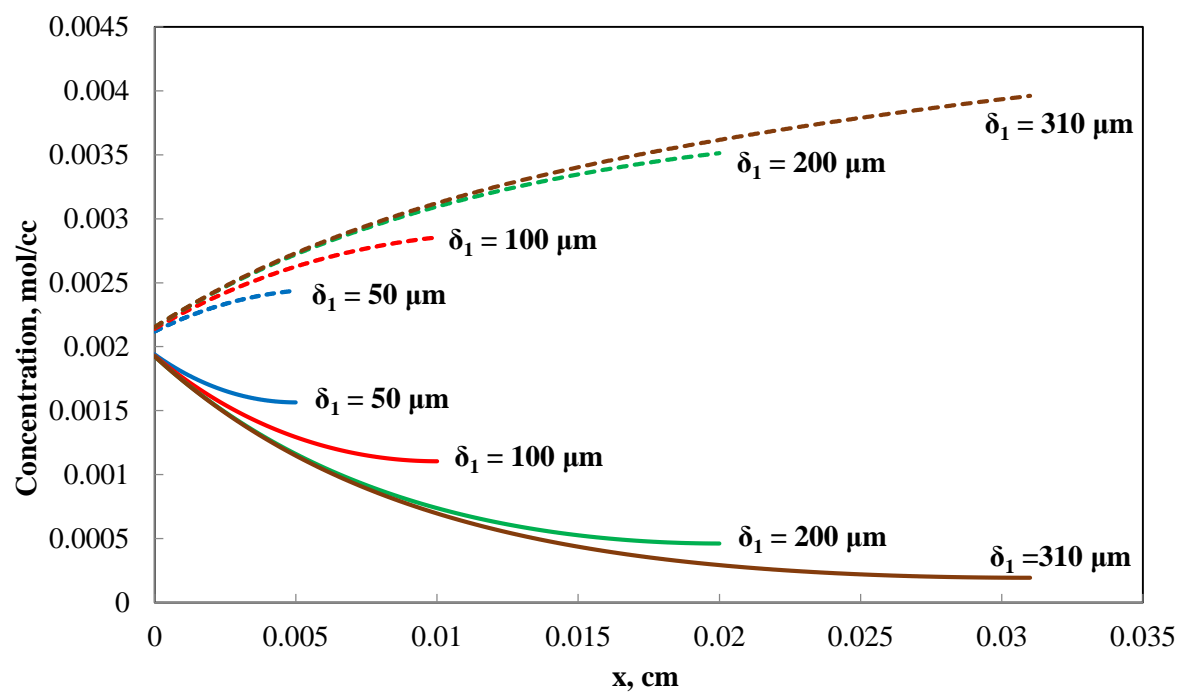
(a)
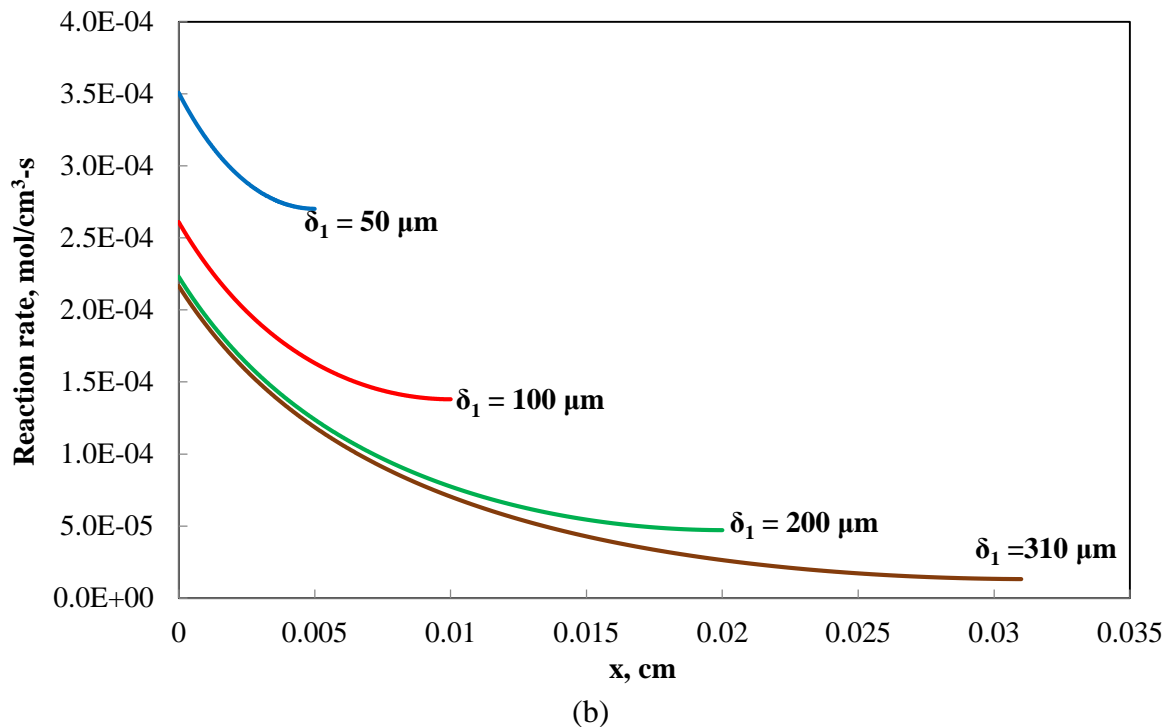
Figure 3.7. Effect of Br$_2$ electrode thickness on the (a) concentration profiles (b) reaction

rate profiles of Br$_2$ and Br$^-$ at 0.8 V (flow-by mode)

3.3.3.2. Flow-Through Mode (Interdigitated)

A similar analysis which is described in the flow-by mode case study was conducted with the

flow-through mode as well. Figure 3.8a shows the discharge performance obtained for

different cathode thicknesses. Figure 3.8b shows the reaction rate profiles at a single applied

voltage in the discharge direction (0.8 V). As shown in Figure 3.8a, the discharge performance

obtained with the flow-through design is better compared to that of the flow-by design. Also,

with the convective transport being the dominant transport mechanism in this flow mode, the

discharge performance improves as the thickness of the Br$_2$ electrode is increased to 310 μm.

There is no significant improvement in the performance beyond 310 μm as diffusive transport

begins to dominate, and the effect of convective transport starts to decrease as the electrode

thickness approaches the length of the flow field shoulder in the interdigitated flow field design. As shown in Figure 3.8b, the reaction rate profile of the 390 μm thick Br_2 electrode drops sharply around 0.025cm which was an effect imposed by the slow diffusive transport. However, the flow-through mode offers higher flexibility in terms of the thickness of the Br_2 electrode for this system.

These results also depend on the active surface area per unit electrode volume (a_{Br_2}). If a_{Br_2} is low, increasing the electrode thickness enhances the fuel cell performance. However, if it is already high, increasing the electrode thickness may not be useful and may actually lead to poor performance because of the high ohmic loss in the electrolyte. Thus, designing a cathode with optimum thickness is required in order to take advantage of the faster bromine reaction kinetics.
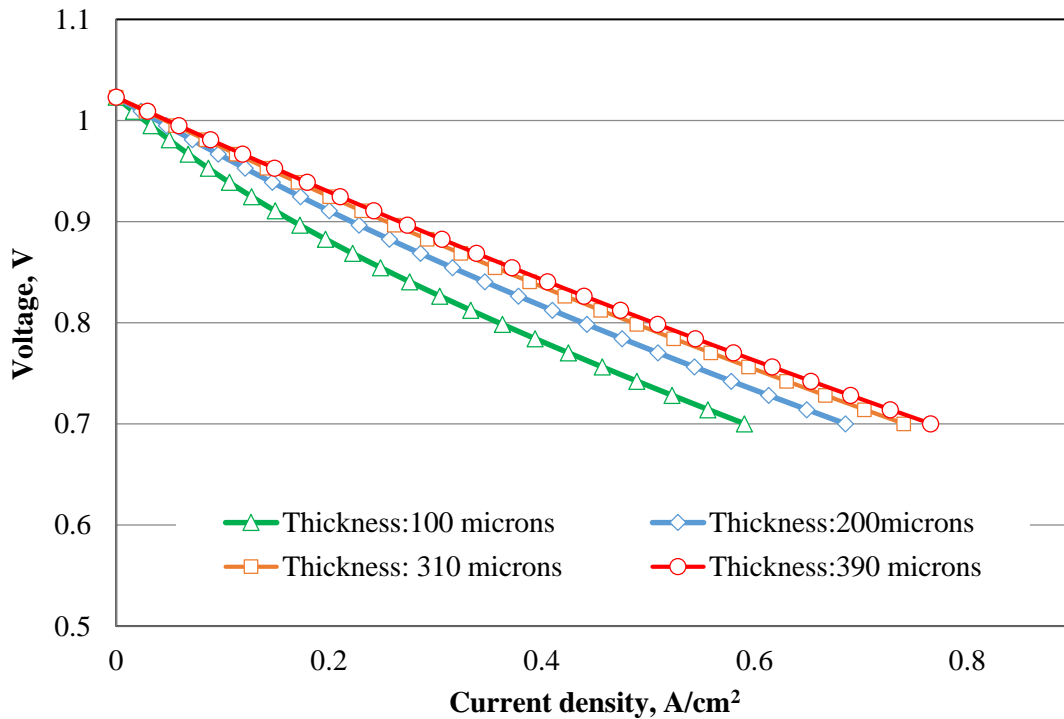
(a)
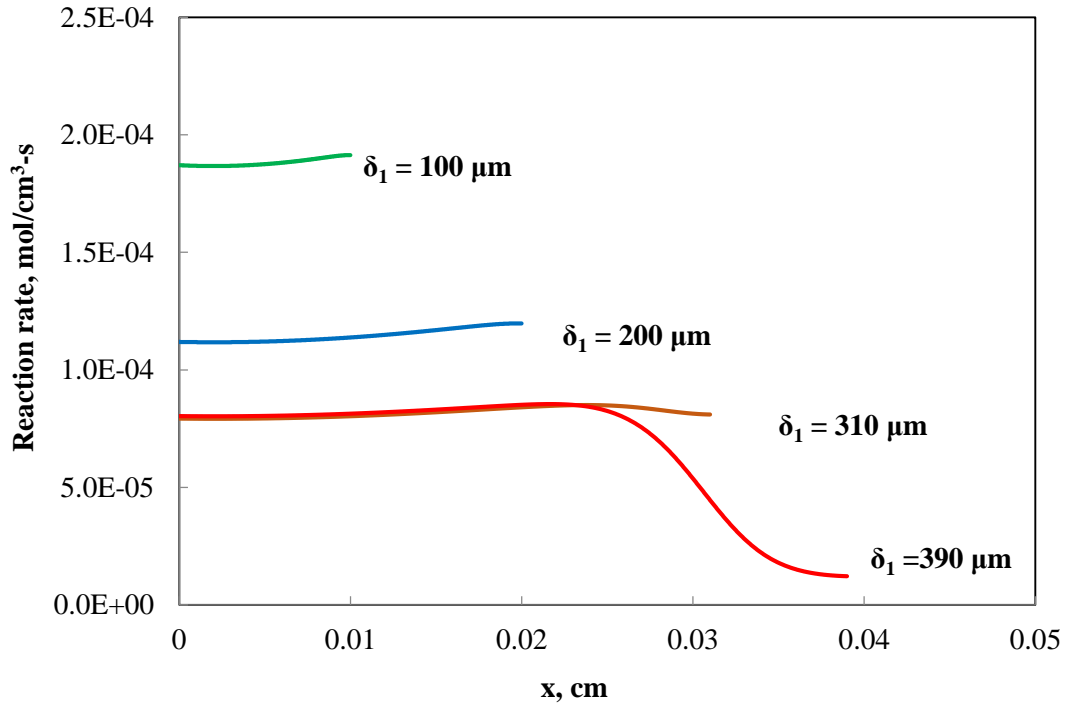
(b)

Figure 3.8. Effect of Br$_2$ electrode thickness on the (a) performance of a H$_2$-Br$_2$ fuel cell (b)

reaction rate profiles at 0.8 V (flow-through mode)

3.3.4. Effect of Average Feed Velocity (Flow-By Mode)

In this case study, the effect of the inlet average feed velocity (v_{avg}) on the CSTM-like boundary

condition is examined. The concentration of HBr and Br$_2$ available at the Br$_2$ electrode entrance

is determined based on v_{avg}. Table 3.7 shows the two different feed velocities used in this case

study and stoichiometric ratios of Br$_2$ (f_{Br_2}) corresponding to them at 0.7 V. The stoichiometric

ratio represents the ratio of molar feed rate of Br$_2$ in the inlet stream to the consumption rate

of Br$_2$ in the electrode, which was calculated based on the average current density at a particular

applied voltage.

Table 3.7. Feed velocities (flow-by case)

Molar feed rate x 10^5 (mol/s)	v_{avg} (cm/s)	f_{Br_2} ($\phi_s = 0.7$ V)
1.0	0.005	3.9:1
4.0	0.02	14:1

As shown in Table 3.7, a stoichiometric ratio of 2:1 or greater was chosen in order to make sure there is enough Br_2 in the feed stream to account for the consumption rate inside the electrode. An applied voltage of 0.7 V is selected to calculate the stoichiometric ratio because the presence of excess Br_2 concentration at higher current densities ensures that there is enough reactant concentration in the feed to meet the consumption rate throughout the entire voltage range (OCV to 0.7 V). Except for the average velocity, base case values shown in Tables 3.5 and 3.6 are used for all other parameters.

Figure 3.9 compares the concentration profiles of Br_2 (solid lines) and Br^- (dashed lines) at different average velocities to their counterparts where infinite flow rate at the Br_2 electrode entrance was used. These profiles are plotted at an applied voltage of 0.8 V. When the CSTM-like boundary condition was not used in the system ($v_{avg}=\infty$), concentrations of Br_2 and Br^- were constant and equal to the feed concentrations at the fuel cell inlet ($C_{j,in}$). The concentration of Br_2 at the electrode entrance was about 80 % of the inlet feed concentration at a feed velocity of 0.005 cm/s . The reduction in the concentration was due to the consumption of Br_2 inside the Br_2 electrode. As the feed velocity was increased to 0.02 cm/s, the concentration at the electrode entrance was almost equal to the feed concentration. The concentration of Br_2 available at the electrode entrance was higher at large feed velocities. This is due to the fact

that increasing the average velocity of the inlet feed enables the convective transport to be dominant over the diffusive transport. The consumption rate of Br_2 due to diffusion is better met by higher convective transport. At high enough feed velocities, the concentration of Br_2 available was much closer to the feed inlet concentration, which further improves the discharge performance of the system. Predicting an optimal flow rate is important especially in reducing the pumping costs and size of the electrolyte storage tanks.
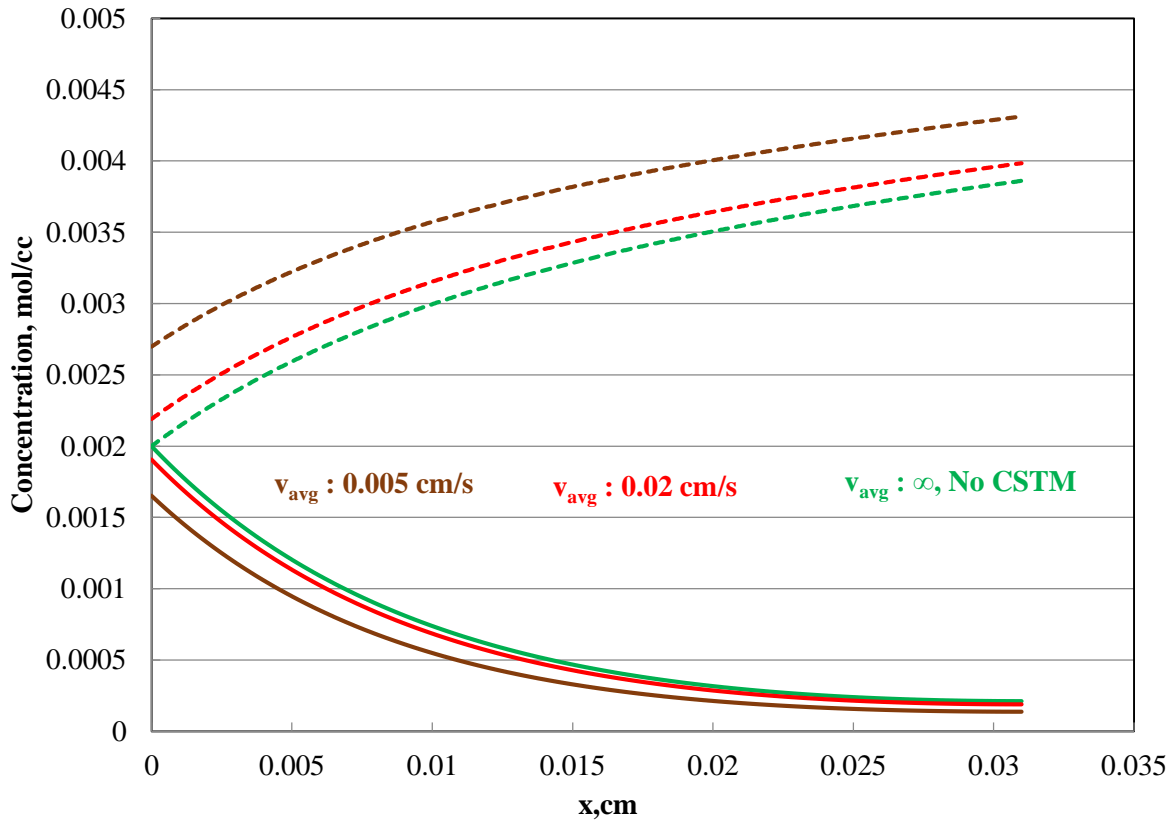
Figure 3.9. Effect of feed velocity on the concentration profiles of Br_2 and Br^- (flow-by mode)

3.3.5. Effect of Convection (Flow-Through Mode)

In this case study, the effect of convection inside the Br_2 electrode on the H_2-Br_2 fuel cell discharge performance was examined. Table 3.8 shows the volumetric feed flow rates (Q) used in this study. Figure 3.10a shows the discharge performance of the fuel cell at three different feed flow rates (Q). The velocity profiles (v_x) at the corresponding flow rates were calculated using the modeling approach described in the supporting material section. Figure 3.10b shows the corresponding reaction rates at an applied voltage of 0.8 V. At low feed flow rates ($Q =$ 0.001 cm^3/s), the fuel cell discharge performance obtained can be attributed to the poor convective transport rate. Also, the reaction rate profile inside the Br_2 electrode showed a decreasing trend, which suggests that the diffusive transport was dominant right from the outset. As the feed flow rate (Q) was increased to 0.01 cm^3/s, the discharge performance was enhanced owing to better convective transport as the electrolyte feed stream penetrates much deeper into the Br_2 electrode. This effect can be seen in the reaction rate profile as well. The effect of diffusion appeared close to the membrane (roughly 0.02cm). There was no significant effect on the discharge performance as the feed flow rate was increased to 0.025 cm^3/s. In the flow-through mode, higher reaction rates can be achieved by operating at low feed flow rates which in turn reduces the pumping costs for this fuel cell system.

Table 3.8. Feed flow rates (flow-through case)

Molar feed rate x 10^5 (mol/s)	Q (cm^3/s)	f_{Br_2} ($\phi_s = 0.7$ V)
0.2	0.001	3.3:1
2.0	0.01	18:1
5.0	0.025	43:1
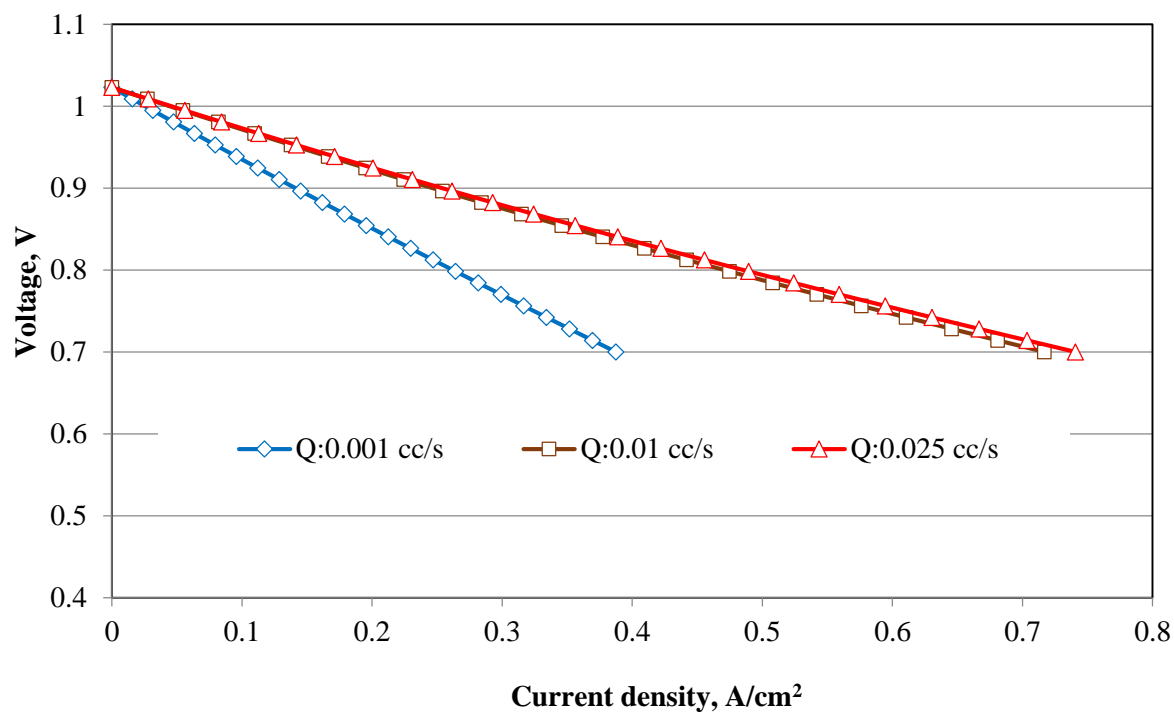
(a)
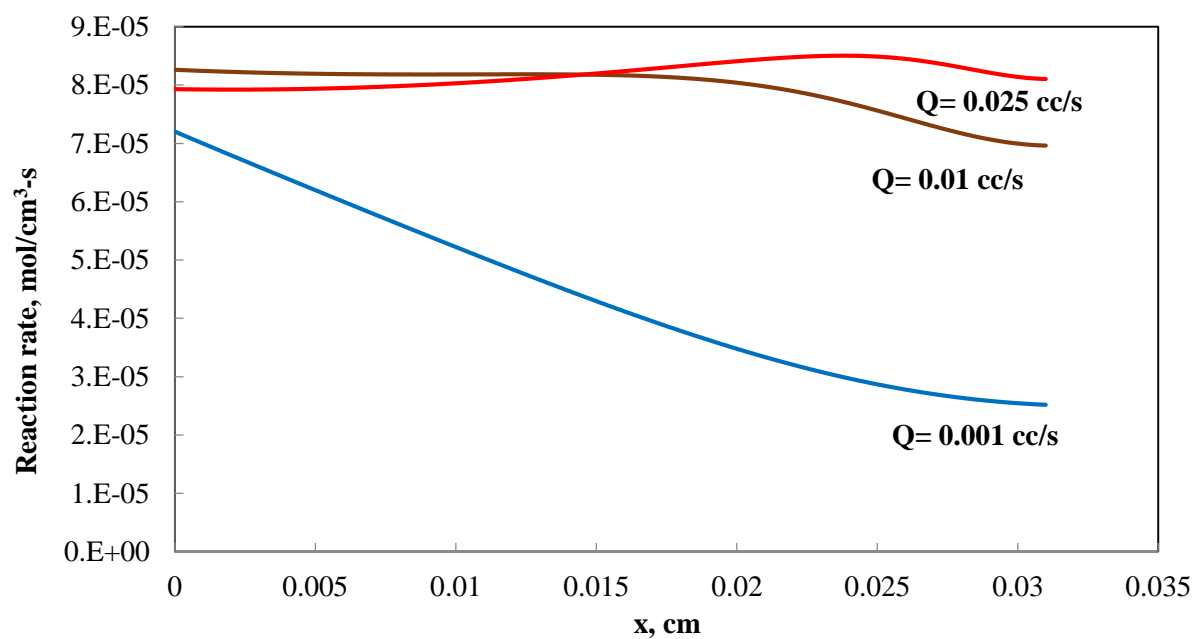
(b)

Figure 3.10. Effect of feed flow rate on the (a) performance of a H_2-Br_2 fuel cell (b) reaction rate profiles of Br_2 and Br^- at 0.8 V (flow-through mode)

3.3.6. Effect of Active Surface Area (a_{Br_2})

The effect of kinetic rate on the performance of the fuel cell was predicted by changing the active cathode surface area per unit electrode volume (a_{Br_2}). Table 3.9 shows the three different active surface areas (a_{Br_2}) used in this case study. This case study was done with the H$_2$-Br$_2$ fuel cell operating under both flow-by and flow-through modes.

Table 3.9. Active surface areas (a_{Br_2})

Case	$a_{Br_2}(\text{cm}^2/\text{cm}^3)$
1	880
2	1760
3	8800

The active surface area of the Br$_2$ electrode plays a significant role in optimizing the performance of the H$_2$-Br$_2$ fuel cell. Since no catalyst layer is employed on the plain carbon electrode, higher electrode active surface area is necessary to obtain good performance. As shown in Figures 3.11 (flow-by) and 3.13a (flow-through), both the discharge and charge performance of the fuel cell improved upon increasing the electrode specific active area $\left(a_{Br_2}\right)$ from 880 to 8800 cm^2/cm^3. The specific surface area of the widely used commercial SGL 10AA electrode is 1600 cm^2/cm^3. The specific surface area used in case 3 was approximately 5 times higher than that of a plain SGL 10AA carbon electrode. The kinetic rate in the Br$_2$ electrode can be improved by either increasing the exchange current density or the active surface area. Since the exchange current density of Br$_2$/Br$^-$ reaction on plain carbon substrates is lower than

that on the noble catalysts like platinum, it should be compensated by improving the active surface area to acquire better performance.

3.3.6.1. Flow-By Mode

The concentration profiles of Br_2 (solid lines) and Br^- (dashed lines) at an applied potential of 0.8 V for different values of a_{Br_2} are shown in Figure 3.12a. At lower values of a_{Br_2} (Case 1 and Case 2), the electrode was being under-utilized which explains the low discharge performance obtained in the activation-controlled region as shown in Figure 3.11. At high enough values of a_{Br_2} (Case 3), there was sufficient active surface area (5 times higher than the plain SGL 10AA carbon electrode) for Br_2 to react utilize the whole electrode region which explains the better performance obtained for Case 3. This hypothesis was confirmed by the reaction rate profiles shown in Figure 3.12b as well.

3.3.6.2. Flow-Through Mode

As shown in Figure 3.13b, the reaction rate profile of Case 1 was a result of low kinetic rate. The reaction rate improves upon enhancing the active surface area as seen in Cases 2 and 3. At high enough active surface areas, the fuel cell operating under flow-through mode generates significantly higher current densities at low overpotentials. This is a desirable characteristic because operating the fuel cell at low overpotentials results in higher round trip voltage efficiency.
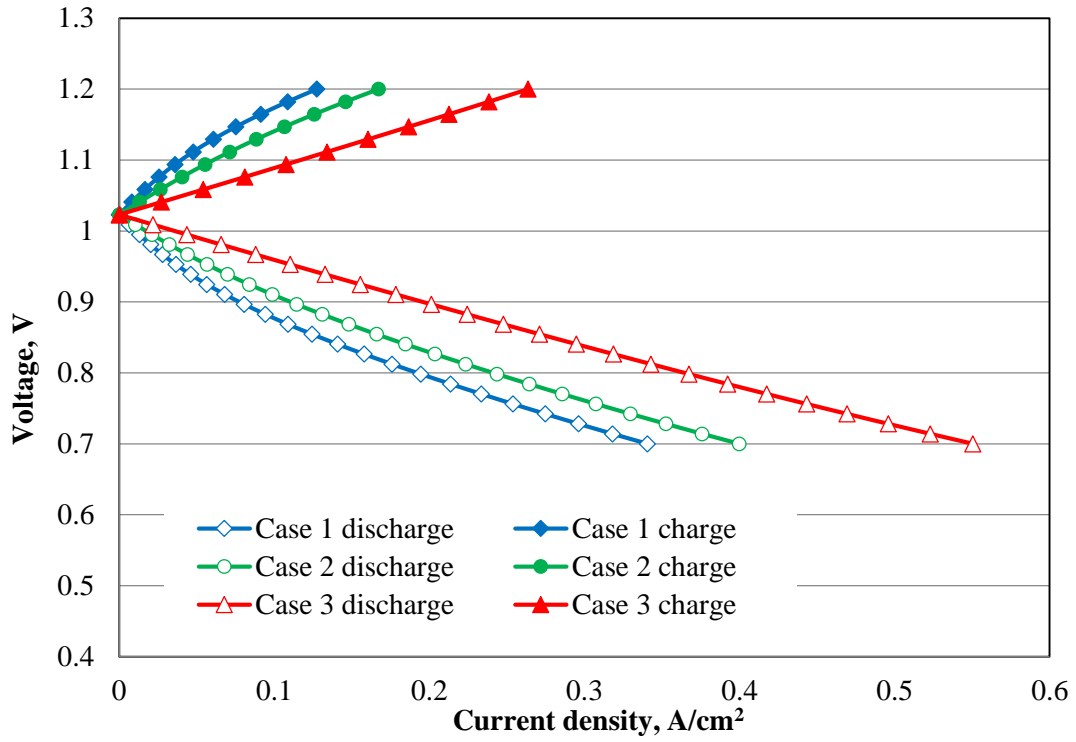
Figure 3.11. Effect of a_{Br_2} on the performance of a H$_2$-Br$_2$ fuel cell (flow-by mode)

(a)

(b)
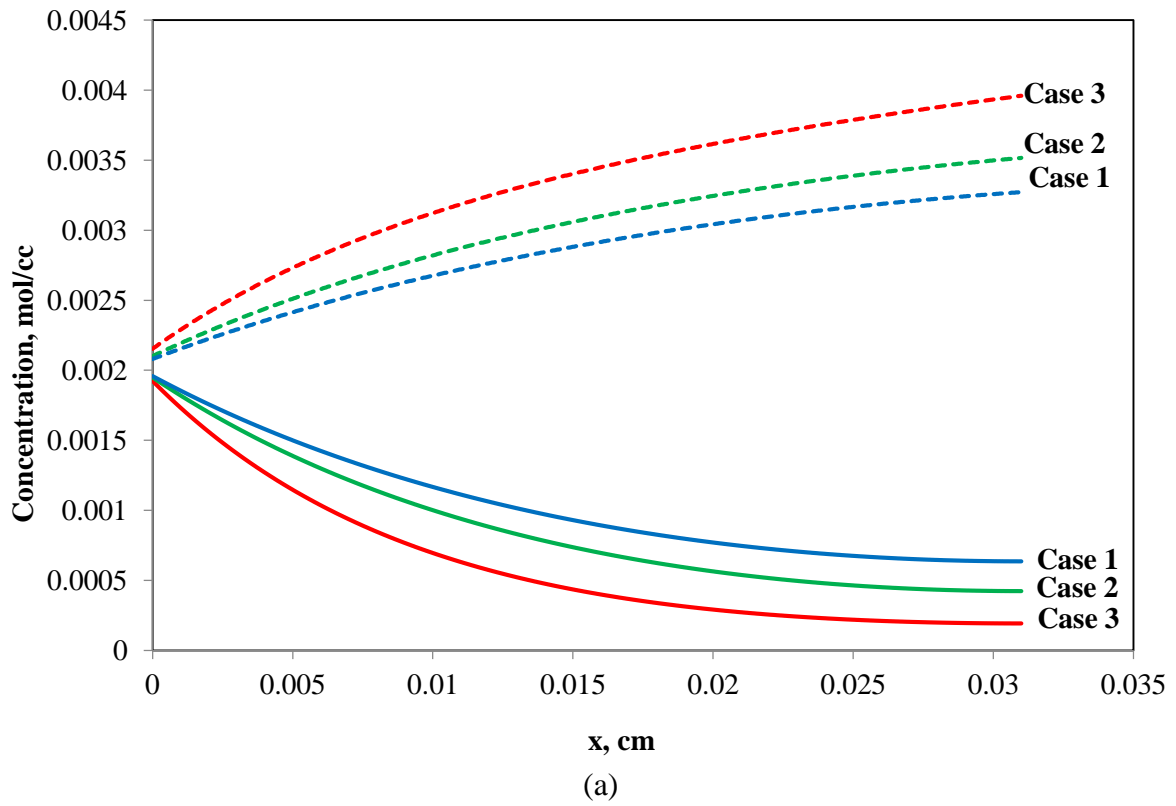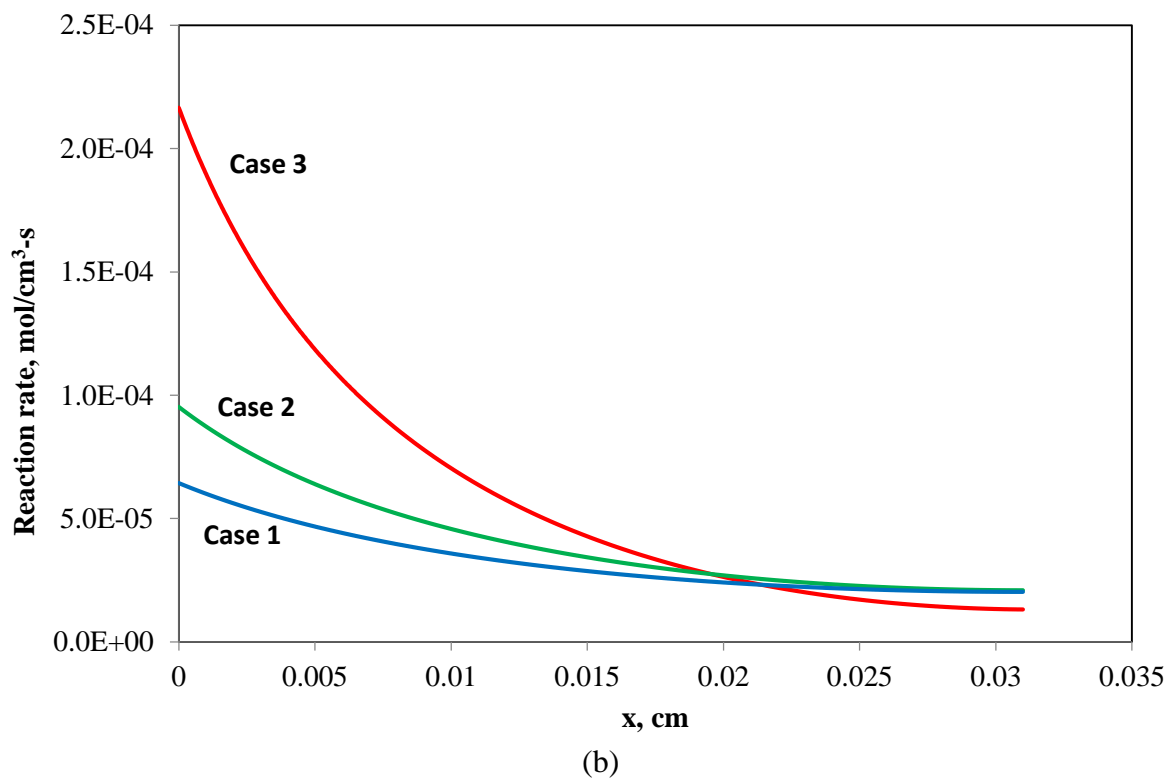
Figure 3.12. Effect of a_{Br_2} on the (a) concentration profiles (b) reaction rate profiles of Br_2

and Br^- (flow-by mode)

(a)

(b)
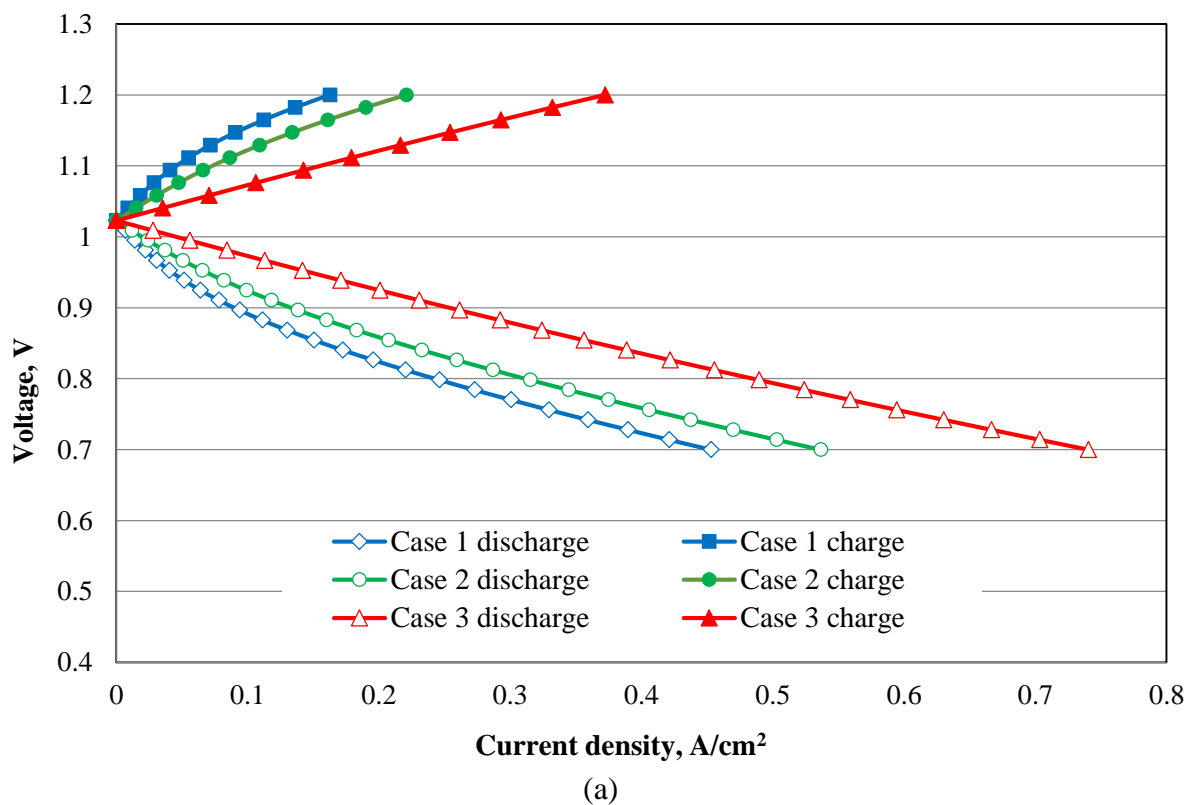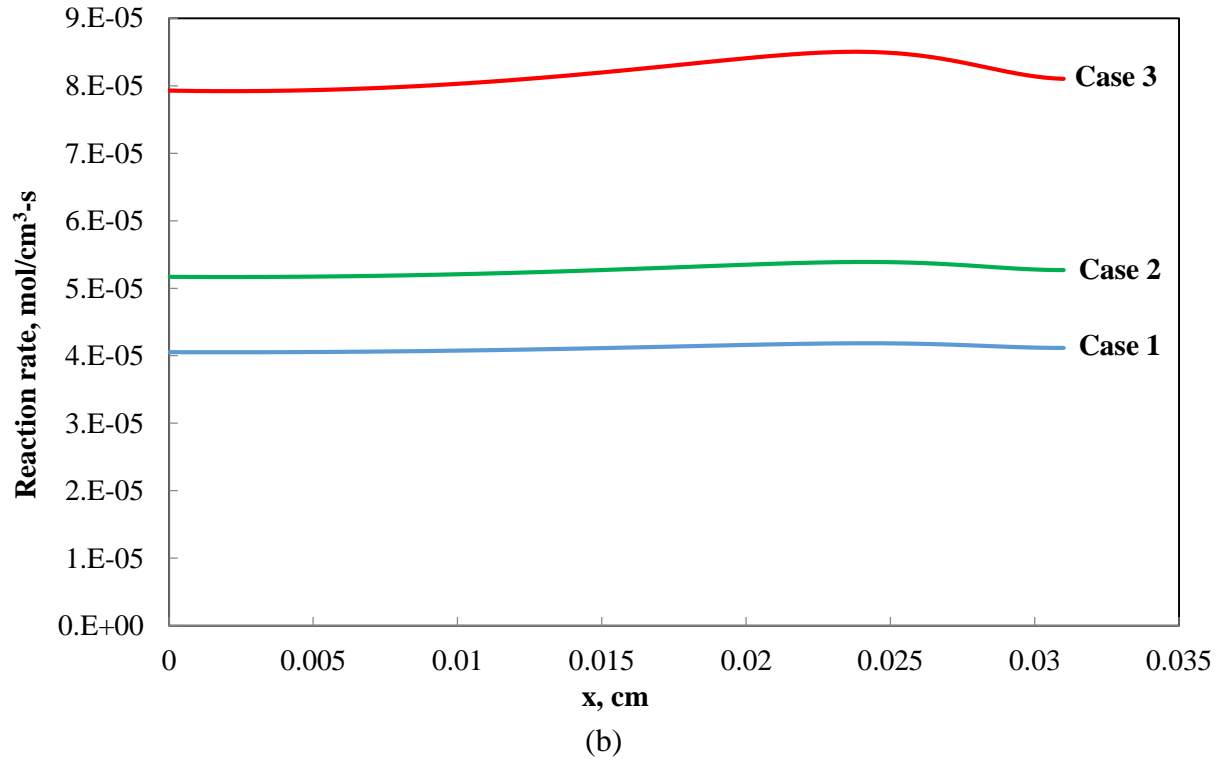
Figure 3.13. Effect of a_{Br_2} on the (a) performance of a H_2-Br_2 fuel cell (b) reaction rate

profiles of Br_2 and Br^- (flow-through mode)

3.3.7. Effect of Membrane Conductivity $(k_{H^+}^m)$

In this case study, the effect of membrane conductivity $(k_{H^+}^m)$ on the H_2-Br_2 fuel cell performance was studied. Table 3.10 shows the three different $k_{H^+}^m$'s used in this study.

Table 3.10. Membrane conductivities $(k_{H^+}^m)$

Case	$k_{H^+}^m$ (S/cm)
1	0.008
2	0.023
3	0.069

As shown in Figures 3.14 (flow-by) and 3.15 (flow-through), the fuel cell performance was greatly improved upon increasing the membrane conductivity (k_{H+}^m) from 0.008 to 0.069 S/cm. This performance trend can be explained as follows. At lower membrane conductivities (Case 1 and Case 2), the conductivity of ionomer in the H_2 electrode was reduced, which hinders the proton transport from H_2 electrode to the Br_2 electrode during discharge and vice versa during charge. This results in poor performance especially in the ohmic-controlled region because the migration rate of proton is not high enough, resulting in high ohmic loss (IR drop) in the membrane. As the membrane conductivity was enhanced (Case 3), the conductivity of the proton in the membrane and H_2 electrode was greatly improved, resulting in lower ohmic loss. The fuel cell performance was greatly enhanced as shown in Figures 3.14 and 3.15. Of the two flow modes, the flow-through mode generated higher performance because the ionic resistance for proton transport was lower near the membrane, thus enhancing the migration rate. The low ionic resistance close to the Br_2 electrode/membrane interface was a result of forced convection of the electrolyte feed into the Br_2 electrode. One way to improve the migration rate of proton was to increase the concentration of ionomer present in the hydrogen electrode. The other option was to reduce the thickness of the membrane to compensate for the low proton conductivity.

Based on the case studies done in this study, the model suggests that the favorable cell configuration to attain optimum performance was to operate with a thinner electrode and an active surface area high enough for the electrode to utilize the reactants more effectively. Also, higher electrolyte flow rates helped in maintaining a high reactant concentration at the Br_2 electrode entrance for a fuel cell operating under flow-by mode and better convective transport

for the one operating under flow-through mode. Also, higher membrane conductivities enhanced the fuel cell performance in the ohmic-controlled region.
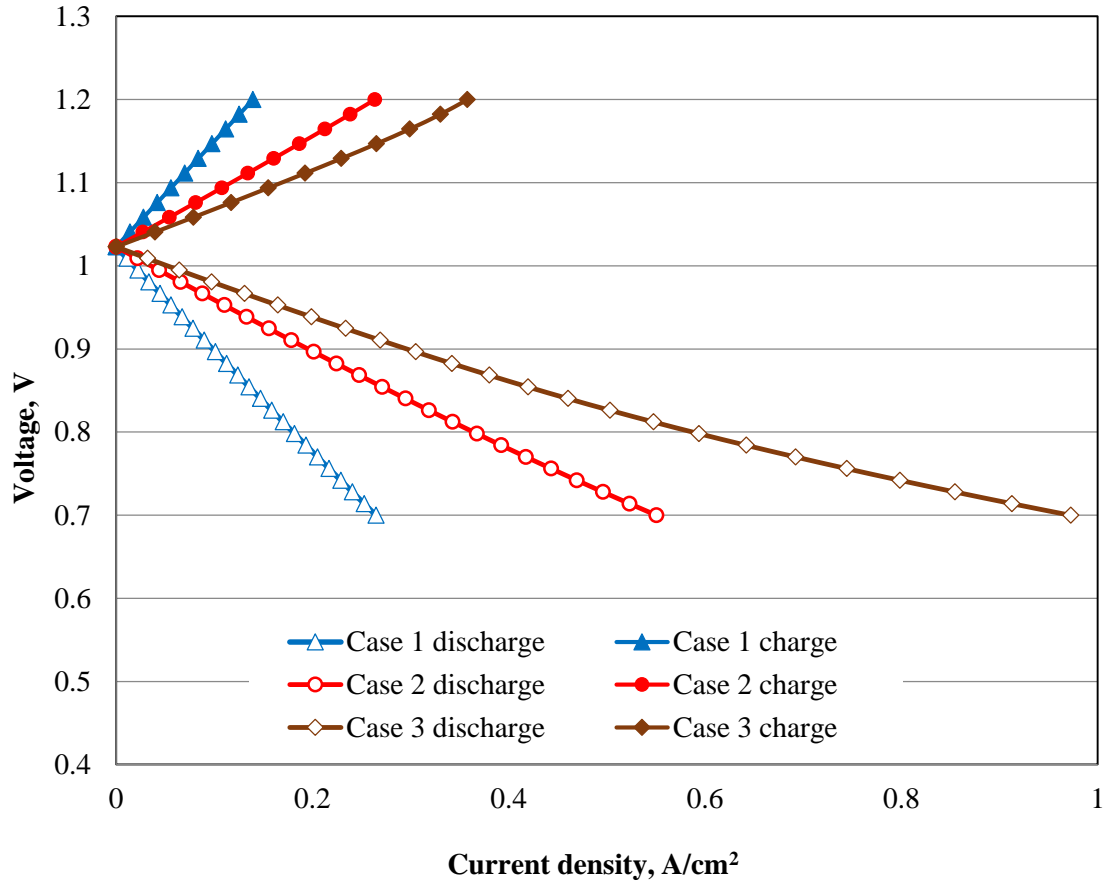
Figure 3.14. Effect of $k_{H^+}^m$ on the H$_2$-Br$_2$ fuel cell performance (flow-by mode)
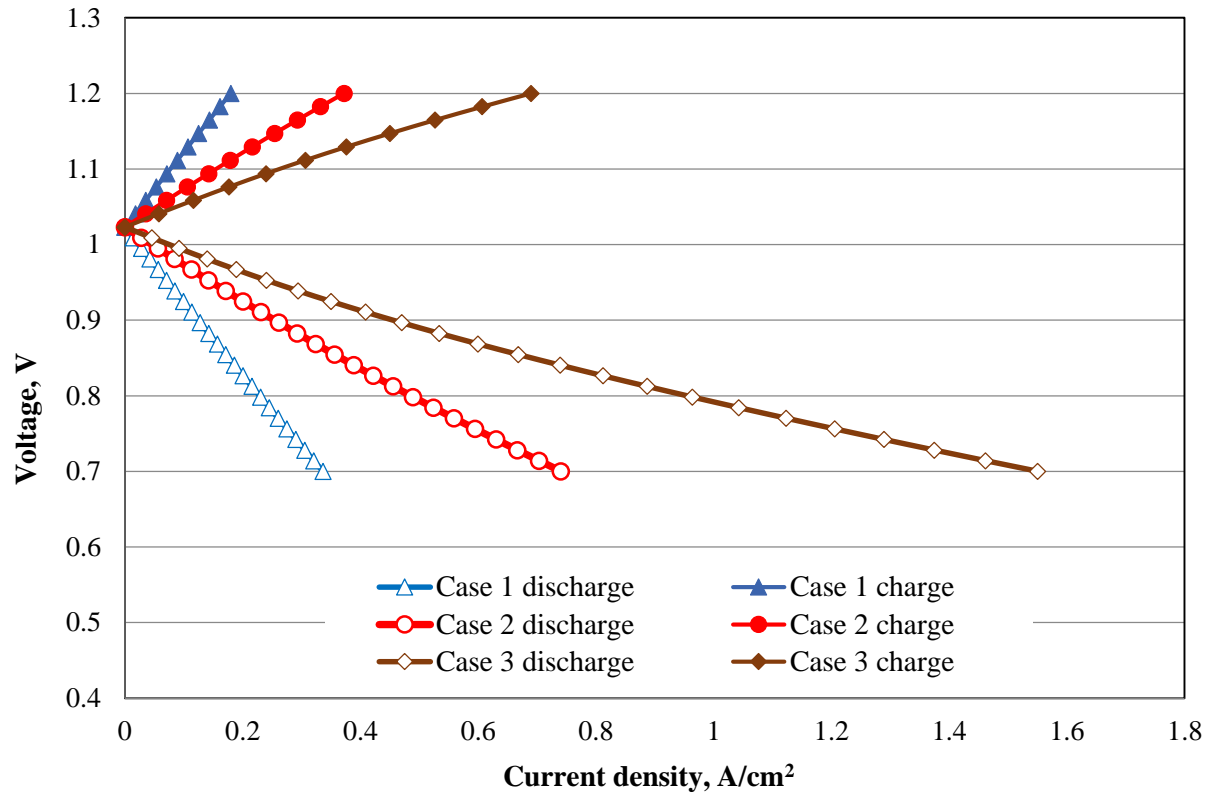
Figure 3.15. Effect of $k_{H^+}^m$ on the H$_2$-Br$_2$ fuel cell performance (flow-through mode)

Figures 3.16 (flow-by) and 3.17 (flow-through) show a case study comparing the performance of a H$_2$-Br$_2$ fuel cell with higher Br$_2$ electrode thickness and lower active surface area (Case 2) to a thinner Br$_2$ electrode with lower and higher active surface areas (Case 1 and Case 3). Table 3.11 shows the corresponding active surface areas and thicknesses used in this study. As shown in Figures 3.16 and 3.17, having a higher active surface area and a thinner electrode (Case 3) decreases the ionic diffusion pathways and enhances the kinetic property and thus improves the performance (discharge and charge). Based on the modeling studies performed in this study, the last case study described above comprises the best configuration possible to obtain optimal performance.

Table 3.11. Electrode thicknesses and active surface areas

Case	δ_1 (μm)	$a_{Br_2} \times 10^{-4}$ (cm²/cm³)
1	100	0.088
2	310	0.088
3	100	8.8
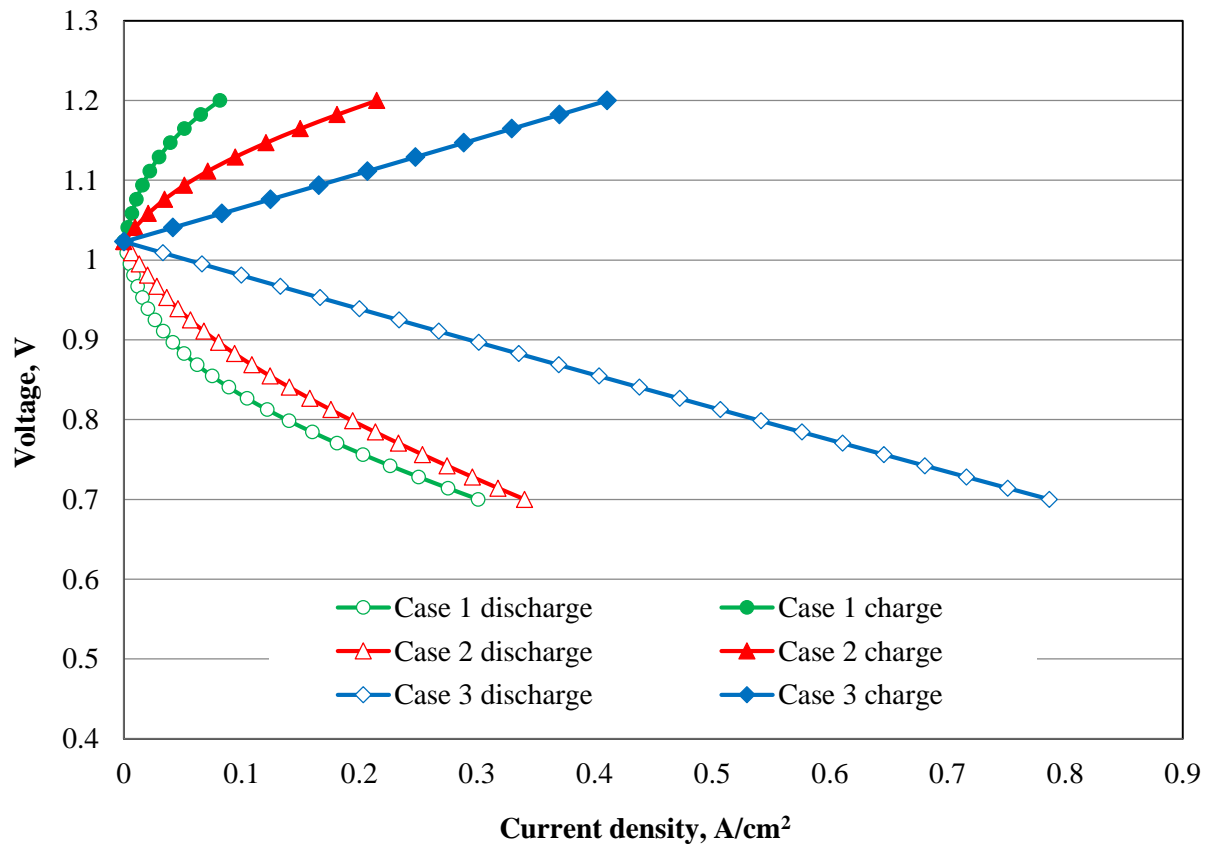
Figure 3.16. Effect of electrode thickness and electrode active surface area on the performance of the fuel cell (flow-by mode)
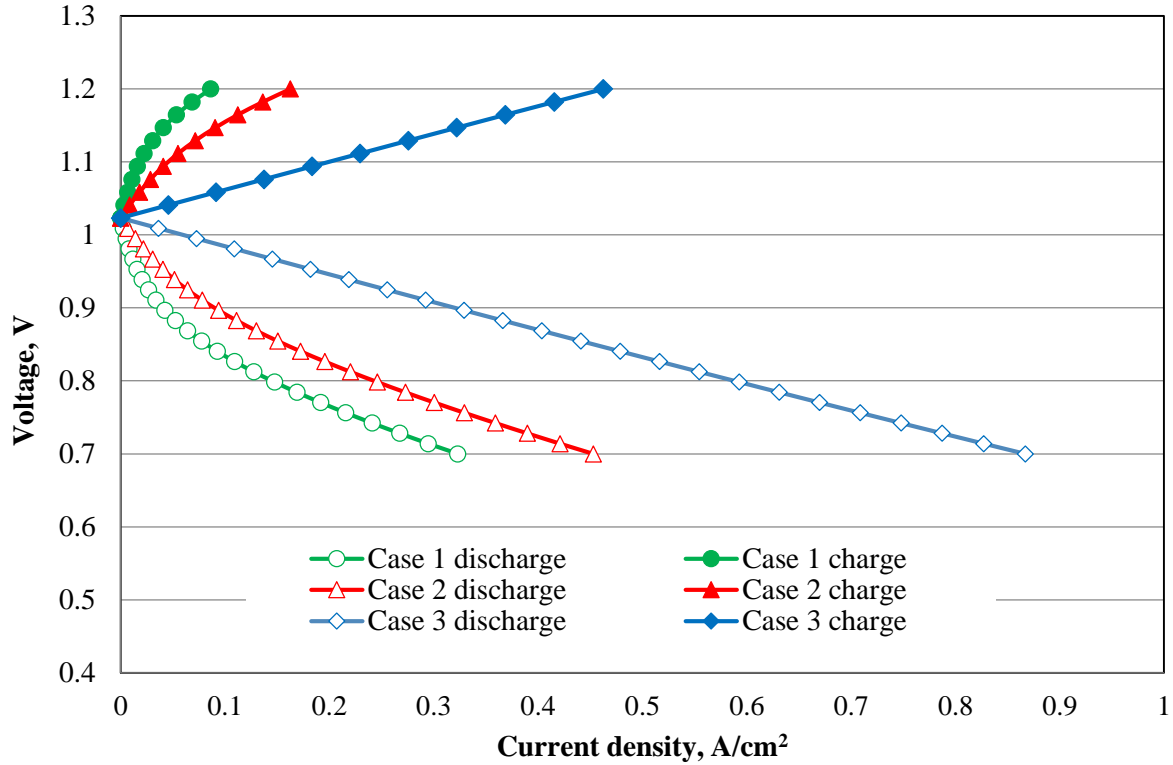
Figure 3.17. Effect of electrode thickness and electrode active surface area on the

performance of the fuel cell (flow-through mode)

3.4. Conclusions

A 1D mathematical model was developed for a H_2/Br_2 fuel cell to predict the performance and act as a theoretical guiding tool for the future experimental studies. The model was experimentally validated and the effect of the Br_2 electrode thickness on the discharge performance of the fuel cell was examined. Of the two flow modes investigated in this study, the performance of the fuel cell operating under flow-through design was better than the flow-by mode. For a fuel cell operating under flow-by mode, the performance was found to be dependent on the utilization of the Br_2 electrode. Under-utilization of the electrode leads to low performance in the activation-controlled region. Both the thickness and the active surface

area should be optimized for the electrode to be completely utilized. Also, high enough electrolyte flow rates are necessary to maintain high reactant concentrations at the Br_2 electrode entrance. On the other hand, the convective transport inside the Br_2 electrode of a fuel cell operating under flow-through mode can be enhanced by operating the cell at high feed flow rates. Higher membrane conductivity led to better performance especially in the ohmic-controlled region. The model suggests that the fuel cell configuration consisting of a thinner Br_2 electrode with high active surface area results in optimal performance of the fuel cell. A thinner electrode minimizes the ionic/molecular diffusion pathways resulting in better mass transport, and the high active surface area improves the kinetic rate. The active surface area of the electrode can be enhanced by either employing multiple plain carbon electrodes, i.e. increasing the electrode thickness, or growing carbon nanotubes on the electrode fiber surface to create higher surface area. However, employing multiple electrodes increases the diffusion pathway for the ions while also increasing the active surface area. This could lead to mass transport limited performance at higher current densities. On the other hand, growing nanotubes on the carbon substrates is a more suitable option because the electrode surface area can be improved without affecting the porosity and the electrode thickness. Also, the process for growing nanofibers onto carbon substrates has been successfully demonstrated in some of the recent studies.[14,15]

3.5. Supporting Information

This section explains the modeling study conducted in order to develop an empirical correlation between velocity of the feed stream (v_x) and the Br_2 electrode thickness (x) for a H_2-Br_2 fuel cell operating under flow-through mode for a 1D model. Figure 3.18 shows the modeling domain of this study. The modeling domain in this study consists of half of an inlet

channel and an outlet channel with a shoulder between them. A porous Br_2 electrode was in continuous contact with the flow field. The feed stream flows into the porous Br_2 electrode through the inlet channel and comes out through the outlet channel. The governing equations and boundary conditions are described below.
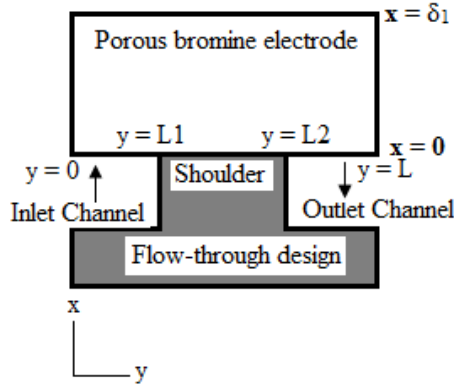
Figure 3.18. Modeling domain of the flow-through mode

3.5.1. Governing Equations

The 2D equation of continuity for an incompressible fluid of constant mass density flowing through a porous electrode is

$$-\frac{dv_x}{dx} - \frac{dv_y}{dx} = 0 \qquad\qquad [3.17]$$

where v_x and v_y are the feed stream velocities in x and y directions. The velocity of the feed stream into the porous electrode is expressed using Darcy's law. Neglecting the effect of gravity, the velocities in x and y directions are specified as follows:

$$v_x = -\frac{k}{\mu}\frac{dP}{dx} \quad \text{and} \quad v_y = -\frac{k}{\mu}\frac{dP}{dy} \qquad\qquad [3.18]$$

where k is the permeability of the electrode, μ is the viscosity of the fluid stream, and P is the total pressure. Both permeability (through-plane and in-plane) and viscosity were assumed to

be constant in this model. Inserting equation 3.18 into equation 3.17 yields a 2D Laplace equation.

$$\frac{d^2 P}{dx^2} + \frac{d^2 P}{dy^2} = 0 \qquad [3.19]$$

3.5.2. Boundary Equations

At the flow field inlet, $x = 0$ and $0 \leq y < L1$, the velocity of the feed stream into the porous electrode was fixed as shown below.

$$v_x = -\frac{k}{\mu}\frac{dP}{dx} \qquad [3.20]$$

At the interface between the shoulder of the flow field and porous electrode, $x = 0$ and $L1 \leq y \leq L2$, the pressure gradient in the x direction was assumed to be zero.

$$\frac{dP}{dx} = 0 \qquad [3.21]$$

At the end interface, $x = 0$ and $L2 < y \leq L$, the outlet pressure was fixed to atmospheric pressure (P_{atm}).

$$P = P_{atm} \qquad [3.22]$$

At the boundaries of the electrode ($y = 0$ and $y = L$) and $0 \leq x \leq \delta_1$, the pressure gradient in the y direction was assumed to be zero.

$$\frac{dP}{dy} = 0 \qquad [3.23]$$

The governing equations and boundary conditions described above were solved in Fortran using the BAND J technique.[9] The result includes the pressure distribution along the axial (y) and normal (x) directions. From the result, the feed stream velocities (v_x and v_y) were calculated along the axial (y) and normal (x) directions. In order to incorporate the 2D effect in the porous electrode into the 1D mathematical model developed in this paper, the feed stream

velocities in the flow channel along the axial direction ($0 \leq y \leq L1$) were averaged to obtain a single data point along the normal direction ($0 \leq x \leq \delta_1$). The feed stream velocities (v_x) along the x direction were then plotted against the electrode thickness (x).

A second order polynomial correlation was used to fit the non-linear velocity distribution in the x direction. The resulting correlation (v_x as a function of x) was then incorporated into the convection term in the flux expression for the flow-through mode in the 1D model. Figure 3.19 shows an example plot containing the velocity distribution and Table 3.12 shows the corresponding parameters used for the case study. As shown in Figure 3.19, the velocity decreases along the normal direction (x) with the maximum being at the electrode entrance ($x = 0$) where the feed stream enters from the flow channel.

Table 3.12. Parameters used for calculating velocity profile (flow-through mode)

Inlet Channel width	0.1 cm
Shoulder width	0.25 cm
Outlet Channel width	0.1 cm
Channel height	1 cm
Electrode height	0.031 cm
Permeability of the electrode (k)[a]	2.5×10^{-6} N/atm
Inlet feed volumetric flow rate	0.025 cm^3/s
Outlet pressure (P)	1 atm
Viscosity of the feed stream (μ)	1.5×10^{-2} g/cm s
Convergence criterion	1×10^{-8}

[a] Obtained from Ref. 16

$$y = 31.734x^2 - 3.5858x + 0.0817$$
$$R^2 = 0.999$$
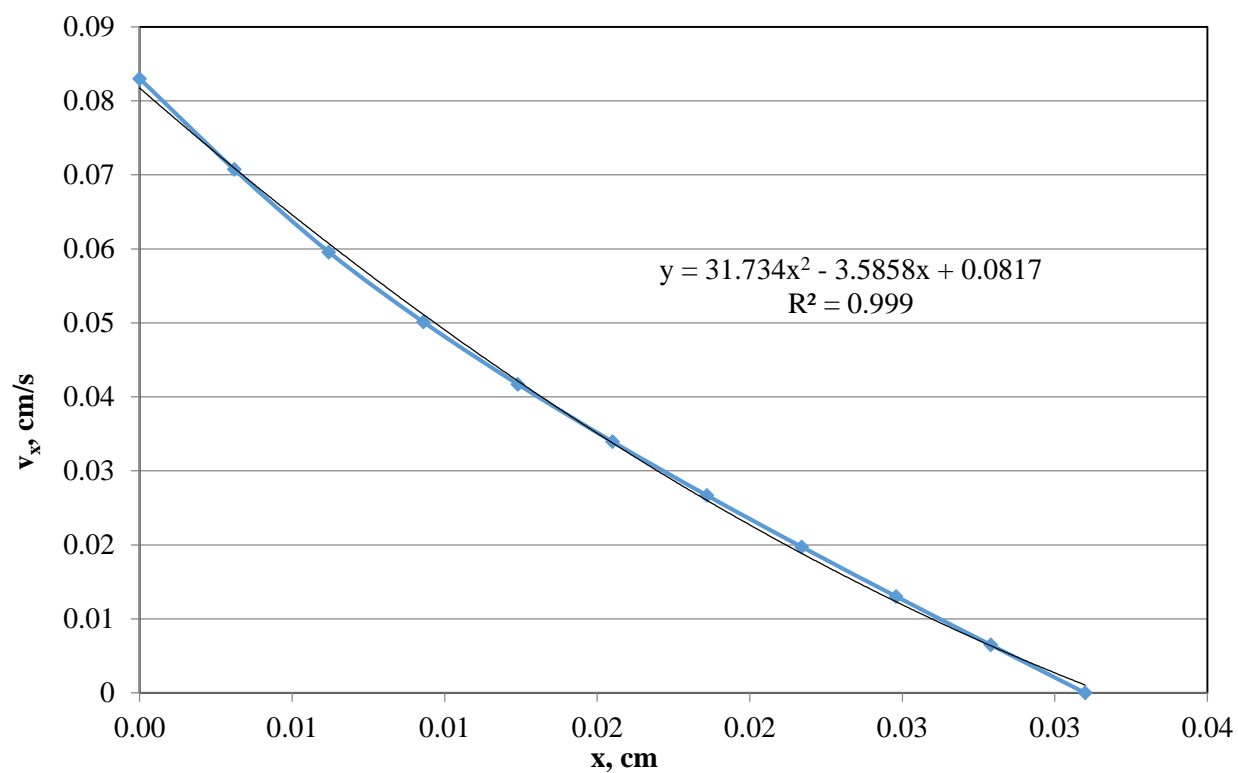
Figure 3.19. Velocity distribution for a H_2-Br_2 flow cell operating under flow-through mode

3.6. References

1. R.F. Savinell and S.D. Fritts, "Theoretical Performance of a Hydrogen-Bromine Rechargeable SPE Fuel Cell," *J. Power Sources*, **22**, 423 (1988).

2. S. D. Fritts and R. F. Savinell, "Simulation Studies on the Performance of the Hydrogen Electrode Bonded to Proton Exchange Membranes in the Hydrogen-Bromine Fuel Cell," J. *Power Sources*, **28**, 301 (1989).

3. Rui Zhang and J. W. Weidner, "Analysis of a gas phase Br_2-H_2 redox flow battery," J. *Appl. Electrochem.*, **41**, 1245 (2011).

4. William A. Braff and Cullen R. Buie, "Hydrogen Bromine Laminar Flow Electrochemical Cell for High Power and Efficiency Energy Storage Applications," *ECS Transactions*, **33**(39), 179 (2011).

5. Kyu Taek Cho, Paul Ridgeway, Adam Z. Weber, Sophia Haussener, Vincent Battagalia, and Venkat Srinivasan, "High Performance Hydrogen/Bromine Flow Battery Redox Flow Battery for Grid-Scale Energy Storage," *J. Electrochem. Soc.*, **159**(11), A1806 (2012).

6. Brian Huskinson and Michael J. Aziz, "Performance Model of a Regenerative Hydrogen Bromine Fuel Cell for Grid-Scale Energy Storage," *Energy Science and Technology*, **5** (1), 1-16 (2013).

7. T. Nguyen, "A Gas Distributor Design for Proton-Exchange-Membrane Fuel Cells" *J. Electrochem. Soc.*, **143**, L103 (1996).

8. R. E. White, S. E. Lorimer, and R. Darby, "Prediction of the Current Density at an Electrode at Which Multiple Electrode Reactions Occur Under Potentiostatic Control," *J. Electrochem. Soc.*, **130**(5), 1123 (1983).

9. John Newman, "Numerical Solution of Coupled, Ordinary Differential Equations," *Ind. Eng. Chem. Fundam.*, **7** (3), 514 (1968).

10. David Wood III, Jung S. Yi, and Trung V. Nguyen, "Effect of direct liquid water injection and interdigitated flow field on the performance of proton exchange membrane fuel cells," *Electrochimica Acta*, **43**, 3795 (1998).

11. Haley Kreutzer, Venkata Yarlagadda, and Trung Van Nguyen, "Performance Evaluation of a Regenerative Hydrogen-Bromine Fuel Cell," *J. Electrochem Soc.*, **159** (7), F331 (2012).

12. Haley M. Kreutzer, "Characterization of the Hydrogen-Bromine Flow Battery for Electrical Energy Storage," MS Thesis, University of Kansas, Lawrence, KS, USA, May 2012.

13. Datong Song, Qianpu Wang, Zhongsheng Liu, Titichai Navessin, Michael Eikerling, and Steven Holdcroft, "Numerical optimized study of the catalyst layer of PEM fuel cell cathode," *J. Power Sources*, **126**, 104 (2004).

14. Jiang Li, Eve S. Steigerwalt, Senthil Sambandam, Weijie Lu, and Charles M. Lukehart, "Carbon Nanofibers "Spot-Welded" to Carbon Paper by Carbothermal Reduction: A Nano/Micron-Scale Hierarchical Architecture having Low Contact Resistance,"*Chem. Matter.*, **19**, 6001 (2006).

15. Chunyu Du, Baorong Wang, and Xinqun Cheng, "Hierarchy Carbon Paper for the Gas Diffusion Layer of Proton Exchange Membrane Fuel Cells,"*J. Power Sources*, **187**, 505 (2009).

16. M. S. Ismail, M. Damjanovic, K. Hughes, D. B. Ingham, L. Ma, M. Pourkashanian, and M. Rosli, "Through-plane permeability for untreated and PTFE-treated gas diffusion layers

in proton exchange membrane fuel cells," *J. Fuel Cell Science and Technology*, **7**(5), 051016 (2010).

CHAPTER 4

A Preliminary Study on the Development of High Surface Area Carbon Electrodes

4.1. Background

The motivation behind the development of high surface area carbon electrodes was the model prediction shown in Figure 3.17. As shown in Figure 3.17, a thinner bromine (Br$_2$) electrode with high specific active surface area was found to be the optimal choice for improving the fuel cell performance. In this study, an experimental approach based on the model prediction was developed to increase the active surface area of existing carbon GDEs.

The specific active surface area (intrinsic property) of commercially available plain carbon gas diffusion electrodes (GDEs) is quite low (0.64 m^2/g^1 compared to 100m^2/g^2 of Pt/C electrodes or 1.6 X 10^3 cm^2/cm^3 compared to 5.6 X 10^5 cm^2/cm^3 of Pt/C electrodes). One of the common approaches reported in the literature to improve the active surface area of a Br$_2$ electrode was to employ a stack of multiple layers of carbon GDEs.[3,4] A major disadvantage of this approach is that the thickness (bulk property) of the Br$_2$ electrode increases with the number of carbon GDE layers used, resulting in longer ionic, electronic and molecular diffusion pathways. This could lead to mass transport limited performance at higher current densities.[5] Several previous studies have investigated high surface area carbon materials such as carbon nanotubes, graphene-based nanoplatelets, and activated carbon powders for battery and electrochemical capacitor applications.[6-8] However, these high surface area carbon materials are normally blended with a polymeric binder to fabricate solid carbon electrodes for fuel cell and battery applications and the resulting electrodes will be quite dense and have low porosity. The low porosity of these electrodes limits the amount of electrolyte and active

materials available for reactions and also lead to high pressure drops in the flow through mode. The other approach to enhance the active surface area of existing carbon GDEs was to coat them with an ink or suspension prepared from high surface area carbon materials. The disadvantage of using this approach is that, the high surface area carbon materials are attached to the carbon electrode fiber surface by means of weak Van Der Waals forces and could be lost at high fluid reactant flow rates. In conclusion, durable high surface area carbon materials with high porosity that could withstand high liquid flow rates are required.

Prior works have investigated different approaches to enhance the active surface area of an existing carbon GDE without affecting its morphological properties. Etching processes such as chemical and plasma (argon or oxygen ion) etching were widely used to improve the active surface area of existing porous carbon electrodes.[9,10] The etching processes create roughness and introduce functional groups onto the carbon electrode fiber surface, which in turn increases the active surface area of the electrode. Some of the limitations associated with the etching techniques involve the expensive nature of plasma etching and chemical impurities that might be incorporated if the chemically etched carbon electrode was not cleaned properly. A recent study by Mayrhuber et al. used a laser perforation technique to improve the transport characteristics of the commercial porous carbon electrodes by creating holes in their microstructure despite losing some active surface area.[11] However, the laser perforation technique is quite expensive and only improves the cell performance in the transport controlled regime. A few approaches reported in the literature have tried to improve the specific surface area of existing porous carbon electrodes by growing carbon nanotubes (CNTs) directly on the carbon electrode fiber surface.[8,12-14] In this case, carbon nanotubes were bound to the carbon

electrode fiber surface by means of a covalent bond. The covalent bond between CNTs and the carbon electrode fiber surface is quite strong and can withstand high liquid reactant flow rates.

4.2. Carbon Nanotube-Based Electrodes

The CNT based electrodes are considered to be one of the prime candidates for electrochemical energy storage devices because of their attractive properties such as high electronic conductivity, large specific surface area, and excellent chemical stability.

4.2.1. Classification of Carbon Nanotubes

The CNTs are classified into two types; single-walled and multi-walled carbon nanotubes (SWCNTs and MWCNTs). A SWCNT is a layer of graphene rolled into a cylinder whereas a MWCNT consists of multiple layers of graphene sheets co-axially bundled into a cylinder. The carbon nanotubes can be either metallic or semi-conducting in nature based on their chirality. Due to their high electrical conductivity and mechanical strength, MWCNTs are preferable for fuel cell and battery applications. Also, MWCNTs have a long life time since their outer graphene shells protect the inner ones from degradation.

4.2.2. Synthesis of CNT Based Electrodes

There are several ways to synthesize CNTs either directly on substrates such as silicon, alumina, and quartz or on the porous carbon electrode fiber surface. Ijima et al. discovered carbon nanotubes in 1991 using arc-discharge technique[15] and since then different techniques were developed to synthesize CNTs. Carbon arc-discharge, laser ablation, and chemical vapor deposition are the widely used techniques to synthesize SWCNTs and MWCNTs.[16-18] The above listed techniques are described in detail in the following sections

4.2.2.1. Carbon Arc-Discharge Technique

The arc-discharge technique is a physical process. Both SWCNT and MWCNT's can be synthesized using this technique. In the arc-discharge technique, two carbon electrodes were placed parallel to each other in a vacuum chamber as shown in Figure 4.1. The whole process is conducted in an inert gas (argon or helium) environment. The experimental procedure is described below.

1. After positioning the carbon electrodes inside the vacuum chamber, the power supply was then switched on (usually a voltage of 18-20 V is applied). The positive electrode was slowly brought closer to the negative electrode until an electrical arc appears.

2. Once the electrical arc is steady, the electrodes were separated. The gap between the electrodes is usually around 1-2 mm.

3. The positive electrode was vaporized and the carbon nanotubes were deposited on to the negative electrode.

4. The power supply was turned off and the CNTs were collected after the system cooled down to room temperature.

The parameters to control in this process are the inert gas pressure, arc current, and synthesis time. The size and yield of nanotubes depend upon these parameters. The carbon arc-discharge technique was widely used to synthesize MWCNTs. In early 1990s, the carbon arc-discharge technique was modified to synthesize SWCNTs as well.[17,19] However, the negative electrode needs a catalyst (Fe, Co, and Ni) to grow SWCNTs, which adds extra cost to the process.
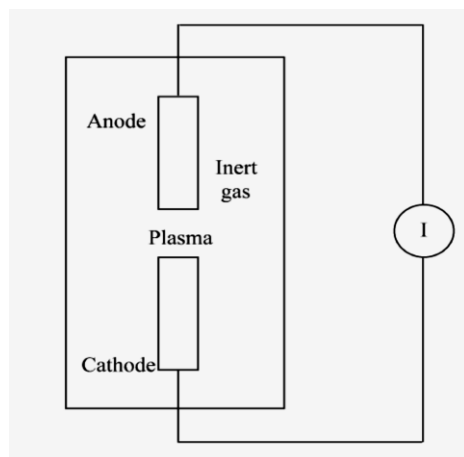
Figure 4.1. Carbon nanotube synthesis with carbon arc-discharge technique[17] [Sinha *et al.*

(2005)]

The limitations associated with using the carbon-arc discharge technique are

1. It is an energy extensive process and not suitable for large scale synthesis.

2. A large portion of the synthesized carbon nanotubes contain amorphous carbon impurities (or carbon soot).

4.2.2.2. Laser Ablation Technique

In this technique, the carbon target is placed in a tube furnace and struck with intense laser pulses in the flow of an inert gas (argon or helium) to synthesize CNTs. Figure 4.2 shows the experimental set up used to grow CNTs using laser ablation technique. The furnace temperature is maintained between 1000°C and 1200°C. The inert gas flowing through the tube furnace carries the grown carbon nanotubes to a copper collector. The CNTs are collected, once the reactor cools down. The parameters to control in this process are the inert gas pressure, laser power and wavelength, temperature and synthesis time.

The laser ablation technique is known to yield high quality MWCNTs but it is quite expensive. On the other hand, a catalyst is required to grow SWCNTs. The limitations of the

laser ablation technique involves amorphous carbon impurities, high cost, and the damaging impact of laser on the carbon target.
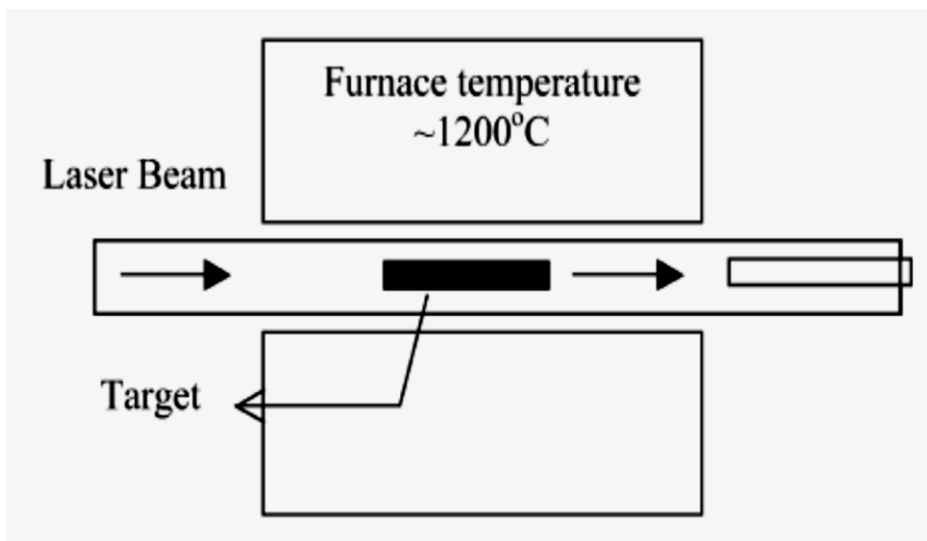
Figure 4.2. Carbon nanotube synthesis with laser ablation technique[17] [Sinha *et al.* (2005)]

4.2.2.3. Chemical Vapor Deposition Technique

Chemical vapor deposition (CVD) is the most widely used technique for growing CNTs. This process requires less energy and hence suitable for large scale synthesis. Both SWNCT and MWCNTs can be synthesized using this process. However, the process is a bit complicated compared to arc-discharge and laser ablation techniques. Figure 4.3 shows the commonly used experimental setup. The procedure is described below.

1. The first step is to deposit a catalyst (composed of nanoparticles) on to the carbon substrate. The purpose of the catalyst is to promote the growth of CNTs. Usually, first row transition metals are used as catalyst materials (Fe, Co, and Ni). [22] The most common techniques to deposit the catalyst are electrodeposition, physical sputtering, solution deposition, and e-beam evaporation. [8,12-14,22]

2. The carbon substrates are then placed in a quartz furnace and heated up to the CNT synthesis temperature (usually between 600 and 850°C) in the presence of hydrogen, and an inert gas (argon or helium).

3. The role of the hydrogen gas is to prevent the interference of spontaneous carbonization (formation of carbon soot by pyrolysis) with the carbon nanotube formation.

4. Once the CNT synthesis temperature is reached, a hydrocarbon gas (usually acetylene or methane) is supplied to the quartz tube furnace. The hydrocarbon gas is the carbon source in this process.

5. The growth rate and size of the nanotubes is directly proportional to the time of the reaction, flow rate of acetylene, and the temperature of the furnace.

6. Finally the furnace is allowed to cool down in the presence of the inert gas.
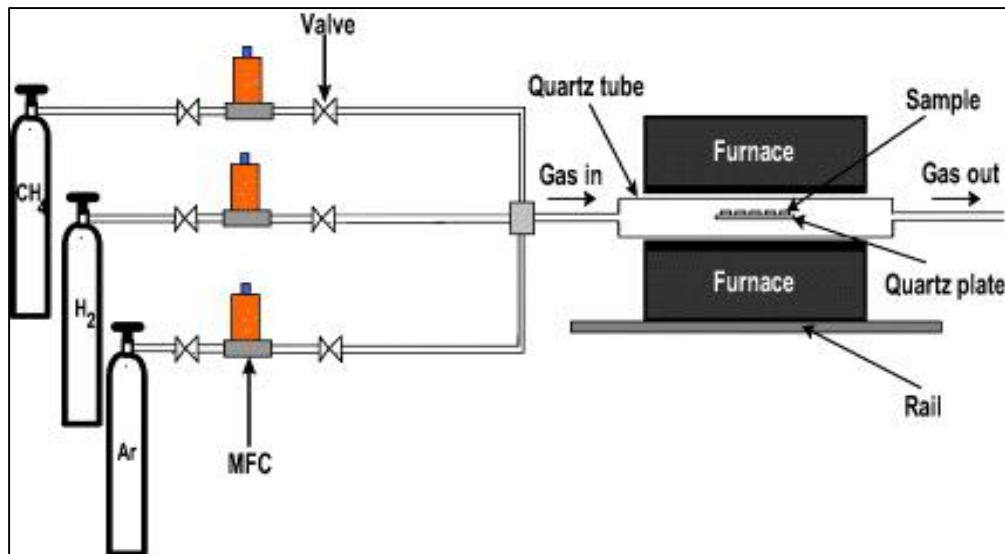
Figure 4.3. Carbon nanotube synthesis with CVD technique[20] [Nguyen *et al.* (2012)]

Despite the numerous advantages associated with this process, there is a major limitation. The metal catalyst nanoparticles are often trapped inside and below the nanotubes. The adhesion between the carbon nanotubes and carbon substrates might be affected as a result of this limitation. Hence, CNT growth mechanism is vital to ensure the contact between CNTs and the carbon electrode fiber surface.

Some of the recent studies have implemented spray pyrolysis approach (also known as thermal CVD technique) to synthesize CNTs by using a xylene (carbon source)/ferrocene (catalyst source) precursor solution.[23,24] However, the spray pyrolysis process is a bit involved since a separate chamber is required to vaporize the xylene/ferrocene precursor solution before introducing it into the reactor furnace. The incomplete vaporization of the precursor solution directly affects the catalyst deposition.

4.3. Significance of CVD Technique

The usage of carbon arc discharge and laser ablation techniques for growing CNTs has been declining over the years. The reason behind the decline of these processes are the high temperatures involved, evaporation of carbon targets, and especially the amount of purification needed to get rid of the amorphous carbon impurities. Also, the CVD process requires less energy compared to arc-discharge and laser ablation techniques, making it a suitable option to synthesize CNTs.[16,17,19]

Several research investigations reported in the literature have successfully grown MWCNTs directly on the carbon electrode fiber surface. These MWCNT-based electrodes were successfully employed in polymer electrolyte membrane (PEM) fuel cells. The MWCNTs were grown on the surface of the GDE, and subsequently platinum (Pt) was electrodeposited in order to improve the catalyst utilization in the PEM fuel cell.[13] The

electronic pathways were secured by depositing Pt nanoparticles directly on the MWCNTs, thus improving the catalyst utilization. Barton et al. used MWCNT modified Toray carbon electrodes to improve the electrochemical performance of biocatalytic electrodes.[12] However, a solution deposition method was used to deposit catalyst nanoparticles on the carbon electrode fiber surface, which is quite expensive.

4.4. Objectives

In this chapter, experimental approaches to deposit cobalt (Co) nanocatalyst seeds and to grow MWCNTs on a carbon GDE substrate (SGL 10AA) are discussed along with some preliminary results. The preliminary results involve electrochemical active surface area (ECSA) measurements of MWCNT-based electrodes in a three electrode arrangement followed by the performance evaluation of MWCNT in comparison to plain porous carbon electrodes in a H_2-Br_2 fuel cell.

4.5. Experimental

4.5.1. Synthesis of MWCNT-Based Carbon Electrodes

The synthesis of MWCNT-based carbon electrodes involves two major steps. The first step involves creating active metal catalyst nanoparticles on the carbon electrode fiber matrix for the hydrocarbon source to react and form MWCNTs.

4.5.1.1. Electrodeposition of Catalyst Nanoparticles

As discussed earlier, electrodeposition, physical sputtering, solution deposition, and e-beam evaporation are the most commonly used techniques to deposit metal nanoparticles. In this study, the electrodeposition technique was chosen to deposit catalyst nanoparticles on the carbon electrode fiber surface because it is cost effective and known to yield quality deposits.[27] Since transition metals are known to be the most active catalysts for carbon nanotube synthesis,

cobalt (Co) was chosen as the catalyst for this study. The Co nanoparticles were deposited on the SGL 10AA carbon electrode fiber surface by both constant and pulse current electrodeposition techniques in a solution containing cobalt sulfate ($CoSO_4$) and boric acid (H_3BO_3). The role of H_3BO_3 in the precursor solution was to avoid the formation of an insoluble hydroxide layer at the carbon electrode/electrolyte interface by maintaining the pH of the electrolyte solution in the acidic range (between 4.4 and 4.6).[25] The electrolyte solution used in this study is a mixture of 0.02M $CoSO_4$ and 0.33M H_3BO_3.
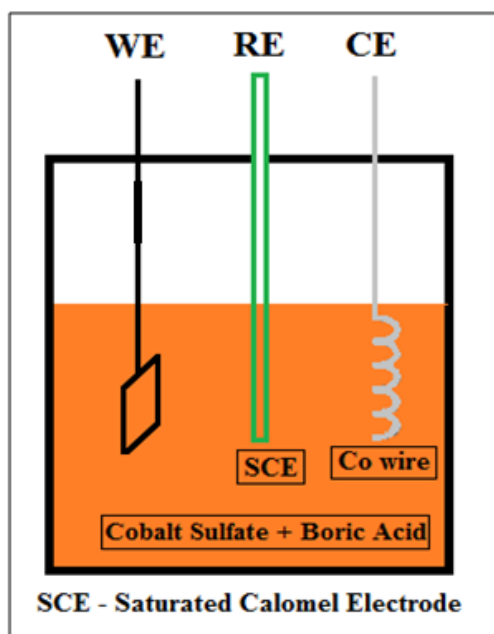
Figure 4.4. Experimental fixture used in the electrodeposition experiment

A three-electrode arrangement was used to implement constant and pulse current electrodeposition techniques. The experimental setup (shown in Figure 4.4) consisted of a SGL 10 AA carbon working electrode (WE) and a saturated calomel reference electrode (RE). A coiled cobalt wire (0.5mm diameter, purchased from Alfa Aesar) was used as the counter

electrode (CE). The Co catalyst nanoparticles were deposited by using the procedure listed below.

1. Initially, the carbon electrode (WE) was boiled in de-ionized (DI) water for 1 hour to make them hydrophilic.

2. The working, counter, and reference electrodes were then placed in a beaker containing a solution of $CoSO_4$ and H_3BO_3.

3. Nitrogen (N_2) gas was bubbled through the solution for 30 minutes to displace any oxygen present in the solution. After 30 minutes, the Teflon tube supplying the N_2 gas was pulled above the surface of the solution to maintain an inert gas blanket. The gas blanket prevents air from entering and interacting with the electrolyte solution.

4. A positive current (anodic) of 50 mA was applied to the WE for 60 seconds to clean the carbon electrode fiber surface.

5. Next, the Co nanoparticles were deposited by applying a cathodic current to the working electrode. The current collection in the electrodeposition step was done using stainless steel alligator clips attached to one side of the electrode. The following reactions take place at the working and counter electrodes.

$$\text{Working electrode (WE): } Co^{2+} + 2e^- \rightarrow Co \qquad E^o = -0.28\,V$$
$$\text{Counter electrode (CE): } Co \rightarrow Co^{2+} + 2e^- \qquad E^o = \ 0.28\,V$$
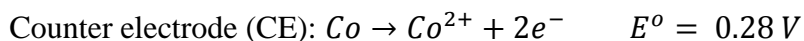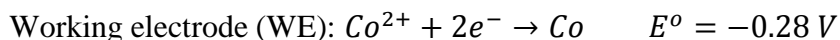
6. Finally, the carbon electrodes were rinsed with DI water and dried at room temperature.

A total of 5 carbon electrode samples were synthesized using constant and pulse current electrodeposition. The first two samples were synthesized using constant current electrodeposition (sample 1: -0.1 mA/cm^2 for 1000s, and sample 2: -0.1 mA/cm^2 for 2000s). The geometric area of sample 1 and sample 2 was 9 cm^2. The rest of the samples were synthesized using pulse current electrodeposition (sample 3: -3.75 mA/cm^2 applied with a single pulse of 1s, sample 4: -5 mA/cm^2 applied with two pulses each with a 0.1s duration, and sample 5: -2.5 mA/cm^2 applied with a single pulse of 1s). The geometric area of sample 3, sample 4, and sample 5 was 4 cm^2. Finally, Scanning Electron Microscopy (SEM) and Energy Dispersive X-ray Spectroscopy (EDX) analysis was used to confirm the electrodeposition of Co nanoparticles on the carbon electrode fiber surface.

4.5.1.2. CVD Process to Grow Carbon Nanotubes

The second step for synthesizing MWCNT-based carbon electrodes involved growing MWCNTs in the presence of acetylene (C_2H_2), argon (Ar), and hydrogen (H_2) gases at high temperatures. The carbon nanotube growth was accomplished using Chemical Vapor Deposition (CVD), which is a widely used process for multi-wall nanotube (MWCNT) growth. The experimental set up used for CVD experiments is shown in Figure 4.5. The MWCNT-based carbon electrodes were synthesized using the procedure listed below.

1. After electrodepositing Co, the carbon electrodes were placed in a quartz tube furnace (purchased from MTI corporation, model: OTF-1200X-S) and heated to 550°C at a ramp rate of 3°C/min, while flowing 20% H_2 and 80% Ar gas (flow rate: 80 cc/min) into the quartz tube. The purpose of Ar was to prevent the carbon paper from combusting and simultaneously dilute the hydrogen gas. The purpose of H_2 was to prevent carbon soot formation resulting from pyrolysis.

2. The carbon electrodes were allowed to stay at 550°C for 45 minutes to reduce any cobalt oxide present on the surface of the Co nanoparticles.

3. Next, the carbon electrodes were heated to 700°C (reaction temperature) from 550°C at a ramp rate of 4°C/min. At 700°C, C_2H_2 (flow rate: 10 cc/min) and Ar (flow rate: 60 cc/min) gases were introduced to initiate MWCNT growth.

4. The carbon electrodes were allowed to stay at 700°C for 30 minutes to grow MWCNTs.

5. Finally, the C_2H_2 and H_2 sources were shut off, and the carbon electrodes were cooled in the presence of Ar gas.
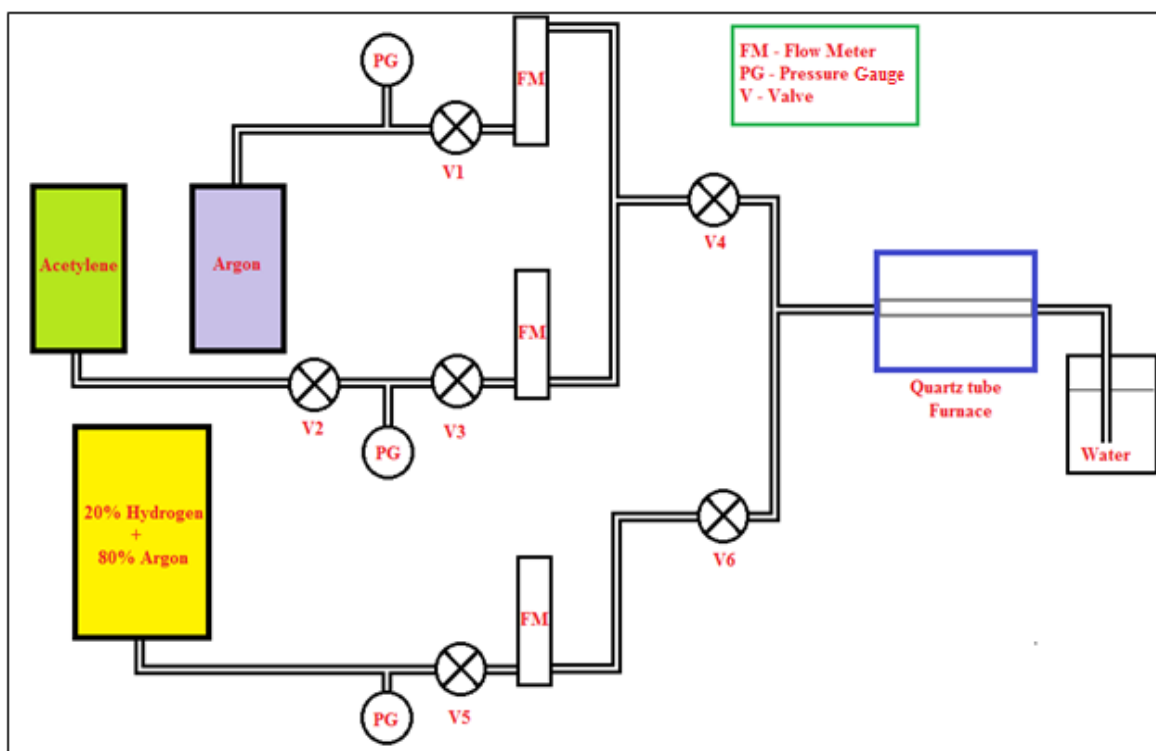
Figure 4.5. CVD experimental set up used to synthesize MWCNTs

After the CVD process, the carbon electrodes were sonicated in de-ionized (DI) water for 30 minutes and subsequently, soaked in 1M nitric acid (HNO_3) overnight to etch away the

exposed Co metal nanoparticles. The DI water sonication gets rid of any amorphous carbon impurities present in the carbon electrode.[26] After the electrodes were sonicated and acid treated, SEM analysis was done to detect the MWCNTs growth. Also, Transmission Electron Microscopy (TEM) and Energy Dispersive X-ray Spectroscopy (TEM-EDX) were done to determine the growth mechanism of MWCNTs on the carbon electrode fiber surface.

4.5.2. Surface Area Enhancement Measurements

The MWCNT-based carbon electrodes were electrochemically analyzed using the linearized Butler-Volmer approach to determine the increase in their specific active areas compared to that of a plain carbon electrode.[2] The Butler-Volmer equation, when the overpotentials are below $\pm$ 25mV, can be linearized as follows:

$$i \cong ai_o\left[\left(\alpha_a + \alpha_c\right)\left(\frac{F}{RT}\eta\right)\right] \cong \frac{ai_oFn}{RT}\eta \qquad [4.1]$$

where i is the electrode current density (in A/g), a is the active surface area (in cm^2/g), i_o is the exchange current density (A/cm^2), F is the Faraday constant, R is the gas constant (in J/mol.K), T is the temperature (in K), η is the overpotential (in V), n is the number of electrons, and α_a and α_c are the anodic and cathodic transfer coefficients.

A three-electrode arrangement shown in Figure 4.6 was used to perform the electrochemical analysis in a solution of 1M HBr and 0.1M Br$_2$. As shown in Figure 4.6, there are two electrode compartments connected by a salt bridge. The carbon electrode (both plain and MWCNT-based) and a saturated calomel electrode were used as the working (WE) and reference electrodes (RE) respectively. A platinum foil spot welded to a tantalum wire was used as the counter electrode and potassium bromide gelified with agar-agar (5% agar in 1M

KBr) was used in the salt bridge. The procedure for measuring the active surface area enhancement of MWCNT-based carbon electrodes is listed below.

1. Initially, the whole experimental setup was arranged as shown in Figure 4.6. The WE compartment was filled with 1M HBr solution and the CE compartment was filled with 1M sulfuric acid (H_2SO_4) solution.

2. The HBr solution was de-aired for 45 minutes and then the Teflon tube supplying the N_2 gas was pulled above the surface of the solution.

3. Subsequently, Br_2 was injected into the HBr solution present in the WE compartment. Once Br_2 solution was injected, it is crucial to maintain the N_2 gas blanket above the surface of the electrolyte for the rest of the experiment. The Br_2 solution has high vapor pressure and it will escape if N_2 gas is bubbled through the electrolyte. H_2 gas was bubbled through the H_2SO_4 solution in the CE compartment.

4. Multi-step chronoamperometry was then conducted with the applied overpotentials ranging between -12 mV and +12 mV. The linearized Butler-Volmer equation approach was used to calculate the product of specific active area (*a*) and exchange current density (i_o) of plain SGL 10AA and MWCNT-based carbon electrodes.

5. Finally, the solution resistance between working and reference electrode was measured using Electrochemical Impedance Spectroscopy (Gamry EIS 300, Amplitude: 5 mV and Frequency range: 0.1 Hz to 100 kHz).
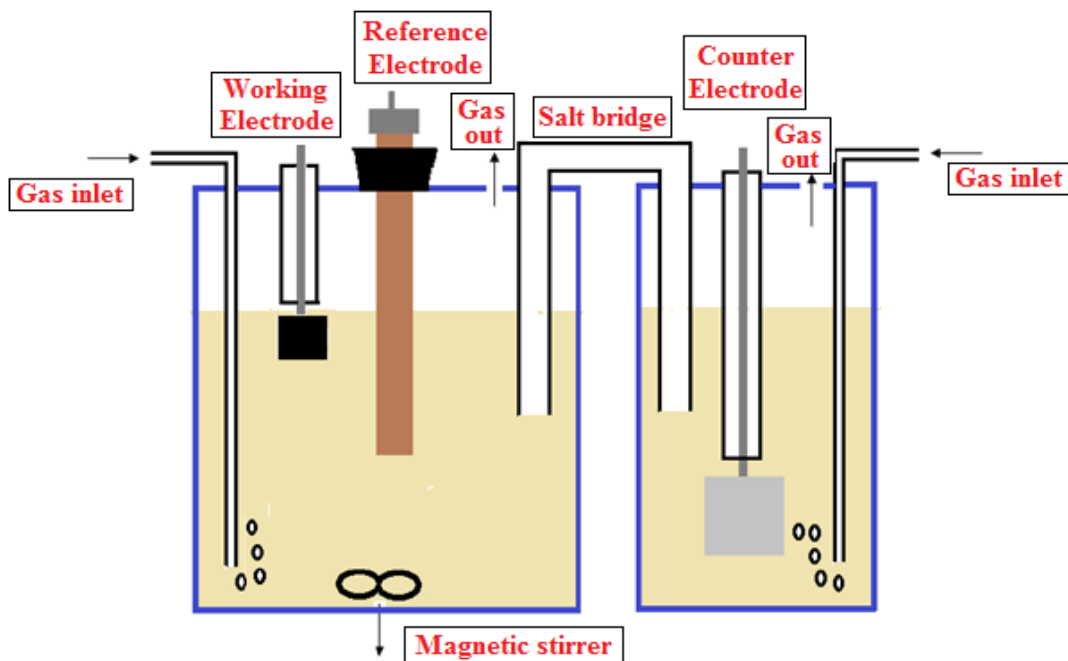
Figure 4.6. Three-electrode arrangement used to measure the active surface area

enhancement

The factor ai_o for all the MWCNT-based carbon electrodes were normalized to that of a plain

SGL 10AA carbon electrode to calculate the active surface area enhancement factors (see

Equation 4.2).

$$\text{Active surface area enhancement factor} = \frac{(ai_o)_{MWCNT}}{(ai_o)_{PLAIN}} \qquad [4.2]$$

4.5.3. Fuel Cell Measurements

The performance of a plain SGL 10AA (3 pieces of SGL 10AA stacked together) and a

MWCNT-based carbon electrodes (1 piece) was evaluated in a H_2-Br_2 fuel cell (1 cm^2 active

electrode area). The fuel cell configuration was similar to the one shown in Chapter 2 (section

2.2.1). An interdigitated graphite flow field plate was used on the H_2 side and traditional flow-through (1 cm distance between the channels) tantalum plate was used on the Br_2 side. The plain SGL 10AA carbon electrodes were boiled in DI water for 1 hour and then soaked and stored in 99.9% H_2SO_4 to improve their wetting characteristics and active area prior to the fuel cell study. A Pt catalyst coated SGL 25BC electrode obtained from TVN systems, Inc., was used as the H_2 electrode. The catalyst loading on the hydrogen electrodes was between 0.4 and 0.45 mg-Pt/cm^2. The Pt coated SGL 25 BC was hot pressed onto a Nafion 212 membrane (135°C for 5 minutes) and later boiled in DI water for 1 hour to enhance the membrane conductivity.[26] The MEA and the flow field plates were compressed between two aluminium end plates under a load of 1500 lbs. A mixture of 1M HBr and 0.9M Br_2 was recirculated through the Br_2 electrode at multiple flow rates (10 and 20 cc/min/cm^2). Humidified H_2 gas at a flow rate of 40 cc/min was pumped through the H_2 electrode and vented out at ambient pressure. All the fuel cell experiments were conducted at 25°C unless otherwise specified.

4.6 Results and Discussion

4.6.1. Constant vs. Pulse Current Electrodeposition

Figure 4.7 shows the schematics for constant and pulse current electrodeposition. A constant current for the required amount of time was applied while implementing the constant current electrodeposition technique whereas current was applied in short time intervals while implementing the pulse current electrodeposition technique. During pulse electrodeposition process, the pulse duration is usually fixed between 0.1 and 10 seconds with a short time gap (1-2 minutes) between the consecutive pulses.[27] The time gap allows the solution concentration near the electrode/electrolyte interface to be replenished.
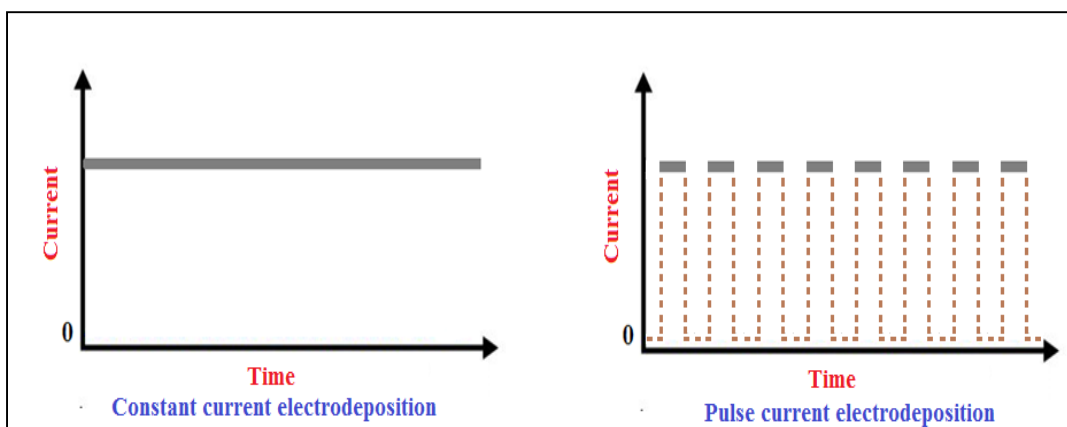
Figure 4.7. Constant and pulse current electrodeposition techniques

4.6.2. Nucleation and Growth of Co Nanoparticles

The Co electrodeposition occurs in two steps: nucleation and growth.[29] The first step is nucleation where nuclei or seeds were formed, which initiates the growth of Co nanoparticles. As soon as nuclei were formed, growth occurs simultaneously. At this stage, the nucleation and growth processes are inseparable. The nucleation process stops once the concentration at the carbon electrode/electrolyte interface of the reactant species drops below the minimum concentration (or minimum critical supersaturation level) required for nucleation and subsequently growth process was initiated. The size and distribution of Co nanoparticles are determined by both nucleation and growth rates. A nonuniform size distribution of nanoparticles will be observed if nucleation and growth processes occur simultaneously (also known as progressive nucleation). On the other hand, uniform size distribution of Co nanoparticles will be seen if the growth process proceeds without the interference of nucleation process (also known as instantaneous nucleation).[29-31] It is preferable to have instantaneous nucleation during the electrodeposition process. Depending on the magnitude of the cathodic

133

current applied on the working electrode (WE), the Co nanoparticle deposition might occur in either kinetic or transport controlled regimes.

While depositing Co nanocatalyst under kinetically controlled regime (low cathodic currents), the growth rate is controlled by surface process since the concentration difference of reactant species in the bulk and the carbon electrode/electrolyte interface is negligible. The surface process occurs through two different growth mechanisms: mononuclear growth and poly-nuclear growth. The electrodeposition of Co proceeds layer by layer in the case of mononuclear growth. The second layer growth begins only after the first layer growth is accomplished. This allows enough time for the growth species to diffuse on the electrode surface. In the case of poly-nuclear growth, the second layer growth occurs before the growth of first layer is finished.[29-31] The surface concentration should be high enough for this mechanism to take place. In conclusion, the duration of electrodeposition must be carefully controlled to avoid a dense layer of Co when operating under kinetically controlled regime.

The concentration of the Co ions at the carbon electrode/electrolyte interface is quickly depleted while electrodepositing Co under mass transport controlled regime (high cathodic currents). The growth process is controlled by the diffusion of Co species from the bulk to the carbon electrode surface. In this case, the nucleation process does not interfere with the growth process (instantaneous nucleation). Hence, there is a high probability of electrodepositing Co nanoparticles with uniform size while operating under mass transport controlled regime.[29,30] However, hydrogen evolution reaction might occur simultaneously with the Co electrodeposition, when high cathodic currents are applied.

4.6.3. Electrodeposition of Co Nanoparticles

In this study, the electrodeposition of Co on the first two carbon electrode samples (1 and 2) was done using the constant current technique. As described in the experimental section, a low current density of -0.1 mA/cm^2 was applied to both samples. The small current ensures slow Co electrodeposition rate and hence provides the best chance to form dense Co layer formation. The time spans of electrodeposition for samples 1 and 2 were 1000 s and 2000 s respectively. Figure 4.8 shows SEM images of samples 1 and 2.
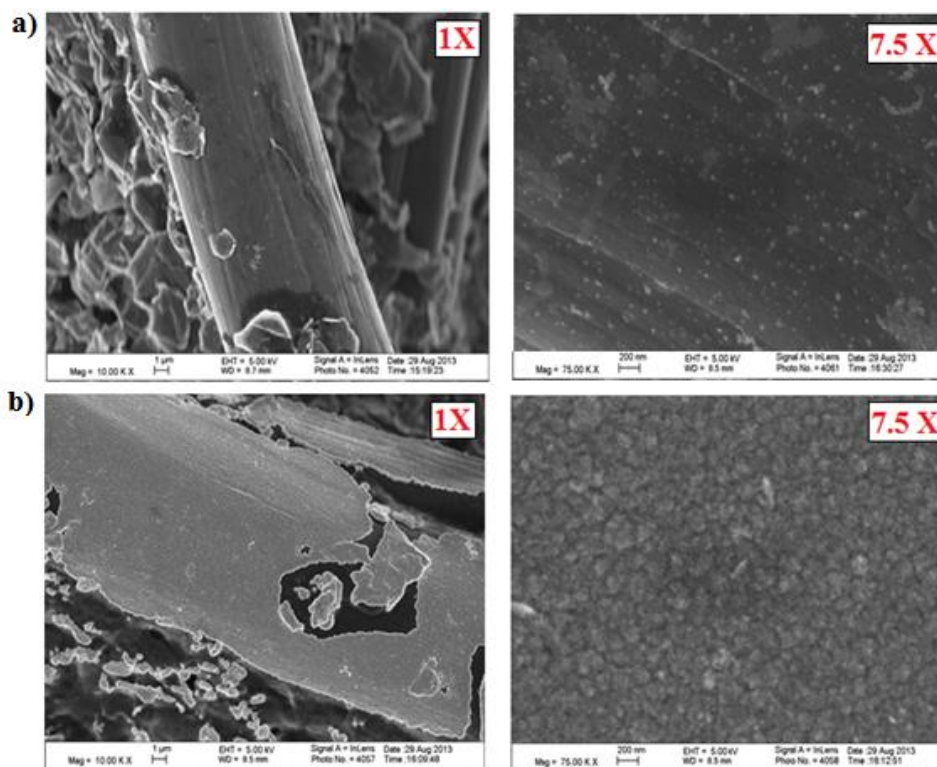
Figure 4.8. Samples obtained after constant current electrodeposition (a. sample 1: -0.1 mA/cm^2 for 1000s and b. sample 2: -0.1 mA/cm^2 for 2000s)

As shown in Figure 4.8, samples 1 and 2 obtained from constant current electrodeposition has a uniform layer of Co on the carbon fiber surface. The Co layer thickens as the span of

electrodeposition increases from 1000 to 2000 s. Also, EDX analysis confirms the growth of cobalt (shown in Figure 4.9). The Co peak can be clearly seen in the carbon electrode sample obtained after electrodeposition. The results show that the constant current method is not suitable for growing Co nanoparticles. So, the rest of the samples (3, 4, and 5) were synthesized using pulse current deposition. High cathodic current densities with short duration pulses were used to deposit Co nanocatalyst in this study. The high current densities applied to the carbon electrode forces the Co electrodeposition to occur close to the mass transport controlled regime. The growth process was controlled by diffusion of Co species from the bulk to the electrode surface. The deposition current, pulse duration, and number of pulses specified in the experimental section were used to control the particle size, density, and uniformity.
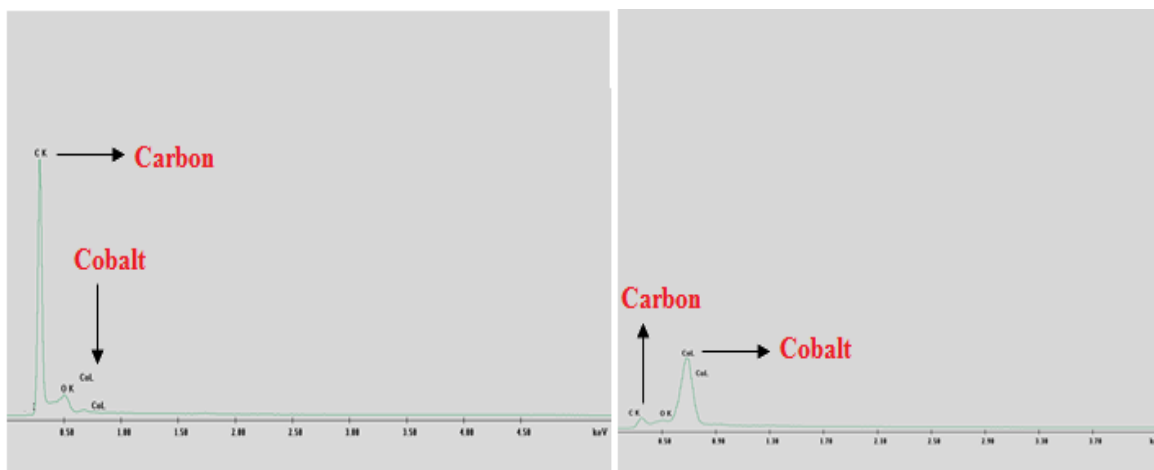
Figure 4.9. EDX images of Plain SGL 10AA (left) and sample1 (-0.1 mA/cm^2 for 1000s)

Figure 4.10 shows the SEM images of samples 3 and 4. The Co nanoparticles with reasonably close packing can be clearly seen in Figure 4.10. As explained in the previous section, electrodeposition under diffusion controlled regime might result in the formation of nanoparticles. The high cathodic current density applied to the carbon electrode results in high

nucleation rate and the short duration pulses limit the growth of nanoparticles. Also, Co

nanoparticles with uniform size distribution were obtained as seen in Figure 4.10. Finally, the

large diameter nanoparticles seen in sample 4.10a was a result of longer electrodeposition

duration (1s, diameter: 70 nm-100 nm) compared to that in sample 4.10b (0.2s, diameter: 40

nm-60 nm).
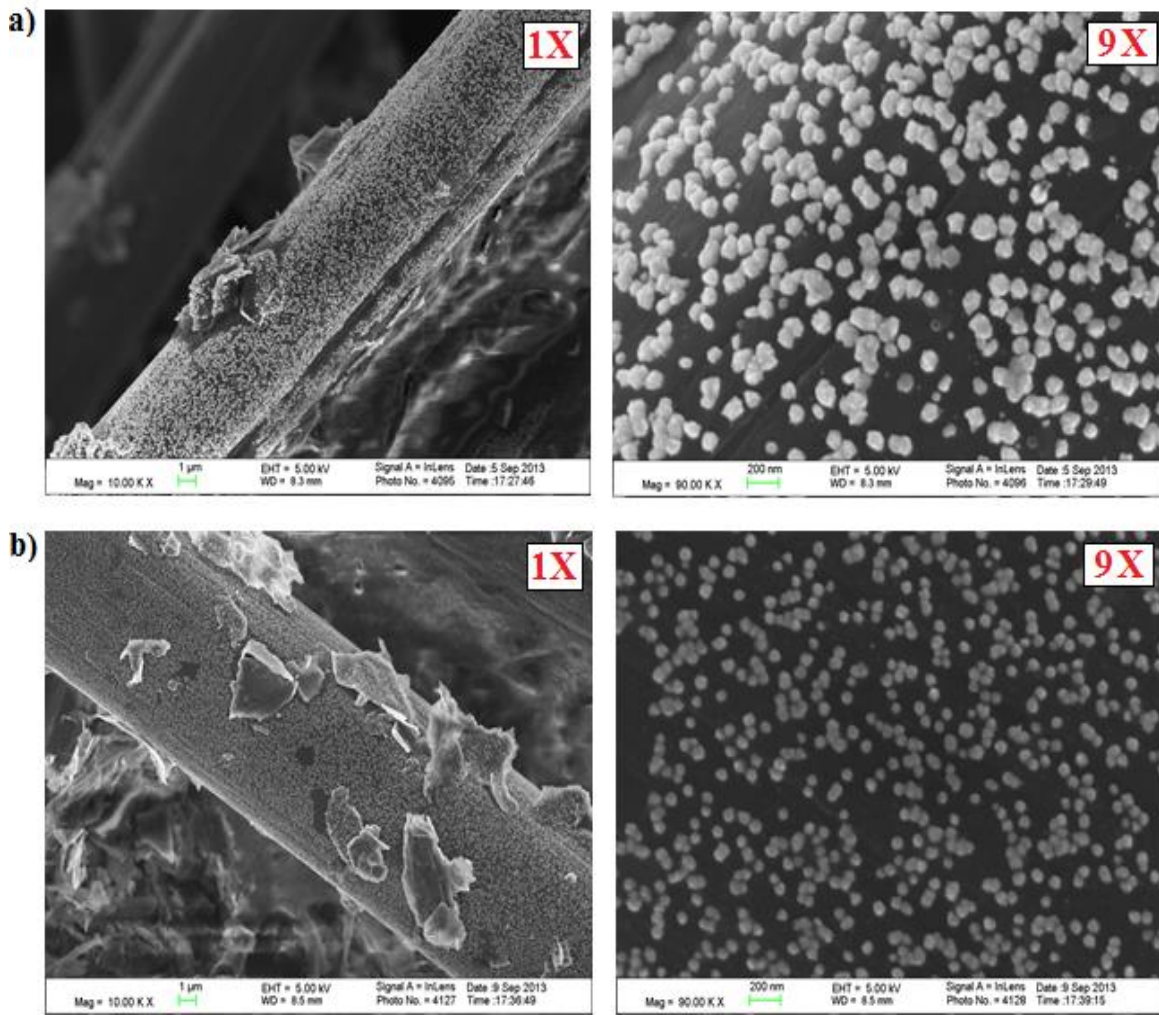
Figure 4.10. Pulse current electrodeposition a) sample 3: -3.75 mA/cm^2 for 1s (single pulse

of 1s duration) and b) sample 4: -5 mA/cm^2 for 0.2s (two pulses each of 0.1s duration

4.6.4. Effect of Pre-soaking on the Electrodeposition of Co Nanoparticles

In this case study, the effect of soaking the carbon electrodes in an electrolyte solution (mixture of $CoSO_4$ and H_3BO_3) on the Co electrodeposition was examined. The soaking step was included after boiling them in DI water and before proceeding to the electrodeposition experiment. The concentration of the electrolyte solution that carbon electrodes were soaked in was same as the one used in the electrodeposition step. The purpose of the pre-soaking step was to enhance the electrodeposition of Co nanoparticles inside the carbon electrode by saturating it with the electrolyte solution (mixture of $CoSO_4$ and H_3BO_3). Samples 4b and 5 were synthesized with the addition of the pre-soaking step. The magnitude of charge applied to synthesize sample 4b was similar to the one applied to obtain sample 4 (-5 mA/cm^2 for 0.2 s), but with the addition of a pre-soaking step. To reduce the size of Co nanoparticles seen in sample 3 (Figure 4.10a), a cathodic current density of -2.5 mA/cm^2 was applied for 1 s to synthesize sample 5. The total charge densities used to synthesize samples 4b and 4 were 1 mC/cm^2 and 2.5 mC/cm^2 respectively. As shown in Figure 4.11, the density of Co nanoparticle distribution in sample 5 is higher compared to that of sample 4b. This can be attributed to the higher charge density used to synthesize sample 5.

Figure 4.11 shows the SEM images of samples 4b and 5 at different resolutions. As explained earlier, samples 4 and 4b were synthesized using similar electrodeposition conditions (Figures 4.10b and 4.11a). The pre-soaking step assists in saturating a large section of the electrode surface area of sample 4b with $CoSO_4$ and thereby improving the uniformity and the extent of Co electrodeposition. As a result, Co nanoparticles with smaller diameter were electrodeposited throughout the bulk volume of the sample 4b (Figure 4.11a). The Co nanoparticle distribution appears to be denser for both samples 4b and 5 (Figures 4.11a and

4.11b). The carbon electrodes with a dense distribution of small Co nanoparticles (Sample 5) were expected to be the ideal candidates for MWCNT growth. Also, the effect of the presoaking step will be discussed further in the electrochemical analysis section. In conclusion, pulse current electrodeposition appears to be an optimal choice to promote dense distribution of Co nanoparticles.
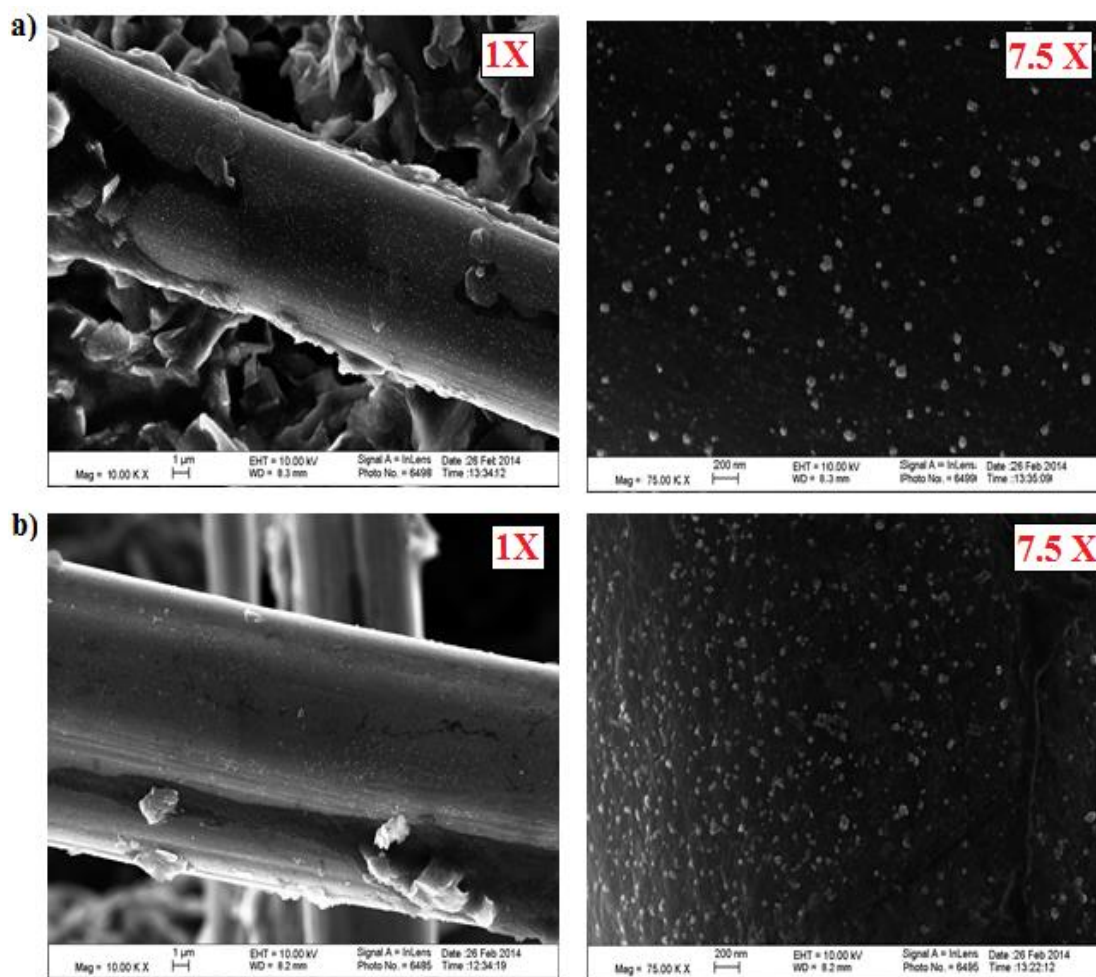
Figure 4.11. Pulse current electrodeposition with the inclusion of presoaking step

a) sample 4b (resynthesized) -5 mA/cm^2 for 0.2s (two pulses each of 0.1s duration) and

b) sample 5: -2.5 mA/cm^2 for 1s (single pulse of 1s duration)

4.6.5. MWCNT Growth Using CVD Process

The carbon electrodes with electrodeposited Co (samples 1 to 5) were then placed in a quartz tube furnace to facilitate MWCNT growth using the CVD process described in the experimental section. The MWCNT growth occurs (or proceeds) according to two different growth models. Figure 7 shows the tip and base models associated with the MWCNT growth.[32] According to the tip model, the hydrocarbon gas reacts at the Co nanoparticle and the carbon substrate interface and lifts the Co nanoparticle simultaneously with the growth of the MWCNT. In this model, the MWCNT is covalently bonded to the carbon fiber matrix. On the other hand, the MWCNT grows on top of the nanoparticle according to the base model. The major disadvantage associated with MWCNTs grown in accordance with the base model is that the nanotubes are lost once the electrodes are exposed to a corrosive acid environment. Therefore, the tip model is the preferred growth mechanism because the nanotubes are directly bonded to the carbon electrode fiber surface.
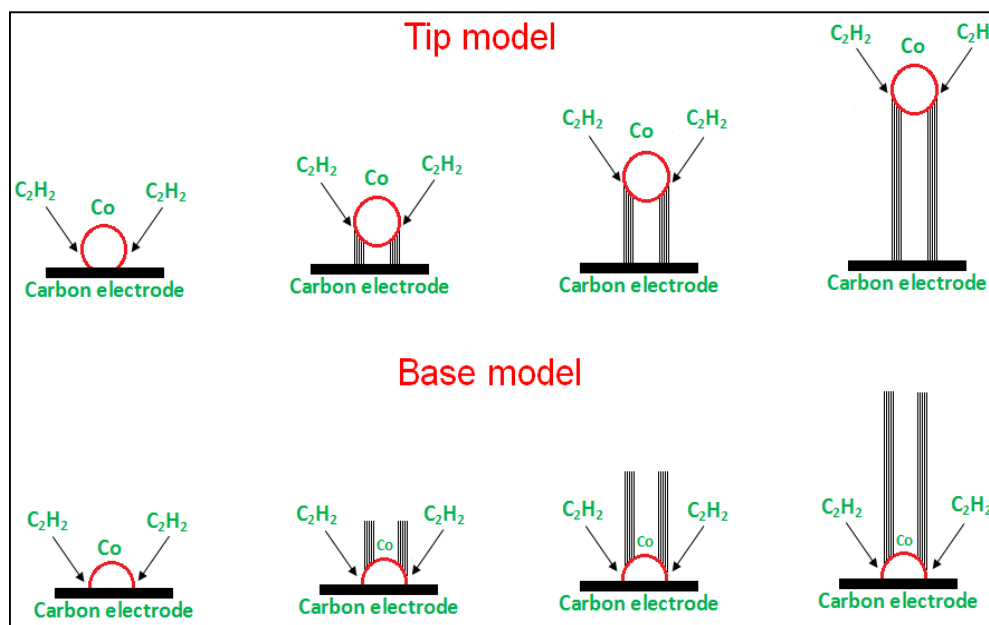
Figure 4.12. Tip and base models explaining the mechanism of MWCNT growth[32]

The SEM images of MWCNT-based carbon electrodes post DI water sonication and acid treatment are shown in Figure 4.13. As shown in Figure 4.13, the MWCNTs still remain on all the carbon electrodes except for sample 2 (Figure 4.13b), which indicates that the dominant growth mechanism was based on the tip model. The Co layer on sample 2 (-0.1 mA/cm^2 for 2000s, as shown in Figure 4.12b) was too dense and covers most of carbon substrate surface rendering it inaccessible to the hydrocarbon gas.

Figure 4.14 shows the SEM images of sample 2 before and after undergoing DI water sonication and acid pre-treatment. The carbon nanotubes were completely lost after the acid pre-treatment step. This indicates that the MWCNTs might have grown on the top of the Co nanoparticles in sample 2.[32] As a result, the MWCNTs may have come loose once the Co nanoparticles underneath them have been etched away during the acid pre-treatment. The diameter of the MWCNTs grown on these samples was between 70 nm and 100 nm.

The effect of pre-soaking the electrodes in a mixture of $CoSO_4$ and H_3BO_3 prior to electrodeposition on the uniformity of MWCNT growth can be clearly seen by comparing Figures 4.13 and 4.15. The MWCNT growth on the carbon fibers was more uniform and denser in the pre-soaked electrodes (shown in Figure 4.15). The pre-soaking step saturates a larger portion of the carbon electrode fiber surface area, thereby improving the uniformity of Co electrodeposition and consequently the MWCNT growth. The diameter of the MWCNTs in the pre-soaked electrodes (sample 4b and sample 5) is smaller compared to the rest of the samples (sample 1, sample 3, and sample 4), which is consistent with the electrodeposition results. The diameter of the MWCNTs in the pre-soaked electrodes was between 40 nm and 70 nm. As shown in Figure 4.13, the MWCNT growth was accomplished only on the surface for samples 1, 3, and 4. On the other hand, the MWCNTs were successfully grown beneath the

electrode surface in the case of pre-soaked electrodes. This highlights the advantage of pre-soaking the carbon electrodes in $CoSO_4$ and H_3BO_3 before electrodepositing Co nanoparticles.
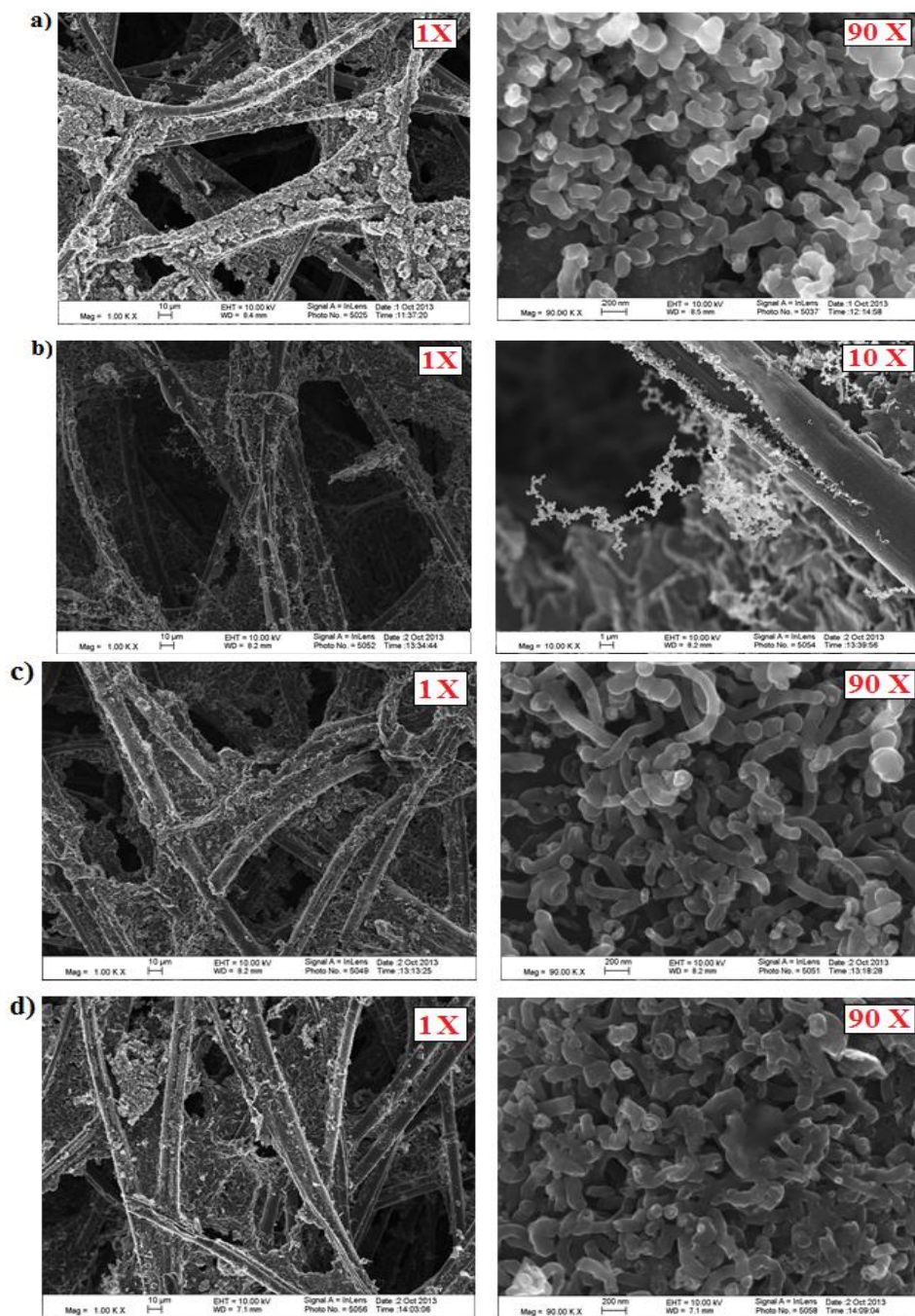
Figure 4.13. Carbon electrodes with MWCNT growth post DI water sonication and acid treatment a) sample 1, b) sample 2, c) sample 3, and d) sample 4
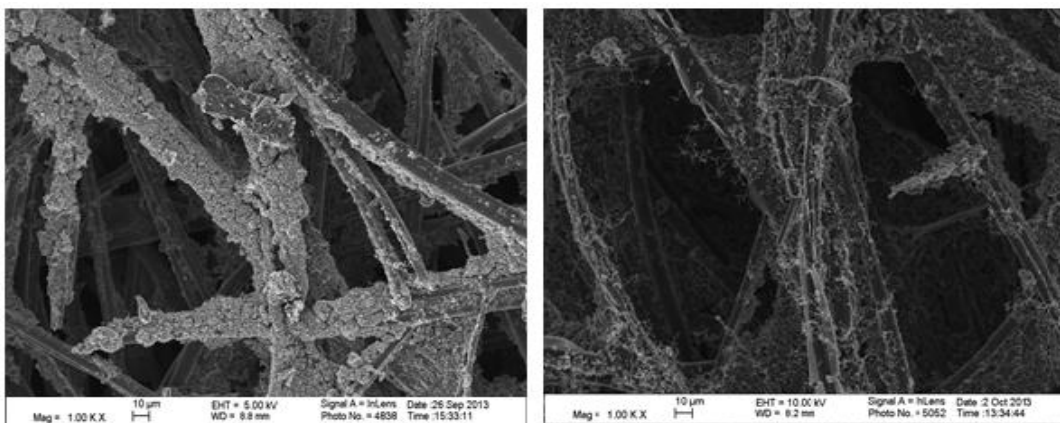
Figure 4.14. Sample 2 before (left image) and after DI water sonication and acid treatment

(right image)
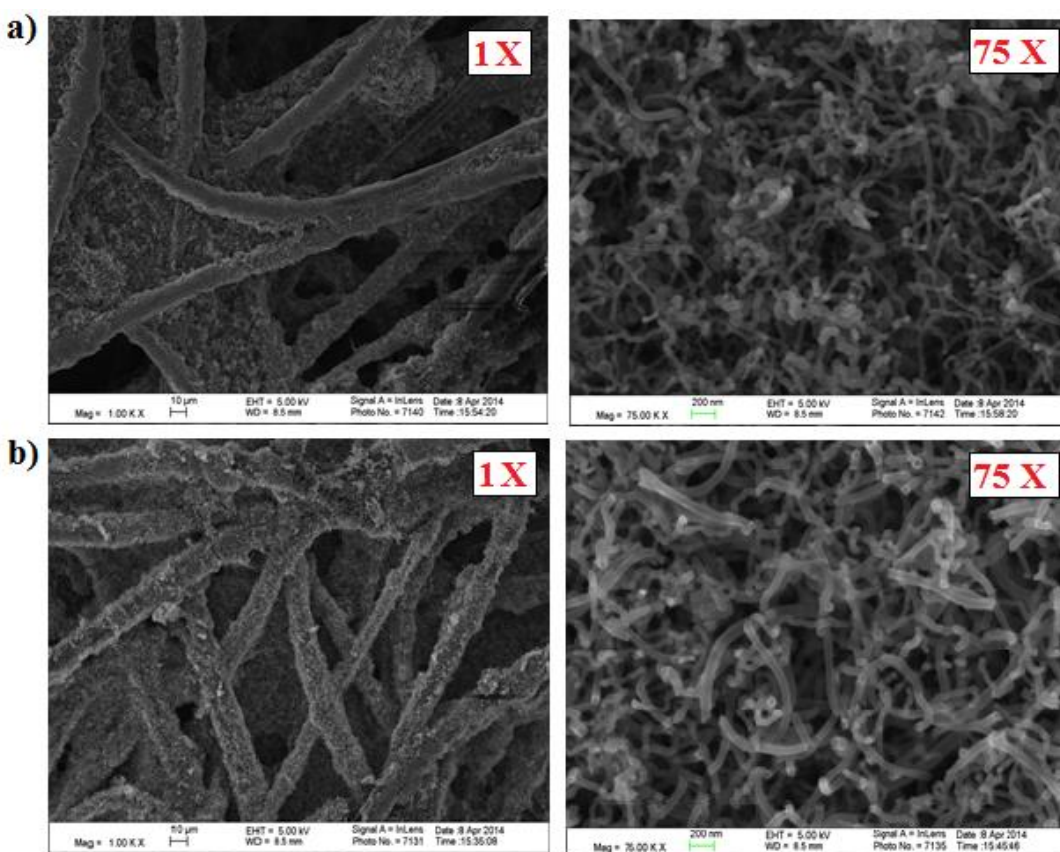
Figure 4.15. Pre-soaked carbon electrodes (in $CoSO_4$ and H_3BO_3) after MWCNT growth

a) sample 4b and b) sample 5

In order to confirm the growth mechanism of MWCNTs, Transmission Electron Microscopy (TEM) analysis was conducted. Figure 4.16 shows the TEM and EDX images of MWCNTs grown on the carbon electrode samples. The carbon nanotubes were scraped using a X-ACTO knife and dissolved in ethanol. The ethanol solution containing the MWCNTs was then analyzed using TEM. The Co nanoparticles trapped inside the MWCNTs were detected using Scanning Transmission Electron Microscopy–Energy Dispersive X-ray Spectroscopy (STEM-EDX) as shown in Figure 4.16a.
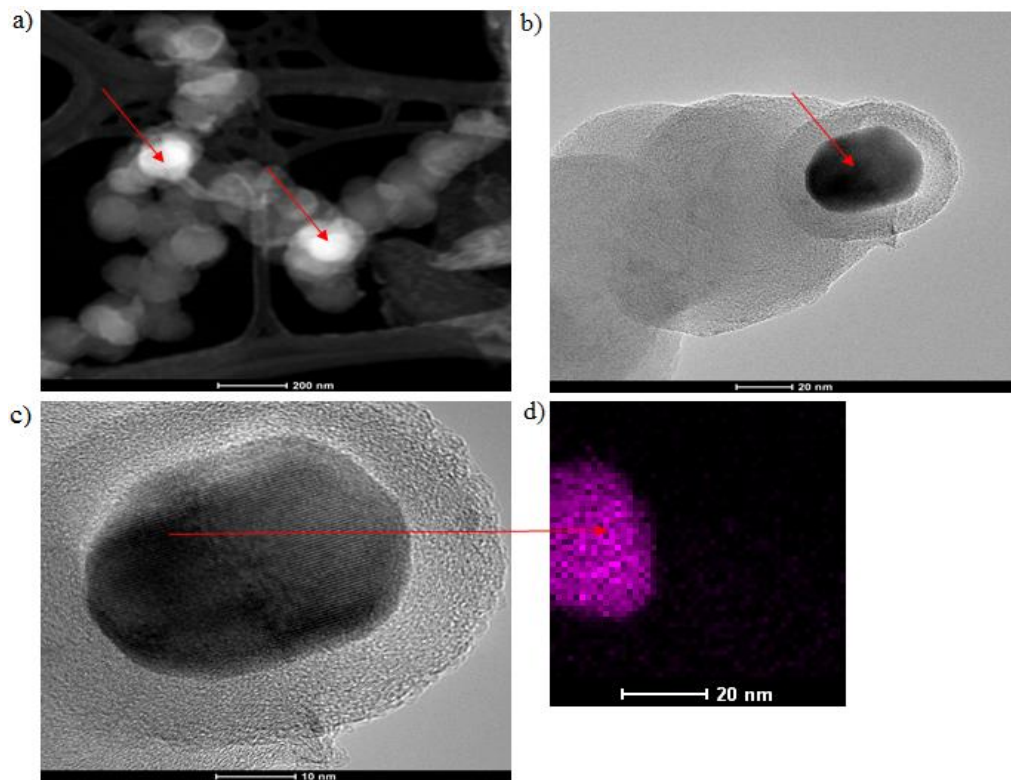
Figure 4.16. TEM images to understand the mechanism of MWCNT growth a) STEM image showing Co nanoparticles trapped inside the MWCNTs, b) TEM image showing a MWCNT, c) TEM image showing multi-walls of the CNT, and d) TEM-EDX analysis confirming the Co nanoparticle at the tip of the MWCNT

The Co nanoparticles propagate through the MWCNTs as they grow according to the tip model. The Co nanoparticles trapped inside the MWCNTs are shown in Figure 4.16a (see the red arrows). Also, Figures 4.16b and 4.16c clearly show the multiple walls of the carbon nanotube. Finally, the EDX analysis confirmed that the Co nanoparticle is situated at the tip of the nanotube as shown in Figure 4.16d.

Finally, SEM analysis was done on the carbon electrode regions next to the stainless steel alligator clips (Figure 4.17a) as well as the regions 2 cm away (Figure 4.17b) from them while conducting the electrodeposition process. The aim of this study was to determine the efficiency of the stainless steel alligator clips as current collectors. As shown in Figure 4.17, the limitation associated with using stainless steel alligator clips as current collectors was the non-uniform MWCNT growth on the carbon electrode fiber surface located far from them (seen in Figure 4.17b). The electronic resistance of the carbon electrode prevented the charge from being delivered uniformly over the entire carbon electrode fiber surface. This effect would be more pronounced when the carbon electrodes with large geometric area were used. In the next chapter, current collectors that aid in uniform electrodeposition and MWCNT growth over the entire carbon electrode fiber surface area will be discussed. Note that all the samples analyzed in the previous sections were taken from the regions close to the stainless steel alligator clips.
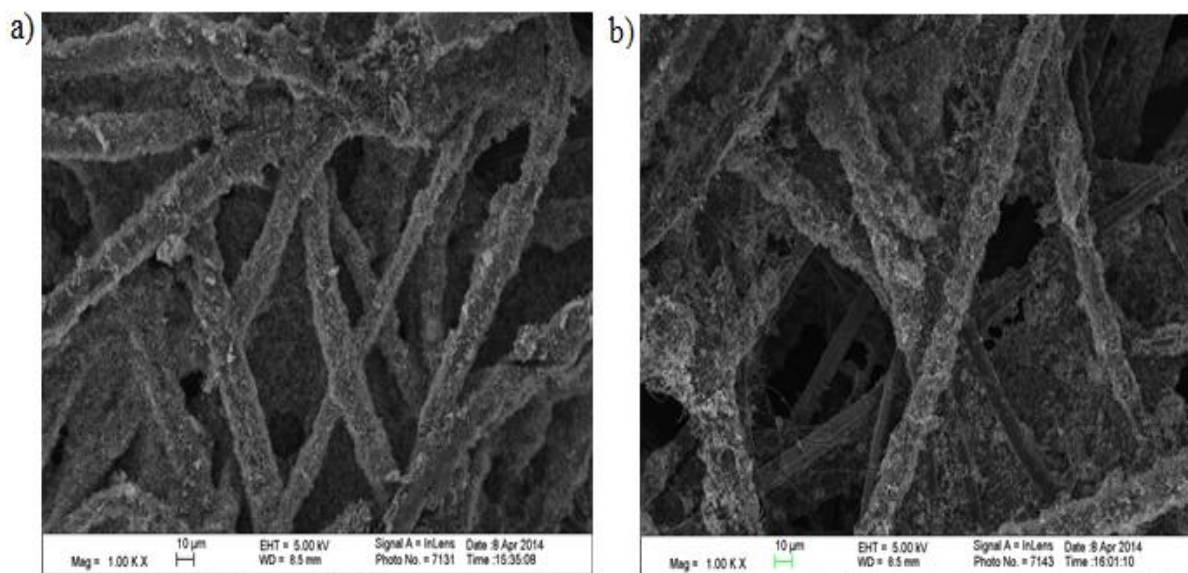
Figure 4.17. SEM images showing the limitation of using alligator clips as current collectors a) SEM image of the carbon electrode close to the alligator clip and b) SEM image of the carbon electrode 2 cm from the tip of the alligator clip

4.6.6. Active Surface Area Enhancement Measurements

The enhancement factors of the MWCNT-based carbon electrodes were measured using a three-electrode arrangement as described in the experimental section. Figures 4.18 and 4.19 show the multi-step chronoamperometry plot of plain SGL 10AA and MWCNT-based carbon electrodes. The overpotentials in Figures 4.18 and 4.19 were corrected for ohmic loss. The product of the active surface area (a) and exchange current density (i_o) was calculated from the slope $\left(\frac{di}{d\eta}\right)$ of the multi-step chronoamperometry plot. The factor ai_o for all the electrodes were normalized to the value of a plain SGL 10AA carbon electrode to calculate the enhancement factors (using equation 4.2). Even though the exchange current density of carbon GDL may be different from that of MWCNTs, it is the product of active area and exchange current density that contributes to the total active surface area enhancement.
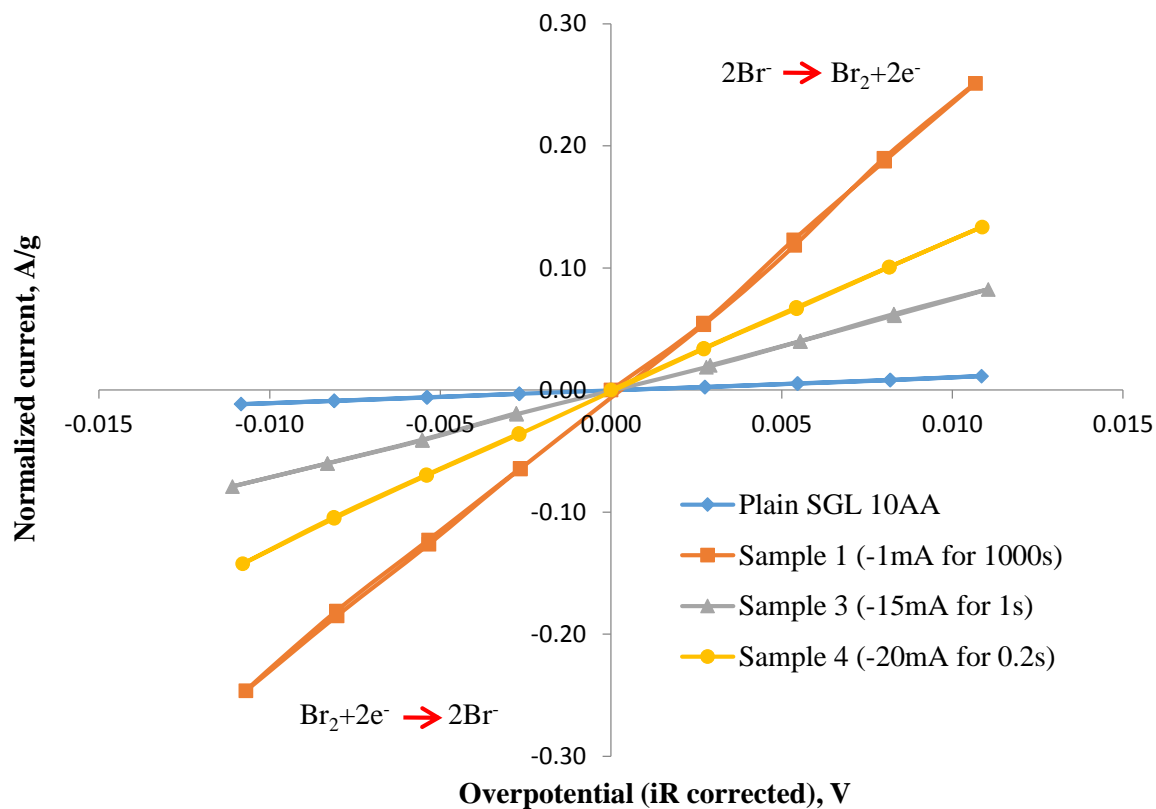
Figure 4.18. Electrochemical analysis of MWCNT-based electrodes in a three electrode arrangement to measure the active area enhancement factors (samples 1, 3, and 4)

Table 4.1. Enhancement factor measurements

Specimen	Active area enhancement factor
Sample 1	22
Sample 3	7
Sample 4	11
Sample 4b	17
Sample 5	50
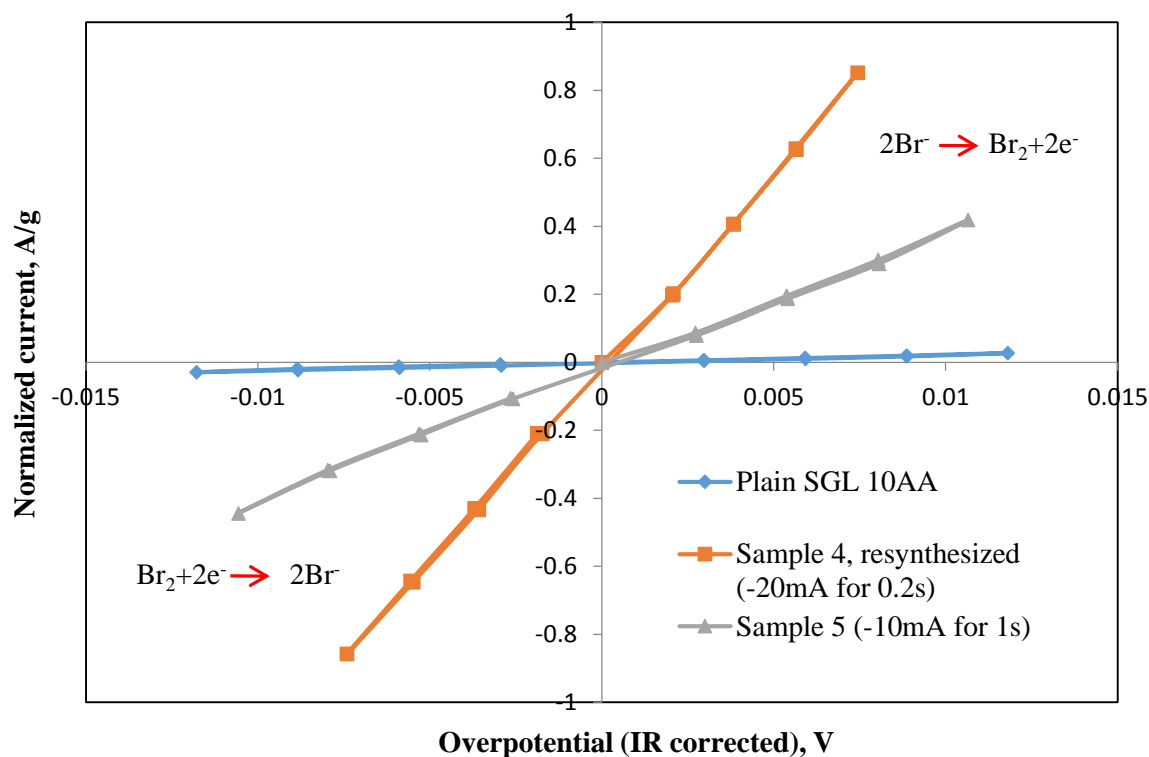
Figure 4.19. Electrochemical analysis of MWCNT-based carbon electrodes (presoaked in CoSO$_4$ and H$_3$BO$_3$ prior to electrodeposition) in a three electrode arrangement to measure active surface area enhancement factors (sample 4b, and sample 5)

As shown in Table 4.1, enhancement factors between 7 and 50 were achieved by using the MWCNT-based carbon electrodes (samples 1, 3, 4, and 5). Also, the enhancement factor of sample 4 (-20 mA for 0.2s, 2 pulses each of 0.1s duration) was improved (enhancement factor increases from 11 to 17) upon presoaking it in a solution of CoSO$_4$ and H$_3$BO$_3$ prior to electrodeposition. This may be a result of uniform Co nanoparticle deposition over a large carbon electrode fiber surface area in the pre-soaked sample. Also, an enhancement factor of 50 was achieved with sample 5 (-10mA for 1s, 1pulse of 1s duration). The smaller nanoparticle

size with dense distribution observed in the SEM images of sample 5 may have contributed to this significant active area enhancement.

4.6.7. Fuel Cell Measurements

Finally, the performance of the MWCNT-based carbon electrode (sample 5) was measured in a H_2-Br_2 fuel cell to determine its effectiveness. As shown in Figure 4.20, the discharge performance of a MWCNT electrode (1 layer) was almost equal or slightly higher compared to that of the plain SGL 10 AA electrode (3 layers) at a lower flow rate (10 cc/min/cm^2 used for MWCNT electrode vs 20 cc/min/cm^2 used for 3 piece SGL 10AA).
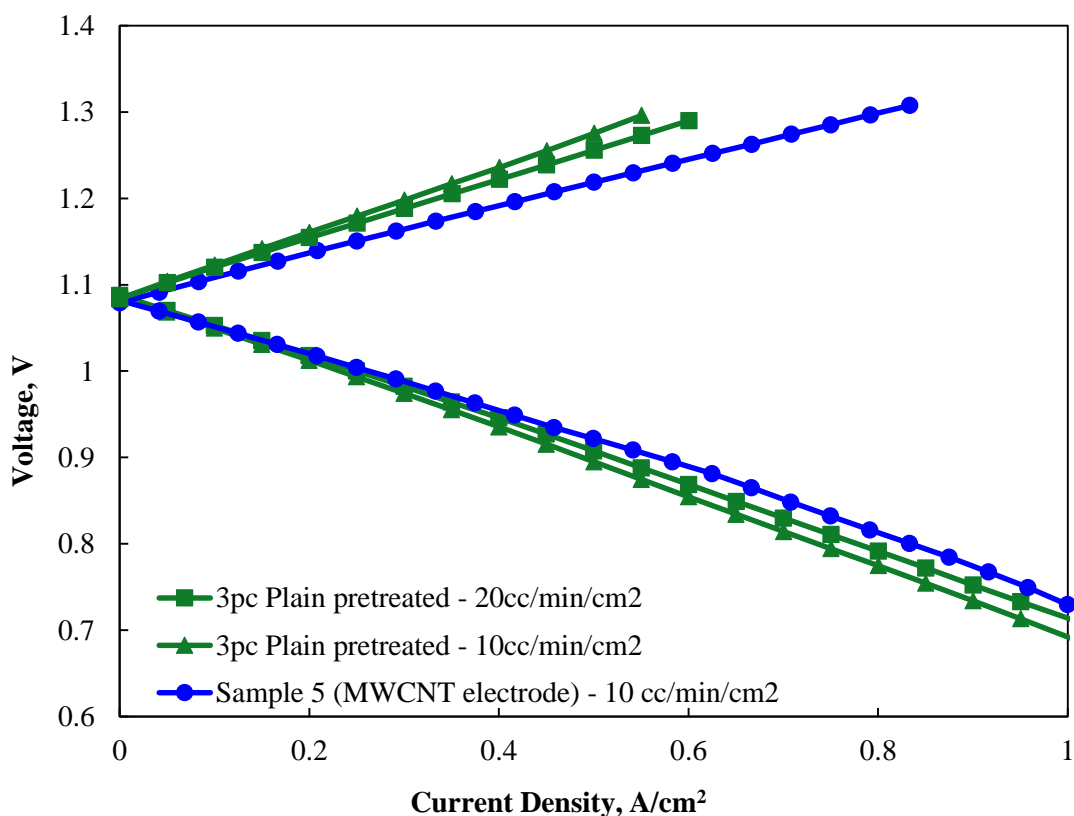
Figure 4.20. Performance comparison between 3 layers of plain SGL 10AA and sample 5 (MWCNT electrode) in an actual H_2-Br_2 fuel cell

A single layer of MWCNT electrode was not only able to provide sufficient surface area for bromine reactions but also reduced the mass-transport distance since its thickness was only one-third compared to that of the 3 layers of plain SGL 10AA electrodes. The preliminary performance of the MWCNT electrode looks very promising for future studies. The bromine electrode cost could be reduced by employing a single MWCNT electrode instead of using multiple layers of plain carbon electrodes. Also, both bromine electrode and pumping costs may be reduced by employing a MWCNT electrode with lower electrolyte flow rate instead of using multiple layers of plain carbon electrodes with higher electrolyte flow rate. The optimization of the electrodeposition and CVD processes to enhance the performance of the MWCNT-based carbon electrodes will be discussed in the next chapter.

4.7. Conclusions

The widely used commercial plain porous carbon electrodes for Br_2 reactions have low specific surface areas. In this section, a preliminary study regarding the growth of MWCNTs directly on the carbon electrode fiber surface to improve the active surface area of conventionally used plain SGL 10AA carbon electrodes was discussed. The Co catalyst nanoparticles were electrodeposited using both constant and pulse current electrodeposition techniques. Subsequently, the Co-catalyzed MWCNT growth was accomplished using the CVD process. The pre-soaking of carbon electrodes in a mixture of $CoSO_4$ and H_3BO_3 prior to electrodeposition led to more uniform Co nanoparticle deposition and MWCNT growth over a larger portion of the carbon electrode fiber surface area. Active area enhancement factors between 7 and 50 were achieved using these MWCNT-based carbon electrodes. Finally, the performance of a MWCNT-based carbon electrode (active surface area enhancement factor of 50) in a H_2-Br_2 fuel cell was found to be equal or slightly better compared to using 3 layers of

plain SGL 10AA as the Br_2 electrode. In conclusion, the preliminary performance of a MWCNT electrode is promising and is expected to reduce the stack cost of H_2-Br_2 fuel cells and other flow batteries that utilize porous carbon media as electrodes.

4.8 References

1. Che-Nan Sun, F. M. Delnick, D. S. Aaron, A. B. Papandrew, M. M. Mench, and T. A. Zawodzinski, "Probing Electrode Losses in All-Vanadium Redox Flow Batteries with Impedance Spectroscopy," *ECS Electrochemistry Letters*, **2** (5), A43-A45 (2013).

2. Haley Kreutzer, Venkata Yarlagadda, and Trung Van Nguyen, "Performance Evaluation of a Regenerative Hydrogen-Bromine Fuel Cell," *J. Electrochem Soc.*, **159** (7), F331-F337 (2012).

3. Kyu Taek Cho, Paul Ridgeway, Adam Z. Weber, Sophia Haussener, Vincent Battagalia, and Venkat Srinivasan, "High Performance Hydrogen/Bromine Flow Battery Redox Flow Battery for Grid-Scale Energy Storage," *J. Electrochem. Soc.*, **159** (11), A1806-A1815 (2012).

4. Michael C. Tucker, Kyu Taek Cho, Adam Z. Weber, Guangyu Lin, and Trung Van Nguyen, "Optimization of electrode characteristics for the Br_2/H_2 redox flow cell," *J. Appl. Electrochem.*, **45**, 11 (2015).

5. Venkata Yarlagadda and Trung Van Nguyen, "A 1D Mathematical Model of a H_2/Br_2 fuel cell," *J. Electrochem Soc.*, **160** (6), F535-F547 (2013).

6. Sasha Stankovich, Dmitriy A. Dikin, Richard D. Piner, Kevin A. Kohlhaas, Alfred Kleinhammes, Yuanyuan Jia, Yue Wu, SonhBinh T. Nguyen, and Rodney S. Ruoff, "Synthesis of graphene-based nanosheets via chemical reduction of exfoliated graphite oxide," *Carbon*, **45**, 1558-1565 (2007).

7. Yunpu Zhai, Yuqian Dou, Dongyuan Zhao, Pasquale F. Fulvio, Richard T. Mayes, and Sheng Dai, "Carbon Materials for Chemical Capacitive Energy Storage," *Adv. Mater.*, **23**, 4828-4850 (2011).

8. Byungwoo Kim, Haegeun Chung, and Woong Kim, "Supergrowth of Aligned Carbon Nanotubes Directly on Carbon Papers and Their Properties as Supercapacitors," *J. Phys. Chem. C.*, **114**, 15223 (2010).

9. D. Tashima, A. Sakamoto, M. Taniguchi, T. Sakoda, M. Otsubo, "Surface modification of carbon electrodes using an argon plasma," *Vacuum,* **83** (3), 695-698 (2009).

10. Chang Ma, Yajuan Li, Jingli Shi, Yan Song, and Lang Liu, "High-performance supercapacitor electrodes based on porous flexible carbon nanofiber paper treated by surface chemical etching," *Chemical Engineering Journal,* **249**, 216-225 (2014).

11. I. Mayrhuber, C.R. Dennison, V. Kalra, and E.C. Kumbur, "Laser-perforated carbon paper electrodes for improved mass-transport in high power density vanadium redox flow batteries," *J. Power Sources*, **260**, 251-258 (2014).

12. Scott Calabrese Barton, Yuhao Sun, Bhupesh Chandra, Sean White, and James Hone, "Mediated Enzyme Electrodes with Combined Micro- and Nanoscale Supports," *Electrochemical and Solid-State Letters*, **10** (5), B96-B100 (2007).

13. Cheng Wang, Mahesh Waje, Xin Wang, Jason M. Tang, Robert C. Haddon, and Yushan Yan, "Proton Exchange Membrane Fuel Cells with Carbon Nanotube-Based Electrodes," *Nano Letters*, **4** (2), 345-348 (2004).

14. Chunyu Du, BaorongWang, and Xinqun Cheng, "Hierarchy carbon paper for the gas diffusion layer of proton exchange membrane fuel cells," *J. Power Sources*, **187**, 505-508 (2009).

15. S. Ijima, "Helical microtubules of graphitic carbon," *Nature*, **354**, 56-58 (1991).

16. Jan Prasek, Jana Drbohlavova, Jana Chomoucka, Jaromir Hubalek, Ondrej Jasek, Vojtech Adam, and Rene Kizek, "Methods for carbon nanotubes synthesis-review," *J. Mater. Chem.*, **21**, 15872-15884 (2011).

17. Niraj Sinha and John T.-W. Yeow, "Carbon Nanotubes for Biomedical Applications," *IEEE Transactions on Nanobioscience*, **4** (2), 180-195 (2005).

18. Hongjie Dai, "Carbon Nanotubes: Synthesis, Integration, and Properties," *Acc. Chem. Res.*, **35**, 1035-1044 (2002).

19. Muhammad Musaddique Ali Rafique, and Javed Iqbal, "Production of Carbon Nanotubes by Different Routes-A Review," *Journal of Encapsulation and Adsorption Sciences*, **1**, 29-34 (2011).

20. Ba Thang Nguyen, Xuan Tinh Than, Van Chuc Nguyen, Thi Thanh Tam Ngo, Hung Thang Bui, Xuan Nghia Nguyen, Hong Khoi Phan, and Ngoc Minh Phan, "Fabrication of horizontally aligned ultra-long single-walled carbon nanotubes of Si substrates using the fast-heating chemical vapor deposition method," *Adv. Nat. Sci: Nanosci. Nanotechnol*, **3**, article id: 025010 (2012).

21. Jean-Philippe Tessonnier and Dang Sheng Su, "Recent Progress on the Growth Mechanism of Carbon Nanotubes: A Review," *ChemSusChem*, **4** (7), 824-847 (2011).

22. Chien-Te Hsieh, Hsisheng Teng, Wei-Yu Chen, and Yu-Shun Cheng, "Synthesis, characterization, and electrochemical capacitance of amino-functionalized carbon nanotube/carbon paper electrodes," *Carbon*, **48**, 4219-4229 (2010).

23. Zhi Yang, Xiaohua Chen, Huagui Nie, Ke Zhang, Wenhua Li, Bin Yi, and Longshan Xu, "Direct synthesis of ultralong carbon nanotube bundles by spray pyrolysis and investigation growth mechanism," *Nanotechnology*, **19** (8), article id: 0856606 (2008).

24. Quihong Zhang, Jianwei Lu, Ryan Sager, Liming Dai, and Jeffery Baur, "Hierarchial composites of carbon nanotubes on carbon fiber: Influence of growth condition on fiber tensile properties," *J. Compscitech*, **69** (5), 594-601 (2009).

25. J. Vanpaemel, M. H. Van Der Veen, C. Huyghebaert, S. De Gendt, and P. M. Vereecken, "Effect of boric acid on the nucleation and growth of Ni nanoparticles for CNT growth," *ECS Transactions*, **50** (20), 29-37 (2013).

26. Michael C. Tucker, Kyu Taek Cho, Fanz B. Spingler, Adam Z. Weber and Guangyu Lin, "Impact of membrane characteristics on the performance and cycling of the Br_2-H_2 redox flow cell," *J. Power Sources*, **284**, 212-221 (2015).

27. M. S. Chandrasekar and Malathy Pushpavanam, "Pulse and pulse reverse plating-Conceptual advantages and applications," *Electrochimica Acta*, 53, 3313–3322 (2008).

28. Peng-Xiang Hou, Chang Liu, and Hui-Meng Cheng, "Purification of carbon nanotubes," *Carbon*, **46** (15), 2003-2025 (2008).

29. Nguyen T. K. Thanh, N. Maclean, and S. Mahiddine, "Mechanisms of Nucleation and Growth of Nanoparticles in Solution," *J. Chem. Rev.*, 114 (15), 7610-7630 (2014).

30. Reginald M. Penner, "Mesoscopic Metal Particles and Wires by Electrodeposition," *J. Phys. Chem. B*, **106**, 3339-3353 (2002).

31. Ying Wang, Eduardo Laborda, Kristopher R. Ward, Kristina Tschulik, and Richard G. Compton, "A kinetic study of oxygen reduction reaction and characterization of electrodeposited gold nanoparticles of diameter between 17 nm and 40 nm in 0.5 M sulfuric acid," *Nanoscale*, **5**, 9699-9708 (2013).

32. Mukul Kumar and Yoshinori Ando, "Chemical Vapor Deposition of Carbon Nanotubes: A Review on Growth Mechanism and Mass production," *J. Nanosci. Nanotechnol.*, **10**, 3739-3758 (2010).

CHAPTER 5

Multi-Wall Carbon Nanotube-Based Electrodes with High Active Surface Area and Durability

5.1. Introduction

The major limitation associated with the synthesis of MWCNT-based carbon electrodes described in the previous chapter is that the MWCNT growth is non-uniform and occurs mostly on the fibers near the outer surfaces of the carbon electrode. Since the majority of the active surface area is present inside (cross section) the porous carbon GDL, it is important to have MWCNT growth over the entire carbon electrode fiber surface area. As discussed in chapter 4, the non-uniform MWCNT growth arises from the poor current collection. In this chapter, a new experimental approach where the current collection was done normal to the surface of the carbon electrodes to improve the electrodeposition of Co nanoparticles inside the carbon electrode is discussed. Also, a new experimental fixture that promotes MWCNT growth inside the carbon electrode has been added to the quartz tube reactor used in the CVD process.

The following studies were included in this chapter. First, the durability of MWCNTs against high liquid flow rates was determined using shear measurements. Second, the optimization process implemented to synthesize highly durable MWCNT-based electrodes is discussed. Third, the performance of MWCNT-based electrodes in a H_2-Br_2 fuel cell was examined. Fourth, the pressure drop across both the plain and the MWCNT-based carbon electrode was measured. Finally, a material cost analysis was performed to highlight the cost benefits of using MWCNT-based carbon electrodes instead of multiple plain carbon electrodes in a H_2-Br_2 fuel cell.

5.2. Experimental

5.2.1. Modified Electrodeposition Setup

A two electrode arrangement was used to implement the pulse current electrodeposition technique. As discussed in the previous chapter (Section 4.5.1.1), the carbon electrodes were boiled in DI water and soaked in a solution of cobalt sulfate and boric acid prior to electrodepositing the Co nanoparticles. The whole process remains the same except for the working electrode configuration. The stainless steel alligator clips were replaced by expanded stainless steel mesh as current collectors.

As shown in Figure 5.1, the carbon electrode was sandwiched between expanded stainless steel mesh (67%-75% open area) and the resulting fixture was enclosed between perforated plexiglass (5mm thick with multiple 2mm diameter openings) plates. Finally, chemically resistant Nylon sleeves (purchased from McMaster Carr) were slid across the sides of the fixture to provide uniform compression in the normal direction. The assembled experimental fixture was then placed in the electrolyte solution and pulse current electrodeposition was carried out to deposit Co nanoparticles. The stainless steel mesh provided uniform current collection as it covered the entire carbon electrode surface. The openings in the plexiglass plates and stainless steel mesh allowed the carbon electrode to access the electrolyte solution. The new electrodeposition fixture assisted in providing cobalt ions access, good electronic conductivity and connectivity to all carbon fibers in the electrode. The dimensions of the carbon electrodes, expanded stainless steel mesh, and perforated plexiglass plates were 5cm by 5cm. Figure 5.2 shows the working electrode fixture used in this study.

The Co nanoparticles were electrodeposited by applying a cathodic pulse current to the working electrode. The pulse current technique offered an additional advantage over the constant current technique since it provided better control over the particle size and distribution of the metal catalyst electrodeposited onto the carbon substrate.[1] The effect of precursor solution concentration on the size and distribution of Co nanoparticles was examined by using two different solution mixtures (A & B). Solution A was a mixture of 0.02M $CoSO_4$ and 0.33M H_3BO_3. Solution B was a mixture of 0.01M $CoSO_4$ and 0.16M H_3BO_3.
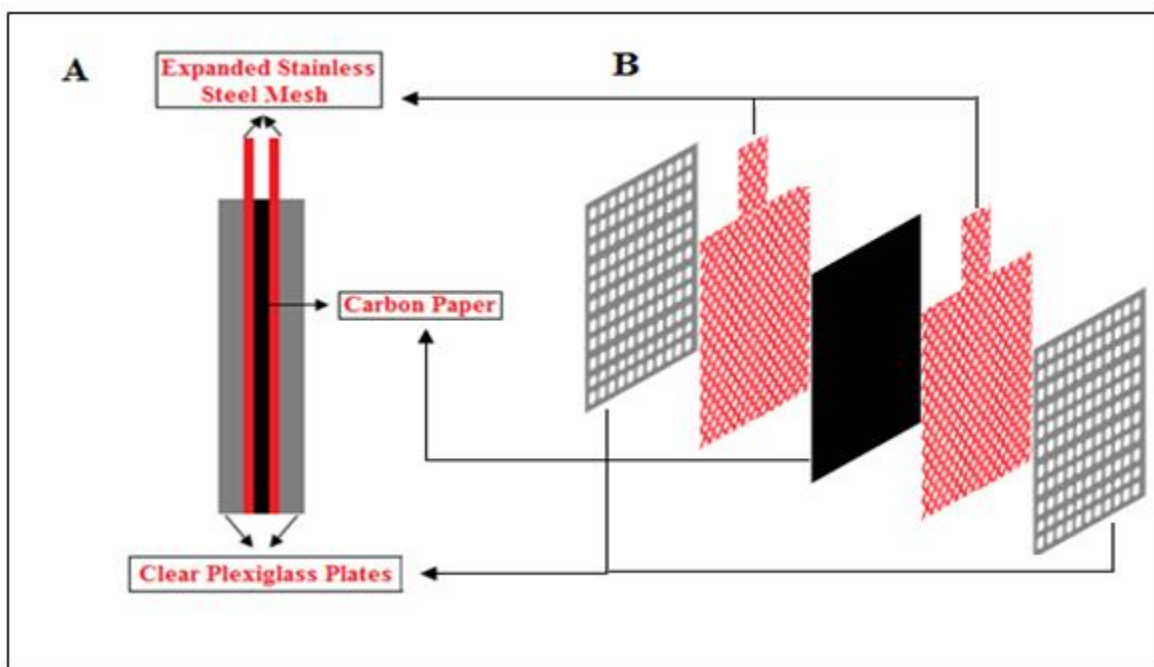
Figure 5.1. Working electrode fixture (A. Side view and B. 3D view) used in the electrodeposition experiment

A cathodic pulse current of -30 mA was applied for 5 seconds (sample 1) and 15 seconds (sample 2), respectively, with each current pulse lasting 1 second when solution A was used. A cathodic pulse current of -10 mA was applied for 45 seconds (sample 3) with each current

pulse lasting 1 second when solution B was used. The solutions were stirred during the rest time in between the pulses.

Figure 5.2. Finished working electrode fixture with stainless steel mesh and nylon sleeves

5.2.2. Experimental Fixture to Promote MWCNT Growth inside the Carbon Electrodes

The experimental procedure for growing MWCNTs on the carbon electrode fiber surface was similar to the one described in chapter 4 (Section 4.5.1.2). The only variation was that the carbon electrodes were enclosed in a fixture to promote MWCNT growth inside the carbon electrode. In order to force the gas mixture through the carbon electrode, the experimental fixture shown in Figure 5.3 was placed inside the quartz tube. As shown in Figure 5.3A (side view), the experimental setup consisted of two dense alumina foam blocks with carbon paper inserted in between them. The diameter of alumina foam blocks approximately matched the inner diameter of the quartz tube. Alumina foam blocks used in the experimental fixture are shown in Figure 5.3B. The side of alumina foam blocks facing the carbon paper (shown in view 1) consisted of a thin vertical slit and multiple openings.
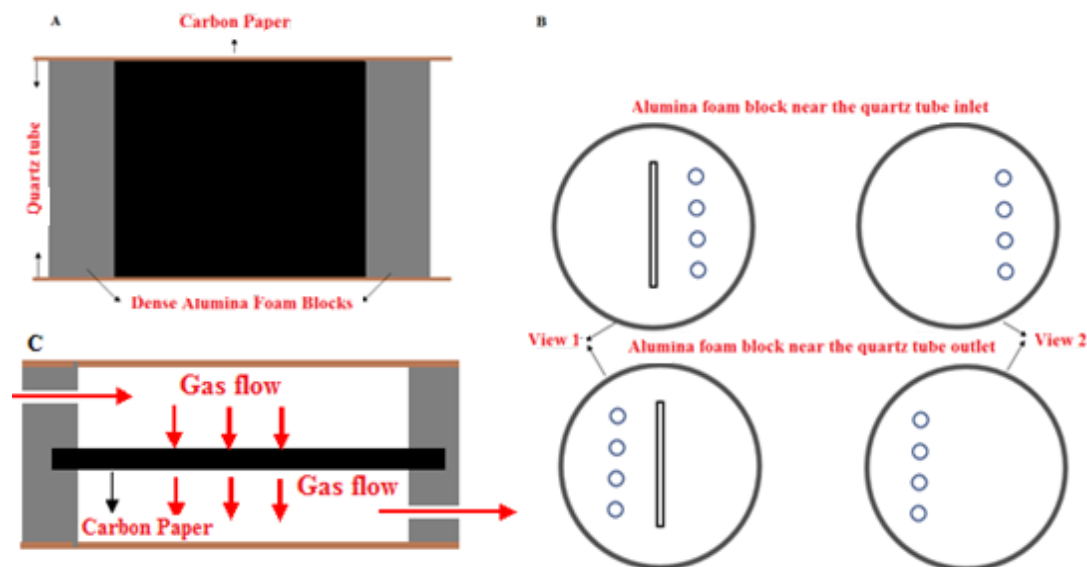
Figure 5.3. Experimental set up used to perform CVD (A. Side view, B. Front view, and C. Top View)

The carbon paper was inserted into the vertical slit and the openings serve as gas-flow channels. The depth of the vertical slit was equal to half the thickness of the alumina foam block whereas the gas-flow channels run all the way through the foam blocks. View 2 shows the side of the foam blocks facing the quartz tube inlet and outlet, respectively. The gas-flow channels were machined to the right side of one of the alumina foam blocks and to the left side on the other to force the gas to flow through the porous carbon electrode. The top view shown in Figure 5.3C depicts the gas flowing through the carbon electrode. This promotes the MWCNT growth inside the carbon electrode. The side of the alumina foam block facing the carbon electrode and the finished experimental fixture are shown in Figure 5.4. The experimental fixture was placed in a quartz tube and subsequently inserted into the quartz tube furnace to grow MWCNTs.

161
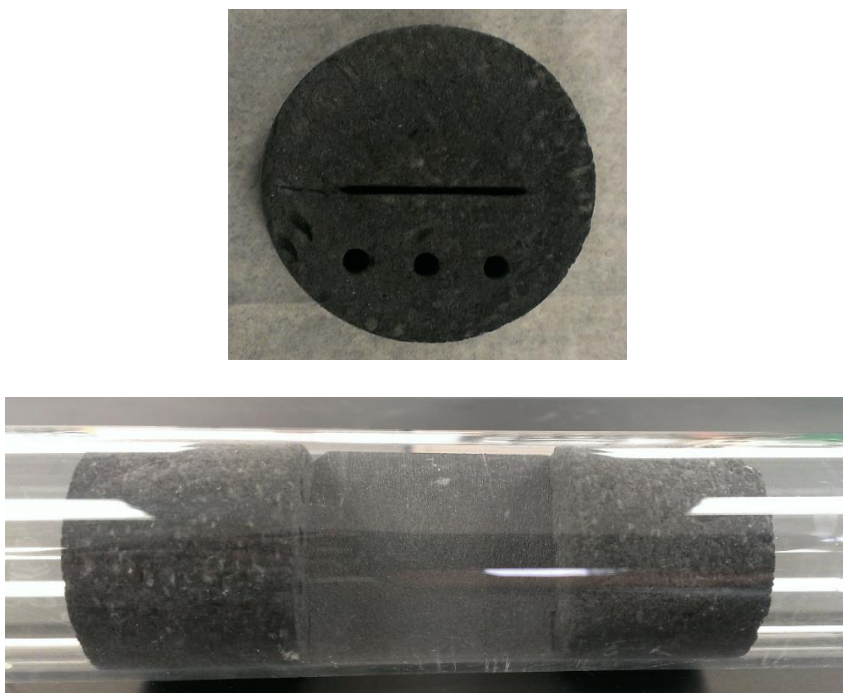
Figure 5.4. Alumina foam block and experimental fixture inside the quartz tube used to

perform CVD

The CVD process used to grow MWCNTs was similar to the one described in chapter 4 (Section 4.5.1.2) except for the reaction temperature and flow rates of C_2H_2, Ar, and H_2. The temperature used for growing MWCNTs was increased from $700^{\circ}C$ to $750^{\circ}C$. The MWCNT growth rate increases as the temperature increases. The flow rate was increased since the quartz tube with a larger diameter (44 mm inner diameter) was used instead of the one with a smaller diameter (20 mm inner diameter) used for the studies conducted in chapter 4. The flow rates for C_2H_2, Ar, and 20% H_2 (rest is Ar), were 20 cc/min, 170cc/min, and 180 cc/min, respectively. The post-treatment and electrochemical analysis (enhancement factor and fuel cell measurements) procedures were described in detail in chapter 4 (Sections 4.5.2 and 4.5.3). The only change made in this study was that the MWCNT-based carbon electrodes were boiled in DI water before testing them in a H_2-Br_2 fuel cell.

5.2.3. Shear Measurements

The shear measurements were conducted in a H_2-Br_2 fuel cell to determine the durability of the MWCNT-based electrodes against high liquid flow rates under the flow-through mode. The fuel cell configuration was shown in chapter 2 (Sections 2.2.1 and 2.2.2). A 1M HBr/0.1M Br_2 electrolyte was fed to the bromine electrode and humidified H_2 gas was recirculated through the hydrogen electrode. The flow rates of HBr/Br_2 solution and H_2 gas are 10 cc/min/cm^2 and 1030 cc/min respectively. A polarization curve was measured using multi-step chronoamperometry with applied overpotentials ranging between +24 mV and -24 mV. The slope (dI/dV) was measured every two hours until reproducible values were obtained. The initial slope (dI/dV) was measured after flowing the HBr/Br_2 electrolyte for 15 min. Both HBr/Br_2 solution and the humidified H_2 gas were recirculated continuously throughout the entire experiment. The difference between initial and finial enhancement factors or slopes (dI/dV) determines the percentage loss of multi-wall carbon nanotubes (MWCNTs).

5.2.4. Pressure Drop Measurements

The pressure drop caused by fluid flow through the plain and the MWCNT-based electrodes was measured using a U-tube water manometer placed between the inlet and outlet of the flow field plate located next to the Br_2 electrode. A plastic sheet was used instead of the membrane to seal (or secure) the H_2 electrode compartment in the fuel cell. Both plain and MWCNT-based carbon electrodes were used as the Br_2 electrodes. Water was pumped through the Br_2 side and the height differential of the liquid columns between the two legs of the manometer was measured. The pressure drop (in cm H_2O) was measured at different water flow rates.

5.2.5. Cost Analysis

The cost analysis was performed to compare the cost of MWCNT electrode synthesis to that of plain carbon electrodes (3 pieces of SGL 10AA). The cost analysis is preliminary since it only includes the material costs. The combined cost of electrodeposition and CVD processes would contribute toward the total cost of MWCNT electrode synthesis. The cost of cobalt sulfate ($CoSO_4$), boric acid (H_3BO_3), and electricity constitutes the total cost of electrodeposition process. The cost of acetylene, argon, hydrogen, and electricity constitute the total cost of CVD process.

5.3. Results and Discussion

5.3.1. Electrodeposition of Co Nanoparticles

Initially, the electrodeposition of Co nanoparticles was done using solution A (0.02M $CoSO_4$ and 0.33M H_3BO_3). The electrodeposition current, time and number of pulses were listed in the experimental section. After electrodepositing Co, the carbon electrodes were soaked in liquid nitrogen for 15 minutes to make them hard and brittle. A small piece of carbon electrode was then broken and the exposed cross section was subsequently analyzed using SEM. The SEM images of cross sectional area of the porous carbon electrodes after electrodepositing Co are shown in Figure 5.5 (a & b). The images on the right in Figures 5a and 5b are magnified 9 times compared to the ones on the left. As the duration of electrodeposition increases from 5 to 15 seconds, while applying the same pulse current magnitude, the density of Co nanoparticles increases. The fact that Co nanoparticles were successfully electrodeposited inside the carbon electrode (cross section) shows the benefit of using stainless steel mesh current collectors. The diameter of the Co nanoparticles was between 30 and 70 nm.
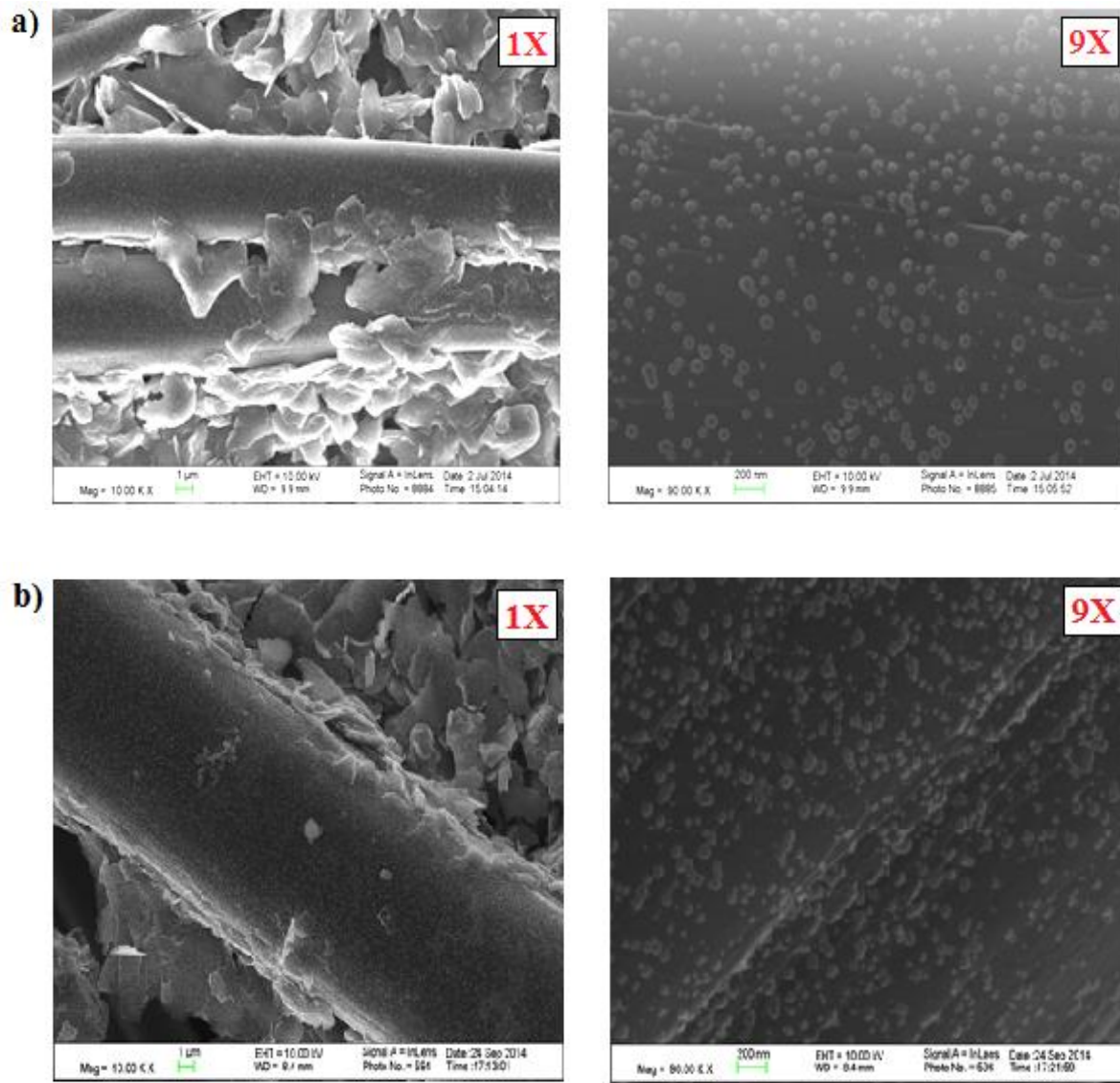
Figure 5.5. SEM analysis of carbon electrode cross section after electrodepositing Co

a) -30mA for 5s (sample 1) and b) -30mA for 15s (sample 2)

5.3.2. MWCNT Growth Using CVD Process

After electrodepositing Co, carbon electrodes were inserted into the fixture shown in experimental section (5.2.2) and then placed inside the quartz oven to grow MWCNTs. The MWCNTs were grown at 750°C for 45 min in the flow of C_2H_2, Ar and H_2. The SEM images

of the electrode cross section of samples 1 and 2 after growing MWCNTs are shown in Figure 5.6. As shown in Figures 5.6a and 5.6b, the MWCNT growth was successfully accomplished in the electrode cross section, which was a result of the flow-through condition created by the experimental fixture used in this study. The dense Co nanoparticle distribution seen in sample 2 (-30 mA for 15s) contributed towards the dense nanotube growth as shown in Figure 5.6b. The MWCNT-based carbon electrodes were then boiled in DI water and soaked in 2M HBr solution overnight before measuring their active surface area enhancement factors.

5.3.3. Electrochemical Analysis

The active surface area enhancement factors of MWCNT electrodes were measured in a solution of 1M HBr and 0.1M Br_2 using a three electrode arrangement described in chapter 4 (Sections 4.5.2 and 4.5.3). Figure 5.7 shows the multi-step chronoamperometry curves obtained with plain SGL 10AA carbon electrode, sample 1, and sample 2. The product of active surface area (a) and exchange current density (i_o) was obtained using the linearized Butler-Volmer equation discussed in chapter 4 (Equation 4.1). As shown in Table 5.1, the active surface area enhancement factors for samples 1 and 2 are 44 and 67, respectively. As expected, the active surface area of sample 2 was higher compared to that of sample 1. The high active surface area of sample 2 can be directly correlated to its dense MWCNT growth.
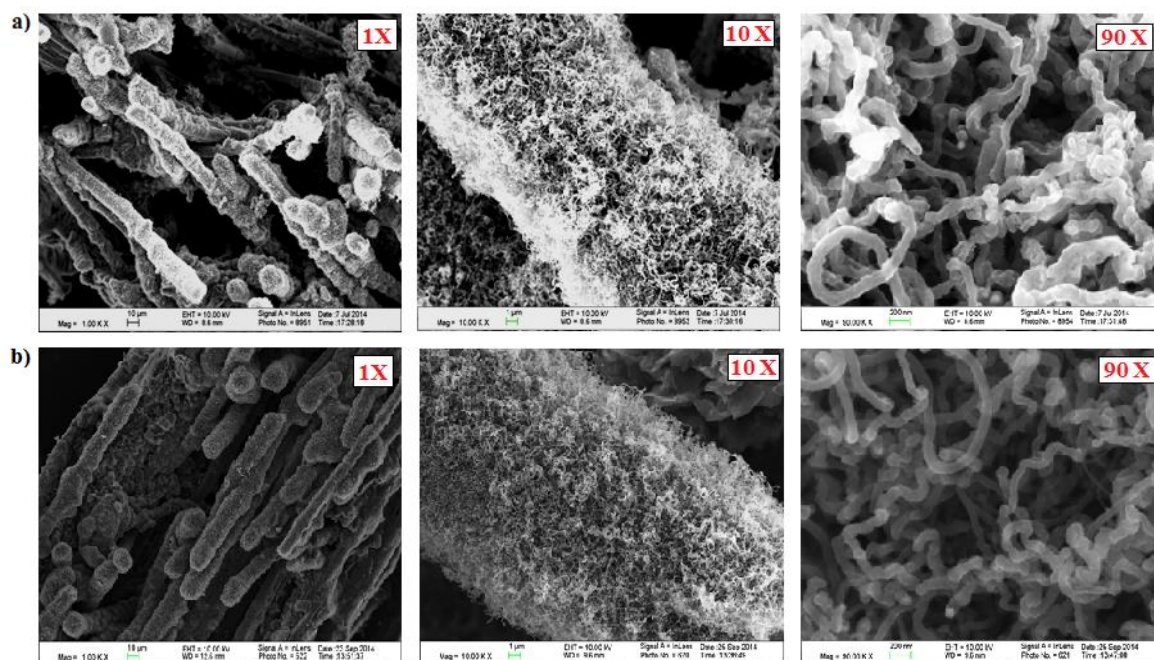
Figure 5.6. SEM images of cross-section of MWCNT-based electrodes (synthesized at 750ºC for 45 min), under different magnifications (a: sample 1 and b: sample 2)
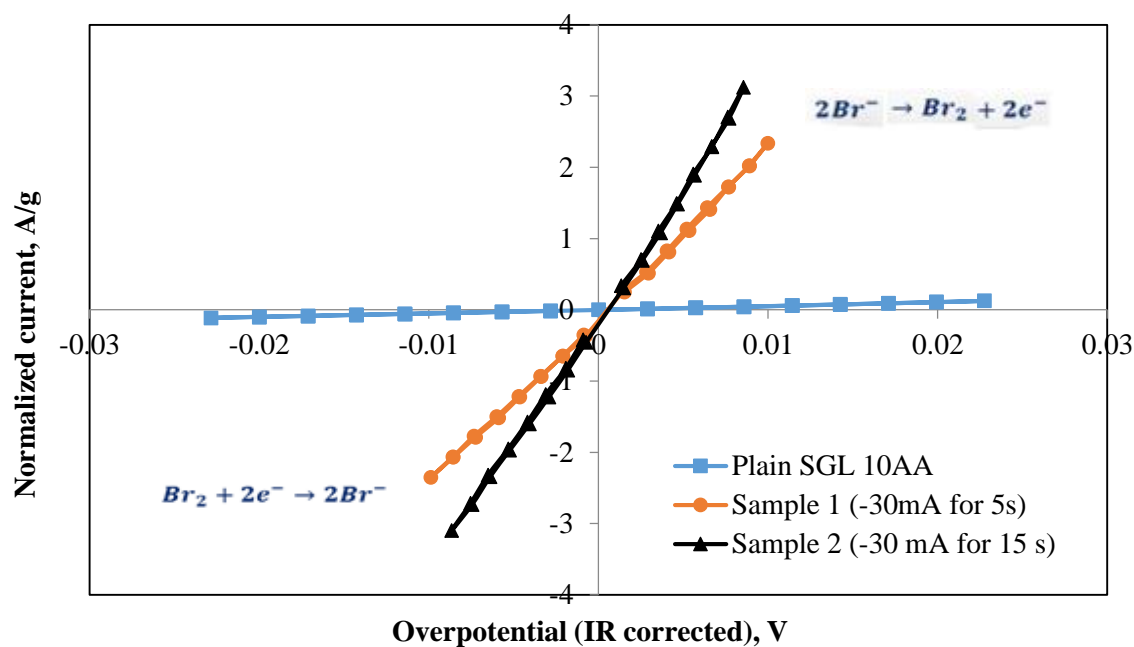
Figure 5.7. Multi-step chronoamperometry curves of MWCNT-based electrodes in a three electrode arrangement (samples 1 and 2)

Table 5.1. Enhancement factors

Specimen	Enhancement factor
1	44
2	67

5.4. Effect of CVD Synthesis Time on Active Surface Area

During the CVD process, the length and density of MWCNTs can be controlled by varying the parameters such as synthesis time, acetylene concentration, and synthesis temperature. In this study, the effect of synthesis time on the active surface area of porous carbon electrodes was examined, while maintaining a constant acetylene concentration and reaction temperature (750°C). Sample 2 was chosen for this study because of its high active surface area. The MWCNTs were grown on sample 2 at different CVD synthesis times (15, 30, 45, and 60 minutes). Based on the CVD synthesis time, the samples were labeled as CVD 15, CVD 30, CVD 45, and CVD 60 respectively.

Figure 5.8 shows the SEM images of samples after growing MWCNTs at different synthesis times. The length and density of MWCNTs increased as the CVD synthesis time increased from 15 to 60 minutes. Beyond a certain length, the MWCNTs bent on their own weight and became tangled as shown in Figure 5.8. One of the advantages of tangled MWCNTs was their increased durability when exposed to high liquid flow rates. However, the tall nanotubes might block the pores in the carbon electrodes, which in turn might result in a larger pressure drop. Long nanotubes also restricted the electrolyte to access to the internal surface area (or cross sectional area) of the porous carbon electrode. Since, a flow-through tantalum flow field plate was used in the Br$_2$ electrode, the active surface area present inside (cross

sectional area) the MWCNT-based carbon electrode played an important role in determining its performance. Hence, it was critical to test these MWCNT-based electrodes in a fuel cell at high flow rates to determine their durability and performance.

The multi-step chronoamperometry curves and active surface area enhancement factors of MWCNT-based carbon electrodes obtained at different CVD synthesis times are shown in Figure 5.9 and Table 5.2 respectively. The active area of the MWCNT-based carbon electrodes increased as the CVD synthesis time increased (active surface area enhancement factors between 43 and 75 were achieved). One of the limitations associated with measuring enhancement factors in a three electrode arrangement is that the electrode remains stagnant in the electrolyte solution under no flow. The total active surface area of MWCNT-based electrodes measured in a three electrode arrangement might be different from the one measured in a fuel cell under fluid flow. The next section introduces the durability study of MWCNT-based electrodes in a H_2-Br_2 fuel cell.
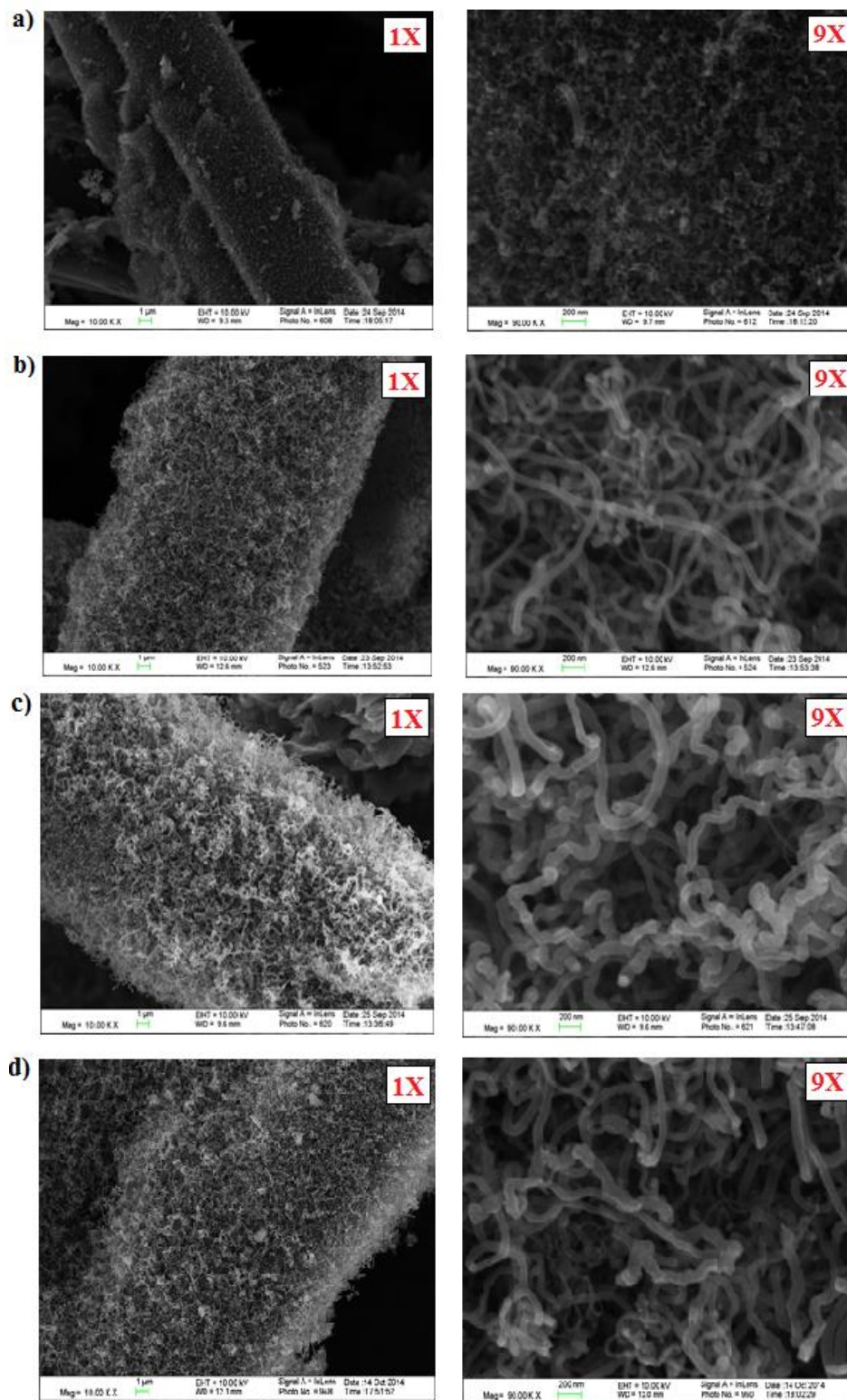
Figure 5.8. SEM images of a cross-section of MWCNT-based electrodes synthesized at different CVD times (a. CVD 15, b. CVD 30, c. CVD 45, and d. CVD 60)
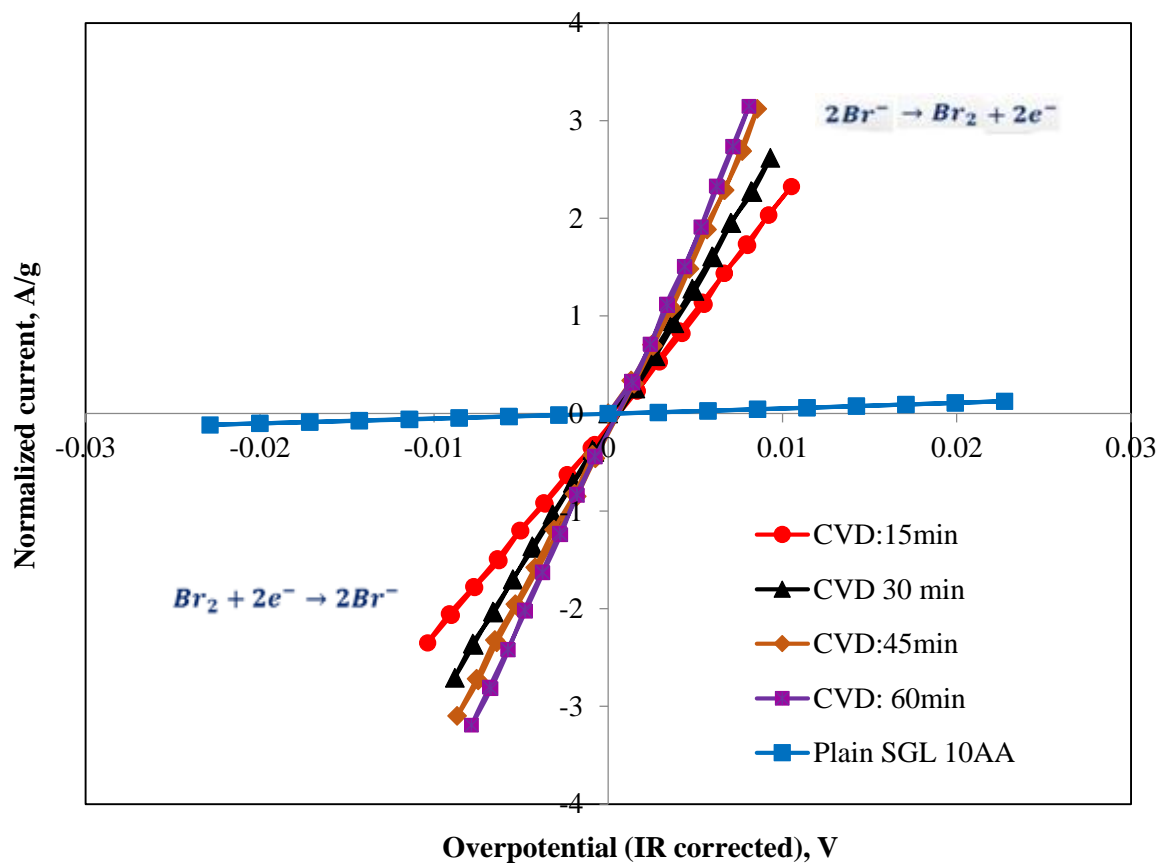
Figure 5.9. Multi-step chronoamperometry curves of MWCNT-based electrodes generated at different CVD synthesis times (CVD 15, CVD 30, CVD 45, and CVD 60)

Table 5.2. Enhancement factors of MWCNT-based electrodes at different CVD synthesis times

Specimen	Enhancement factor
CVD 15	43
CVD 30	55
CVD 45	67
CVD 60	75

5.5. Durability of MWCNT Electrodes Based on Shear Measurements

As described in the experimental section, the shear measurements were conducted in a H_2-Br_2 fuel cell. The flow rates of HBr/Br_2 electrolyte and H_2 were specified in the experimental section. The slope (dI/dV) was measured periodically while maintaining continuous HBr/Br_2 and H_2 recirculation. Initially, a plain SGL 10AA carbon electrode was tested in a H_2-Br_2 fuel cell to ensure there was no effect of HBr/Br_2 crossover on the fuel cell performance over an extended period (7 hours). As shown in Figure 5.10, reproducible polarization curves were obtained over 7 hours of testing, which shows that there was no noticeable HBr/Br_2 or H_2 crossover within the duration of testing. The durability results from the fluid shear experiment for the MWCNT-based carbon electrodes are shown in Figure 5.11 (a & b) and Table 5.3.
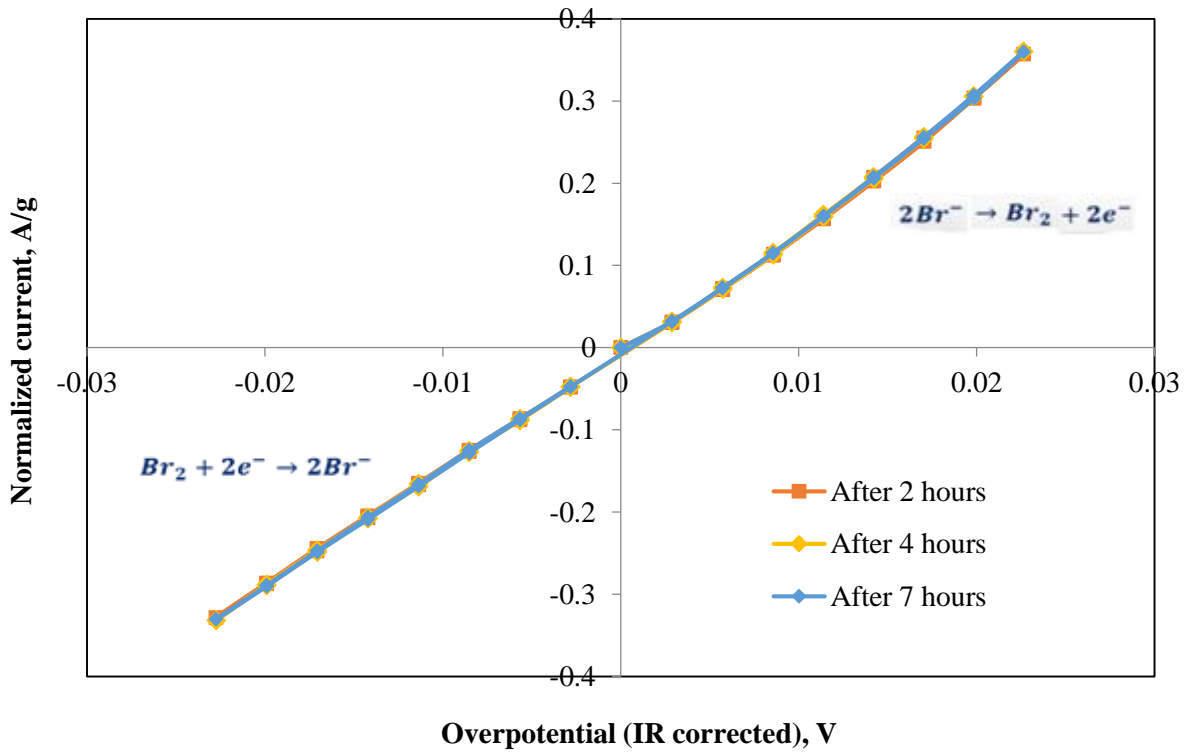
Figure 5.10. Effect of fluid shear rate on a plain SGL 10AA carbon electrode

Figure 5.11a shows the slopes (dI/dV) measured as a function of time whereas Figure 5.11b shows the initial (after 15 min) and final (7-9 hours later) polarization curves. The initial and final enhancement factors are shown in Table 5.3. Two observations were noted in the durability test. First, the surface areas of MWCNT-based carbon electrodes decreased as soon as the electrodes were subjected to high fluid shear stress. This initial decrease in active surface areas was as much as 70% (shown in Table 5.3), which is determined by comparing the enhancement factor obtained from the three electrode arrangement and the initial slope (dI/dV) measured after 15 min from the durability study. Second, after this initial loss in surface area, additional loss during prolonged operation was minimal, especially with electrodes with longer MWCNTs. The carbon electrodes with long and dense MWCNTs were able to withstand high liquid flow rates as shown in Table 5.3 (percentage drop in surface area decreased from 29 % to 9% as the CVD synthesis time increased from 15 to 60 min). The results also show that longer CNTs created beyond 45 minutes of CVD did not contribute to an additional increase in active surface area. The final surface areas after the durability test are much higher than that of conventional carbon electrodes. The SEM images of MWCNT-based carbon electrodes before and after the shear measurement are shown in Figure 5.12.
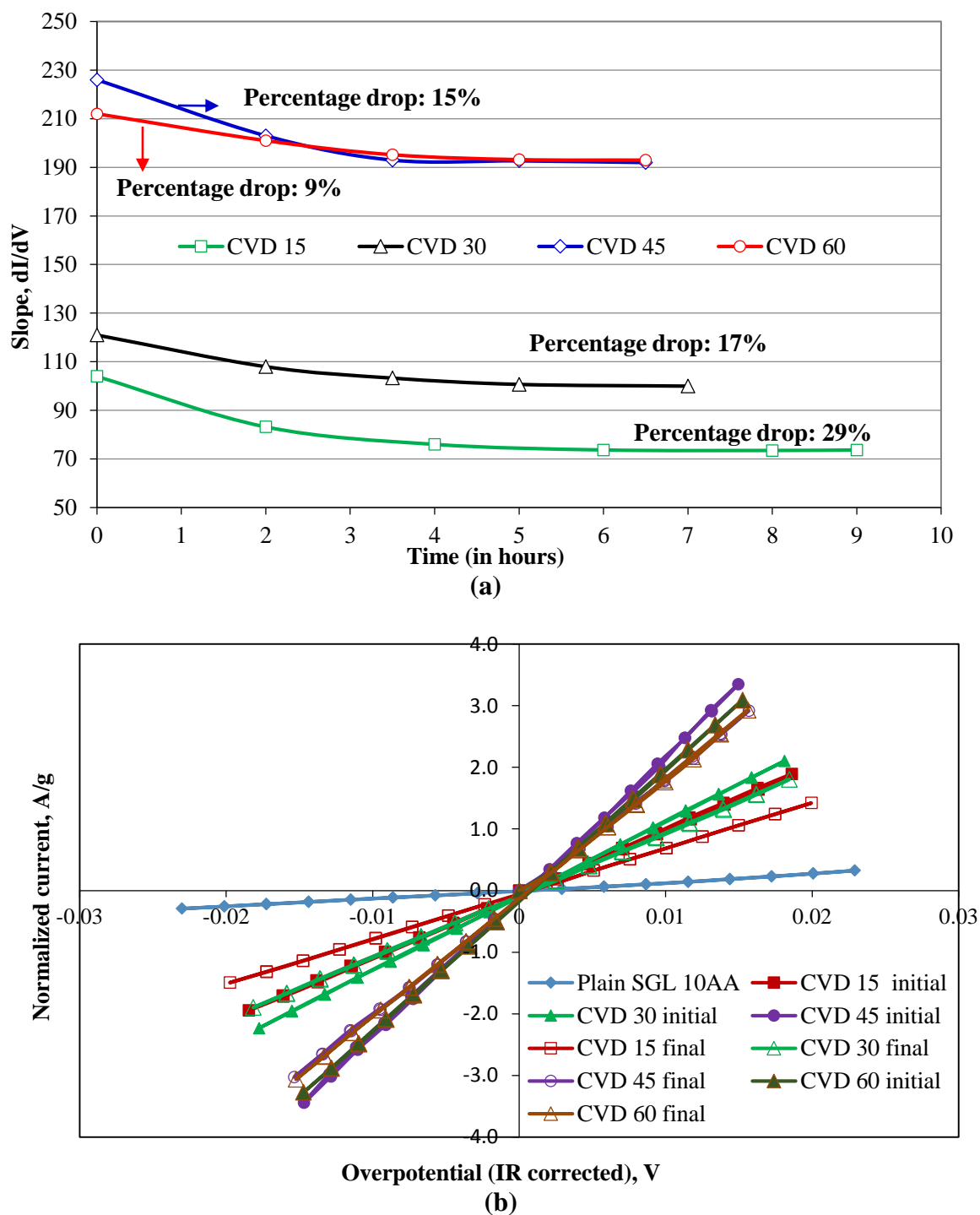
Figure 5.11. Effect of fluid shear rate on the surface area of CNT electrodes treated at different CVD times (a) changes in the dI/dV slope (surface activity) as the samples were subjected to continuous shear rate (b) initial and final (7-9 hrs. later) polarization curves

Table 5.3. Summary of effect of fluid shear rate on surface enhancement factor of MWCNT electrodes

Specimen	Enhancement factor (three-electrode set up)	Initial enhancement factor	Final enhancement factor	Percentage drop
CVD 15	43	8X	5.6X	29%
CVD 30	55	9.3X	7.7X	17%
CVD 45	67	17.3X	14.7X	15%
CVD 60	75	16.2X	14.8X	9%

The location where the MWCNT bends on its own weight is very fragile. The part of the MWCNT beyond the bend is vulnerable and can be severed at high liquid flow rates. As shown in Figure 5.12, a certain percentage of MWCNTs is lost, leaving behind short MWCNTs on the carbon electrode fiber surface for all the four samples synthesized at different durations using the CVD process (samples: CVD 15, CVD 30, CVD 45, and CVD 60).. Note that, after the long MWCNTs were truncated, one could see that a large fraction of the carbon fiber surface area was still available for additional CNT growth. In the following sections, the optimized electrodeposition process that produces dense MWCNTs will be discussed
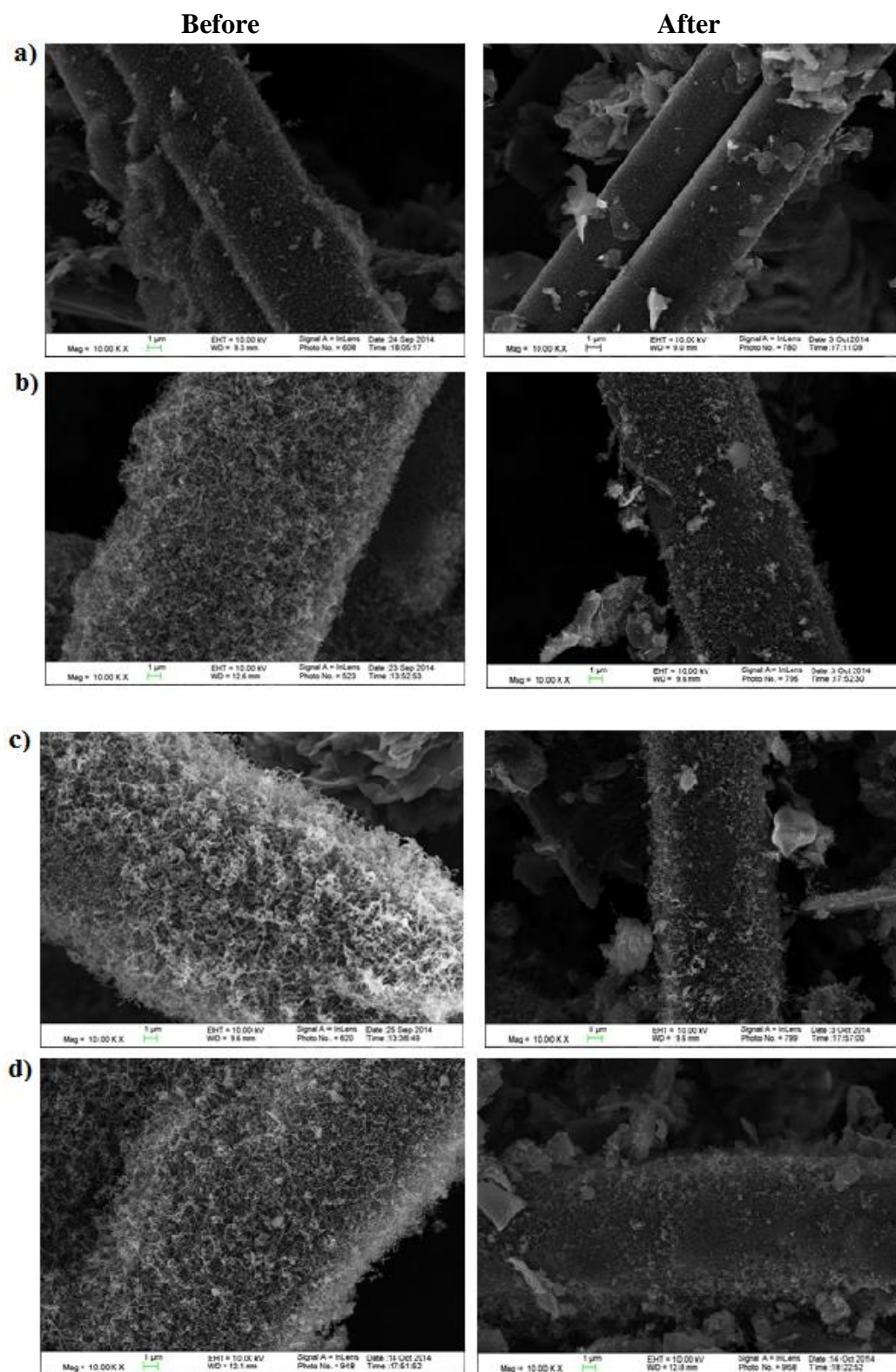
Before   **After**

Figure 5.12. SEM images of the cross-section of a MWCNT electrodes before and after the

durability test (a. CVD 15, b. CVD 30, c. CVD 45, and d. CVD 60)

5.6. Fuel cell Performance with Plain and MWCNT-Based Carbon Electrodes

The synthesized MWCNT electrodes were tested in a H_2-Br_2 fuel cell and the results are presented below in Figures 5.13 and 5.14. The experimental procedure and fuel cell configuration were similar to the ones described in chapter 4 except for the concentration of HBr and Br_2. In this study, a mixture of 2M HBr and 0.9M Br_2 was recirculated through the bromine electrode. Figure 5.13 shows the performance of the fuel cell under the above described operating condition with 3 layers of the conventional SGL 10AA electrode at 10 cc/min/cm^2 and 1 layer of MWCNT-based carbon electrode at 5 and 10 cc/min/cm^2. The MWCNT-based carbon electrode used in the study is the sample labeled CVD 45 (15X active surface area). This sample was chosen as it has the highest active surface area after the durability measurements. Figure 5.14 shows the performance of the fuel cell under the same operating conditions described above with 3 layers of the conventional SGL 10AA electrode at 10 cc/min/cm^2 and 1 and 3 layers of MWCNT electrode at 10 cc/min/cm^2. Prior to collecting the data for the polarization curve, multiple discharge and charge cycles were carried out to hydrate the membrane electrode assembly (MEA).

The results in Figure 5.13 show that the fuel cell with a single layer of MWCNT-based carbon electrode exceeded the performance of 3 layers of the conventional SGL 10AA electrode (~12% higher current and power density at 80% discharge efficiency) even at half the flow rate during both discharge and charge. This higher performance acquired with few Br_2 electrodes will increase the power output, reduce the size and lower the cost of the fuel cell system. These results are consistent with previous results obtained with lower HBr concentrations (1M HBr/0.9M Br_2). The results in Figure 5.14 indicate that, since a single layer of MWCNT-based carbon electrode has sufficiently high surface area to give good

performance, adding more layers of MWCNT electrode would only increase the ionic transport distance (ohmic resistance) in the cell and result in poorer performance, as observed previously by Cho et al.[2] when more than 3 layers of conventional electrodes were used in the bromine side of the cell. Also, the multiple electrode layers used in the fuel cell system result in an additional cost.
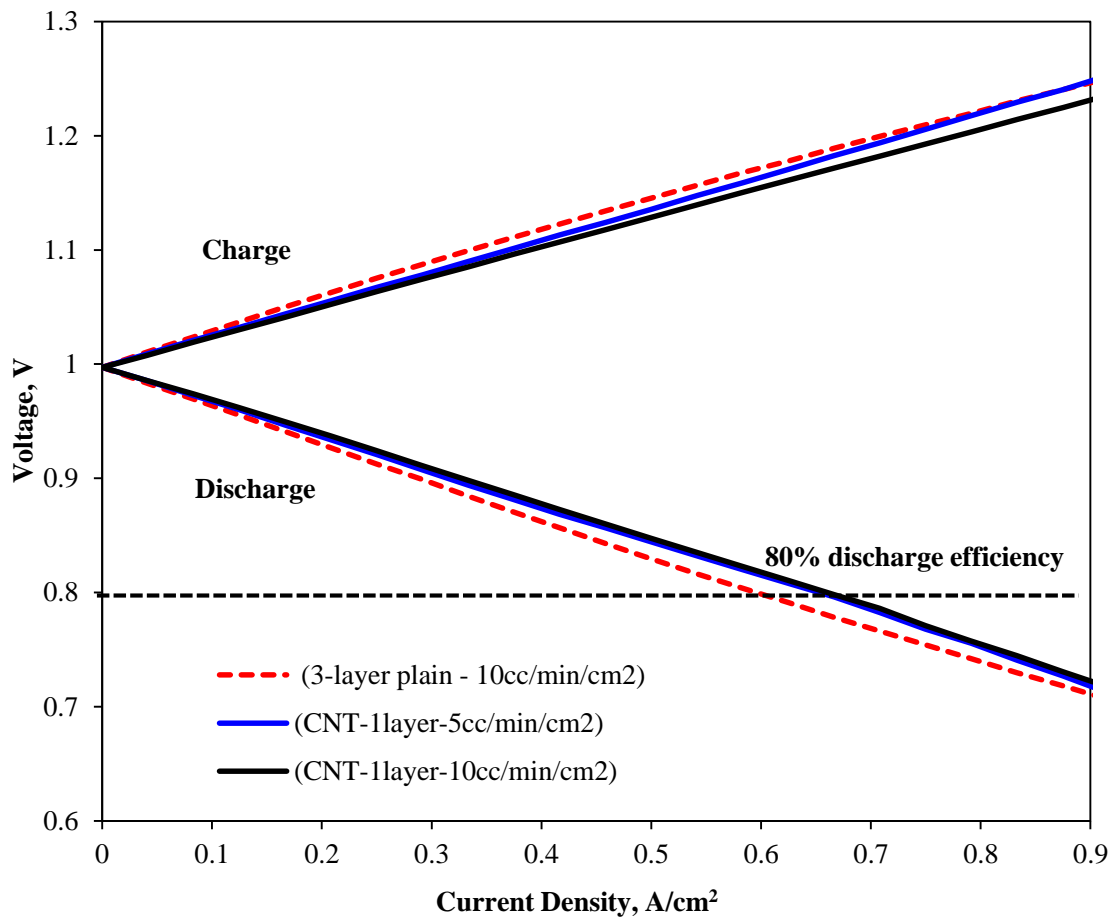
Figure 5.13. Fuel cell performance with 3 layers of conventional electrode and 1 layer of CNT electrode at different HBr/Br$_2$ flow rates
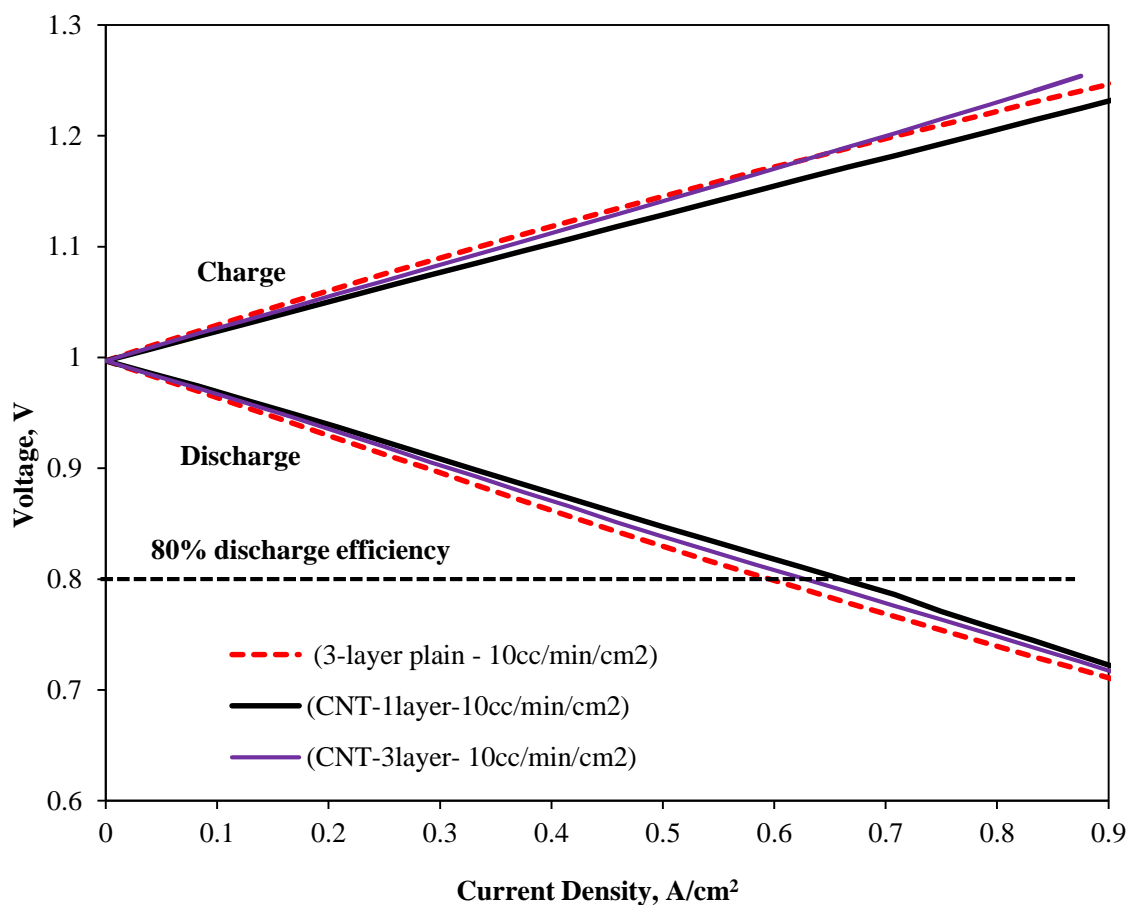
Figure 5.14. Fuel cell performance with 3 layers of conventional electrode and 1 and 3 layers of CNT electrode at the same HBr/Br$_2$ flow rate

5.7. Short, Dense MWCNTs for High Durability

As seen in Figure 5.12, long MWCNTs are lost once they were subjected to high liquid flow rates. Hence, the reasonable way to improve the durability of MWCNT-based carbon electrodes was to grow short, dense MWCNTs on the electrode fiber surface. As the density of MWCNT distribution increases, the active surface area of the MWCNT-based carbon electrode improves as well. One way to improve the MWCNT density is by modifying the electrodeposition conditions to generate small Co nanoparticles with dense distribution. The

optimized electrodeposition conditions along with SEM and electrochemical analysis will be discussed in the following sections.

5.7.1. Effect of CoSO₄ Concentration on Co Electrodeposition

The $CoSO_4$ and H_3BO_3 concentration in solution A specified in the experimental section was reduced to half (solution B) and subsequently Co was electrodeposited. Sample 3 (-10mA applied for 45 seconds) was synthesized using solution B (0.01M $CoSO_4$ and 0.16M H_3BO_3). Figure 5.15 shows the SEM images of samples 2 and 3 after electrodepositing Co. The concentration of $CoSO_4$ determines the number of moles of Co available in the solution near the electrode surface. As expected, the diameter of Co nanoparticles decreased as the concentration of Co decreased in the solution used for electrodeposition (seen in Figure 5.15). Also, the density of Co nanoparticles was high in sample 3, which in turn aids in obtaining dense MWCNT distribution. The MWCNTs were grown on sample 3 using the same conditions described previously (section 5.4). Since previous durability measurements
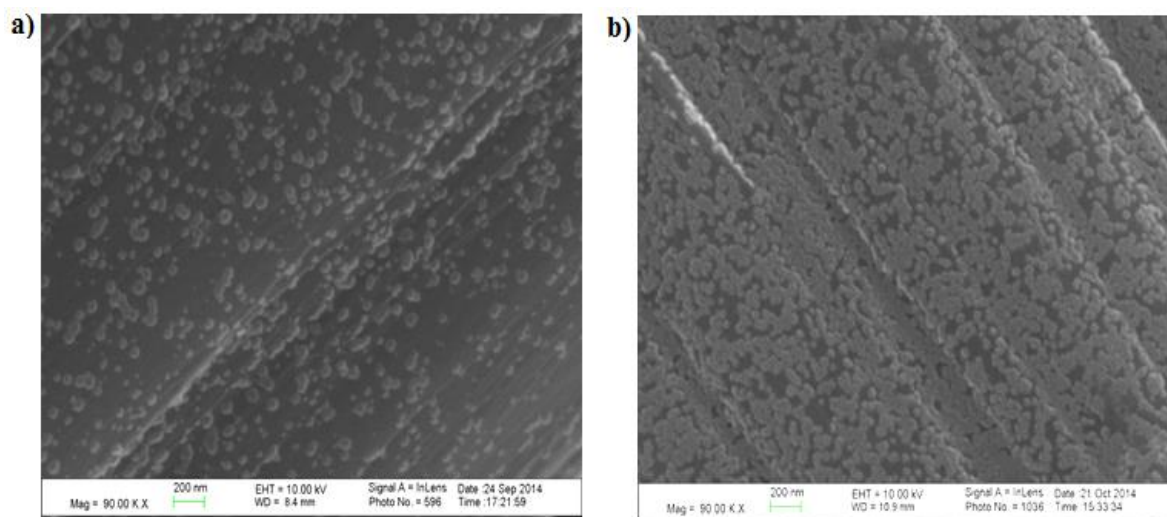
Figure 5.15. Effect of $CoSO_4$ concentration on the diameter and density of Co nanoparticles

(a. sample 2: 0.33M $CoSO_4$ and b. sample 3: 0.16M $CoSO_4$)

indicated that tall MWCNTs will be lost at high liquid flow rates, the CVD synthesis time for sample 3 in this study was reduced to 15 minutes in order to grow short MWCNTs. Subsequently, the active surface area enhancement and durability of sample 3 were measured.

5.7.2. Effect of CoSO$_4$ Concentration on Active Surface Area and Durability of MWCNT Electrodes

Figures 5.16 and 5.17 compare the enhancement factors and durability measurements of samples 2 and 3 (MWCNTs were synthesized at 750°C for 15 minutes). The active surface area enhancement factor of sample 3 is 20% higher than that of the sample 2 as shown in Figure 5.16 and Table 5.4. Two observations were noted from the shear measurements shown in Figure 5.17. First, the resistance of MWCNTs against high liquid flow rate is higher for sample 3 as shown in Figure 5.17 (12% drop in surface area of sample 3 compared to 29 % drop in surface area of sample 2). This might be a result of dense MWCNT growth obtained in sample 3 (shown in Figure 5.18), which is directly correlated to its dense Co nanoparticle distribution. Second, the active surface area of sample 3 after subjecting it to fluid shear stress is still 5 times higher than that of sample 2 (shown in Table 5.5). As shown in Figure 5.18, a large amount of the short MWCNTs still remain on the sample 3. Finally, sample 3 was tested in a H$_2$-Br$_2$ fuel cell to determine its performance.

Table 5.4. Effect of CoSO$_4$ concentration on active surface area

Specimen	Enhancement factor
Sample 2 (0.33M CoSO$_4$)	43
Sample 3 (0.16M CoSO$_4$)	54
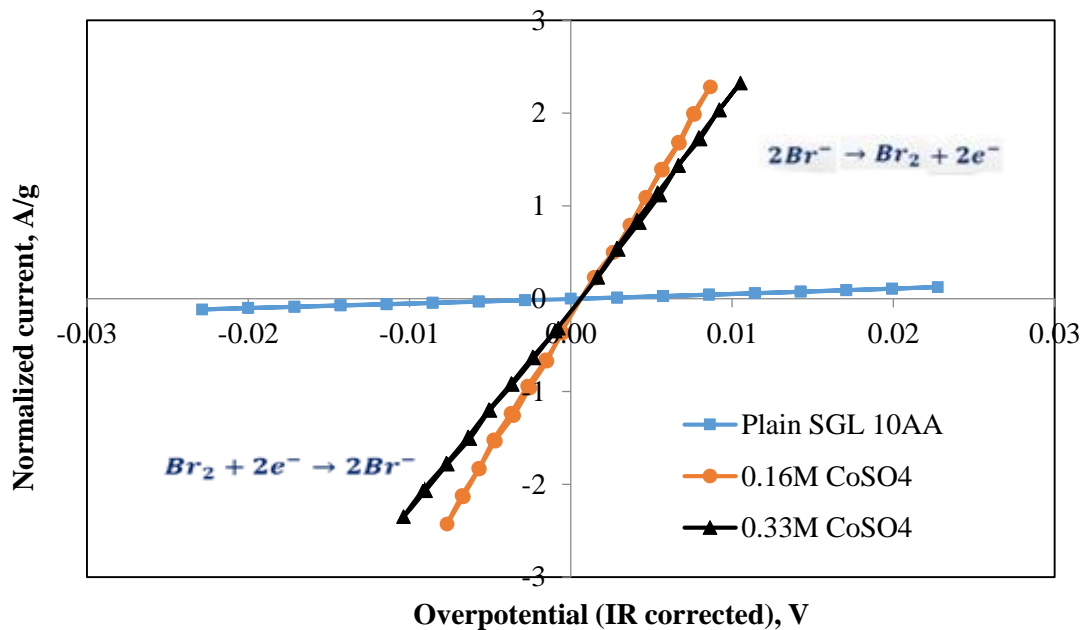
Figure 5.16. Effect of CoSO$_4$ on active area enhancement factors (sample 2: 0.33M CoSO$_4$ and sample 3: 0.16M CoSO$_4$)
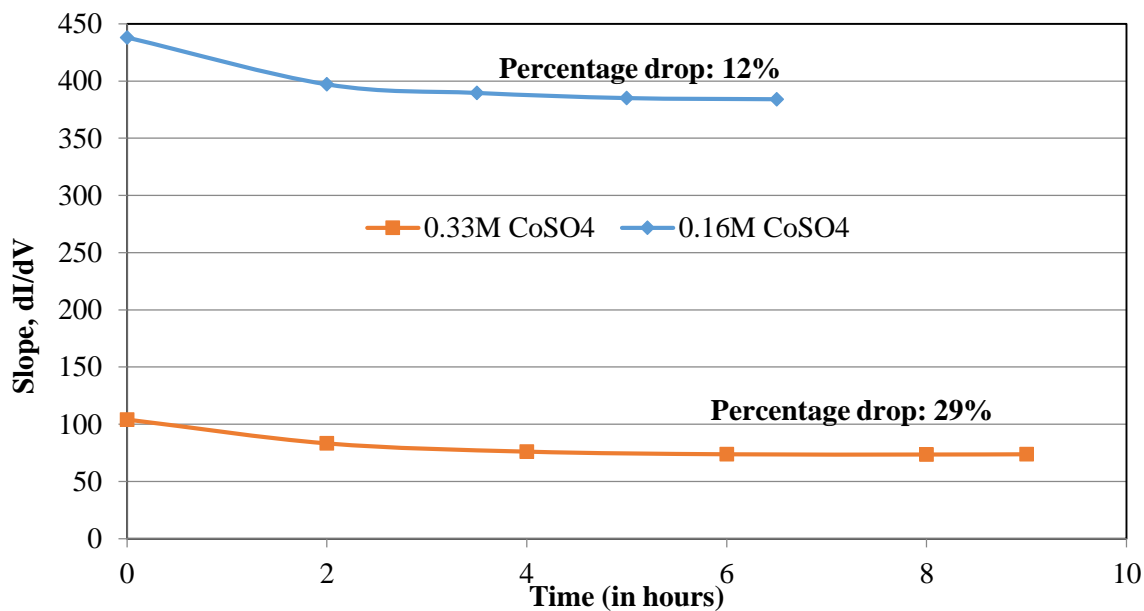
Figure 5.17. Effect of fluid shear rate on the surface area of MWCNT electrodes synthesized at different CoSO$_4$ concentrations (sample 2: 0.33M CoSO$_4$ and sample 3: 0.16M CoSO$_4$)
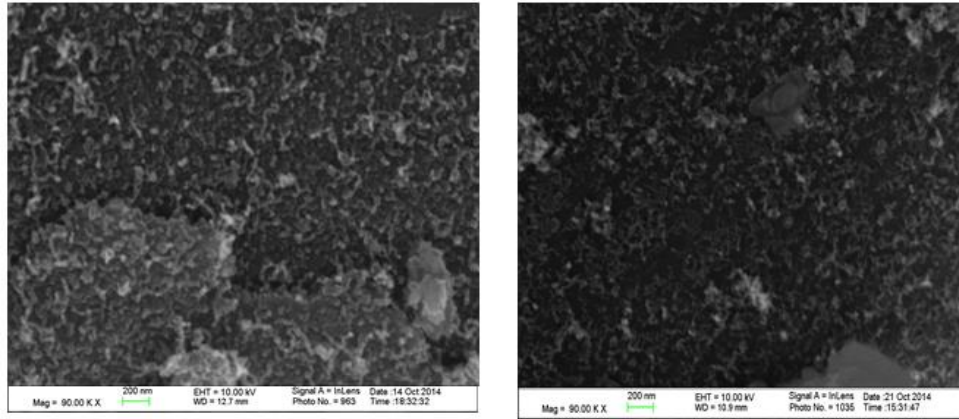
Figure 5.18. Sample 3 (0.16M CoSO$_4$) before (left) and after (right) shear measurements

Table 5.5. Effect of CoSO$_4$ concentration on active surface area (durability)

Specimen	Enhance factor (three electrode set up)	Initial enhancement factor	Final enhancement factor	Percentage drop
Sample 2 (0.33M CoSO$_4$)	43	8X	5.6X	29%
Sample 3 (0.16M CoSO$_4$)	54	33X	29X	12%

5.7.3. Fuel Cell Performance with Durable and High Surface Area MWCNT Electrode

A new H$_2$-Br$_2$ fuel cell using sample 3 as the Br$_2$ electrode was tested at different HBr/Br$_2$ flow rates. Also, 3 layers of plain SGL 10AA have been tested and their performance is compared to that of the new MWCNT-based carbon electrode with high durability. As shown in Figure 5.19, the discharge performance obtained with a single layer of MWCNT-based carbon electrode at a low flow rate (2 cc/min/cm^2) matched that obtained with 3 layers of plain SGL 10AA carbon electrode at high flow rate (10cc/min/cm^2). Also, better discharge performance

was obtained when the H_2-Br_2 fuel cell system with the MWCNT-based carbon electrode was operated at high flow rates (7 and 10 cc/min/cm^2). For example, at 80 % discharge efficiency, the current and power density of H_2-Br_2 fuel cell system acquired with the MWCNT-based carbon electrode is approximately 16% higher than that acquired with 3 layers of plain SGL 10AA carbon electrode.
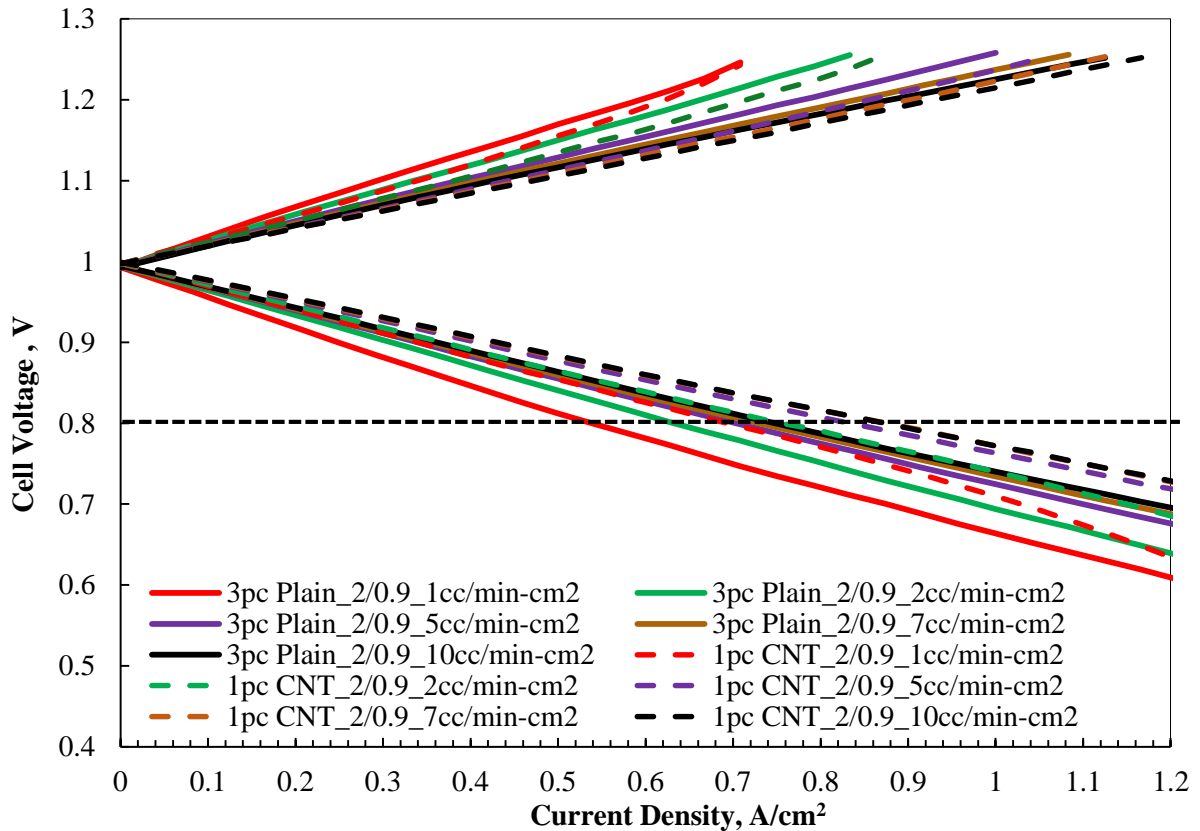
Figure 5.19. Fuel cell performance with 3 layers of conventional electrode and 1 layer of MWCNT electrode (sample 3) at different HBr/Br_2 flow rates

There are two ways to use MWCNT-based carbon electrodes to gain cost advantages. The first option is to operate a H_2-Br_2 fuel cell with the MWCNT-based carbon electrode at low flow rates so that it matches the fuel cell performance obtained with multiple plain carbon

electrodes. This option reduces pumping costs and possibly the bromine electrode cost as well. A detailed cost analysis will be shown in the following sections to determine whether there is a cost advantage of using a MWCNT-based carbon electrode instead of the plain ones. The second option is to operate a H_2-Br_2 fuel cell with the MWCNT-based carbon electrode at high flow rates so that it exceeds the fuel cell performance obtained with multiple plain carbon electrodes. While this option doesn't reduce the pumping costs, it reduces the material and fuel cell stack costs, which is very significant. Since higher fuel cell performance could be obtained with MWCNT-based carbon electrodes, the number of fuel cells in a stack can be reduced for a required stack power.

5.8. Pressure Drop Measurements

Pressure drop measurements were done on both plain SGL 10AA (single layer) and MWCNT-based carbon electrodes (sample 3: Co electrodeposition done at 0.16M $CoSO_4$) using the procedure described in the experimental section. Sample 3 was chosen since it is the best performing MWCNT-based carbon electrode. Figure 5.20 shows the pressure drop across the Br_2 electrode (in cm H_2O) as a function of H_2O flow rate. This is a comparative study since the pressure drop related to the minor losses in the tubing was included in the total pressure drop measured for both plain SGL 10AA and MWCNT-based carbon electrodes. The pressure drop curves shown in the graph were obtained after multiple measurements. Also, the uncertainties in the flow rates were represented by the error bars.

As shown in Figure 5.20, the pressure drop with a MWCNT-based electrode is higher than that observed with plain SGL 10 AA (single layer) carbon electrode. The high pressure drop seen in the MWCNT-based carbon electrode might be a result of slight decrease in porosity due to the MWCNT growth on the carbon electrode fiber surface. The increase in

185

pressure drop seen in MWCNT-based carbon electrode is still insignificant to cause any severe resistance to the fluid flow. This can be attributed to the short nanotubes remaining after being subjected to the fluid shear stress and also the very high porosity of SGL 10 AA carbon electrode material compared to the other commercially available ones (Toray, Avcarb, etc.,).
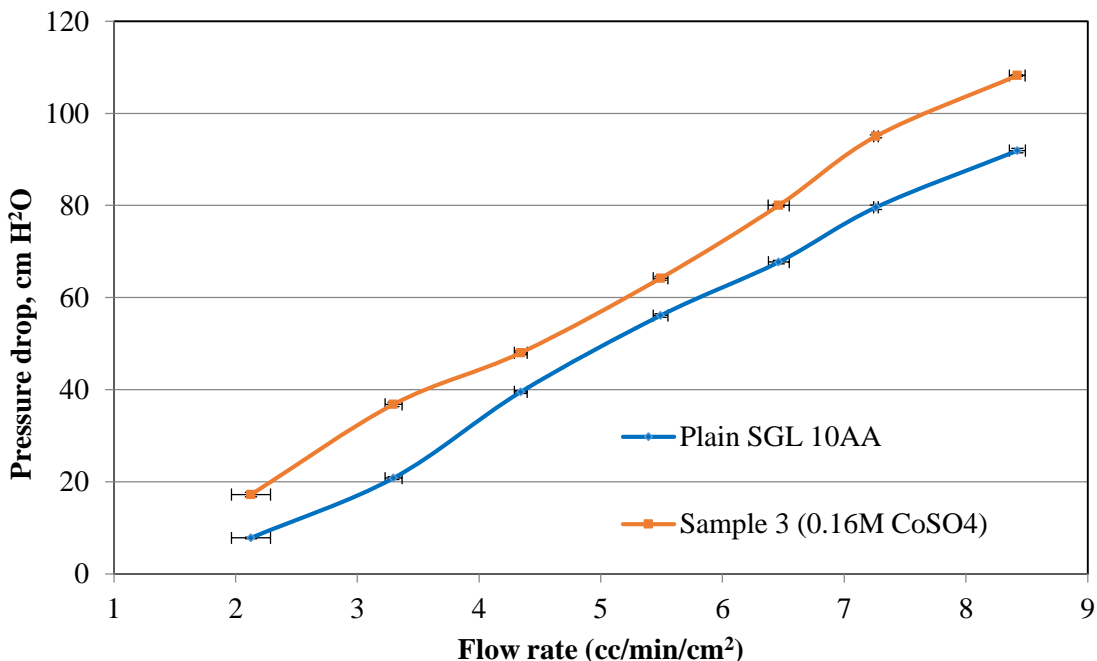
Figure 5.20: Pressure drop measurements of plain SGL 10AA (single layer) and sample 3 (synthesized at 0.16M $CoSO_4$) at different H_2O flow rates

5.9. Cost Analysis (Materials Perspective)

A preliminary cost analysis was performed to highlight the cost advantage of using MWCNT electrodes instead of commercially available carbon electrodes. In this study, commercially available SGL 10 AA carbon electrode material was chosen because of their high porosity.

5.9.1. Cost of AA Carbon Electrode Material

Cost of plain carbon electrode $(10AA)^2$: **70 \$/m²**

Thickness of SGL 10AA carbon electrode: **415 μm**

Gravimetric BET area of plain carbon electrode (AA material): **0.65 m^2/g**

BET area per unit volume of plain carbon electrode (AA material): **0.16 m^2/cm^3**

BET density of plain carbon electrode (AA material): **0.25 g/cm^3**

5.9.2. Material Costs for Electrodeposition

Cost of cobalt sulfate required per gm of carbon electrode: **0.00025 \$/g of GDL**

Cost of boric acid required per gm of carbon electrode:[3] **0.000012 \$/g of GDL**

Cost of electricity per gm carbon electrode:[3] **0.0083 \$/g of GDL**

Electrodeposition
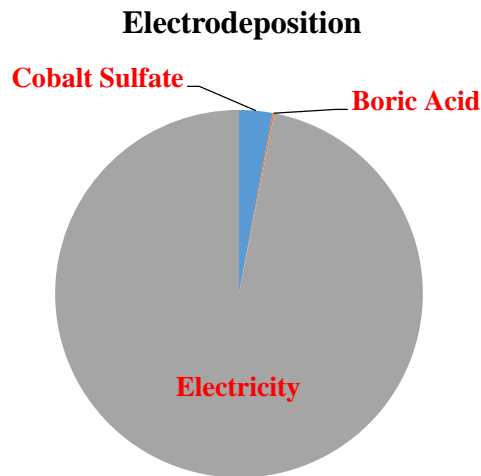
Figure 5.21. Material costs involved with electrodeposition

5.9.3. Material Costs for Chemical Vapor Deposition

Cost of acetylene required per gm of carbon electrode: **0.00089 \$/g of GDL**[4]

Cost of argon required per gm of carbon electrode: **0.026 \$/g of GDL**[4]

Cost of hydrogen required per gm of carbon electrode: **0.005 \$/g of GDL**[4]

Cost of electricity required per gm of carbon electrode: **0.225 \$/g of GDL**[4]

Chemical Vapor Deposition
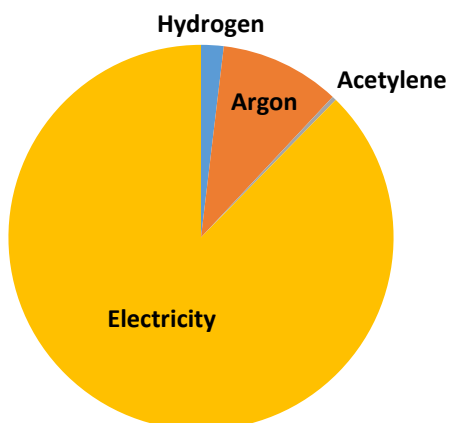
Figure 5.22. Material costs involved with chemical vapor deposition

5.9.4. Cost Benefits of Using MWCNT Electrodes

There are two cost benefits of using MWCNT-based carbon electrodes, which are explained in the following sections.

5.9.4.1. Benefit-1

The first benefit of using a MWCNT-based carbon electrode is as follows. In the case with plain porous carbon materials, an electrode with a certain thickness, or multiple layers of thinner electrodes, is needed for each H_2/Br_2 fuel cell in a stack to create the required active surface area to achieve optimal fuel cell performance. Electrode thickness is a limiting factor because a mass transport limitation is reached beyond a certain value. However, in the case with porous MWCNT-based carbon materials, one can use a thinner MWCNT-based carbon electrode to obtain the same active area as in the thicker plain electrode. The advantages resulting from this approach are better performance due to shorter mass transport distance and lower ohmic resistance. Another advantage is lower cost if the cost of a single shorter

MWCNT-based carbon electrode is lower than the cost of a thicker plain electrode. A case study was conducted to evaluate this point.

Case Study

In the case of SGL 10AA material frequently used in literature, it was found that using three pieces of plain 10 AA resulted in optimal performance of the H_2/Br_2 fuel cell. As the plain carbon electrodes have low specific surface areas, multiple layers or thick electrodes are required to enhance the fuel cell performance.

Thickness of 1 piece of plain SGL 10 AA: **0.0415 cm**

Thickness of 3 pieces of plain SGL 10 AA: **0.1245 cm**

In order to obtain a better understanding of plain carbon electrode thickness to growing multi-walled carbon nanotubes, a plot (Figure 5.23) has been generated for the cost ratio (ratio of the cost of MWCNT-based carbon electrode which involves both the cost of plain electrode used for MWCNT synthesis as well as the electrodeposition and CVD cost for the respective electrode to the cost of a 0.1245 cm thick plain electrode) versus thickness of MWCNT-based carbon electrode. The geometric area of the electrode is kept constant as the thickness is varied. Note that there are plain carbon electrodes with high porosity and wide range of thicknesses available in the market (SGL, Toray, Avcarb, etc.).

$$Cost\ ratio = \frac{Cost\ of\ MWCNT\ based\ carbon\ electrode\ at\ the\ respective\ thickness}{Cost\ of\ a\ 0.1245\ (3\ x\ 0.0415\ cm)\ cm\ thick\ plain\ carbon\ electrode} \qquad [5.1]$$

From Figure 5.23, we can see that using an electrode with thickness beyond 900 microns offers no cost advantage for the MWCNT-based carbon electrode compared to the cost of a thick plain electrode. The cost ratio exceeding 1 indicates that the cost of the MWCNT-based

carbon electrode is higher than that of the plain electrode. On the other hand, the cost is reduced when a thinner MWCNT-based carbon electrode is used. For example, by using a 415 micron thick MWCNT-based carbon electrode, same as one layer of SGL 10AA plain electrode, the cost of a MWCNT-based carbon electrode is about 47% that of a plain carbon electrode of 1245 micron thickness. We could use an even thinner MWCNT-based carbon electrode to obtain a lower cost if the thinner MWCNT-based carbon electrode has equal or higher surface area than the thicker plain electrode. A 20X increase in surface area by this method means we could use a MWCNT-based carbon electrode, 1/20 as thick or about 62.2 microns. This 62.2 micron thick MWCNT-based carbon electrode should give us the same or better performance at about $1/15^{th}$ the cost of a thicker plain electrode. As reported in the last section, using a single MWCNT-based 10AA carbon electrode resulted in higher performance than three layers of 10AA plain electrode. This shows both performance and cost advantages.
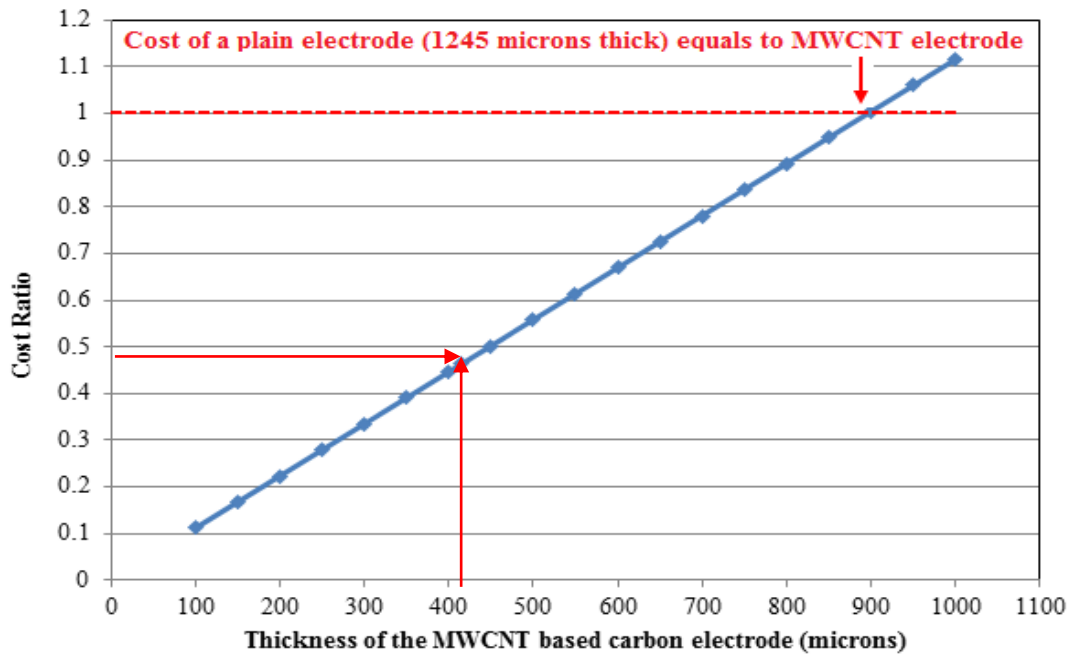
Figure 5.23. Cost versus thickness of a MWCNT-based carbon electrode

5.9.4.2. Benefit-2

The second benefit is that the performance enhancement resulting in the usage of a MWCNT-based carbon electrode might enable us to reduce the number of H_2/Br_2 fuel cells required per stack of a given power rating. This approach could result in a significant cost reduction when fewer more expensive components like membrane, catalyst, bipolar plates, gas diffusion layers, MEA frames, gaskets, endplates, etc. are used in the fuel cell stack. Also, the size and weight of the fuel cell stack are reduced due to using thinner CNT electrodes in each cell resulting in higher volumetric and gravimetric stack power densities.

Enhancement in discharge performance (at 80% discharge efficiency) with a single layer of (0.0415cm thickness) MWCNT electrode was **16 % (as reported in the previous section)** So, for every 7 fuel cells employing thicker plain carbon electrodes in a stack, one entire fuel cell could be eliminated by employing thinner MWCNT-based carbon electrodes. For a required stack power, the number of cells in a stack can be reduced by 15% using MWCNT-based carbon electrodes.

5.10. Conclusions

In this study, MWCNT-based carbon electrodes with high surface area and durability were synthesized using modified electrodeposition and CVD experimental configurations. It was found that tall MWCNTs were quickly lost once they were exposed to high fluid flow rates. Smaller Co nanoparticles with dense distribution were obtained by lowering the $CoSO_4$ concentration. The durability of carbon electrodes with a dense distribution of short MWCNTs was found to be ideal against high liquid flow rates. The higher fuel cell performance obtained with MWCNT-based carbon electrodes was expected to lower the fuel cell system cost. The increase in pressure drop in the MWCNT-based carbon electrode is quite low to cause any

resistance to the fluid flow. The preliminary cost analysis has shown that the CNT electrode material could provide significant cost advantages over that of conventional porous gas diffusion electrode materials.

5.11. References

1. M. S. Chandrasekar and Malathy Pushpavanam, "Pulse and pulse reverse plating-Conceptual advantages and applications," *Electrochimica Acta*, **53**, 3313–3322 (2008).

2. Kyu Taek Cho, Paul Albertus, Vincent Battaglia, Aleksander Kojic, Venkat Srinivasan, and Adam Z. Weber, "Optimization and Analysis of High-Power Hydrogen/Bromine-Flow Batteries for Grid-Scale Energy Storage," *Energy Technol.*, **1**, 596-608 (2013).

3. http://www.icis.com/chemicals/channel-info-chemicals-a-z/

4. http://bgs.vermont.gov/sites/bgs/files/pdfs/purchasing/Airgas-Price-List.pdf

CHAPTER 6

Future Work and Recommendations

6.1. Catalyst Development

Since it is very challenging to fabricate a membrane that completely prevents the crossover of bromine (Br_2, Br^-, and Br_3^-) species to the hydrogen (H_2) electrode, an active catalyst that is stable in HBr/Br_2 solution is necessary. The rhodium sulfide catalyst (Rh_xS_y) exhibits excellent stability in HBr/Br_2 environment but its hydrogen oxidation activity is quite low. Hence, it is very important to understand the hydrogen oxidation electrochemistry of the Rh_xS_y catalyst material. The active phases of Rh_xS_y that will improve the activity of hydrogen oxidation reaction (HOR) must be identified and synthesized. The other option is to develop Pt-alloy catalysts with higher stability than pure Pt.[1] This option might prolong the life time of the fuel cell but eventually fails due to the presence of Pt. Research in this area is undergoing in our research group.

6.2 Alkaline H_2-Br_2 Fuel Cell Development

Recently, an alkaline version of the H_2-Br_2 system has been developed and tested by our research group, which doesn't require Pt or any noble metal catalyst for H_2 reactions. The hydrogen evolution and oxidation reactions in alkaline medium can be accomplished using inexpensive catalysts such as Ni. The other advantages of alkaline H_2-Br_2 system include high open circuit potential and low corrosivity of electrolytes (HBr solution is replaced with KBr). However, the performance of alkaline based H_2-Br_2 system is limited by the two phase H_2 reactions and low ionic conductivity of membranes used in this system due to slow K^+ ion diffusivity.[2] A complex electrode structure is required to handle the two phase reactions, which is an engineering challenge. The engineering challenges are much easier to solve as opposed

to the material related challenges such as catalyst development discussed in the previous section.

6.3 High Surface Area Carbon Electrodes

The high surface area carbon electrodes developed in this study can be used in different flow battery systems (all-vanadium, iron-chromium, vanadium-polyhalide, zinc-bromine etc.). Hence, it is worthwhile to come up with a carbon nanotube (CNT) electrode synthesis procedure that is cost effective and suitable for large scale synthesis. In this study, the CNT based electrodes were synthesized using two steps: electrodeposition and chemical vapor deposition. For future studies, a process that facilitates the synthesis of CNT based electrodes in a single step is recommended. The cost of CNT electrode synthesis will be greatly reduced by this approach. One way to synthesize CNT electrodes in a single step is to deposit Co nanoparticles by thermal reduction.[3] The Co nanoparticle deposition and CNT growth can be accomplished in a single step using the quartz tube furnace. The Co nanoparticle deposition by thermal reduction is the major challenge in this area.

6.4 Contributions to this Area

This research contributed to the H_2-Br_2 fuel cell area through the following publications.

1. Venkata Yarlagadda, Guangyu Lin, Pau Ying Chong, and Trung Van Nguyen, "Durable and High Surface Area Carbon Nanotube Electrodes for Reversible H_2-Br_2 Fuel Cell Applications," (**manuscript in preparation**).

2. Venkata Yarlagadda, Guangyu Lin, Pau Ying Chong, and Trung Van Nguyen, "H_2-Br_2 Fuel Cell Performance with High Surface Area Bromine Electrode Materials," (**manuscript in preparation**).

3. Venkata Yarlagadda, Regis P. Dowd Jr., Jun Woo Park, Peter N. Pintauro, and Trung Van Nguyen, "A Comprehensive Study of an Acid-Based Reversible H_2-Br_2 Fuel Cell System," *Journal of the Electrochemical Society*, Vol. 162 (8), F919-F926 (2015).

4. Venkata Yarlagadda and Trung Van Nguyen, "High Surface Area Carbon Electrodes for the Bromine Reactions in H_2-Br_2 Fuel Cells," *ECS Transactions*, Vol.58 (36), 25-32 (2014).

5. Venkata Yarlagadda and Trung Van Nguyen, "A 1D Mathematical Model of a H_2/Br_2 fuel cell," *Journal of the Electrochemical Society*, Vol.160 (6), F535-F547 (2013).

6. Haley Kreutzer, Venkata Yarlagadda, and Trung Van Nguyen, "Performance Evaluation of a Regenerative Hydrogen-Bromine Fuel Cell," *Journal of the Electrochemical Society*, Vol.159 (7), F331-F337 (2012).

6.4. References

1. Bernard O. Odera, "Electrolytic etching of Platinum-Aluminum Based Alloys," *Platinum Metals Rev*., 56 (4), 257–261 (2012).

2. Trung Van Nguyen, Venkata Yarlagadda, Guangyu Lin, Guoming Weng, Chi-Ying Vanessa Li, Kwong-Yu Chan, "Comparison of Acid and Alkaline Hydrogen-Bromine Fuel Cell systems," *ECS Transactions*, **58** (37), 29 (2014).

3. Andrei Y. Khodakov, "Enhancing Cobalt Dispersion in Supported Fischer-Tropsch Catalysts Via Controlled Decomposition of Cobalt Precursors," *Brazilian Journal of Physics*, 39 (1A) (2009).

APPENDIX A

Experimental Data (CHAPTER 2)

Table A.1. Experimental data for Figure 2.4 (Pt on Toray 090)

Voltage (V)	Current density (A/cm^2)	Power density (W/cm^2)
1.0206	0	0
0.9737	0.0868	0.084517
0.9487	0.1328	0.125987
0.9236	0.1769	0.163385
0.8989	0.2231	0.200545
0.8739	0.2665	0.232894
0.8487	0.3078	0.26123
0.8235	0.3536	0.29119
0.799	0.3927	0.313767
0.7741	0.434	0.335959
0.7488	0.4715	0.353059
0.7241	0.5017	0.363281
0.6991	0.5361	0.374788
0.6743	0.5585	0.376597
0.6489	0.582	0.37766
0.6243	0.5993	0.374143
0.5993	0.6112	0.366292
1.0206	0	
1.0489	0.0538	
1.0741	0.1004	
1.0989	0.1451	
1.124	0.1857	
1.149	0.2241	
1.1739	0.2588	
1.1989	0.2914	

Table A.2. Experimental data for Figure 2.4 (Plain SGL 10AA)

Voltage (V)	Current density (A/cm²)	Power density (W/cm²)
1.020829	0	0
0.948992	0.134	0.127165
0.899019	0.220404	0.198147
0.849142	0.29583	0.251202
0.799265	0.36841	0.294457
0.748968	0.435418	0.326114
0.699148	0.503794	0.352226
0.648946	0.570823	0.370433
0.598878	0.648871	0.388594
1.022357	0	
1.049224	0.042912	
1.09933	0.133867	
1.149437	0.232692	
1.199429	0.32923	
1.249439	0.425977	

Table A.3. Experimental data for Figure 2.5 (Untreated first run)

Voltage (V)	Current density (A/cm²)	Voltage (V)_IR	Power density (W/cm²)
1.03357	0	1.03357	0
0.949122	0.132247	0.976497	0.129139
0.899241	0.20511	0.941699	0.193152
0.849527	0.282738	0.908054	0.256742
0.800008	0.354219	0.873331	0.30935
0.749988	0.42684	0.838344	0.357839
0.700191	0.50718	0.805178	0.40837
0.65045	0.588875	0.772347	0.454816
0.600403	0.667537	0.738583	0.493031
1.032857	0	1.032857	
1.04891	0.024177	1.043906	
1.098902	0.101563	1.077878	
1.149116	0.173916	1.113115	
1.19908	0.244873	1.148391	
1.249543	0.311118	1.185142	

Table A.4. Experimental data for Figure 2.5 (Untreated second run)

Voltage (V)	Current density (A/cm^2)	Voltage (V)_IR	Power density (W/cm^2)
1.033265	0	1.033265	0
0.948983	0.148382	0.979698	0.14537
0.899158	0.244159	0.949699	0.231878
0.849388	0.330969	0.917899	0.303796
0.799647	0.4159	0.885738	0.368378
0.74985	0.501367	0.853633	0.427984
0.700108	0.576714	0.819488	0.47261
0.650172	0.666302	0.788097	0.52511
0.600486	0.760643	0.757939	0.576521
1.032654	0	1.032654	
1.048994	0.027761	1.043247	
1.09893	0.122934	1.073482	
1.149171	0.213542	1.104968	
1.19908	0.279318	1.141261	
1.24946	0.357523	1.175453	

Table A.5. Experimental data for Figure 2.5 (Acid treated first run)

Voltage (V)	Current density (A/cm^2)	Voltage (V)_IR	Power density (W/cm^2)
1.030515	0	1.030515	0
0.948705	0.139644	0.981382	0.137044
0.898797	0.232816	0.953276	0.221938
0.848944	0.327211	0.925511	0.302837
0.799258	0.417605	0.896977	0.374582
0.749377	0.503032	0.867087	0.436172
0.699858	0.581452	0.835918	0.486046
0.649894	0.659295	0.804169	0.530185
0.600014	0.736131	0.772268	0.568491
1.030617	0	1.030617	
1.048605	0.033614	1.040739	
1.098624	0.12284	1.06988	
1.148885	0.192211	1.103907	
1.198774	0.272123	1.135097	
1.248849	0.332054	1.171148	

Table A.6. Experimental data for Figure 2.5 (DI water boiled first run)

Voltage (V)	Current density (A/cm²)	Voltage (V)_IR	Power density (W/cm²)
1.029955	0	1.029955	0
0.948844	0.134328	0.985717	0.132409
0.898963	0.215379	0.958085	0.206352
0.84925	0.295826	0.930454	0.275253
0.799508	0.376784	0.902935	0.340211
0.7496	0.453647	0.874126	0.396544
0.699969	0.54004	0.84821	0.458068
0.650089	0.617038	0.819466	0.505641
0.600264	0.704143	0.793551	0.558773
1.029395	0	1.029395	
1.048772	0.033708	1.039519	
1.098819	0.116799	1.066757	
1.148977	0.189313	1.09701	
1.199191	0.259424	1.127979	
1.249182	0.321508	1.160928	

Table A.7. Experimental data for Figure 2.6, Figure 2.11

Temperature: 25C (Nafion 115)

Voltage (V)	Current density (A/cm^2)	Voltage (V)_IR	Power density (W/cm^2)
1.031024	0	1.031024	0
0.949205	0.086084	0.958502	0.082512
0.89938	0.138973	0.914389	0.127075
0.849694	0.191163	0.87034	0.166377
0.79998	0.238374	0.825724	0.196831
0.749877	0.288282	0.781012	0.225152
0.701219	0.33599	0.737506	0.247794
0.650783	0.386583	0.692534	0.267722
0.600875	0.433082	0.647648	0.280484
1.030006	0	1.030006	
1.049299	0.021465	1.046981	
1.099346	0.084274	1.090245	
1.149532	0.153432	1.132962	
1.199441	0.221932	1.175472	
1.249599	0.272606	1.220157	

Table A.8. Experimental data for Figure 2.6, Figure 2.11

Temperature: 45C (Nafion 115)

Voltage (V)	Current density (A/cm²)	Voltage (V)_IR	Power density (W/cm²)
1.021401	0	1.021401	0
0.949316	0.117522	0.962008	0.113057
0.899408	0.20307	0.921339	0.187096
0.849666	0.285692	0.880521	0.251557
0.79973	0.356434	0.838225	0.298772
0.749877	0.424075	0.795677	0.337427
0.700052	0.493434	0.753343	0.371725
0.6507	0.550914	0.710198	0.391258
0.600458	0.614017	0.666772	0.40941
1.020637	0	1.020637	
1.049299	0.048822	1.044026	
1.099263	0.142693	1.083852	
1.14931	0.24145	1.123234	
1.199607	0.336623	1.163252	
1.250071	0.410801	1.205704	

Table A.9. Experimental data for Figure 2.6, Figure 2.10: Temperature: 25C (Nafion 212)

Figure 2.7: Single layer (25C)

Voltage (V)	Current density (A/cm²)	Voltage (V)_IR	Power density (W/cm²)
1.020829	0	1.020829	0
0.948992	0.134	0.958942	0.128498
0.899019	0.220404	0.915384	0.201754
0.849142	0.29583	0.871108	0.2577
0.799265	0.36841	0.826619	0.304535
0.748968	0.435418	0.781297	0.340191
0.699148	0.503794	0.736554	0.371071
0.648946	0.570823	0.691329	0.394626
0.598878	0.648871	0.647056	0.419856
1.022357	0	1.022357	
1.049224	0.042912	1.046038	
1.09933	0.133867	1.089391	
1.149437	0.232692	1.132159	
1.199429	0.32923	1.174983	
1.249439	0.425977	1.217811	

Table A.10. Experimental data for Figure 2.6, Figure 2.10

Temperature: 45C (Nafion 212)

Voltage (V)	Current density (A/cm^2)	Voltage (V)_IR	Power density (W/cm^2)
1.006062	0	1.006062	0
0.949431	0.156996	0.961088	0.150887
0.899337	0.288374	0.920749	0.26552
0.849333	0.406769	0.879536	0.357768
0.799399	0.514834	0.837625	0.431238
0.749235	0.604438	0.794114	0.479993
0.699319	0.678778	0.749719	0.508893
0.648602	0.740287	0.703568	0.520842
0.598305	0.785958	0.656662	0.516109
1.004331	0	1.004331	
1.048422	0.120014	1.039511	
1.098452	0.266041	1.078698	
1.148577	0.415931	1.117694	
1.198512	0.552344	1.1575	
1.248919	0.663501	1.199654	

Table A.11. Experimental data for Figure 2.7

Double layer (25C)

Voltage (V)	Current density (A/cm²)	Voltage (V)_IR	Power density (W/cm²)
1.0227	0	1.0227	0
0.949684	0.144628	0.97832	0.13961002
0.899868	0.236269	0.946649	0.2186395
0.850109	0.323111	0.914085	0.28595434
0.800407	0.402837	0.880169	0.33995958
0.750514	0.485037	0.846552	0.38943526
0.700889	0.564117	0.812584	0.42975228
0.65092	0.635427	0.776735	0.45721924
0.601238	0.69905	0.739649	0.47307126
1.022267	0	1.022267	
1.049622	0.052792	1.039169	
1.099725	0.155045	1.069026	
1.149827	0.257733	1.098796	
1.199892	0.360208	1.128571	
1.249956	0.451073	1.160644	

Table A.12. Experimental data for Figure 2.7

Double layer (45C)

Voltage (V)	Current density (A/cm^2)	Voltage (V)_IR	Power density (W/cm^2)
1.010047	0	1.010047	0
0.949589	0.182595	0.969309	0.176991
0.89981	0.323526	0.934751	0.302416
0.84988	0.450069	0.898487	0.404382
0.799796	0.566794	0.86101	0.488015
0.749923	0.678534	0.823204	0.558572
0.700755	0.766087	0.783493	0.600223
0.650958	0.852587	0.743038	0.633504
0.60118	0.922983	0.700862	0.646884
1.009028	0	1.009028	
1.049603	0.115971	1.032068	
1.099687	0.258711	1.060569	
1.149866	0.404976	1.088633	
1.199873	0.539881	1.118243	
1.249842	0.631881	1.154301	

Table A.13. Experimental data for Figure 2.10

Temperature: 25C (25 micron composite)

Voltage (V)	Current density (A/cm^2)	Voltage (V)_IR	Power density (W/cm^2)
1.030261	0	1.030261	0
0.949188	0.123744	0.962552	0.11911
0.899314	0.196752	0.920563	0.181122
0.849612	0.263641	0.878086	0.231499
0.799853	0.329534	0.835443	0.275307
0.749999	0.389363	0.79205	0.308395
0.700221	0.429729	0.746632	0.32085
0.650443	0.507416	0.705244	0.357852
0.600455	0.578459	0.662928	0.383477
1.029395	0	1.029395	
1.049202	0.023472	1.046667	
1.099209	0.096628	1.088773	
1.149369	0.181984	1.129715	
1.199357	0.27571	1.169581	
1.249689	0.359562	1.210856	

Table A.14. Experimental data for Figure 2.10

Temperature: 45C (25 micron composite)

Voltage (V)	Current density (A/cm^2)	Voltage (V)_IR	Power density (W/cm^2)
1.015444	0	1.015444	0
0.948901	0.151799	0.965295	0.146531
0.899104	0.269686	0.92823	0.25033
0.849288	0.37756	0.890064	0.336052
0.799624	0.475494	0.850978	0.404635
0.749808	0.572663	0.811656	0.464805
0.700087	0.674511	0.772934	0.521352
0.650137	0.785808	0.735005	0.577573
0.600436	0.88031	0.695509	0.612263
1.014018	0	1.014018	
1.048954	0.076768	1.040663	
1.098904	0.200755	1.077222	
1.149216	0.338954	1.112609	
1.198498	0.490341	1.145541	
1.248887	0.590177	1.185148	

Table A.15. Experimental data for Figure 2.11

Temperature: 25C (65 micron composite)

Voltage (V)	Current density (A/cm²)	Voltage (V)_IR	Power density (W/cm²)
1.031432	0	1.031432	0
0.948672	0.09615	0.959056	0.092213
0.898798	0.151383	0.915148	0.138538
0.84904	0.204864	0.871165	0.17847
0.799777	0.259488	0.827802	0.214805
0.74935	0.312719	0.783123	0.244898
0.699763	0.367731	0.739478	0.271929
0.649774	0.426684	0.695856	0.296911
0.600092	0.488073	0.652804	0.318616
1.031024	0	1.031024	
1.048553	0.016265	1.046796	
1.098541	0.072246	1.090738	
1.148701	0.139467	1.133638	
1.198746	0.212641	1.175781	
1.248925	0.285972	1.21804	

Table A.16. Experimental data for Figure 2.11

Temperature: 45C (65 micron composite)

Voltage (V)	Current density (A/cm²)	Voltage (V)_IR	Power density (W/cm²)
1.018728	0	1.018728	0
0.948615	0.13515	0.963211	0.130178
0.89876	0.227179	0.923296	0.209753
0.848944	0.307034	0.882104	0.270836
0.799242	0.378593	0.84013	0.318068
0.74935	0.451555	0.798118	0.360394
0.699801	0.52053	0.756018	0.39353
0.649851	0.591222	0.713703	0.421957
0.600016	0.667552	0.672111	0.448669
1.017735	0	1.017735	
1.048591	0.055293	1.042619	
1.098636	0.150302	1.082404	
1.148796	0.25561	1.12119	
1.198727	0.361804	1.159652	
1.248906	0.471718	1.197961	

Table A.17. Experimental data for Figure 2.12, Figure 2.14

Pt: day 1

Voltage (V)	Current density (A/cm^2)	Voltage (V)_IR
0.995892	0	0.995892
0.948939	0.073272	0.961716
0.899104	0.143465	0.924121
0.849269	0.203332	0.884725
0.799624	0.260337	0.845021
0.74977	0.319631	0.805506
0.700011	0.388699	0.76779
0.650118	0.475624	0.733055
0.600416	0.563324	0.698646
0.996197	0	0.996197
1.048858	0.061236	1.03818
1.098808	0.146878	1.073196
1.149102	0.254567	1.104712
1.199071	0.376072	1.133493
1.249307	0.49479	1.163028

Table A.18. Experimental data for Figure 2.12

Pt: day 3

Voltage (V)	Current density (A/cm^2)	Voltage (V)_IR
0.990698	0	0.990698
0.9485	0.009751	0.950082
0.898703	0.01718	0.90149
0.848906	0.018389	0.851889
0.799204	0.017032	0.801967
0.749292	0.014559	0.751654
0.699705	0.012058	0.701661
0.649794	0.009714	0.651369
0.600035	0.007841	0.601307
0.98917	0	0.98917
1.048534	0.032941	1.04319
1.09856	0.079776	1.085618
1.148701	0.13345	1.127052
1.198708	0.191831	1.167588
1.248887	0.252888	1.207862

Table A.19. Experimental data for Figure 2.12

Pt: day 5

Voltage (V)	Current density (A/cm^2)	Voltage (V)_IR
0.990392	0	0.990392
0.948882	0.005432	0.949875
0.899009	0.009585	0.90076
0.849173	0.009797	0.850963
0.799471	0.008505	0.801025
0.749483	0.006872	0.750739
0.699801	0.005432	0.700793
0.649985	0.004085	0.650731
0.600168	0.003069	0.600729
0.983671	0	0.983671
1.048744	0.022798	1.044578
1.09877	0.058818	1.088024
1.148968	0.103808	1.130002
1.198861	0.152009	1.171089
1.249097	0.207778	1.211136

Table A.19. Experimental data for Figure 2.12, Figure 2.14

Pt: day 7

Voltage (V)	Current density (A/cm^2)	Voltage (V)_IR
0.984741	0	0.984741
0.948481	0.003365	0.949056
0.898741	0.00593	0.899755
0.848887	0.006069	0.849925
0.799166	0.005091	0.800036
0.74935	0.004075	0.750047
0.699686	0.003088	0.700214
0.649774	0.002165	0.650145
0.599939	0.001556	0.600205
0.970076	0	0.970076
1.048725	0.018682	1.04553
1.098636	0.051223	1.089877
1.148911	0.093066	1.132997
1.198765	0.139237	1.174956
1.249078	0.189339	1.216701

Table A.20. Experimental data for Figure 2.13, Figure 2.14

RhxSy: day 1

Voltage (V)	Current density (A/cm^2)	Voltage (V)_IR
0.996401	0	0.996401
0.948787	0.015039	0.951544
0.898913	0.02652	0.903776
0.849192	0.037446	0.856059
0.799433	0.048751	0.808373
0.749617	0.060869	0.760779
0.699896	0.074795	0.713612
0.650004	0.090004	0.666508
0.600168	0.10728	0.619841
0.994975	0	0.994975
1.048706	0.032442	1.042778
1.098713	0.086356	1.082935
1.148892	0.156716	1.12026
1.198803	0.242801	1.154444
1.249135	0.332227	1.188437

Table A.21. Experimental data for Figure 2.13

RhxSy: day 3

Voltage (V)	Current density (A/cm^2)	Voltage (V)_IR
0.996706	0	0.996706
0.948557	0.015888	0.951453
0.898741	0.028098	0.903862
0.848944	0.039956	0.856226
0.799223	0.052184	0.808734
0.74935	0.064671	0.761136
0.699591	0.078237	0.713849
0.649832	0.092957	0.666773
0.599977	0.110085	0.62004
0.995281	0	0.995281
1.048553	0.031501	1.042812
1.098579	0.08188	1.083656
1.148834	0.148105	1.121842
1.198765	0.229318	1.156972
1.249021	0.318753	1.190928

Table A.22. Experimental data for Figure 2.13

RhxSy: day 5

Voltage (V)	Current density (A/cm^2)	Voltage (V)_IR
0.995051	0	0.995051
0.948748	0.015002	0.951607
0.898779	0.026575	0.903844
0.849116	0.037732	0.856307
0.7993	0.049425	0.808719
0.749483	0.060878	0.761085
0.699858	0.072395	0.713655
0.64987	0.084817	0.666034
0.600073	0.099518	0.619038
0.995433	0	0.995433
1.048648	0.028769	1.043166
1.098636	0.074784	1.084384
1.148758	0.135637	1.122909
1.19888	0.205701	1.159678
1.248963	0.291759	1.193361

Table A.23. Experimental data for Figure 2.13, Figure 2.14

RhxSy: day 7

Voltage (V)	Current density (A/cm^2)	Voltage (V)_IR
0.995281	0	0.995281
0.948596	0.013719	0.951257
0.898722	0.025015	0.903574
0.84902	0.035711	0.855947
0.799223	0.046278	0.808199
0.749369	0.056734	0.760372
0.699705	0.066996	0.712699
0.649755	0.078523	0.664985
0.599996	0.090613	0.617571
0.996044	0	0.996044
1.048648	0.024866	1.043826
1.09856	0.064521	1.086046
1.148796	0.118075	1.125896
1.198765	0.184485	1.162984
1.248983	0.258997	1.19875

Table A.24. Experimental data for Figure 2.15

First run

Voltage (V)	Current density (A/cm^2)	Voltage (V)_IR
1.000321	0	1.000321
0.949122	0.05874	0.963131
0.899213	0.110434	0.925552
0.849388	0.159511	0.887432
0.799675	0.205016	0.848571
0.749961	0.256267	0.81108
0.700025	0.316431	0.775494
0.650366	0.386999	0.742666
0.600514	0.45362	0.708702
1.000321	0	1.000321
1.049077	0.039869	1.039568
1.099124	0.101456	1.074927
1.149282	0.179366	1.106503
1.199163	0.264981	1.135965
1.249432	0.354798	1.164813

Table A.25. Experimental data for Figure 2.15

After 8 hours

Voltage (V)	Current density (A/cm^2)	Voltage (V)_IR
1.000932	0	1.000932
0.949649	0.019248	0.954301
0.899713	0.032014	0.907449
0.850111	0.037397	0.859147
0.800341	0.035826	0.808999
0.750405	0.031343	0.757979
0.700691	0.026014	0.706977
0.650839	0.021289	0.655983
0.601125	0.01749	0.605351
1.00078	0	1.00078
1.049605	0.032875	1.04166
1.09968	0.075535	1.081426
1.149866	0.123833	1.119941
1.199774	0.181594	1.155891
1.25725	0.25446	1.19576

Table A.26. Experimental data for Figure 2.16

First run

Voltage (V)	Current density (A/cm^2)	Voltage (V)_IR
1.002002	0	1.002002
0.949538	0.043907	0.959951
0.899713	0.081694	0.919087
0.850055	0.123254	0.879285
0.800258	0.173055	0.841298
0.7504	0.228581	0.804608
0.700858	0.291222	0.769921
0.650755	0.368193	0.738072
0.601097	0.444801	0.706581
1.001543	0	1.001543
1.049605	0.029707	1.04256
1.099652	0.083026	1.079962
1.149754	0.156654	1.112604
1.199802	0.229047	1.145483
1.249099	0.34073	1.168295

Table A.27. Experimental data for Figure 2.16

After 8 hours

Voltage (V)	Current density (A/cm^2)	Voltage (V)_IR
1.000576	0	1.000576
0.948955	0.04376	0.959362
0.899047	0.081842	0.918511
0.849333	0.123227	0.878639
0.799702	0.169363	0.839981
0.749877	0.223836	0.803111
0.700247	0.285974	0.768259
0.650839	0.35783	0.735939
0.600902	0.432303	0.703715
1.001391	0	1.001391
1.04966	0.03011	1.042499
1.099707	0.08265	1.080051
1.149866	0.154264	1.113178
1.199802	0.237289	1.143368
1.250071	0.332394	1.171019

APPENDIX B

Experimental Data (CHAPTER 4 AND CHAPTER 5)

Table B.1. Experimental data for Figure 4.18

Plain SGL 10AA		Sample 1 (-1mA for 1000s)		Sample 3 (-15mA for 1s)		Sample 4 (-20mA for 0.2s)	
η (V)	I (A/g)	η (V)	I (A/g)	η (V)	I (A/g)	η (V)	I (A/g)
0.00276	0.00242	0.00271	0.05496	0.00291	0.02019	0.00271	0.03418
0.00545	0.00540	0.00535	0.12308	0.00554	0.03991	0.00543	0.06764
0.00817	0.00825	0.00801	0.18754	0.00828	0.06218	0.00815	0.10085
0.01085	0.01140	0.01067	0.25122	0.01105	0.08246	0.01087	0.13355
0.00818	0.00807	0.00800	0.18996	0.00830	0.06100	0.00815	0.10064
0.00547	0.00527	0.00537	0.11843	0.00554	0.03976	0.00544	0.06668
0.00274	0.00253	0.00272	0.05355	0.00279	0.01855	0.00272	0.03363
-0.00269	-0.00303	-0.00266	-0.06456	-0.00277	-0.01996	-0.00269	-0.03625
-0.00539	-0.00605	-0.00533	-0.12633	-0.00552	-0.04132	-0.00541	-0.07004
-0.00811	-0.00881	-0.00802	-0.18490	-0.00831	-0.06030	-0.00811	-0.10515
-0.01084	-0.01149	-0.01070	-0.24642	-0.01109	-0.07906	-0.01080	-0.14239
-0.00811	-0.00876	-0.00804	-0.18105	-0.00831	-0.06013	-0.00812	-0.10416
-0.00541	-0.00588	-0.00535	-0.12284	-0.00553	-0.04079	-0.00541	-0.06941
-0.00269	-0.00308	-0.00266	-0.06409	-0.00278	-0.01901	-0.00270	-0.03560

Table B.2. Experimental data for Figure 4.19

Plain SGL 10AA		Sample 4r (-20mA for 0.2s)		Sample 5 (-10mA for 1s)	
η (V)	I (A/g)	η (V)	I (A/g)	η (V)	I (A/g)
0.0030	0.0060	0.0027	0.0867	0.0021	0.1719
0.0059	0.0128	0.0054	0.1952	0.0038	0.4065
0.0089	0.0198	0.0080	0.3009	0.0056	0.6283
0.0118	0.0274	0.0107	0.4186	0.0074	0.8520
0.0148	0.0344	0.0133	0.5268	0.0092	1.0803
0.0177	0.0416	0.0159	0.6378	0.0109	1.3309
0.0206	0.0495	0.0186	0.7508	0.0126	1.5654
0.0236	0.0565	0.0212	0.8575	0.0143	1.8101
0.0207	0.0476	0.0186	0.7369	0.0127	1.5601
0.0177	0.0400	0.0160	0.6244	0.0109	1.3245
0.0148	0.0324	0.0133	0.5126	0.0092	1.0771
0.0118	0.0249	0.0107	0.4046	0.0075	0.8496
0.0089	0.0175	0.0081	0.2901	0.0057	0.6252

0.0059	0.0105	0.0054	0.1866	0.0038	0.4068
0.0030	0.0042	0.0027	0.0787	0.0021	0.1770
-0.0029	-0.0096	-0.0026	-0.1277	-0.0017	-0.2364
-0.0059	-0.0163	-0.0053	-0.2306	-0.0036	-0.4531
-0.0088	-0.0225	-0.0079	-0.3393	-0.0055	-0.6566
-0.0118	-0.0293	-0.0106	-0.4441	-0.0074	-0.8578
-0.0147	-0.0360	-0.0132	-0.5529	-0.0095	-1.0349
-0.0177	-0.0430	-0.0159	-0.6510	-0.0114	-1.2365
-0.0206	-0.0496	-0.0186	-0.7460	-0.0134	-1.4241
-0.0236	-0.0565	-0.0212	-0.8554	-0.0151	-1.6576
-0.0207	-0.0488	-0.0186	-0.7407	-0.0133	-1.4420
-0.0177	-0.0410	-0.0159	-0.6438	-0.0113	-1.2449
-0.0148	-0.0339	-0.0133	-0.5330	-0.0094	-1.0474
-0.0118	-0.0263	-0.0106	-0.4260	-0.0075	-0.8461
-0.0089	-0.0194	-0.0080	-0.3174	-0.0056	-0.6427
-0.0059	-0.0127	-0.0053	-0.2106	-0.0037	-0.4297
-0.0030	-0.0058	-0.0027	-0.1061	-0.0019	-0.2095

Table B.3. Experimental data for Figure 4.20

3 pc Plain – 10 cc/min/cm²		3 pc Plain – 20 cc/min/cm²		Sample 5(MWCNT – 10 cc/min/cm²)	
I (A.cm²)	V	I (A.cm²)	V	I (A.cm²)	V
0	1.086478	0	1.087604	0	1.081869
0.099848	1.049714	0.09979745	1.052786	0.124717	1.043774
0.199883	1.012438	0.19978136	1.017763	0.208037	1.017661
0.299918	0.974344	0.29996912	0.982229	0.333093	0.976801
0.400004	0.93543	0.40000399	0.945875	0.416413	0.948845
0.500141	0.895082	0.50003886	0.907575	0.49958	0.92181
0.600074	0.854427	0.60017566	0.868661	0.624637	0.881257
0.700312	0.814182	0.70021053	0.829747	0.707957	0.848385
0.800245	0.774756	0.80034733	0.791345	0.833013	0.800459
0.900331	0.733998	0.90028028	0.752226	0.916486	0.76728
1.000417	0.692012	1.00041707	0.713824	0.999806	0.729492
0	1.083713	0	1.08402	0	1.079104
0.10017	1.122729	0.10017039	1.120271	0.12509	1.115663
0.200307	1.160721	0.20025622	1.154577	0.208563	1.139319
0.300291	1.197997	0.30039301	1.188268	0.29173	1.162053
0.400581	1.235785	0.4005298	1.22196	0.416939	1.196154
0.500514	1.275313	0.50046275	1.255754	0.500259	1.21858
		0.60054859	1.290059	0.583426	1.2407

Table B.4. Experimental data for Figure 5.7

Plain SGL 10AA		Sample 1 (-30mA for 5s)		Sample 2 (-30mA for 15s)	
η (V)	I (A/g)	η (V)	I (A/g)	η (V)	I (A/g)
0.0029	0.0127	0.0015	0.2467	0.0013	0.3388
0.0057	0.0289	0.0029	0.5120	0.0025	0.7059
0.0086	0.0440	0.0041	0.8100	0.0035	1.1057
0.0114	0.0601	0.0053	1.1122	0.0046	1.4940
0.0142	0.0760	0.0066	1.4068	0.0056	1.9037
0.0171	0.0925	0.0077	1.7222	0.0067	2.2891
0.0199	0.1092	0.0089	2.0208	0.0076	2.7056
0.0227	0.1266	0.0100	2.3365	0.0085	3.1214
0.0199	0.1085	0.0089	2.0176	0.0077	2.6884
0.0171	0.0920	0.0076	1.7252	0.0067	2.2899
0.0143	0.0753	0.0064	1.4333	0.0057	1.8866
0.0114	0.0586	0.0052	1.1341	0.0047	1.4828
0.0086	0.0433	0.0040	0.8278	0.0036	1.0813
0.0057	0.0279	0.0028	0.5306	0.0026	0.6933
0.0029	0.0124	0.0015	0.2566	0.0015	0.3072
-0.0028	-0.0167	-0.0008	-0.3705	-0.0007	-0.4563
-0.0057	-0.0311	-0.0021	-0.6486	-0.0018	-0.8463
-0.0085	-0.0457	-0.0034	-0.9308	-0.0029	-1.2249
-0.0114	-0.0603	-0.0047	-1.2144	-0.0041	-1.6010
-0.0143	-0.0733	-0.0060	-1.4989	-0.0052	-1.9709
-0.0171	-0.0879	-0.0074	-1.7741	-0.0064	-2.3433
-0.0200	-0.1002	-0.0086	-2.0666	-0.0075	-2.7344
-0.0229	-0.1151	-0.0099	-2.3514	-0.0087	-3.0970
-0.0200	-0.1008	-0.0086	-2.0711	-0.0076	-2.7159
-0.0171	-0.0862	-0.0073	-1.7897	-0.0065	-2.3196
-0.0143	-0.0714	-0.0059	-1.5167	-0.0053	-1.9526
-0.0114	-0.0570	-0.0047	-1.2247	-0.0042	-1.5755
-0.0086	-0.0438	-0.0034	-0.9373	-0.0031	-1.1883
-0.0057	-0.0288	-0.0021	-0.6478	-0.0019	-0.8211
-0.0028	-0.0151	-0.0009	-0.3540	-0.0009	-0.4218

Table B.5. Experimental data for Figure 5.9

CVD: 15 min		CVD: 30 min		CVD: 45 min		CVD: 60 min	
η (V)	I (A/g)	η (V)	I (A/g)	η (V)	I (A/g)	η (V)	I (A/g)
0.0016	0.2338	0.0000	0.0000	0.0000	0.0000	0.0000	0.0000
0.0028	0.5440	0.0015	0.2710	0.0013	0.3388	0.0013	0.3311
0.0041	0.8456	0.0026	0.6139	0.0025	0.7059	0.0024	0.7081
0.0054	1.1409	0.0037	0.9444	0.0035	1.1057	0.0033	1.1214
0.0067	1.4375	0.0048	1.2785	0.0046	1.4940	0.0044	1.5093
0.0079	1.7373	0.0060	1.6117	0.0056	1.9037	0.0053	1.9085
0.0092	2.0339	0.0070	1.9557	0.0067	2.2891	0.0063	2.3212
0.0105	2.3253	0.0083	2.2683	0.0076	2.7056	0.0072	2.7308
0.0092	2.0343	0.0093	2.6208	0.0085	3.1214	0.0081	3.1475
0.0080	1.7227	0.0082	2.2811	0.0077	2.6884	0.0071	2.7402
0.0067	1.4366	0.0071	1.9503	0.0067	2.2899	0.0062	2.3323
0.0055	1.1195	0.0060	1.5997	0.0057	1.8866	0.0053	1.9131
0.0042	0.8208	0.0050	1.2563	0.0047	1.4828	0.0044	1.5035
0.0029	0.5302	0.0038	0.9268	0.0036	1.0813	0.0034	1.1047
0.0017	0.2316	0.0027	0.5872	0.0026	0.6933	0.0024	0.7110
-0.0010	-0.3486	0.0016	0.2571	0.0015	0.3072	0.0014	0.3115
-0.0023	-0.6388	-0.0008	-0.3932	-0.0007	-0.4563	-0.0008	-0.4446
-0.0036	-0.9250	-0.0020	-0.7120	-0.0018	-0.8463	-0.0018	-0.8260
-0.0050	-1.2018	-0.0032	-1.0419	-0.0029	-1.2249	-0.0027	-1.2396
-0.0063	-1.5062	-0.0043	-1.3748	-0.0041	-1.6010	-0.0037	-1.6312
-0.0077	-1.7821	-0.0055	-1.6982	-0.0052	-1.9709	-0.0048	-2.0253
-0.0090	-2.0669	-0.0066	-2.0391	-0.0064	-2.3433	-0.0058	-2.4143
-0.0104	-2.3490	-0.0078	-2.3559	-0.0075	-2.7344	-0.0068	-2.8010
-0.0091	-2.0494	-0.0088	-2.7068	-0.0087	-3.0970	-0.0079	-3.1910
-0.0077	-1.7722	-0.0077	-2.3679	-0.0076	-2.7159	-0.0067	-2.8189
-0.0064	-1.4879	-0.0066	-2.0277	-0.0065	-2.3196	-0.0057	-2.4228
-0.0051	-1.1943	-0.0055	-1.7012	-0.0053	-1.9526	-0.0048	-2.0113
-0.0037	-0.9139	-0.0044	-1.3606	-0.0042	-1.5755	-0.0038	-1.6208
-0.0024	-0.6264	-0.0032	-1.0332	-0.0031	-1.1883	-0.0028	-1.2257
-0.0008	-0.3174	-0.0020	-0.7067	-0.0019	-0.8211	-0.0018	-0.8371
		-0.0009	-0.3731	-0.0009	-0.4218	-0.0008	-0.4347

Table B.6. Experimental data for Figure 5.10

After 2 hours		After 4 hours		After 7 hours	
η (V)	I (A/g)	η (V)	I (A/g)	η (V)	I (A/g)
0.0029	0.0314	0.0029	0.0315	0.0029	0.0318
0.0057	0.0723	0.0057	0.0728	0.0057	0.0725
0.0086	0.1137	0.0086	0.1154	0.0086	0.1151
0.0114	0.1577	0.0114	0.1616	0.0114	0.1601
0.0142	0.2072	0.0142	0.2077	0.0142	0.2076
0.0170	0.2549	0.0170	0.2563	0.0170	0.2561
0.0199	0.3036	0.0198	0.3058	0.0198	0.3069
0.0227	0.3569	0.0226	0.3601	0.0226	0.3598
0.0199	0.3032	0.0198	0.3058	0.0199	0.3035
0.0171	0.2507	0.0170	0.2544	0.0170	0.2542
0.0142	0.2025	0.0142	0.2053	0.0142	0.2060
0.0114	0.1566	0.0114	0.1591	0.0114	0.1599
0.0086	0.1124	0.0086	0.1131	0.0086	0.1149
0.0057	0.0708	0.0057	0.0712	0.0057	0.0728
0.0029	0.0306	0.0029	0.0306	0.0029	0.0320
-0.0028	-0.0476	-0.0028	-0.0474	-0.0028	-0.0474
-0.0057	-0.0864	-0.0057	-0.0867	-0.0057	-0.0862
-0.0085	-0.1247	-0.0085	-0.1254	-0.0085	-0.1247
-0.0114	-0.1649	-0.0114	-0.1659	-0.0114	-0.1661
-0.0142	-0.2047	-0.0142	-0.2064	-0.0142	-0.2063
-0.0171	-0.2445	-0.0171	-0.2465	-0.0171	-0.2469
-0.0199	-0.2865	-0.0199	-0.2884	-0.0199	-0.2892
-0.0228	-0.3283	-0.0227	-0.3321	-0.0228	-0.3304
-0.0199	-0.2873	-0.0199	-0.2891	-0.0199	-0.2902
-0.0171	-0.2473	-0.0171	-0.2485	-0.0171	-0.2484
-0.0142	-0.2071	-0.0142	-0.2080	-0.0142	-0.2089
-0.0114	-0.1671	-0.0114	-0.1691	-0.0114	-0.1685
-0.0085	-0.1263	-0.0085	-0.1271	-0.0085	-0.1280
-0.0057	-0.0877	-0.0057	-0.0885	-0.0057	-0.0877
-0.0028	-0.0480	-0.0028	-0.0481	-0.0028	-0.0477
0.0029	0.0314	0.0029	0.0315	0.0029	0.0318

Table B.7. Experimental data for Figure 5.11a

CVD: 15 min		CVD: 30 min		CVD: 45 min		CVD: 60 min	
Time (hrs)	Slope (dI/dV)	Time (hrs)	Slope (dI/dV)	Time (hrs)	Slope (dI/dV)	Time (hrs)	Slope (dI/dV)
0	104	0	121	0	226	0	212
2	83.2	2	108	2	203	2	201
4	76	3.5	103.3	3.5	193	3.5	195.2
6	73.7	5	100.7	5	192.7	5	193.2
8	73.5	7	100	6.5	192	6.5	193
9	73.7						

Table B.8. Experimental data for Figure 5.11b

CVD: 15 min				CVD: 30 min			
Initial		Final		Initial		Final	
η (V)	I (A/g)	η (V)	I (A/g)	η (V)	I (A/g)	η (V)	I (A/g)
0.0024	0.1931	0.0026	0.1335	0.0024	0.2074	0.0025	0.1671
0.0047	0.4437	0.0051	0.3248	0.0047	0.4770	0.0047	0.4095
0.0070	0.6900	0.0075	0.5095	0.0069	0.7492	0.0070	0.6399
0.0093	0.9343	0.0100	0.6902	0.0091	1.0260	0.0093	0.8698
0.0116	1.1873	0.0125	0.8753	0.0114	1.3005	0.0116	1.1026
0.0139	1.4212	0.0150	1.0610	0.0136	1.5663	0.0139	1.3303
0.0163	1.6633	0.0175	1.2427	0.0159	1.8352	0.0162	1.5688
0.0186	1.8910	0.0199	1.4224	0.0181	2.1039	0.0184	1.8028
0.0163	1.6369	0.0175	1.2388	0.0159	1.8327	0.0162	1.5550
0.0140	1.3965	0.0150	1.0592	0.0136	1.5610	0.0140	1.3136
0.0117	1.1544	0.0125	0.8759	0.0114	1.2844	0.0117	1.0837
0.0094	0.9125	0.0100	0.6867	0.0092	1.0129	0.0094	0.8520
0.0071	0.6692	0.0076	0.5070	0.0069	0.7489	0.0071	0.6270
0.0048	0.4258	0.0051	0.3247	0.0047	0.4709	0.0048	0.3986
0.0025	0.1831	0.0026	0.1344	0.0025	0.1917	0.0025	0.1576
-0.0021	-0.3005	-0.0024	-0.2275	-0.0020	-0.3494	-0.0021	-0.2940
-0.0045	-0.5417	-0.0048	-0.4105	-0.0043	-0.6197	-0.0044	-0.5243
-0.0068	-0.7799	-0.0073	-0.5955	-0.0065	-0.8871	-0.0067	-0.7578
-0.0091	-1.0178	-0.0098	-0.7782	-0.0088	-1.1539	-0.0090	-0.9881
-0.0114	-1.2511	-0.0123	-0.9589	-0.0110	-1.4137	-0.0113	-1.2146
-0.0138	-1.4904	-0.0147	-1.1424	-0.0133	-1.6925	-0.0136	-1.4394
-0.0161	-1.7215	-0.0172	-1.3210	-0.0155	-1.9621	-0.0159	-1.6719
-0.0185	-1.9429	-0.0197	-1.4930	-0.0177	-2.2328	-0.0182	-1.8976
-0.0161	-1.7049	-0.0173	-1.3147	-0.0155	-1.9552	-0.0159	-1.6641
-0.0138	-1.4581	-0.0148	-1.1360	-0.0133	-1.6816	-0.0136	-1.4279
-0.0115	-1.2195	-0.0123	-0.9529	-0.0110	-1.4114	-0.0113	-1.2023
-0.0092	-0.9928	-0.0098	-0.7703	-0.0088	-1.1382	-0.0090	-0.9723
-0.0068	-0.7618	-0.0073	-0.5881	-0.0066	-0.8687	-0.0067	-0.7455
-0.0045	-0.5255	-0.0048	-0.4066	-0.0043	-0.6107	-0.0044	-0.5200
-0.0022	-0.2873	-0.0024	-0.2246	-0.0020	-0.3487	-0.0021	-0.2914

CVD: 45 min				CVD: 60 min			
Initial		Final		Initial		Final	
η (V)	I (A/g)	η (V)	I (A/g)	η (V)	I (A/g)	η (V)	I (A/g)
0.0021	0.3340	0.0022	0.2910	0.0021	0.3097	0.0022	0.2877
0.0040	0.7518	0.0041	0.6690	0.0040	0.7016	0.0041	0.6602
0.0058	1.1761	0.0060	1.0515	0.0059	1.1000	0.0060	1.0343
0.0076	1.6196	0.0079	1.4281	0.0078	1.4994	0.0080	1.4069
0.0094	2.0579	0.0099	1.7798	0.0096	1.8945	0.0099	1.7927
0.0113	2.4738	0.0119	2.1434	0.0115	2.2924	0.0118	2.1735
0.0131	2.9278	0.0138	2.5313	0.0134	2.6916	0.0137	2.5549
0.0150	3.3467	0.0157	2.9178	0.0152	3.0898	0.0156	2.9290
0.0131	2.9105	0.0137	2.5451	0.0134	2.6842	0.0137	2.5353
0.0113	2.4787	0.0118	2.1730	0.0115	2.2784	0.0119	2.1341
0.0096	2.0117	0.0099	1.7970	0.0097	1.8732	0.0100	1.7609
0.0077	1.5867	0.0080	1.4116	0.0078	1.4750	0.0080	1.3926
0.0058	1.1817	0.0060	1.0409	0.0059	1.0793	0.0061	1.0286
0.0039	0.7687	0.0041	0.6706	0.0041	0.6835	0.0041	0.6587
0.0021	0.3455	0.0022	0.2931	0.0022	0.2885	0.0022	0.2858
-0.0017	-0.4902	-0.0017	-0.4662	-0.0015	-0.5122	-0.0017	-0.4566
-0.0035	-0.9145	-0.0036	-0.8373	-0.0034	-0.9072	-0.0036	-0.8280
-0.0054	-1.3297	-0.0056	-1.2098	-0.0053	-1.3038	-0.0056	-1.1962
-0.0073	-1.7591	-0.0075	-1.5846	-0.0072	-1.6999	-0.0075	-1.5661
-0.0091	-2.1809	-0.0095	-1.9381	-0.0091	-2.0944	-0.0094	-1.9412
-0.0110	-2.5846	-0.0115	-2.2845	-0.0109	-2.4950	-0.0114	-2.3110
-0.0128	-3.0191	-0.0134	-2.6609	-0.0128	-2.8865	-0.0133	-2.6882
-0.0147	-3.4457	-0.0154	-3.0298	-0.0147	-3.2738	-0.0152	-3.0650
-0.0130	-2.9802	-0.0134	-2.6514	-0.0128	-2.8795	-0.0133	-2.6931
-0.0111	-2.5403	-0.0115	-2.2674	-0.0110	-2.4793	-0.0114	-2.3091
-0.0092	-2.1473	-0.0095	-1.9199	-0.0091	-2.0791	-0.0094	-1.9407
-0.0074	-1.7146	-0.0075	-1.5718	-0.0072	-1.6831	-0.0075	-1.5762
-0.0055	-1.3031	-0.0056	-1.1994	-0.0053	-1.2935	-0.0056	-1.2039
-0.0036	-0.8955	-0.0036	-0.8286	-0.0035	-0.8986	-0.0036	-0.8289
-0.0017	-0.4779	-0.0017	-0.4581	-0.0016	-0.5071	-0.0017	-0.4520